



UNIVERSITAT POLITÈCNICA
DE CATALUNYA
BARCELONATECH

Control and operation of wind power plants connected to DC grids

Kevin Schönleber

ADVERTIMENT La consulta d'aquesta tesi queda condicionada a l'acceptació de les següents condicions d'ús: La difusió d'aquesta tesi per mitjà del repositori institucional UPCommons (<http://upcommons.upc.edu/tesis>) i el repositori cooperatiu TDX (<http://www.tdx.cat/>) ha estat autoritzada pels titulars dels drets de propietat intel·lectual **únicament per a usos privats** emmarcats en activitats d'investigació i docència. No s'autoritza la seva reproducció amb finalitats de lucre ni la seva difusió i posada a disposició des d'un lloc aliè al servei UPCommons o TDX. No s'autoritza la presentació del seu contingut en una finestra o marc aliè a UPCommons (*framing*). Aquesta reserva de drets afecta tant al resum de presentació de la tesi com als seus continguts. En la utilització o cita de parts de la tesi és obligat indicar el nom de la persona autora.

ADVERTENCIA La consulta de esta tesis queda condicionada a la aceptación de las siguientes condiciones de uso: La difusión de esta tesis por medio del repositorio institucional UPCommons (<http://upcommons.upc.edu/tesis>) y el repositorio cooperativo TDR (<http://www.tdx.cat/?locale-attribute=es>) ha sido autorizada por los titulares de los derechos de propiedad intelectual **únicamente para usos privados enmarcados** en actividades de investigación y docencia. No se autoriza su reproducción con finalidades de lucro ni su difusión y puesta a disposición desde un sitio ajeno al servicio UPCommons No se autoriza la presentación de su contenido en una ventana o marco ajeno a UPCommons (*framing*). Esta reserva de derechos afecta tanto al resumen de presentación de la tesis como a sus contenidos. En la utilización o cita de partes de la tesis es obligado indicar el nombre de la persona autora.

WARNING On having consulted this thesis you're accepting the following use conditions: Spreading this thesis by the institutional repository UPCommons (<http://upcommons.upc.edu/tesis>) and the cooperative repository TDX (<http://www.tdx.cat/?locale-attribute=en>) has been authorized by the titular of the intellectual property rights **only for private uses** placed in investigation and teaching activities. Reproduction with lucrative aims is not authorized neither its spreading nor availability from a site foreign to the UPCommons service. Introducing its content in a window or frame foreign to the UPCommons service is not authorized (*framing*). These rights affect to the presentation summary of the thesis as well as to its contents. In the using or citation of parts of the thesis it's obliged to indicate the name of the author.



Departament d'Enginyeria Elèctrica



UNIVERSITAT POLITÈCNICA DE CATALUNYA

Doctoral Thesis

Control and Operation of Wind Power Plants Connected to DC Grids

Kevin Schönleber

Thesis advisors:

Prof. Oriol Gomis Bellmunt

Dr. Sergio Ratés Palau

Barcelona, November 2017

Control and operation of wind power plants connected to dc grids

by Kevin Schönleber

Examination Committee:

Dr. Jon Are Suul, Norwegian University of Science and Technology, Norway

Dr. Nicolaos A. Cutululis, Technical University of Denmark, Denmark

Dr. Daniel Montesinos Miracle, Polytechnic University of Catalonia, Spain

Universitat Politècnica de Catalunya
Escola Tècnica Superior
d'Enginyeria Industrial de Barcelona
Departament d'Enginyeria Elèctrica
Av. Diagonal, 647.
08028 Barcelona, Spain

Copyright © Kevin Schönleber, 2017

Printed in Barcelona

First Edition, November 2017



The research leading to this thesis has received funding from the People Programme (Marie Curie Actions) of the European Union's Seventh Framework Programme (FP7/2007-2013) under REA grant agreement number 317221. Any opinions, findings, and conclusions or recommendations expressed in this material are those of the author and do not necessarily reflect those of General Electric.

*"Man geht nicht nach dem Klettern zum Kaffeetrinken,
Kaffeetrinken ist integraler Bestandteil des Kletterns."*

Wolfgang Güllich

Abstract

Remote offshore wind power plants (WPPs) are being linked through high-voltage dc voltage-source converter (VSC-HVdc) transmission to the main grids. The current deployments of HVdc grid connections for offshore WPPs are point-to-point transmission systems. Moreover, WPPs connected to the offshore VSC-HVdc form an offshore ac grid which operates non-synchronously to the main grids. It is characterized by extensive submarine cabling and, in the case of full-scale power converter-based wind turbines, by being purely converter-based.

This thesis goes into two main aspects regarding the operation of HVdc-connected WPPs: i) reactive power and voltage control and ii) fault ride through (FRT) in the ac offshore grids.

Optimization-based reactive power control strategies are enhanced to the application of an ac grid consisting of one grid-forming and several grid-connected converters. A reactive power and voltage control method is introduced which aims to increase the annual energy production from a single WPP. In the industrial application, several WPPs might be clustered which leads to multi-layered controllers and operation boundaries. Taking this into account, an operation strategy with reasonable communication requirements is suggested and evaluated against conventional methods.

The work further proposes a control framework for the grid-forming offshore VSC-HVdc. Special emphasis is put on the FRT of unbalanced faults in the offshore grid and the provision of controlled currents for ease of fault detection. Furthermore, the internal variables of the offshore modular multi-level VSC-HVdc are analyzed. Moreover, four FRT strategies for the grid-connected converters are evaluated for unbalanced faults in the offshore grid. This consequently implies that control strategies in symmetrical components are considered. Furthermore, the reduction of over-modulation and over-voltages by the power converters in the offshore grid is dealt with.

Zusammenfassung

Hochspannungs-Gleichstrom-Übertragung (HGÜ) stellt eine effiziente Lösung zur Netzanbindung weit entfernter Offshore-Windkraftanlagen dar. Die derzeit verwendeten Punkt-zu-Punkt-Anbindungen basieren dabei auf spannungsgeführten Umrichtertopologien. Das seeseitige Wechselstromnetz verbindet die Windkraftanlagen mit der netzbildenden HGÜ-Umrichterstation. Es charakterisiert sich im Vergleich zu gewöhnlichen Netzen durch das ausschließliche Verwenden von Seekabeln und, im Fall einer Verwendung von Windkraftanlagen mit Vollumrichtern, durch das Fehlen gewöhnlicher, direkt gekoppelter Synchrongeneratoren.

Die vorliegende Dissertation behandelt zwei Kernaspekte bezüglich dem Betrieb HGÜ-angebundener Windparks: i) die kontinuierliche Regelung der Blindleistung und Spannung und ii) das Umrichterverhalten bei Spannungseinbrüchen aufgrund von Netzkurzschlüssen [*engl.* fault ride through (FRT)] im seeseitigen Wechselspannungsnetz.

Hierfür werden Blindleistungsoptimierungsverfahren präsentiert, die für die Anwendung in Wechselstromnetzen mit einem netzbildenden Umrichter und weiteren netzsynchronen Umrichtern geeignet sind. Die vorgeschlagene Blindleistungs- und Spannungsregelungsmethode verringert die Energieverluste im seeseitigen Netz und erhöht damit die Energieausbeute des Systems. Häufig werden verschiedene Windparks zu Clustern zusammengeschlossen, die mehrschichtige Regelungsansätze fordern. Hierfür wird ein weiteres Verfahren vorgeschlagen, das ähnliche Kommunikationsanforderungen wie herkömmliche Betriebsverfahren aufweist, jedoch geringere Verluste verursacht.

Die Arbeit untersucht ferner ein dynamisches Regelungsverfahren für den seeseitigen HGÜ-Umrichter. Dabei wird speziell das Verhalten während unsymmetrischer Kurzschlüsse im seeseitigen Netz berücksichtigt. Darüber hinaus wird der Betrieb des modularen Mehrpunktumrichters (*engl.* MMC)

für diese Anwendung analysiert. Bezüglich des Verhaltens netzsynchroner Umrichter während asymmetrischer Spannungseinbrüche im seeseitigen Netz werden weiterhin vier Verfahren untersucht. Diese zielen unter anderem auf die Verringerung von möglicher Übermodulation der Umrichter und Überspannungen im seeseitigen Netz ab.

Resumen

Los parques eólicos marinos suelen conectarse a redes eléctricas terrestres a través de corriente continua de alta tensión (siglas en inglés: HVdc) utilizando convertidores de fuente de tensión (siglas en inglés: VSC) cuando la corriente alterna de alta tensión (siglas en inglés: HVac) resulta tecnológicamente e económicamente desfavorable. Los parques eólicos conectados al convertidor HVdc marino crean redes eléctricas marinas de corriente alterna que operan asincrónicamente a las redes terrestres. Dichas redes se caracterizan por tener cables submarinos, y, en el caso de aerogeneradores con convertidores de plena potencia, resultan en redes constituidas únicamente por convertidores de potencia.

Esta tesis investiga dos de los aspectos principales de la operación de parques eólicos marinos conectados en corriente continua de alta tensión: i) la regulación de potencia reactiva y tensión y ii) la operación durante faltas eléctricas en las redes marinas.

Se han propuesto estrategias de optimización del control de reactiva para su aplicación a una red ac con varios convertidores conectados. Se ha introducido un método de regulación de potencia reactiva y tensión cuyo objetivo es incrementar la generación eléctrica del parque eólico. En la implementación práctica, varios parques eólicos podrían pertenecer a la misma red lo cual conduce a reguladores multicapas y a la consideración de las interfaces entre los operadores. Teniendo esto en cuenta, se propone una estrategia de regulación de potencia reactiva asumiendo unos tiempos de comunicación razonables, y se compara a conceptos convencionales.

La segunda parte de la tesis sugiere un método de control para el convertidor marino en secuencia directa e inversa. Está diseñado para la operación normal y la operación durante faltas asimétricas y permite la inyección de corrientes reguladas para la detección de la falta. Además, se analizan las variables internas del convertidor modular multinivel (siglas en inglés: MMC) en

estas situaciones. Asimismo, se han evaluado cuatro estrategias de respuesta a faltas asimétricas por parte de los convertidores de los aerogeneradores. Estas estrategias también incluyen el control en secuencia directa e inversa. Finalmente, se investiga la reducción de sobremodulación en los convertidores y sobretensiones en la red marina.

Acknowledgements

At the end of a long journey, it is the right moment to express my profound gratitude to those who constantly encouraged and supported me during the time of my doctoral thesis.

Antes de todo, un gran abrazo especial a mi pareja, Camille, para tu soporte infinito y tu amor. Muchas gracias por tu entusiasmo de mudarse a un sitio desconocido, darle vida y transformarle inmediatamente en nuestro hogar.

I am very grateful and owe my deepest respect to my academic thesis advisor, Prof. Oriol Gomis Bellmunt. Oriol, your support, guidance, and openness pushed me through the crucial parts of this journey. I am thankful for your unique sense to bring people together. My profound gratitude goes to my principal supervisor at GE Renewable Energy, Dr. Sergi Ratés Palau. Supervising a doctoral student besides the daily business might be challenging but you always showed interest and encouraged me in my work. Moltíssimes gràcies pel vostre suport!

I would also like to thank the thesis reviewers, Dr. Jon Are Suul and Dr. Nicolaos A. Cutululis, who agreed to judge my work and who contributed with their comments to the improvement of the thesis.

On the academic side, I would like to express my special thanks to all the MEDOW peers. MEDOW has been an amazing and thriving experience from the first day thanks to all of you. It has been very interesting and stimulating to meet and collaborate with people from all over the planet joined for a common European project. Thanks to Cath, for her great work, to the ESR and ER fellows, Li Gen, Alejandro, Marc, Ata, Abel, Robert, Raza, Jayachandra (Jayc), Mohammad, Jorge, Tibin, Sahar, Qing, Domenico, Rodrigo, and Agustí, and to the supervisors, to Jun, Dirk, Nikos, Helder, Nuno, Miquel, for their great guidance and for giving birth to this project. Another big thumbs up goes to the team from CITCEA–UPC: to Paz who

went the extra mile at the very beginning of our arrival. Many thanks for the fruitful collaboration, great discussions, cafés i calçotada a Carlos, Edu, Mònica, Joan, Enric, Ricard, Ana, and all the other members of the HVDC–Wind research group. I would like to thank Mikel de Prada Gil from IREC for the seamless collaboration on wake effects in wind power plants.

I owe many thanks to my great colleagues at GE Renewable Energy (formerly Alstom Wind): the grid integration team, Javier S., Domenico, David, Viçenc, Jordi, Lourdes, Gabriel; *los eléctricos*, Javier C., Xavi C., Marc O., Juan, Youssef, Xavi A., Ferrán, Ramón, Pedro, Hector, and Pablo. Thank you all for the integration into your great team. I also owe gratitude to Marc S. for his great support since the very start of the project.

I would also like to thank my former colleagues at IEH of KIT, especially Simon who from time to time provided a profound refresh of my native language by means of telephone calls in German.

Besides my research work, I was lucky to share memorable moments in the mountains with colleagues who became friends, namely the *pure torque ski tourers* and *pure torque climbers*, Jordi A., Oriol C., Thomas, Efren, and Jordi J.. In diesem Sinne auch besten Dank an die *Neujahrskletterer*, Florian, Anja und Jacky.

I was fortune to have research stays in lovely Wales and Denmark. I will always remember our daily escapes to Nata&Co with Abel and Marc and the beautiful nature and climbs (thanks for showing me around, Cerith and Seb) in Wales. In Denmark, I was very pleased with the snow and ice–free cycling lanes from Roskilde to Risø, the Friday breakfasts (Hygge) with the amazing team at DTU Wind, and the great people at Roskilde Klatreklub. Many, many thanks for these experiences.

Finally, I would like to express my gratitude to my parents, Judith and Peter, and my brother, Björn, for their unconditional support, encouragement, and frequent visits to Barcelona.

Barcelona, November 2017.

Kevin Schönleber

Contents

- Acknowledgements** **ix**

- List of Figures** **xv**

- List of Tables** **xix**

- Abbreviations** **xxi**

- 1 Introduction** **1**
 - 1.1 Background 1
 - 1.2 Objectives and limitations 4
 - 1.3 Contributions 5
 - 1.4 Outline of the thesis 7
 - 1.5 Simulation and modeling 8

- 2 Literature review** **11**
 - 2.1 Offshore wind energy and grid integration technology 11
 - 2.1.1 Offshore WT technology 12
 - 2.1.2 Offshore wind power plants 15
 - 2.1.3 Main grid connection with ac 18
 - 2.1.4 Main grid connection with dc 23
 - 2.1.5 Other concepts with connection in dc 26
 - 2.1.6 Grid code requirements 28
 - 2.2 Converter control in HVdc-connected WPPs 30
 - 2.2.1 Grid-connected operation 31
 - 2.2.2 Grid-forming operation 37
 - 2.2.3 Modular multilevel converter 45
 - 2.3 Reactive power in offshore WPPs 48
 - 2.3.1 Reactive power dispatch 49

2.3.2	Reactive power in HVdc-connected WPPs	51
2.4	Faults in offshore WPPs	53
2.4.1	Fault ride through by the WT converters	55
2.4.2	Fault ride through in HVdc-connected WPPs	57
2.5	Summary	59
3	Reactive power control in an HVdc-connected WPP	61
3.1	Introduction	61
3.1.1	Related publications	62
3.2	Methodology	62
3.2.1	Calculation of relevant losses	62
3.2.2	Reactive power allocation strategies	66
3.2.3	Formulation of the optimization problem	68
3.2.4	Implementation of the optimization-based strategies	70
3.2.5	Feasibility for the industrial application	71
3.2.6	Wakes effect modeling	71
3.3	Case study	73
3.3.1	Wind data	74
3.4	Results	75
3.4.1	Fixed voltage strategy with wake effect	75
3.4.2	Variable and fixed voltage strategies	81
3.5	Summary	90
4	Reactive power control for HVdc-connected WPP clusters	93
4.1	Introduction	93
4.1.1	Related publication	94
4.2	Methodology	94
4.2.1	System description and loss assessment	94
4.2.2	Reactive power control strategies	97
4.2.3	Optimization problem formulation	100
4.2.4	Active power variation within the cluster	103
4.2.5	Operational feasibility of the proposed strategies	104
4.3	Case study	105
4.4	Results	106
4.4.1	Analysis of WPP and VSC loss functions	107

4.4.2	Loss reduction for $\sigma^2 = 0$	108
4.4.3	Loss reduction for $\sigma^2 \geq 0$	110
4.4.4	Annual energy production and economic value	111
4.5	Summary	113
5	Fault ride through of the offshore MMC–HVdc	115
5.1	Introduction	115
5.1.1	Related publication	116
5.2	Methodology	116
5.2.1	Proposed grid–forming VSC–HVdc control	117
5.2.2	Current references saturation	120
5.2.3	MMC–HVdc in the grid–forming application	124
5.3	Case study	128
5.4	Results	131
5.4.1	LLLG fault at 150 kV	131
5.4.2	LL fault at 150 kV	132
5.4.3	SLG fault at 150 kV	138
5.5	Summary	143
6	Fault ride through of the WTs during unbalanced faults	145
6.1	Introduction	145
6.1.1	Related publications	146
6.2	Methodology	146
6.2.1	DDSRF implementation	146
6.2.2	Voltage sag detection	147
6.2.3	Active current limitation and reduction	148
6.2.4	Current and voltage limitations	148
6.2.5	Considered FRT strategies	152
6.3	Case study	154
6.4	Results	156
6.4.1	Comparison of the FRT strategies	156
6.4.2	FRT and impact on the offshore MMC–HVdc	167
6.5	Summary	174

7	Conclusions	177
7.1	Main conclusions	177
7.2	Future work	179
	Bibliography	181
	Appendix A: Mathematical transformations and converter losses	209
A.1	Reference frame and sequence transformations	209
A.2	Converter loss model for power system studies	210
	Appendix B: List of publications	213
B.1	Journal publications	213
B.2	Journal publications submitted/under revision	213
B.3	Conference publications/presentations	214
B.4	Co-authored publications	214
B.5	Patent applications	215
	Curriculum vitae	217

List of Figures

1.1	Schematic of large-scale deployment of remote offshore wind.	2
2.1	Drive-train/power conversion concepts used in offshore WTs.	14
2.2	Power curve of a generic WT.	16
2.3	Exemplary layout of an offshore WPP.	17
2.4	Main connection concepts for offshore WPPs.	20
2.5	Active power transmission capability of ac submarine cables.	22
2.6	Point-to-point HVdc connection of multiple WPPs.	24
2.7	Schema of grid-connected VSC and upper level control. . .	32
2.8	Current control in positive and negative sequence.	36
2.9	Grid-forming VSC state-of-the-art control options.	39
2.10	Grid-forming VSC with control option I.	40
2.11	Grid-forming VSC with control option II.	43
2.12	MMC basic layout schematic.	46
2.13	Grid code requirements on steady-state reactive power. . .	49
2.14	Reactive power dispatch in an ac-connected WPP.	50
2.15	Reactive power dispatch in an HVdc-connected WPP cluster.	52
2.16	Grid code requirements on FRT behavior.	56
3.1	Offshore grid system boundaries for loss assessment.	64
3.2	VSC relative losses in dependance of power output.	65
3.3	VSC absolute losses variation in dependance of reactive power.	65
3.4	Reactive power control concepts and communication paths.	67
3.5	Layout of the reference WPP Fécamp.	75
3.6	Wind rose and wake effect visualization.	76
3.7	Annual power productions under consideration of wakes. . .	78
3.8	Relative losses compared to strategy S1.	79
3.9	Reactive power production by the VSC-HVdc.	80
3.10	Reactive power production by WT7.	80
3.11	Relative system losses respective to S1.	82

3.12	Reactive power injection by the VSC–HVdc.	82
3.13	Reactive power injection by two WTs.	83
3.14	Voltage reference at PCC.	85
3.15	Loss distribution in the system.	86
3.16	Voltage distribution of fixed and variable strategies.	88
3.17	Reactive power injections of fixed and variable strategies.	89
4.1	Offshore grid of exemplary HVdc–connected WPP cluster.	95
4.2	Geographical distribution of the WPP cluster.	106
4.3	Loss functions of WPP1.	108
4.4	Absolute system losses for different strategies.	109
4.5	Absolute system losses under variable active power injections.	112
5.1	Grid–forming VSC–HVdc control in symmetrical components.	118
5.2	Voltage measurement decoupling.	119
5.3	Normal saturation method implementation.	122
5.4	Phasor diagram for the extended saturation.	123
5.5	MMC model schematic for the grid–forming application.	125
5.6	MMC inner current dependency of angle and voltage.	128
5.7	Electrical layout of the network configuration I.	129
5.8	Grid results for network configuration I.	135
5.9	MMC results for network configuration I.	136
5.10	Zoomed results for network configuration I.	137
5.11	Grid results for the SLG fault in network configuration I.	140
5.12	MMC results for the SLG fault in network configuration I.	141
5.13	Zoomed results for the SLG fault in network configuration I.	142
6.1	DDSRF–PLL implementation.	147
6.2	Impact of over–modulation on voltage and THD.	151
6.3	Electrical layout of the network configuration II.	154
6.4	Grid–related results for LL fault.	159
6.5	Detailed results for LL fault.	160
6.6	Converter–related results for the LL fault.	161
6.7	Grid–related results for SLG fault.	164
6.8	Detailed results for SLG fault.	165
6.9	Converter–related results for the SLG fault.	166
6.10	Grid–related results for network configuration II.	171

6.11	MMC-related results for network configuration II.	172
6.12	Zoomed results for network configuration II.	173

List of Tables

2.1	Industrial offshore WT platforms.	13
2.2	Typical parameters for submarine XLPE ac cables.	19
2.6	HVdc connections for offshore wind.	23
2.13	Comparison of control options for grid-forming operation.	44
2.15	Fault statistics in the Nordic and Baltic transmission grids.	54
3.4	Reactive power allocation strategies.	68
3.8	System parameter of the test system.	74
3.10	Mean, minimum, and maximum AEP with and without wakes.	77
3.11	Annual reactive power production of WTs and VSC-HVdc.	77
3.12	Annual energy production under consideration of wakes.	80
3.13	Annual energy loss comparison for all strategies.	88
4.2	Reactive power control strategies for WPP cluster.	99
4.6	Feasibility ranking of reactive power control strategies.	105
4.7	System parameter of the test system.	106
4.8	Polynomial coefficients of WPP loss functions.	107
4.9	Load flow results for full power scenario.	110
4.10	AEP of WPP cluster.	111
5.5	System parameter of the test system.	130
6.3	Overview of reference calculation strategies for FRT.	153
6.4	System parameter of the test system.	155
6.5	Mean THDs of VSC applied voltage and fault currents.	158
A.1	Typical converter loss parameter values.	211

Abbreviations

2L–HVdc	two–level VSC–HVdc.
AEL	annual energy loss.
AEP	annual energy production.
ARP	annual reactive power production.
CAPEX	capital expenditure.
CB	circuit–breaker.
CC	current control.
CD	central dispatcher.
DDSRF	decoupled double synchronous reference frame.
DDSRF–PLL	decoupled double synchronous reference frame phase–locked loop (PLL).
DFIG	doubly fed induction generator.
DFIG–WT	doubly fed induction generator–based wind turbine (type 3).
DR–HVdc	diode rectifier–based high–voltage dc.
DSOGI–FLL	double second–order generalized integrator frequency–locked loop (FLL).
DSRF	double synchronous reference frame.
EMT	electromagnetic transient.
FA	fault location A.

ABBREVIATIONS

FACTS	flexible ac transmission system.
<i>FINO</i>	Forschungsplattformen in Nord- und Ostsee (engl. Research platforms in the North Sea and Baltic Sea).
FLL	frequency-locked loop.
FRT	fault ride through.
FSC	full-scale converter.
FSC-WT	full-scale power converter-based wind turbine (type 4).
GC	grid code.
GSC	grid-side converter.
HVdc	high-voltage dc.
HVac-OS	high-voltage ac offshore substation.
IEC	International Electrotechnical Commission.
IGBT	insulated gate bipolar transistor.
ITN	Initial Training Network.
LCC	line-commutated converter.
LCC-HVdc	high-voltage dc line-commutated converter.
LFac	low frequency ac.
LL	line-to-line.
LLG	line-to-line-to-ground.
LLL	three-phase.
LLLG	three-phase-to-ground.
LPF	low-pass filter.
LV	low-voltage.
ME	monetary equivalent.

<i>MEDOW</i>	Multi-terminal dc grids for offshore wind.
MMC	modular multilevel converter.
MMC-HVdc	modular multi-level VSC-HVdc.
MSC	machine-side converter.
MV	medium-voltage.
neg.	negative.
OLTC	on-load tap changer.
OM	over-modulation.
OPEX	operating expenditure.
OPF	optimal power flow.
OSS	offshore substation.
OVRT	over-voltage ride through.
PCC	point of common coupling.
PF	power factor.
PI	proportional-integral.
PLL	phase-locked loop.
POC	point of connection.
pos.	positive.
PSC	partial-scale converter.
PSO	particle swarm optimization.
RC	reference calculation.
seq.	sequence.
SG	synchronous generator.
SLG	single-line-to-ground.
SM	sub-module.
SRF	synchronous reference frame.

ABBREVIATIONS

SRF-PLL	synchronous reference frame PLL.
STATCOM	static compensator.
THD	total harmonic distortion.
TSO	transmission system operator.
UK	United Kingdom.
USA	United States of America.
UVRT	under-voltage ride through.
VC	voltage control.
VSC	voltage-source converter.
VSCC	VSC control system.
VSC-HVdc	high-voltage dc voltage-source converter.
WPP	wind power plant.
WPPC	WPP control system.
WT	wind turbine.
WTC	WT control system.
XLPE	cross-linked polyethylene.

1 Introduction

The evidence of the global climate change ultimately pushes society to opt for cleaner energy generation alongside with other technological and cultural turnarounds. Renewable energy generation is one opportunity to lower the global carbon footprint when replacing conventional power generation.¹ However, its relatively low power density, dependence on the natural resource and derived remoteness from the load centers, and historical alignment of the industrialized states' power grids to the conventional generation demands for substantial transition of power grid planning, infrastructure, and operation. Offshore wind power plants (WPPs) are an emerging technology among renewable power generation whose large-scale deployment and high capacity factor² qualifies them as equivalent or even enhanced replacement for conventional power plants. When it comes to grid integration of very remote WPPs, at distances beyond around 100 km, high-voltage dc voltage-source converter (VSC-HVdc) transmission is the state of the art technology currently deployed in the industry. This thesis goes into the control and operation of such high-voltage dc (HVdc)-connected WPPs.

1.1 Background

Grid integration of very remote offshore WPPs is an emerging industrial reality which has passed the transition between research and industrial implementation. The early projects represented the increased risks associated with the installation of novel technology in harsh environments which resulted in project delays. As an example, the first HVdc-connected WPP project

¹The use of nuclear power plants equally results in a lower carbon footprint than coal-fired power plants but entails the risk of releasing radioactivity during a possible nuclear accident and involves the management of toxic nuclear waste.

²Capacity factor is the relation between the average power generation and nameplate power rating of a power plant.

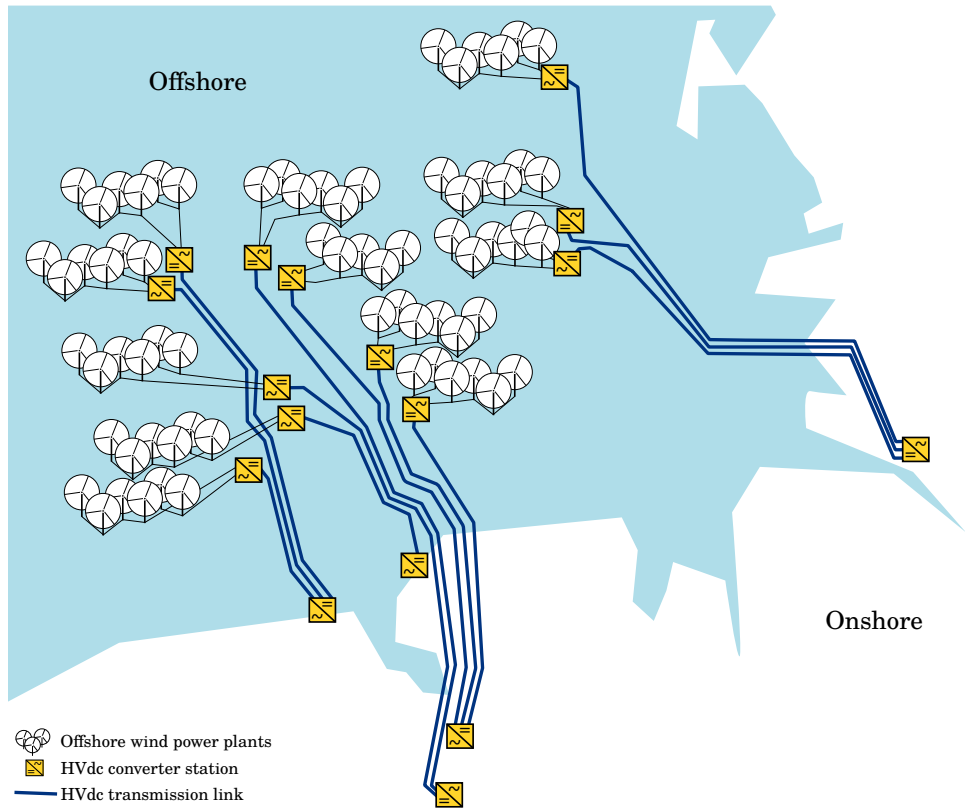


Figure 1.1: Schematic of large-scale deployment of remote offshore WPPs connected via HVdc to shore.

BorWin1 experienced significant delays and downtime due to harmonic issues in the offshore grid which were unknown in the planning phase [1]. Despite these risks, VSC-HVdc technology remains the currently viable technical-economical solution to connect remote offshore WPPs to the main power grids. Figure 1.1 sketches the large-scale deployment of HVdc-connected WPPs and their connection to shore.

Besides that, VSC-HVdc technology is a strong candidate for a pan-European overlay transmission grid. Such a dc grid might enhance flexible power exchange in Europe and facilitate the integration of large-scale renewable power generation [2]. Regardless of the HVdc connection topology (point-to-point, multi-terminal or meshed), the offshore ac grid formed by the WPPs and the offshore voltage-source converter (VSC) operates

asynchronously to the main grids³. Furthermore, the offshore ac grid is characterized by extensive submarine cabling and interfaced by multiple power converters. Several challenges are addressed in this thesis to improve the operation and control of those systems.

The research work was developed during an industrial PhD assignment at General Electric⁴ in collaboration with CITCEA–UPC⁵ in Barcelona, Spain. General Electric is a solution provider for onshore and offshore wind turbines (WTs), substations, and HVdc converters, among other businesses. CITCEA–UPC is a technology transfer center of the Technical University of Catalonia (UPC) with broad knowledge and technical expertise to build functional prototypes and is a reliant partner for industry. Besides that, the researcher conducted two three–month research stays at the Centre for Integrated Renewable Energy Generation and Supply (CIREGS) of Cardiff University (CU) in Wales, and at DTU Wind Energy, a department of Danmarks Tekniske Universitet (DTU) in Denmark.

The research assignment received funding from the People Programme (Marie Skłodowska–Curie Actions) of the European Union’s Seventh Framework Programme (FP7/2007-2013) under REA grant agreement n°317221, project title Multi–terminal dc grids for offshore wind (*MEDOW*)⁶. *MEDOW* is an Initial Training Network (ITN) with eleven partners (five universities and six industrial organizations) from six countries. The project aimed to tackle the different technical challenges of a pan–European overlay dc grid to integrate offshore wind. Therefore, twelve PhD researchers (early–stage researchers) and five postdoctoral fellows (experienced researchers) were appointed and worked in established research teams on four main pillars in the field of offshore wind integration through multi–terminal dc grids: connection of offshore wind power to dc grids (work package 1), investigation of VSCs for dc grids (work package 2), relaying protection (work package 3), and interactive ac/dc grids (work package 4). Furthermore, ITNs aspire to

³Obviously, this does not hold true for an embedded HVdc link with a parallel ac connection. To the knowledge of the author, such schemes are currently not planned for offshore wind integration, however, they might be applied in the future.

⁴The offshore wind business formed part of the energy division of Alstom which was acquired by General Electric (GE) in 2015. GE website: <http://www.ge.com/>

⁵CITCEA-UPC website: <http://www.citcea.upc.edu/>

⁶*MEDOW* project website: <http://sites.cardiff.ac.uk/medow/>.

train early-career researchers through experiences abroad and in the private sector as well as individual skill training to enhance and guide their careers in a key research field in an international environment.

1.2 Objectives and limitations

This thesis studies the control and operation of HVdc-connected WPPs under normal and faulted conditions.

The main objectives are outlined as follows:

- analysis, proposition and recommendation of reactive power dispatch strategies for the offshore ac grid of HVdc-connected WPPs. The particularities of such systems must be thoroughly addressed (decoupled operation, operation of multiple converters, and reactive power requirements and capabilities of key components);
- definition, analysis, and recommendation of reactive power/voltage control in HVdc-connected WPP clusters. WPP clusters connect multiple WPPs to a common offshore VSC-HVdc. Here, the actual operator boundaries for operation and control play a crucial role for the operation and control framework deployment;
- control method proposal and suitable current injection during fault ride through (FRT) of unbalanced faults by the grid-forming offshore VSC-HVdc;
- and analysis and recommendation of FRT strategies by the WT converters during unbalanced faults in the offshore ac grid.

The work performed in this thesis is bounded:

- from a technology perspective the focus is on offshore WPP(s), which are connected to the main grid by the state-of-the-art VSC-HVdc technology and, in particular with modular multilevel converter (MMC) technology;
- operation and control is uniquely focused on the decoupled offshore grid. The interaction of the HVdc transmission system with the main grid is out of scope;

- from electrical system perspective,
 - on WT side, only full-scale power converter-based wind turbine (type 4) (FSC-WT) are considered and specifically the grid-side converter (GSC) until the dc link interface. The control of the WT itself (pitch control, generator-side converter) is out of scope;
 - and on HVdc transmission system side, the offshore modular multi-level VSC-HVdc (MMC-HVdc) is the only focus. Again, the dc link interface presents the boundary for this thesis;
- and simulation models and tools are developed with a special purpose for this thesis in environments suitable for large-scale modeling. The implementation in experimental platforms is not aimed.

1.3 Contributions

The work done in this thesis contributed specifically to the field of operation and control of the decoupled offshore grid in HVdc-connected WPPs:

- formulation and implementation of a power loss model which combines grid and converter losses. It ultimately represents the power losses in the offshore grid for reactive power control studies more accurately;
- proposition of reactive power allocation strategies for the offshore grid in HVdc-connected WPPs. Fixed and variable strategies are defined which either rely on dispatch of reactive power set-points or additionally on a variable reference voltage;
- detailed analysis of the application of reactive power allocation strategies on the power losses occurring in the offshore grid,
 - emphasis on reactive power sharing between WT converters and the offshore VSC-HVdc. Conventional strategies relying solely on either the WT converters or the VSC-HVdc result in higher power losses than optimization-based ones which split the reactive power among the system;

- influence of non-uniform active power operating points caused by wake effects on the reactive power dispatch. The impact on the overall losses and reactive power by the VSC-HVdc depend mainly on the overall power output. The reactive power exchange by the individual WTs, however, is more influenced by their actual active power operating point;
- and impact of power output of the WPP on the optimal voltage reference. For low powers a decreased grid voltage effectively reduces the reactive power needs in the offshore grid. On the contrary, for higher power up to nominal an increased grid voltage is advantageous as the power losses are reduced;
- proposition of reactive power dispatch strategies for HVdc-connected WPP clusters. WPP clusters are the current industrial implementation and an additional control layer, as well as operator boundaries, must be considered;
- analysis of reactive power sharing, power losses, and voltage level in HVdc-connected WPP clusters under application of the proposed strategies. Suggestion of an optimization-based central reactive power dispatch for HVdc-connected WPP clusters;
- proposition of a control method for the grid-forming VSC-HVdc to cope with unbalanced faults in the offshore grid,
 - control method for grid-forming VSC-HVdc in symmetrical components;
 - enhancement of the short-circuit current provision during unbalanced faults in the offshore grid through two current reference saturation methods;
 - and analysis of impact on MMC internal variables by unbalanced faults in the offshore grid;
- proposition and analysis of FRT strategies for the WT converters during unbalanced faults in the offshore grid;

- recommendation to limit active current injection by the WT converters during unbalanced faults in the offshore grid to avoid over-voltages;
- and evaluation of converter over-modulation (OM) during unbalanced voltage conditions in the offshore grid for various FRT strategies.

1.4 Outline of the thesis

The thesis is structured in seven chapters:

- Chapter 2 provides a literature review on the basics and an overview of the relevant research that had been performed within the scope of the thesis. All the relevant aspects for the research work in the other chapters are intended to cover;
- Chapter 3 focuses on reactive power control strategies for steady-state operation of a single HVdc-connected WPP. Reactive power allocation concepts are developed which aim to reduce the power losses associated to the internal reactive power/voltage control. The distribution of reactive power between the WT converters and the offshore VSC-HVdc is proposed and the impact of wake effects and variable reference voltage demonstrated;
- Chapter 4 applies the findings of Chapter 3 to HVdc-connected WPP clusters where multiple WPPs are connected to the same offshore VSC-HVdc. The resulting operator and control layers are thoroughly considered. Reactive power allocation strategies are deployed which rely on an optimization of the reactive power injection by the WPPs and the reactive power/reference voltage by the VSC-HVdc;
- Chapter 5 proposes a control method for the grid-forming offshore VSC-HVdc based on symmetrical components. The voltage and current controls are implemented as loops in symmetrical components. The control method aims to enhance the FRT response during unbalanced faults in the offshore grid. Furthermore, two current reference saturation methods are defined and discussed for the network configuration where

the offshore VSC–HVdc is the sole converter operating in the offshore grid;

- Consequently, Chapter 6 analyzes unbalanced faults in the offshore grid when the WT converters are connected. Four FRT strategies for the WTs are evaluated and the impact on the overall system behavior is evaluated for different unbalanced voltage conditions. Special emphasis is paid to avoidance/reduction of OM by the WT converters which might introduce further disturbances during the fault. Furthermore, the control method and proposed saturation principles of Chapter 5 are demonstrated for the offshore grid with WT converters in operation;
- And Chapter 7 concludes the thesis and provides suggestions on future work in the field of remote offshore wind grid integration.

It is intended to provide standalone chapters in terms of contributions from this thesis. However, it should be mentioned that all the relevant state of the art is summarized in Chapter 2. Furthermore, Appendix A adds brief information on transversal topics of the Chapters 2 to 6.

1.5 Simulation and modeling

The thesis deploys power system simulation for the development of the different studies. Steady–state, load flow calculation models are used for the reactive power control management introduced in Chapters 3 and 4. Here, MATLAB is utilized with the open–source package Matpower [3] and fmincon of the Optimization Toolbox. The ability of flexible optimal power flow (OPF) integration in fmincon was the major driver for the choice of MATLAB. The load flow results were verified with a DIgSILENT Power Factory load flow model and showed the expected match. Alternatively, it might be also possible to implement the OPF directly in DIgSILENT Power Factory which has more advanced possibilities for integration of power converter constraints e.g. capability curves. As it is demonstrated in the mentioned chapters, the simulations were capable to handle a series of operating scenarios and, besides that, MATLAB offered a straight–forward post–processing of the result

data. Load flow calculations are widely accepted to provide a good accuracy for this type of studies.

The Chapters 5 and 6 treat fault analysis in the time domain by means of electromagnetic transient (EMT) simulations. For the simulations, MATLAB Simulink/SimPowerSystems is used. The models were developed from scratch using the well-known control blocks of Simulink/SimPowerSystems. VSC modeling was performed with the average model available in SimPowerSystems, relating ac and dc side under assurance of the power balance [4]. The MMC-HVdc model was adopted for the grid-forming operation mode from [5]. For the scope of the work on the FRT strategies of the converters, the use of switching models with accurate representation of the insulated gate bipolar transistor (IGBT) behavior might be too detailed and time consuming.

In the beginning of the work, it was decided not to utilize manufacturer specific models. In contrast to manufacturer specific models and also generic models, self-developed models allow i) to reduce the complexity for the phenomena under study, ii) built up the model in a step by step approach, having full control and understanding of its behavior, and iii) a certain academic freedom to publish in the case of an industrial PhD. For instance, generic or manufacturer specific models with the functionalities needed for the conducted work, such as e.g. negative sequence current control and grid-forming controllers, were not available at the time of the simulation studies for this thesis.

2 Literature review

This chapter treats offshore wind energy and the current state-of-the-art technology to transform it into electrical energy. The main grid connection options for offshore WPPs are described among other system approaches. Further emphasis is paid to the principles of power converter for the grid-connected and the grid-forming operation mode which are both present in HVdc-connected WPPs. Then, the operation and control of these systems is described and oriented to the two main research areas of this thesis, namely reactive power control and FRT in the offshore grid.

2.1 Offshore wind energy and grid integration technology

The offshore wind resource is characterized by higher intensity, steadiness, and frequency compared to the onshore wind resource as shown by microscale local measurement campaigns at offshore locations [6], [7] and mesoscale wind resource assessments [8], [9]. Simultaneously, the environment of the open sea leads to less perturbation due to the low surface roughness and lack of obstacles [10]. The remoteness of offshore locations makes them favorable in terms of reduced noise emission restrictions, social acceptance, and vast space availability for large-scale deployment. However, offshore deployment might be unfavorable due to the likely lack of an existing power grid infrastructure, complexity of access for commissioning, operation and maintenance, and decommissioning, and more sophisticated foundations compared to onshore locations [11]. Today, the use of offshore wind energy by WPPs still incurs around double the cost of the onshore counterpart [12]. The higher price is mainly due to the different foundation and substructure and the lack of electrical grid infrastructure [11]. By comparison, an onshore WT encounters

75 % of the total project costs, whereas offshore WT presents only 40 % to 50 % (excluding foundation) [11]. The dedicated grid connection accounts for usually around 15 % to 20 % of the overall project capital expenditure (CAPEX) cost, but is highly project dependent [11], [12].

2.1.1 Offshore WT technology

The first generation of offshore WTs during the late 20th century were usually modified designs of their onshore counterparts [10]. Dedicated designs for offshore WTs have been developed since the ratings reached the multi-megawatt class. Such offshore WTs are three-bladed, variable-speed and pitch-controlled upwind machines. Thus the general concept is still similar to their onshore peers. Nevertheless, there are significant technical differences:

- foundation and substructure,
- component dimension and weight,
- and drive-train/generator/power converter concept.

The foundation and substructure establishes the mechanical interface between the WT and the seabed. It is obvious that there is a difference in complexity compared to land-based foundations due to the sea environment, water depth, and soil conditions [13]. As of late 2016, the rotor diameter reaches around 150 m for a power rating of 6 MW ¹. The longest blade produced and tested at that time is of 88.4 m [14]. Tower heights are rather moderate (around 100 m) as the low surface roughness allows energy capture at lower heights than onshore.

Larger rotor diameters and higher power ratings are the major driver for cost reduction efforts for offshore wind [12]. Increased individual WT power ratings intrinsically lower the number of WT units per WPP and therefore the CAPEX (lower part count, reduced installation time, logistics) and the operating expenditure (OPEX) (maintenance simplification). WTs in the 10 MW class and beyond might be feasible within the next decade [15]. Prior to the development of entirely new platforms, WT manufacturers aim to

¹e.g. GE Haliade 150-6MW with 150 m rotor diameter and an individual blade length of 73.5 m or Siemens SWT-6.0-154 with 154 m rotor diameter and 75 m-long blades.

upgrade their current platform maintaining the largest number of components possible. An example is the evolution of the Siemens SWT–6.0–154 with the same rotor diameter to the Siemens SWT–7.0–154 [16].

WT systems might be divided into a mechanical and electrical sub–system linked by the generator [17]. The drive–train concepts (mechanical part) are almost as numerous as the number of different manufacturers, whereas the electrical part can be classified into two main types: partial–scale converter (PSC)–based or full–scale converter (FSC)–based [18]–[20]. The current drive–train/generator/power converter concepts are compared for the main offshore WT platforms in the market in Tab. 2.1.

Table 2.1: Offshore WTs in the market. The information shown is limited to the largest model of the market–relevant manufacturers as of December 2016 [16], [21]–[24].

Model	Power	Drive	Generator	Power converter
Adwen AD 5-132 ¹	5 MW	gearbox	PMG (medium–speed)	full–scale
Adwen AD 5-135 ²	5 MW	gearbox	PMG (medium–speed)	full–scale
GE Haliade 150–6MW ³	6 MW	DD	PMG (low–speed)	full–scale
MHI Vestas V168– 8MW	8 MW	gearbox	PMG (medium–speed)	full–scale
Senvion 6.2M152	6.15 MW	gearbox	DFIG (high–speed)	partial–scale
Siemens SWT–7.0–154	7 MW	DD	PMG (low–speed)	full–scale

¹ Formerly named Gamesa G132-5.0 MW.

² Formerly named Areva M5000.

³ Formerly named Alstom Haliade 150–6MW.

From Tab. 2.1 it can be observed that there is a clear trend for FSC–WTs in the multi–megawatt class. Only one manufacturer (Senvion) remains with a doubly fed induction generator–based wind turbine (type 3) (DFIG–WT) product. The two prevailing WT power conversion concepts are drawn schematically in Fig. 2.1.

The PSC–based option or DFIG–WT uses an induction generator whose rotor windings are excited and controlled through the rotor–side converter. Slip rings with brushes give access to the rotor windings. The stator of the

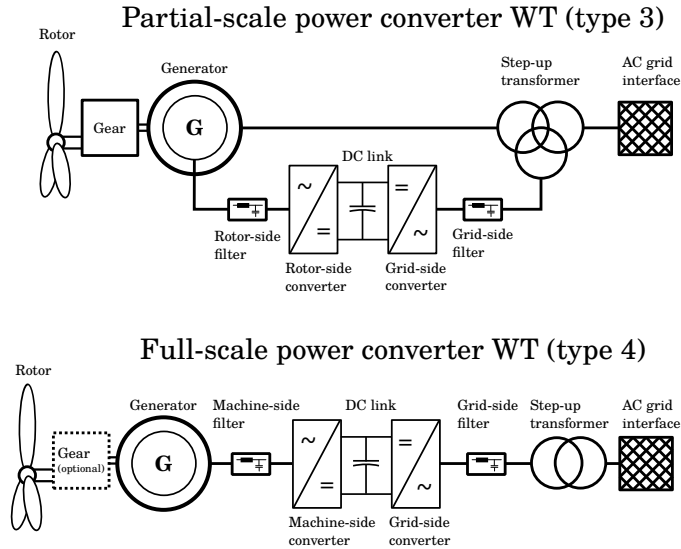


Figure 2.1: Drive-train/power conversion concepts used in offshore WTs.

generator is directly connected to the grid as well as the GSC. The output power of the system is the combination of the stator and rotor power. The power converter system is usually rated to 30% of the nominal power to provide a limited speed range of $\pm 30\%$. The advantage of the DFIG-WT is a lower CAPEX but a higher OPEX mainly due to expected maintenance costs for the multi-staged gearbox and slip-rings [19], [20]. For the onshore market the doubly fed induction generator (DFIG) wind turbine has a significant share. Regarding DFIG-WTs, the reader is further referred to [17], [19], [20], [25], [26].

The FSC-WT consists of a drive-train/generator system which is connected through a FSC. The drive-train/generator might be based on a geared concept or a direct-drive solution without gearbox [27], [28]. Moreover, the generator might be permanently excited through permanent magnets or externally by excitation windings. The FSC couples the machine-side and the grid-side through the dc link. The dc link transmits purely active power $p_{dc} = u_{dc}i_{dc}$ and decouples both sides in terms of frequency, voltage, and reactive power. Therefore, FSC-WTs advantageously meet grid codes and especially under-voltage ride through (UVRT) requirements which exceed flexibility in fast control requirements [25]. For instance, they might provide reactive power

during no-wind conditions [in static compensator (STATCOM) mode] where DFIG-WTs encounter problems due to the direct stator connection to the grid [25]. For higher power ratings ($> 5\text{ MW}$), it is likely to have n power channels ($n > 1$) in parallel to successfully matching the full power rating of the machine with state-of-the-art low-voltage (LV) converters. Hence, it still permits a reduced power production when up to $(n - 1)$ power channel(s) fail [17], [28]–[31]. For larger power ratings, even multi-channel structures might use medium-voltage (MV) in the power conversion part to reduce power losses. On the generator side, multi-channel structures permit the design of poly-phase system with the objective of increased reliability [31]–[33].

Regardless of whether the electrical interface of the WT is of type 3 or type 4, the variable-speed, pitch-controlled machine is designed for rated wind speed and power. The rated wind speed roughly divides the power output into two operating areas:

- partial power production;
- and full power production.

Partial power production usually relies on a speed/torque control, whereas for wind speeds above the rated wind speed the energy capture is controlled through pitch control. Outside these areas, power production is either not efficient with respect to the power consumption of the WT (below cut-in wind speed) or exceeds the design limitations (above cut-out wind speed). The power for wind speeds above the cut-out speed might be partially captured through load-dependent turbine control [34]. The cut-in and cut-out wind speeds for common offshore WT designs are around 3 m s^{-1} and 25 m s^{-1} [16], [22]. Moreover, WTs are designed for a lifetime of at least 20 yrs [35].

2.1.2 Offshore wind power plants

Owing to the relatively low power rating of a singular WT compared to conventional large-scale power plants, multiple units are grouped to form a WPP. The WTs are positioned with respect to several conditions e.g. spacing rules in the prevailing wind direction, soil characteristics, shipping and pipeline routing, etc. [36]. The WPP covers thus a large geographical area with distributed power generation. Therefore, WPPs have a low power density

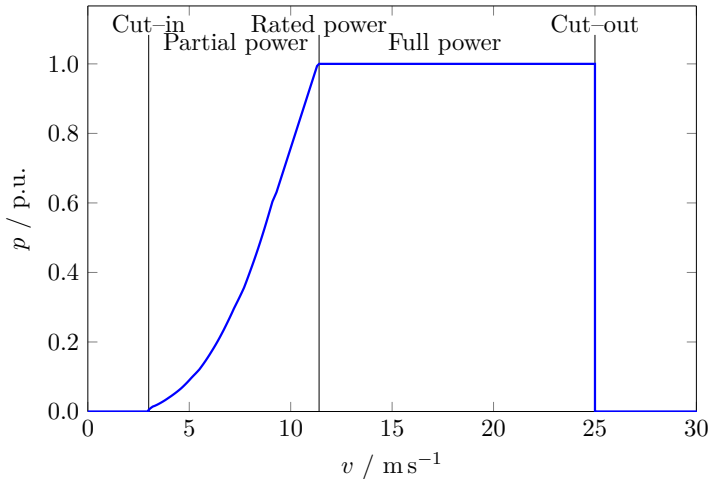


Figure 2.2: Power curve of a generic WT.

of around 8 MW km^{-2} to 10 MW km^{-2} compared to around 2500 MW km^{-2} for conventional power plants². A medium-voltage ac (MVac) collection grid assembles the generated power to a common point of connection (POC). It operates at a standard frequency of 50 Hz or 60 Hz (depending on the regional standard) and nominal voltages of 20 kV or 33 kV. The standardized grid frequency features the use of fully commercialized electrical components like transformers, cables, and switchgear which comes along with significant advantages in terms of costs, expertise, and availability. The nominal voltage level of 20 kV or 33 kV is deployed due to the individual power rating, availability of standard components, and a broad experience in the installation, operation, and maintenance thereof in land-based environments (e.g. distribution level, rural MV power systems, onshore WPPs). In general, the evolution of WT power rating is directly followed by the application of the next standard voltage level to reduce the nominal currents and to inherently lower the power losses. High-voltage (HV) collection grids, namely operating at 66 kV, are currently in the standardization process and to be employed with higher individual WTs ratings within the immediate future [38]–[40].

²Indicative estimations calculated from the leasing area of Fécamp offshore WPP [37] against an exemplary conventional power plant such as *Grosskraftwerk Mannheim Block 9* (steam power plant, 911 MW, area of 2.75 km^2 estimated with OpenStreetMap) in Mannheim, Germany.

An exemplary collection grid is shown in Fig. 2.3. A plurality of WTs forms a feeder when the WTs are linked together as a radial to a common POC [41]. The collection is done by means of submarine cables. The cross-sections of the submarine cables are adopted according to the rated power of the connected WTs. Usually, only two to three different cable cross-sections are deployed in a large-scale WPP for ease of logistics, simplification, and cost [42]. Furthermore, some projects employ ring or meshed grids for emergency supply during commissioning, maintenance, grid loss, or cable damage [43]. Ref. [36] gives a complete overview on grid topologies and proposes a tool for the cable selection process for different WPPs ratings.

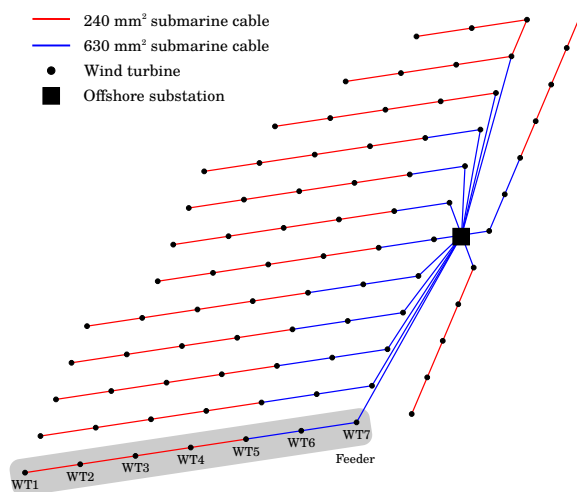


Figure 2.3: WPP layout with WT positions, inter-array cables, and offshore substation [37].

The submarine (or subsea) cable consists of either a unique three-core cable incorporating the conductors and usually a communication link (e.g. fiber optics) or, for larger cross-sections, three individual single-phase cables [44]. In the latter case, the communication link needs to be installed separately and is normally bundled with the power cables in the same trench. The conductor material is generally aluminum or copper. Submarine cables with cross-linked polyethylene (XLPE) insulation are the primary choice for underground and submarine cables because of environmental reasons, higher efficiency, smaller bending radius, lower weight, and increased operational

temperatures compared to liquid-filled cable systems [44], [45]. The cross-section of the conductor(s) is the relevant characteristic for the loading current(s), whereas the insulation material and thickness determine the nominal and maximum voltage limitations. Typical cable parameters as published by the manufacturers are listed in Tab. 2.2. The resistance R' and inductance L' p.u.-length decrease for larger cross-sections, respectively. The capacitance p.u.-length C' increases for larger cross-sections and decreases for higher nominal voltages U_{nom} .

In offshore WPPs, the submarine cables are laid on or buried in the seabed, respectively. To provide the routing of the cable from the seabed to the fixed offshore foundations, i.e. WTs or platforms, so-called J-tubes made of steel or polymeric materials are used. J-tubes provide effective routing, stability, and additional protection to the cable at these interfaces [45]. Burying the cables in the seabed reduces the risk of threats from very small anchors and fishing equipment. Nevertheless, ship anchors and fishing (especially trawling nets) and other marine activities form the primary threat of external damage of submarine cables. Consequently, during installation and maintenance phases the risk for cable damages is higher [44]. The laying of the cables is performed by dedicated installation vessels and is highly relevant for the effective operation and lifetime of the cables. Failure rates between 0.07 to 0.3 per 100 km yr⁻¹ might be feasible, although there is a lack of experience in the specific application of offshore WPPs [44], [48].

2.1.3 Main grid connection with ac

The main grid connection might be done with ac technology. The transmission voltage from offshore towards onshore is mainly dependent on a technical-economical assessment considering the distance from shore and the power rating of the connected WPP(s).

For nearshore projects with a lower power rating, the WTs are connected without intermediate offshore platform to shore. The MV cables of the collection grid are extended to shore and assembled at the point of common coupling (PCC). To interface them to the main power system at transmission voltage (≥ 110 kV) a voltage transformation via ac power transformers is necessary. The advantage of such systems are the savings of an additional

Table 2.2: Typical electrical parameters for submarine XLPE ac cables with copper conductors of different cross-sections and voltage levels: 33 kV [46], [47], 66 kV to 220 kV [47].

Nominal voltage $U_{\text{nom}}/$ kV	Cross-section $A/$ mm^2	Nominal current $I_{\text{nom}}/$ A	Nominal power $S_{\text{nom}}/$ MVA	Resistance $R'/$ $\Omega \text{ km}^{-1}$	Inductance $L'/$ mH km^{-1}	Capacitance $C'/$ $\mu\text{F km}^{-1}$
33	95	300	17.15	0.25	0.42	0.17
	240	480	27.44	0.10	0.36	0.23
	500	655	37.44	0.05	0.32	0.32
	630	715	40.87	0.04	0.31	0.34
	800	775	44.30	0.03	0.30	0.37
66	95	300	34.29	0.25	0.44	0.17
	240	480	54.87	0.10	0.38	0.22
	500	655	74.88	0.05	0.34	0.29
	630	715	81.74	0.04	0.33	0.32
	800	775	88.59	0.03	0.32	0.35
132	1000	825	94.31	0.02	0.31	0.38
	500	655	149.75	0.05	0.38	0.20
	630	715	163.47	0.04	0.37	0.21
	800	775	177.19	0.03	0.36	0.23
150	1000	825	188.62	0.02	0.35	0.25
	500	655	170.17	0.05	0.40	0.17
	630	715	185.76	0.04	0.38	0.19
	800	775	201.35	0.03	0.37	0.21
220	1000	825	214.34	0.02	0.36	0.23
	500	655	249.59	0.05	0.43	0.14
	630	715	272.45	0.04	0.41	0.16
	800	775	295.31	0.03	0.40	0.17
	1000	825	314.37	0.03	0.38	0.19

offshore platform. Nevertheless, smaller projects are connected with MVac connection such as Block Island [United States of America (USA)], Burbo Bank, Lynn and Inner Dorsing [all United Kingdom (UK)], Middelgrunden (Denmark), and Egmond aan Zee (The Netherlands). In the future, the direct connection to shore without intermediate offshore high-voltage ac (HVac) substation might regain interest when 66 kV HV collection grids are deployed, e.g. Blyth offshore demonstrator wind farm (UK).

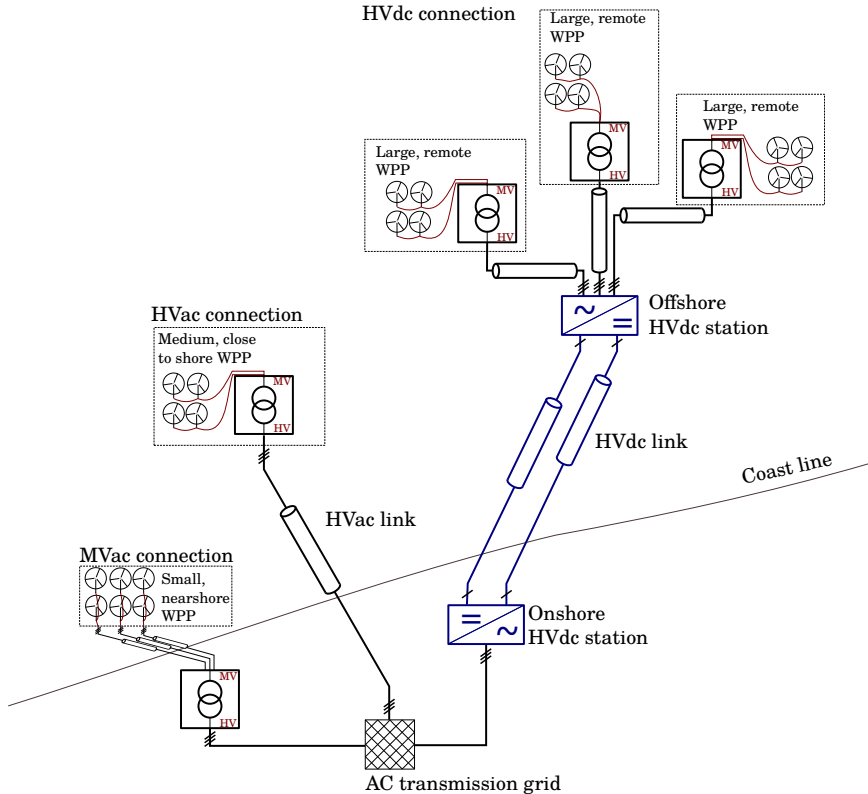


Figure 2.4: Three concepts for the main grid connection of offshore WPPs. Integration of a small, nearshore WPP might utilize a MVac connection, a medium-sized WPP in moderate distance to shore an HVac connection, and a remote WPP cluster an HVdc connection, respectively.

For remote WPPs with larger power ratings, it is economically beneficial to employ a dedicated offshore platform, incorporating an HVac substation, and to transmit the power via an HVac grid connection to shore. The ac transformer(s) on the HVac substation converts the MV or HV collection grid voltage to a higher transmission voltage. The employed voltage levels for the grid connection are the International Electrotechnical Commission (IEC) standard voltage levels of 110 kV, 132 kV, 150 kV, or 220 kV [49]. Exemplary WPPs connected in HVac technology are London Array (UK), Alpha Ventus (Germany), and Lillgrund (Sweden).

Similarly to the collection grid, submarine cables are used for the HVac grid

connection because overhead lines are not an option for offshore application. As the cable length becomes greater compared to the collection grid cables, there is a significant impact on the reactive power management of the cable. An ac submarine cable might be represented as a cylindrical capacitor [50]. The capacitance p.u.-length C' of the cable depends on the length, insulation material and its thickness (mainly dictated by the nominal voltage), and the conductor cross-section:

$$C' \propto \varepsilon_r \cdot \log(d_{\text{out}}/d_{\text{in}})^{-1} \quad (2.1)$$

where:

- C' = cable capacitance p.u.-length;
- ε_r = relative permittivity of the insulation;
- d_{out} = outer diameter of insulation;
- d_{in} = inner diameter of insulation.

Submarine cables have a higher per-unit capacitance than overhead lines because firstly, d_{out} is significantly smaller for cables (equivalent to approx. the insulation thickness) and secondly, the relative permittivity of XLPE ($\varepsilon_{r,\text{XLPE}} \approx 2.25$) is higher than the one of air ($\varepsilon_{r,\text{air}} = 1$) [51], [52]. The per-unit capacitance causes a reactive charging current I_{charg} [51]:

$$I_{\text{charg}} = \omega C' l \cdot U_{\text{nom}} \quad (2.2)$$

where:

- ω = angular frequency;
- l = cable length.

Besides, the active power transfer of a three-phase ac cable is hence decreased by the reactive power generated by the capacitive charging current [2]:

$$P_{\text{ac}} = \sqrt{S_{\text{nom}}^2 - Q_{\text{ac}}^2} - 3R'lI_{\text{nom}}^2 \quad (2.3)$$

where:

P_{ac} = transmittable ac active power;

Q_{ac} = total ac reactive power of the cable.

The active power transmission capability for submarine cables is plotted in Fig. 2.5. The plot presents the active power transmittable over a conductor cross-section of 1000 mm^2 at the voltage levels 66 kV to 220 kV. The capability might be roughly doubled when the capacitive nature of submarine and underground cables is compensated by the installation of shunt reactors at both ends of the cable [50]. For very long cables, it might be necessary to provide such compensation as well at intermediate sections of the cable route due to the distributed capacitance. In case of a submarine cable, this leads to intermediate compensator platforms where cables are routed up on both sides of the platform with an intermediate compensation [53], [54]. It is obvious that such engineering practice contradicts a simple solution and is very likely to have a significant increase in cost.

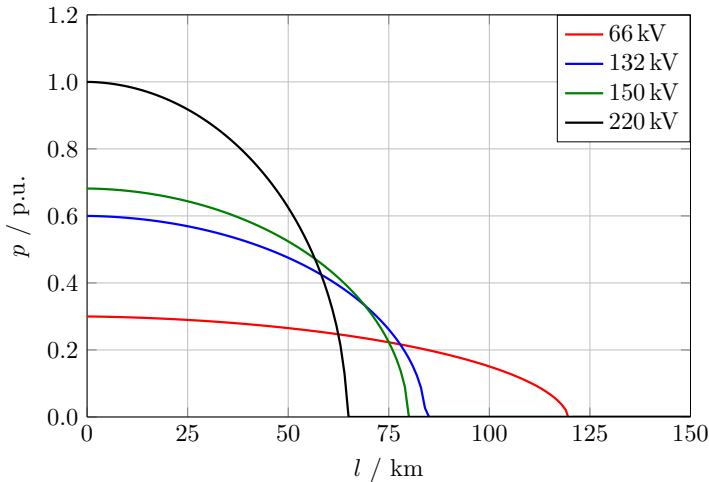


Figure 2.5: Active power transmission capability of ac submarine cables with a fixed cross-section of 1000 mm^2 and at different voltage levels. The active power p is scaled to the rating of the 220 kV cable.

One WPP might be connected with redundant grid connection systems to the grid. Multiple HVac substations might be caused by the area of the WPP and/or its power rating. It is usual that parallel transformers are deployed on the HVac substation to avoid complete loss of production in the case of

failure [42].

2.1.4 Main grid connection with dc

For very remote offshore WPPs grid connection through HVac becomes cumbersome: the reactive power compensation requirements increase with the transmission distance, which inherently decreases the active power capability [50], [55], [56]. Staying with ac technology would require either more parallel submarine cables and/or intermediate compensation platforms. Both solutions imply a significant cost increase and a larger environmental impact. At that point, HVdc transmission becomes more cost-effective. For land-based bulk power transmission over a large distance with overhead lines, the break-even area is around 600 km to 800 km [57]. For the application of the grid connection of very remote offshore WPPs, the HVac/HVdc break-even area identified in literature oscillates between 60 km to 120 km [2], [50], [55], [56]. The data of installed projects with dc technology are shown in Tab. 2.6. It might be highlighted that the total transmission length exceeds at least 130 km for the listed projects. However, projects with shorter transmission length, e.g. NOR-3-3 (DolWin6) of 90 km, are also planned [58].

Table 2.6: Installed HVdc connections for offshore wind as of mid 2017 [55], [58]. All projects are in the German North Sea.

Name	Transmission capacity P / MW	Transmission voltage U_{dc} /kV	Transmission length ¹ l / km	Converter technology
BorWin1	400	± 150	200 (125/75)	2L-HVdc
BorWin2	800	± 300	200 (125/75)	MMC-HVdc
DolWin1	800	± 320	165 (75/90)	MMC-HVdc
DolWin2	900	± 320	135 (90/45)	MMC-HVdc
HelWin1	576	± 250	130 (85/45)	MMC-HVdc
HelWin2	690	± 320	130 (85/45)	MMC-HVdc
SylWin1	864	± 320	205 (160/45)	MMC-HVdc

¹ Total length (submarine/underground cable).

In principle, two asynchronous grids are linked for an HVdc-connected WPP [50], [59], [60]. The basic scheme to interface two asynchronous grids is made by the offshore and onshore HVdc converters, respectively, and the

intermediate dc link. Furthermore, the offshore VSC–HVdc interfaces the offshore ac grid with the WPP(s), whereas the onshore VSC–HVdc interfaces the main ac grid [55]. Apart from the decoupled operation, the offshore grid is as well as an isolated grid with no synchronous generator (SG) connected which in conventional power systems provides system inertia and manages the power balance between generation and consumption. Consequently, the offshore grid needs a voltage reference to operate. Being the central and largest capable unit for this task, the offshore HVdc converter provides the voltage reference and acts as an infinite ac bus which inherently sinks all power from the offshore grid. The onshore VSC–HVdc is operated in grid–connected mode. A schematic of an HVdc grid connection is drawn in Fig. 2.6 and further shown in the offshore wind grid connection overview in Fig. 2.4.

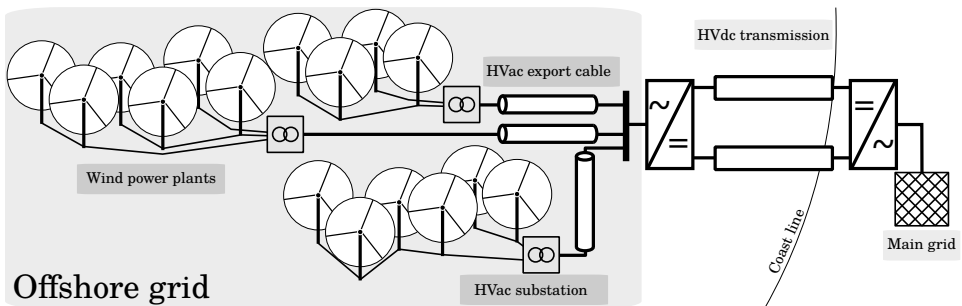


Figure 2.6: Point-to-point HVdc connection of multiple WPPs.

There are two technologies for HVdc converters: line-commutated converter (LCC) and VSC. High-voltage dc line-commutated converter (LCC–HVdc) technology is based on semi-controllable switches (e.g. thyristor valves). These switches can be turned on through a gating signal, whereas the current interruption (turn off) is dictated by the following zero-crossing of the current. The commutation process of the converter is however determined by the connected ac system [61]. An LCC–HVdc draws 0.5 p.u. to 0.6 p.u. of reactive power from the connected ac grid, which is caused by the converter transformer, the commutation inductance, and the delay firing angle [50]. This results in an additional reactive power compensation requirement which is usually satisfied by switchable compensation devices installed at its ac terminals. Being a six- or twelve-pulse converter, there are ac filter requirements

to attenuate the harmonics in the ac waveform [50]. Bi-directional power flow is possible under a polarity change of the dc voltage. The devices used to meet the reactive power compensation and harmonic filter requirements require significant space. Furthermore, connection of LCC-HVdc needs an ac voltage to operate satisfactorily. If an ac voltage is not present (such as in an isolated grid without SGs), it might be provided by an additional converter which is capable of supplying ac voltage. An additional converter again requires space and presents an extra cost. Therefore, LCC-HVdc technology is discarded for the application of grid connection for offshore wind where space is premium and grid-forming operation capability a hard requirement.

VSC-HVdc technology uses self-commutated switches (e.g. IGBTs valves) [62]. Self-commutated or fully controllable switches allow control of the timing of current flow and current interruption through a gating signal [61]. This flexibility permits full control of active and reactive power exchange with the interfaced ac terminals. There is no inherent reactive power requirement due to the behavior of the switching devices as mentioned earlier for LCCs. As the name indicates, a VSC is capable of synthesizing a controlled ac voltage at its terminals. There are several VSC topologies suitable for different applications [61]. However, for the VSC-HVdc mainly two-level, three-level, or multi-level topologies are used. A VSC-HVdc station might comprise harmonic filters to smooth the distorted ac output voltage and current obtained by chopping the dc voltage. Considering the same switching frequency, an increase of the number of levels inherently decreases the need for harmonic filtering. An infinite number of levels would lead to a perfect sinusoidal fundamental ac voltage. In terms of footprint, the VSC-HVdc station equals around 0.5 to 0.6 times the LCC-HVdc station at the same power rating [63]. Furthermore, VSC-HVdc units can startup a de-energized power system (black start capability) and interface power systems with very low or nil short-circuit ratio. These features qualify VSC-HVdc technology for the application of offshore wind grid connection.

As of 2017, the grid connection of very remote offshore WPPs with VSC-HVdc technology is planned and built in classical, independent point-to-point schemes (see Fig. 2.6). Besides that, multi-terminal HVdc grids are proposed to connect offshore wind more efficiently to the main grids [2], [4], [50],

[64], [65]. In the latest stage, this might result in meshed dc overlay grids which are operated in parallel to the existing ac grids [50], [62]. From the WPP perspective this might require additional features, e.g. fast frequency response [66]–[69]. Furthermore, multi-VSC-HVdc systems are introduced in [55], [70], [71] for advanced power sharing among several offshore VSC-HVdc systems interfacing the same offshore grid WPPs are connected to.

2.1.5 Other concepts with connection in dc

Besides the employed system concepts described in the previous sections, other topologies are proposed in the literature for the integration of (very) remote offshore WPPs. All the schemes presented here use the characteristic of HVdc to provide a decoupling stage between the main grid(s) and the WPPs at some stage:

- low frequency ac (LFac) transmission and collection [72]–[74];
- HVdc transmission and optimized fixed frequency in the offshore grid [75];
- HVdc transmission and variable frequency in the offshore grid [36], [76], [77];
- diode rectifier-based high-voltage dc (DR-HVdc) transmission and ac collection [78]–[83];
- and HVdc transmission with medium-voltage dc (MVdc) collection [84]–[90].

The LFac scheme proposes the use of a grid frequency of $16\frac{2}{3}$ Hz throughout the collection and transmission system. The decreased reactive power requirement permits the avoidance of the offshore HVdc converter [72]. However, a back-to-back HVdc converter must be placed onshore to couple the asynchronous grids. The proposed value is $16\frac{2}{3}$ Hz, motivated from the operational experience of the single-phase railway electrification network in Austria, Germany, Norway, Sweden, and Switzerland. The use of LFac aims to extend the capability of ac connections as the reduction of the grid frequency lowers the charging current of the ac cables [refer to Eqn. (2.2)]

and therefore increases the active power transmission capability for the same distance [73], [74]. The lower frequency imposes a size and weight increase of the WT and WPP transformers. There is a further impact on the design of some electrical components (auxiliaries, protection devices, etc. in the case of FSC–WT, as well as generator for DFIG–WT). In terms of performance, Ref. [74] claims that up to 600 MW could be transmitted over a up to 400 km with state-of-the-art 245 kV–XLPE submarine cables.

The operation scheme with an optimized, non-standard frequency utilizes the HVdc technology as transmission system [75]. On the one hand, a reduction of the frequency below 50 Hz might lower the reactive power requirement and increase the transmission capability of the system. However, it increases size and weight of the electrical components, e.g. transformers, simultaneously. On the other hand, higher frequencies reduce the size and weight of the transformers and might be of interest for smaller offshore collection grids. Ref. [75] concludes for a detailed case study conducted on a leasing area of 2000 km² and rating of 1 GW that an operating frequency of around 100 Hz is the optimum under consideration of the frequency-dependent component costs.

The operation scheme of multiple WT generators with a common VSC–HVdc is proposed and studied in [36], [76], [77]. The WTs would house only the generator and are controlled in a group by the common VSC–HVdc. The authors highlight that for the efficient operation of such systems only a small deviation of the wind conditions within a group is acceptable. Besides that, the configuration might result in less installation and maintenance costs for the WTs due to the common VSC–HVdc. The drawback of this proposal is the lack of maximum power extraction when the operating conditions of the WTs differ too much within a group.

The DR–HVdc scheme claims a simplification of the offshore HVdc substation replacing the VSC–HVdc by a HVdc diode rectifier [78]–[83]. The WPPs are deployed as conventional ac systems (nominal voltage of 33 kV, 66 kV, or 155 kV) which connect to an offshore diode rectifier interlinked on the dc side via dc cables to shore. The onshore converter might be a VSC–HVdc (or LCC–HVdc) [80]. The offshore diode rectifier is inherently uni-directional and uncontrolled, i.e. the offshore grid voltage must be controlled by any other

suitable device. A dedicated STATCOM or WT converters are proposed for this task [82]. When no additional converter is installed, the WT converters need to adapt their control strategy, from conventionally grid-connected to grid-forming, to enable a suitable operation of the offshore grid. During a grid loss or commissioning phase, when auxiliary power supply is required by the WTs, the disadvantage of uni-directional power flow might be overcome by an external power supply, an umbilical ac cable, or an additional converter to enable reverse power flow on the dc link. Ref. [79] claims a loss reduction of 20% and significant further cost reduction of offshore wind compared to VSC-HVdc grid connection.

The MVdc collection scheme aims to use dc technology in the offshore grid [84]. There are two main topologies proposed: parallel and series WT (or WPP) interconnection [85]–[90]. The first uses at least one (central) offshore dc/dc converter station and therefore becomes even more costly than ac technology [88]. The latter might allow building up the HVdc voltage by series connection of the WT or WPP dc output voltages and therefore avoids the offshore VSC-HVdc. Several challenges are identified, e.g. cost-effective WTs with dc grid connection interface [91], efficient high power HV dc/dc converter topologies [91], and extended insulation requirements in the case of the series interconnection [85], [86].

The plurality of the proposed concept underlines that grid connection of (very) remote offshore WPPs is still an emerging technology and lacks maturity of standard ac power system principles in terms of design, operation, and control.

2.1.6 Grid code requirements

Ultimately, the aim of using wind power (as one of the renewable energy sources) must be to supersede conventional power plants. Therefore, WTs should operate in favor of the power system they are connected to. WPPs are demanded to support the main grid such as power plants rather than to challenge it.

The requirements for grid connection of generation units to the transmission grids are defined in grid codes (GCs) issued by the national transmission system operators (TSOs). For instance, the current grid connection require-

ments for offshore WPPs connected to the HV transmission grid of Tennet, the German TSO with responsibility for the North Sea area, are summarized (“Requirements for Offshore Grid Connections in the Grid of TenneT TSO GmbH” [92] expanding the requirements given in “Grid Code for high and extra high voltage” [93]):

- operation in a voltage range of 0.9 p.u. to 1.1 p.u. of the nominal voltage of 155 kV;
- operation in a frequency range of 0.93 p.u. to 1.07 p.u. around the nominal frequency of 50 Hz otherwise obliged disconnection of the WPP;
- use of generating plant transformer(s) with:
 - a star–delta vector group to separate the zero–sequence networks;
 - a remotely controllable on–load tap changer (OLTC) with ± 6 steps in a range of ± 0.13 p.u. of the nominal transformer ratio;
- operation the power plant with the capability at the grid connection point to inject or absorb reactive power [92, Fig. 4a];
- recommended compensation of the capacitive charging current in the offshore grid with switchable shunt reactor(s);
- and definition of data exchange specifications between WPP owner/operator and TSO.

Furthermore, grid support functionalities are specified for grid–connected offshore WPPs [92]:

- a minimum reactive power capability of up to 0.3 p.u. inductive and up to 0.4 p.u. capacitive in a range of 0.95 p.u. to 1.05 p.u. of the nominal voltage (at LV–side of WT transformer) [92, Fig. 4b]; reactive power provision/demand is decreased linearly to zero for active power values lower than 0.2 p.u.;
- fast voltage support through reactive current provision to ride through temporary under–voltage conditions [92, Fig. 7];

- fast voltage reduction through reactive current absorption during over-voltage conditions [92, Fig. 7];
- and active power reduction in the case of over-frequency (from 1.004 p.u. to 1.054 p.u. with a slope of $-0.4 \text{ p.u. Hz}^{-1}$) [92, Fig. 8].

As of 2017, the implemented national GCs (e.g. by the Danish TSO Energinet.dk [94], the French TSO Réseau de transport d'électricité [95], the German TSOs 50Hertz [96] and Tennet [92], [93], and the UK's National Grid [97]) do not differ between ac- or dc-connected power plants. The new generation of GCs in Europe will adopt the binding European Union regulations establishing “a network code on requirements for grid connection of generators” [98] and “a network code on requirements for grid connection of high voltage direct current systems and direct current-connected power park modules” [99]. The regulations might motivate imposing different requirements on the generating units in dependence of the type of the main grid connection.

2.2 Converter control in HVdc-connected WPPs

The basic topology of an HVdc-connected WPP is described in Section 2.1.4. In the following the operation and widely accepted standard control approach from a system perspective will be outlined [42], [55]:

- onshore VSC-HVdc operates in grid-connected mode and controls the dc link voltage and the reactive power exchange with the main grid;
- offshore VSC-HVdc operates in grid-forming mode and controls the voltage magnitude and the frequency of the offshore grid;
- and WT-GSCs operate in grid-connected mode and control their active and reactive current injection into the offshore grid.

A different system control architecture is discussed in [100] proposing that the WT-GSCs operate as grid-forming converters and the onshore and offshore VSC-HVdc as a conventional point-to-point HVdc system. It

must be noted that controller interactions and stability have to be thoroughly addressed when using multiple grid-forming converters. The control architecture has similarities to the ones proposed for the operation of DR-HVdc-connected WPPs (see Section 2.1.5). It was highlighted that these require a black start capability and an independent auxiliary supply system for the offshore WTs.

Conventional controllers for VSC systems connected to power systems are either developed in the stationary $\alpha\beta$ -reference frame or in the synchronous dq -reference frame [17], [61]. Both techniques reduce the controlled plants from three to two compared to a control architecture in the stationary abc -reference frame. Furthermore, control design in the $\alpha\beta$ -frame uses proportional-resonant controllers which are tuned to the fundamental frequency of the sinusoidal $\alpha\beta$ -components. In contrast to that, in the dq -reference frame proportional-integral (PI) regulators control dq -components, which comprise only dc quantities in steady-state. The transformations between the abc -reference frame to the $\alpha\beta$ - and dq -reference frame, respectively, and vice-versa are shown in the Appendix A.1. Unless otherwise stated, controllers in the dq -reference frame are used in this thesis due to the compatibility in power system studies and the ease of visualization. Regarding implementation of controllers in the $\alpha\beta$ -reference frame, the reader is pointed to [17], [61].

2.2.1 Grid-connected operation

The onshore VSC-HVdc and the WT-GSCs operate each in grid-connected mode [61]. Given the scope of this thesis, in the following only the GSC of a WT will be considered. However, the methodology might be similarly applied to the onshore VSC-HVdc. The objective of the operation in grid-connected mode (also referred as grid-imposed frequency VSC system in [61]) is the controlled exchange of active and reactive power/current with the synchronized ac system. There are two operation modes: active/reactive power control or controlled dc voltage with reactive power control. Both modes are used in a conventional point-to-point HVdc link where the first operation mode is applied by one converter station, whereas the latter is utilized for the other station [61]. Similarly, in the FSC-WT the GSC aims to

evacuate the active power from the dc link and therefore uses the controlled dc voltage with reactive power control mode³. The schematic of a grid-connected VSC and the upper level control architecture for the controlled dc voltage with reactive power control mode are depicted in Fig. 2.7. The external dc power input p_{dc}^{ext} corresponds here to the injected power from the machine-side converter (MSC) of the WT. An active power imbalance of $p_{dc}^{ext} > p_{dc}$ leads to an increase in the dc voltage u_{dc} following $u_{dc}(t) = \frac{1}{C_{dc}} \int (i_{dc}^{ext} - i_{dc}) dt$. Therefore, the dc voltage is continuously controlled to the reference magnitude u_{dc}^{ref} which inherently adopts the active power set-point. In the case that the active power flow is limited, the surplus energy might be dissipated by the dc braking resistor R_{dc}^b through activation of the switch S_1 [17], [101].

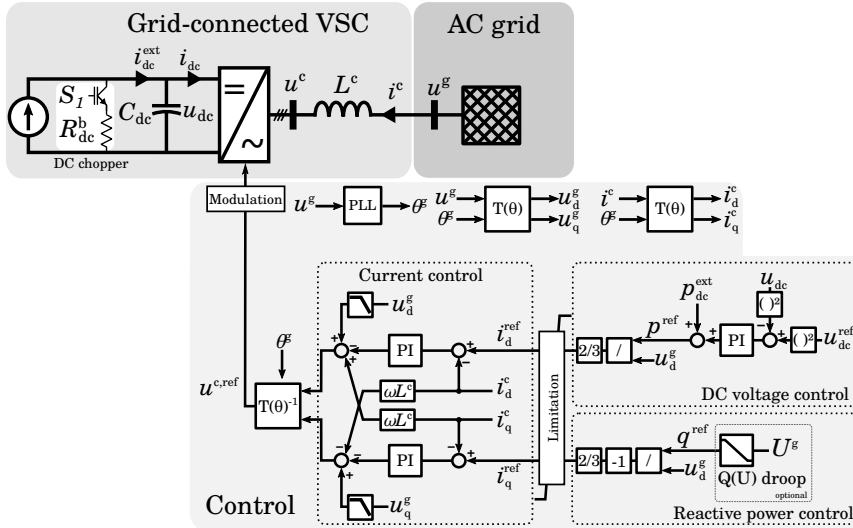


Figure 2.7: Grid-connected VSC layout and upper level control schematic.

The dc voltage control might be implemented with a feed-forward term of the external dc power input p_{dc}^{ext} and a PI controller that regulates the variation on u_{dc} ² [61]. The reactive power set-point might originate from a $Q(U)$ droop characteristic dependent on the ac voltage or a dedicated ac voltage control loop. A viable droop characteristic $Q(U)$ at WPP level is outlined in [102, Fig. 6]. The current control (CC) regulates the active and reactive power exchange (p_{ac} and q_{ac}) with the grid. Following instantaneous

³The reactive power control might also be implemented as an ac voltage control [61].

power theory, the active and reactive power expressed in the dq -reference frame is [103], [104]:

$$p_{ac} = \frac{3}{2}(u_d i_d + u_q i_q) \quad (2.4)$$

$$q_{ac} = \frac{3}{2}(u_q i_d - u_d i_q) \quad (2.5)$$

where:

u_d, u_q = voltage dq -components;

i_d, i_q = current dq -components.

The synchronous reference frame (SRF) voltage vector might be aligned to maintain $u_q = 0$ p.u. and hence achieve a simpler relation for the active power $p_{ac} \approx \frac{3}{2}u_d i_d$ and for the reactive power $q_{ac} \approx -\frac{3}{2}u_d i_q$. In that case, i_d denotes the active current and i_q the reactive current, respectively. The active and reactive current references might then be directly calculated from the active power p^{ref} which is determined by the dc voltage control and the reactive power set-point q^{ref} . To achieve correct alignment of converter currents and ultimately exchange the desired powers, the phase angle θ^g of the grid voltage u^g must be tracked through a PLL system. There is a variety of PLLs described in the literature in general [105] and for the grid-connected application [17]: the conventional synchronous reference frame PLL (SRF-PLL), the decoupled double synchronous reference frame PLL (DDSRF-PLL) [106], [107], and the double second-order generalized integrator FLL (DSOGI-FLL) [108]. A conventional SRF-PLL achieves the desired alignment by controlling the q -component u_q^g continuously to zero by means of a PI-controlled feedback loop. In ideal conditions, i.e. balanced and pure sinusoidal phases, this results in the d -component u_d^g being the voltage magnitude with phase angle θ^g . In case of non-ideal conditions, i.e. unbalance among the three phases or appearance of harmonic components, the conventional SRF-PLL starts to oscillate and is not capable tracking the magnitude and the phase angle with sufficient accuracy [17].

Unbalanced three-phase systems might be described by three independent balanced systems, namely positive (pos.) sequence, negative (neg.) sequence, and zero sequence. The mathematical transformation between a

three-phase vector x_{abc} and the symmetrical components x_{120} is described in Appendix A.1. In the dq -reference frame, the coupling between the sequences pronounces double fundamental frequency components [17]. The neg. sequence (seq.) components appear in the pos. seq. components and vice-versa:

$$u_1 = \begin{bmatrix} u_{1d} \\ u_{1q} \end{bmatrix} = U_1 \begin{bmatrix} \cos(\phi_1) \\ \sin(\phi_1) \end{bmatrix} + U_2 \begin{bmatrix} \cos(2\omega t) & \sin(2\omega t) \\ -\sin(2\omega t) & \cos(2\omega t) \end{bmatrix} \begin{bmatrix} \cos(\phi_2) \\ \sin(\phi_2) \end{bmatrix} \quad (2.6)$$

$$u_2 = \begin{bmatrix} u_{2d} \\ u_{2q} \end{bmatrix} = U_2 \begin{bmatrix} \cos(\phi_2) \\ \sin(\phi_2) \end{bmatrix} + U_1 \begin{bmatrix} \cos(2\omega t) & -\sin(2\omega t) \\ \sin(2\omega t) & \cos(2\omega t) \end{bmatrix} \begin{bmatrix} \cos(\phi_1) \\ \sin(\phi_1) \end{bmatrix} \quad (2.7)$$

where:

u_1, u_2 = pos. and neg. seq. voltage;

U_1, U_2 = pos. and neg. seq. voltage magnitude;

ϕ_1, ϕ_2 = pos. and neg. seq. angles.

The deterministic behavior of Eqns. (2.6) and (2.7) (both u_1 and u_2 are dc plus 2ω terms, respectively) motivates cancellation of the double frequency terms rather than attenuation through low-pass filters (LPFs) [17]. Thus, more advanced PLLs should be used, such as the DDSRF-PLL [106], [107], or the DSOGI-FLL [108]. The DDSRF-PLL uses a decoupling network to cancel out the mentioned 2ω oscillations [17], [106]. Therefore, both pos. and neg. seq. magnitude and phase angle can be tracked accurately during balanced and unbalanced conditions. The DSOGI-FLL is the counterpart for the $\alpha\beta$ -reference frame and provides similar performance using adaptive filters [17], [109], [110].

The CC displayed in Fig. 2.7 shows the implementation in the SRF. In that case, the neg. seq. current might be uncontrolled when unbalanced grid voltages arise [17]. To gain full control over the converter currents under balanced and unbalanced conditions, the system equations are separated into pos. and neg. seq., respectively. The relations for the pos. and neg. seq. of a VSC coupled to the grid through an inductive filter L^c with its parasitic resistance R^c are:

$$\begin{bmatrix} u_{1d}^c \\ u_{1q}^c \end{bmatrix} = \begin{bmatrix} u_{1d}^g \\ u_{1q}^g \end{bmatrix} - \begin{bmatrix} R^c & -\omega L^c \\ \omega L^c & R^c \end{bmatrix} \begin{bmatrix} i_{1d}^c \\ i_{1q}^c \end{bmatrix} - L^c \frac{d}{dt} \begin{bmatrix} i_{1d}^c \\ i_{1q}^c \end{bmatrix} \quad (2.8)$$

$$\begin{bmatrix} u_{2d}^c \\ u_{2q}^c \end{bmatrix} = \begin{bmatrix} u_{2d}^g \\ u_{2q}^g \end{bmatrix} - \begin{bmatrix} R^c & \omega L^c \\ -\omega L^c & R^c \end{bmatrix} \begin{bmatrix} i_{2d}^c \\ i_{2q}^c \end{bmatrix} - L^c \frac{d}{dt} \begin{bmatrix} i_{2d}^c \\ i_{2q}^c \end{bmatrix} \quad (2.9)$$

where:

- $u_{1d}^c, u_{1q}^c =$ pos. seq. dq -components of converter voltage;
- $u_{2d}^c, u_{2q}^c =$ neg. seq. dq -components of converter voltage;
- $u_{1d}^g, u_{1q}^g =$ pos. seq. dq -components of grid voltage;
- $u_{2d}^g, u_{2q}^g =$ neg. seq. dq -components of grid voltage;
- $i_{1d}^c, i_{1q}^c =$ pos. seq. dq -components of converter current;
- $i_{2d}^c, i_{2q}^c =$ neg. seq. dq -components of converter current.

Equations (2.8) and (2.9) would suggest a straight-forward implementation as separate CC loops for each seq., respectively denoted as double synchronous reference frame (DSRF). Nevertheless, the cross-coupling between the sequences [Eqns. (2.6) and (2.7) obviously also hold for currents] leads to a poor performance and more advanced control architectures should be used [17]. Similarly to the decoupling principle in the DDSRF-PLL, the implementation of such current controllers aims to mitigate the 2ω terms through notch filtering, a decoupling network based on the measured signals, or a decoupling network based on the reference and error signals [17]. The differences regarding performance are highlighted in [17]. Figure 2.8 depicts the implementation with a decoupling network based on the reference and error signals as used in this thesis. Furthermore, Ref. [111] compares the control performance in only pos. seq. SRF and separate control loops in pos. and neg. sequence. The authors conclude that the latter has a higher implementation complexity but provides a better performance and flexibility with respect to dynamic voltage control and current limitation.

The active and reactive powers consist of average power and oscillating power terms under expression by symmetrical components [104]. For unbalanced grid conditions and under consideration of the fundamental frequency

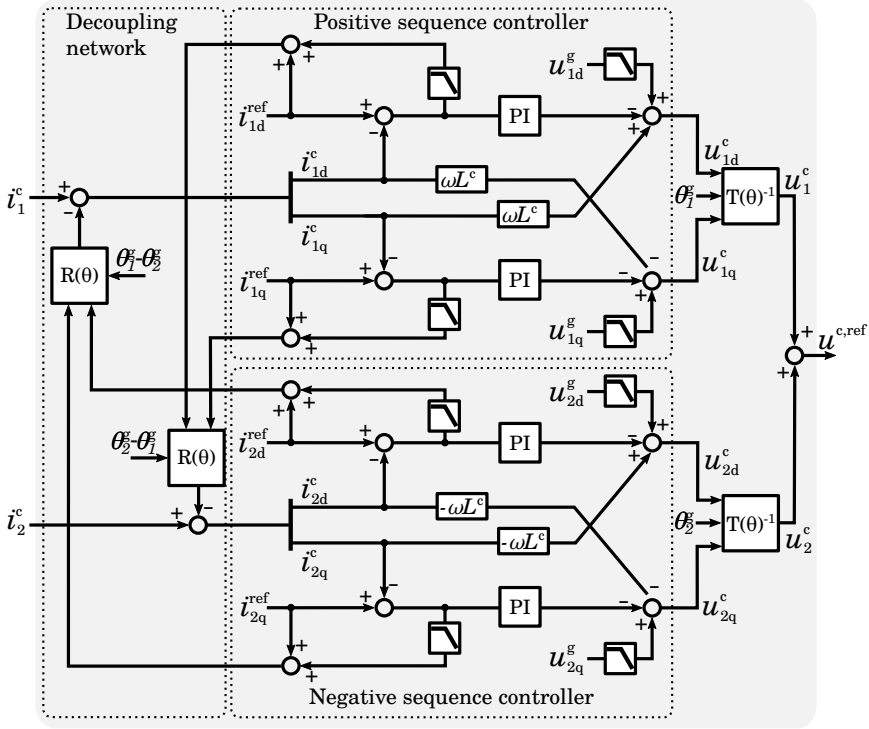


Figure 2.8: Current control in pos. and neg. seq. with the decoupling network based on the reference and error signals.

only the oscillating terms appear as 2ω -terms [17]:

$$p_{ac} = P_{av} + P_{c2} \cos(2\omega t) + P_{s2} \sin(2\omega t) \quad (2.10)$$

$$q_{ac} = Q_{av} + Q_{c2} \cos(2\omega t) + Q_{s2} \sin(2\omega t) \quad (2.11)$$

where:

P_{av}, Q_{av} = average terms of instantaneous active and reactive power;

P_{c2}, P_{s2} = oscillating terms of instantaneous active power;

Q_{c2}, Q_{s2} = oscillating terms of instantaneous reactive power.

The DSRF permits the control of four variables: the d - and the q -component of the pos. and neg. seq. currents, respectively. The six magnitudes P_{av} , Q_{av} , P_{c2} , P_{s2} , Q_{c2} , and Q_{s2} of Eqns. (2.10) and (2.11) might be expressed by u_{1dq} , u_{2dq} , i_{1dq} , and i_{2dq} [17]. Hence, four out of the six magnitudes

might be controlled and, for instance, the two average power terms plus two oscillating terms are targeted [17]. On the one hand, a very common control objective for VSCs might be the provision of a constant dc power/avoidance of dc voltage oscillations and therefore the active power oscillating terms are controlled to zero [17], [112], [113]. On the other hand, GCs might demand defined current responses in pos. and neg. seq. to gain controlled short-circuit currents by the distributed converter-based generation [102], [114]–[117]. The latter implies that the pos. and neg. seq. dq -components of the currents are set through a voltage-dependent scheme presented as fast voltage support in Section 2.1.6.

Lastly, control aspects for pos. and neg. seq. are analyzed in [118], [119]. It is highlighted that the neg. seq. voltage angle is difficult to estimate under balanced grid voltages given the small magnitude of the neg. seq. voltage vector. This leads to neg. seq. current alignment delays during transient conditions. For a small magnitude of the neg. seq. voltage vector, for instance below 0.05 p.u., it is therefore recommended to use the negative pos. seq. phase angle $\theta_2^g = -\theta_1^g$. Furthermore, it is outlined that a neg. seq. current injection might limit the pos. seq. counterpart.

Controller design and tuning of the PI controller gains for the dc voltage control and CC, e.g. applying internal model control theory, is outlined in detail in [4], [61]. If not otherwise stated, the design principles of the mentioned references are used to tune the controllers in this thesis.

2.2.2 Grid-forming operation

The offshore VSC-HVdc works in grid-forming operation mode. The objective is the provision of a controlled ac voltage at its terminals and to sink all the active and reactive power injected from the offshore grid. In addition to that, there are the well-known technical limitations of the VSC-HVdc given the current and voltage capability of the switching devices (e.g. IGBTs). IGBTs might operate continuously up to its rated current I_r . Beyond that, IGBTs might drive also higher currents for self-protecting measures and a very short time (e.g. a standard 4.5 kV device can handle 2 p.u. of I_r for 1 ms [120]). Obviously, the converter current must be kept in stringent limits to avoid any over-current in the semiconductors and consequently a shut-down of a power

module or even a whole converter. In terms of ac voltage, the maximum VSC output voltage is dictated by the available dc voltage. Normally, the converter might be kept in the linear region but once u_{ac} exceeds $\frac{u_{dc}}{2}$ (considering no third-harmonic injection scheme) the converter operates in the over-modulated region [121]. Moreover, both current and voltage limitations hold regardless whether two-, three-, or multi-level-converter topology is used. Furthermore, they are design parameters of the VSC. They might be biased by arranging more semiconductor devices in parallel or series to increase the capability for current or voltage, respectively. However, this might end up in the need for additional components (e.g. snubber devices [122]) and increased control complexity.

Generally, the grid-forming operation mode should be able to set or control the voltage magnitude $U^{ref} = \sqrt{u_d^{ref2} + u_q^{ref2}}$ and angle φ^{ref} at the converter terminals. Normally, the voltage magnitude is set to 1.0 p.u.. However, other set-points are possible within the voltage capability of the converter. A possible design requirement might be the GC which specifies the continuous operation in a voltage band of e.g. 0.9 p.u. to 1.1 p.u. for connection to the 155 kV grid [92]. Transient operation at higher or lower values might be required, too. For instance, controlled ac voltage sags by the grid-forming converter are proposed to gain a fast active power reduction response by the WPPs in the offshore grid [123]. The angle of the reference voltage might be set to any value in the range of 0 rad to 2π rad as it simply represents the reference angle of the system [61]. In the most convenient approach, the d -component is set to the voltage magnitude and the q -component consequently to zero ($\varphi^{ref} = 0$ rad).

Different control principles are proposed in the literature for the grid-forming operation of the VSC. The simplest solution might be to set the converter output voltage magnitude to a fixed reference value [124]. Normal operation might work satisfactorily but neither voltage nor current is controlled in a loop structure. Consequently, extensive over-currents might occur during ac faults in the offshore grid resulting from the large voltage drop over the converter impedance. Therefore, at least one outer control loop structure should be introduced to allow current limitation. This might be implemented either indirectly by tackling the excessive voltage drop or

directly by limiting the current flowing into the converter. Overall, two state-of-the-art control principles stand out and are extensively described for HVdc-connected WPPs in [71], [125]: option I, cascaded voltage control (VC) and CC, and option II, directly applied VC. The grid-forming operation mode overview is shown in Fig. 2.9 to support the following review.

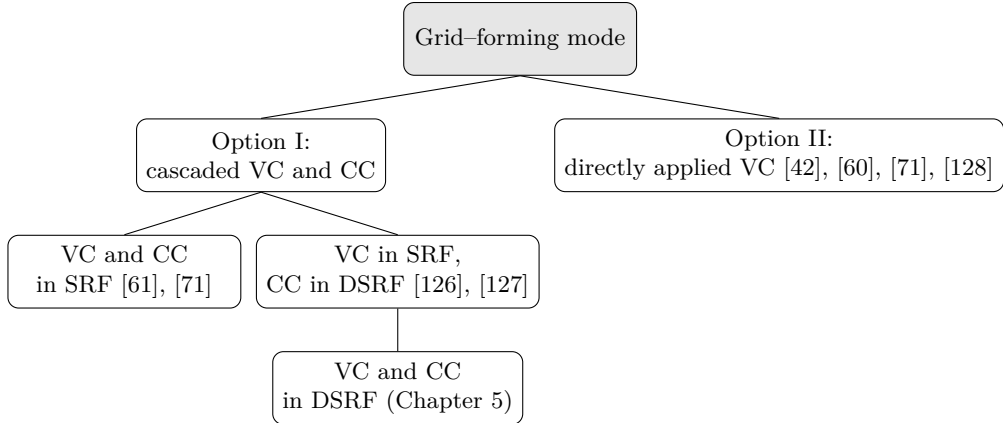


Figure 2.9: Grid-forming operation mode state-of-the-art control options and derivations.

Option I is discussed in [61] as controlled-frequency VSC system to provide voltage and frequency reference at the PCC of an ac system. Ref. [61] also mentions suitability for several applications, e.g. the supply of an isolated load, the supply of passive or weak ac systems, or uninterruptible power supply systems. The ac dynamics regulated by the VC in the SRF result in current references $i_d^{g,\text{ref}}$ and $i_q^{g,\text{ref}}$:

$$\begin{bmatrix} i_d^{g,\text{ref}} \\ i_q^{g,\text{ref}} \end{bmatrix} = \begin{bmatrix} i_d^{\text{load}} \\ i_q^{\text{load}} \end{bmatrix} - \begin{bmatrix} 0 & -\omega C^c \\ \omega C^c & 0 \end{bmatrix} \begin{bmatrix} u_{1d}^g \\ u_q^g \end{bmatrix} - \frac{1}{C^c} \frac{d}{dt} \begin{bmatrix} u_d^g \\ u_q^g \end{bmatrix} \quad (2.12)$$

where:

- C^c = capacitance of the HV capacitor;
- $i_d^{g,\text{ref}}, i_q^{g,\text{ref}}$ = dq -components of converter current references;
- $i_d^{\text{load}}, i_q^{\text{load}}$ = dq -components of load current;
- u_d^g, u_q^g = dq -components of grid voltage.

The converter current references $i_d^{g,\text{ref}}$ and $i_q^{g,\text{ref}}$ are fed into a standard CC

such as the one described for pos. seq. by Eqn. (2.8). The feed-forward compensation strategy by i^{load} results in a similar performance under all operating points as without feed-forward terms under no-load [61]. The control scheme is shown in Fig. 2.10. Firstly, it depicts that a phase angle

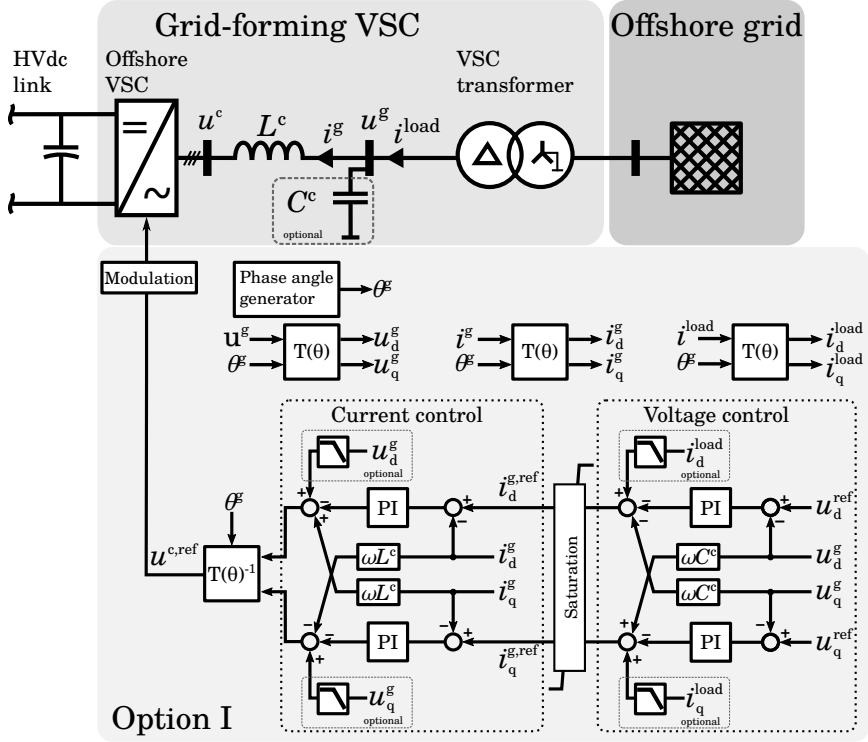


Figure 2.10: Grid-forming VSC layout control schematic with option I.

generator is used to set the phase angle of the system. A PLL which is conventionally present in the grid-connected operation is not needed in the grid-forming operation mode. The phase angle generator calculates the phase angle according to:

$$\theta^g = \int \omega dt + \varphi^{\text{ref}} \quad (2.13)$$

where:

θ^g = phase angle;
 φ^{ref} = reference angle.

Secondly, the feed-forward concept for the CC is proposed as follows: as the voltage is imposed by the system itself it might be suitable to feed-forward the reference voltage u^{ref} or zero [71], [127].

Thirdly, the dedicated capacitor on the HV-side of the converter transformer is discussed [70], [71]. Its need might be questioned as the offshore grid is already characterized by a considerable amount of submarine cables which have a large capacitance built up in the dielectric isolation material between the conductor(s) and ground (see Section 2.1.3). This fact might motivate the use of the distributed effective capacitance C_{eff}^c in the control design of the VC. Nonetheless, there are two drawbacks when the dedicated HV capacitor is avoided: first, the control design is dependent on C_{eff}^c whose value might change throughout the operation (e.g. disconnection of parts of the offshore grid, start-up sequence) and second, the load current feed-forward could not be used as Eqn. (2.12) loses its validity. The first disadvantage might be counteracted by gain scheduling of the control parameters in dependence of the actual network configuration [125]. However, the second disadvantage might be solely solved by installation of a dedicated capacitor at the HV terminals as drawn in Fig. 2.10. For two- or three-level converters harmonic filters are installed anyway to improve the sinusoidal voltage output. However, for MMCs, which are the state-of-the-art technology for new VSC-HVdc installations, harmonic filters become superfluous and a dedicated HV capacitor might be installed. Ref. [71] reiterates that the feed-forward of the load current leads to an improvement of the ac dynamics.

Option I foresees deployment in the SRF (in pos. seq.). With respect to neg. seq. current and voltage, the feed-forward terms in the VC might contain neg. seq. and thus any neg. seq. converter current injection is avoided (neg. seq. voltage measured at the terminals is fed through and applied at the converter terminals). However, this might lead to over-voltages in one or more phase(s). In contrast to that, if neg. seq. voltage is attenuated before feeding it into the VC, the converter might inject also neg. seq. current. Given the control scheme in the SRF, the neg. seq. current is uncontrolled, bypasses the saturation of the current references and might therefore represent

over-currents in one or more phase(s). Overall, the implementation in the SRF might result in poor performance when facing unbalanced grid voltages. Control in pos. and neg. seq. seems obvious to counteract these problems. Therefore, a variation of option I which is using a DSRF in the CC is presented in [126], [127]. The original control scheme [61], [129] is altered by an additional neg. seq. CC loop. The neg. seq. CC loop is fed with the current references i_{2d}^{ref} and i_{2q}^{ref} . During normal operation those references are set to zero, which equals zero neg. seq. current injection by the offshore VSC-HVdc. When neg. seq. voltage arises, Ref. [126] proposes calculating the references specifically to suppress double grid frequency oscillations in the active power terms (and dc voltage). Such current references calculation is known from the grid-connected operation mode under unbalanced voltage conditions (see Section 2.2.1,[17]). The discussion in [126] reveals that the neg. seq. controllers in the grid-forming application perform slightly superior than solely pos. seq. controllers. Nevertheless, the grid voltage shows a poor performance due to OM during unbalanced voltage conditions even when using the proposed controller structure. Additionally, the suppression of oscillations in the dc link voltage might be interesting for two- and three-level converters but is not necessarily advantageous for MMCs. In a MMC, such oscillations are buffered in the internal sub-module (SM) capacitors (further reading in Section 2.2.3).

In the following section, option II for the grid-forming operation mode is outlined. Ref. [42] discusses this control scheme which is shown in a simplified manner in Fig. 2.11. The main objective foresees controlling the ac voltage magnitude at the PCC busbar to a given reference. The applied converter voltage might be directly synthesized from the PI-controlled difference of the measured grid voltage magnitude u^g and the reference magnitude u^{ref} . Deployment in the SRF is not necessary. However, a sudden voltage drop in the offshore grid might lead to a large converter current if no countermeasures are taken. To prevent the over-current, a dynamic saturation scheme is proposed. It uses a dynamic upper saturation limit which continuously limits the voltage drop over the converter inductance to 0.1 p.u.. Hence, the converter current is indirectly limited. However, the response to, e.g. unbalanced faults, might lead to over-currents in one or more phase(s) or

insufficient usage of the full converter capability. Ref. [42] also comments on the desired behavior of the offshore VSC-HVdc during offshore grid faults: for three-phase faults the VSC should deliver the full short-circuit current in the three phases without blocking the converter, whereas for single-line-to-ground (SLG) faults the VSC should provide a reduced current to avoid over-currents in the healthy phases (around 0.6 p.u. is suggested). These suggestions are made under the condition that the magnitude of the converter current might be controlled indirectly as for option II and therefore its limitation is not being enforced by a dedicated CC.

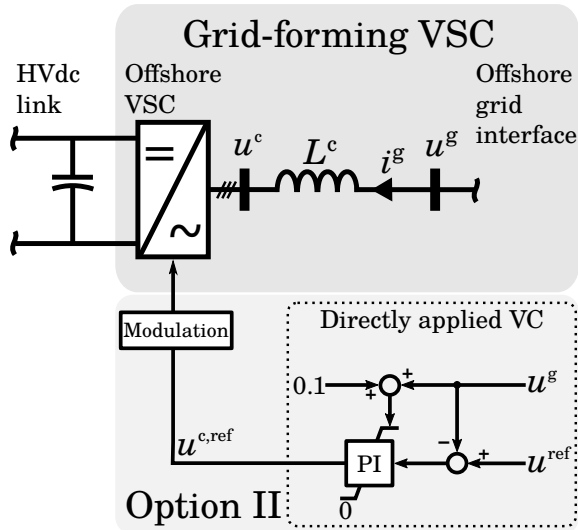


Figure 2.11: Grid-forming VSC layout control schematic with option II.

To sum up, the work done by [71] on the comparison of the two state-of-the-art control principles is listed in Tab. 2.13. Ref. [71] does not decide on an overall winner of the comparison but reiterates that in the case of offshore grid faults the inherent CC of option I is advantageous. However, for normal operation and in terms of simplicity option II is superior. Regarding future work, the author suggests deploying pos. and neg. seq. control structures for option I. This was partly done in [126] as highlighted earlier. However, the full implementation in pos. and neg. seq. of both VC and CC was not promoted in the literature yet and is proposed in Chapter 5 of this thesis.

Table 2.13: Comparison of state-of-the-art control principles for grid-forming operation from [130, Tab. 20].

	Option I (cascaded VC and CC)	Option II (directly applied VC)
Advantages:	<ul style="list-style-type: none"> • inherent CC capability, • fault handling with directly controlled currents, • and better performance for multiple VSC-HVdc. 	<ul style="list-style-type: none"> • tuning at no-load, • simple controller implementation, • performance independent from operating point, • and performance independent from network configuration/connected capacitance.
Disadvantages:	<ul style="list-style-type: none"> • tuning at no-load, • performance dependent on operating point, • performance dependent on network configuration/connected capacitance, • and dedicated HV capacitor (space and weight) needed to diminish poor performance. 	<ul style="list-style-type: none"> • no inherent CC capability, • and insufficient performance during faults.

2.2.3 Modular multilevel converter

A high number of classical VSC applications (e.g. variable-speed motors connection, grid connection of renewable generation, micro grids, etc.) use two-level VSC or three-level VSC topologies [61]. Multi-level converters for the VSC-HVdc application with more than three level had been disregarded due to the large number of semiconductors and the increased complexity. In contrast to that, the presentation of the MMC by Prof. R. Marquardt in 2001 literally revolutionized converter architectures for the VSC-HVdc technology and other high-power, high-voltage applications [131], [132]. Currently, the MMC is the state-of-the-art topology for VSC-HVdc given that:

- power losses are lower than for 2L-HVdc or three-level VSC-HVdc and in a similar range of LCCs mainly because of the reduced IGBT switching frequency;
- modular architecture comprising hundreds of SMs is advantageous from a manufacturing and redundancy perspective;
- ac output voltage is almost pure sinusoidal which results in low or no need for harmonic filters;
- and higher cost for the increased number of IGBTs is outweighed by the lower power losses during operation.

The MMC is extensively covered in literature [133]–[142]. The general structure of a MMC consists of three phase legs (or phase branches) which have an upper and a lower converter arm, respectively, as depicted Fig. 2.12. A converter arm is set up of a stack of N switchable half-bridge SMs and the arm inductance L^a . The basic operation foresees that the energy storage (in the original realization a capacitor) in the half-bridge SM might be either switched in or by-passed through respective control signals to the semiconductor switches. The series connection of switchable SMs synthesizes a controllable voltage source per arm. Contrary to conventional VSCs, the energy storage is distributed among the SMs and not centralized in dc link capacitors.

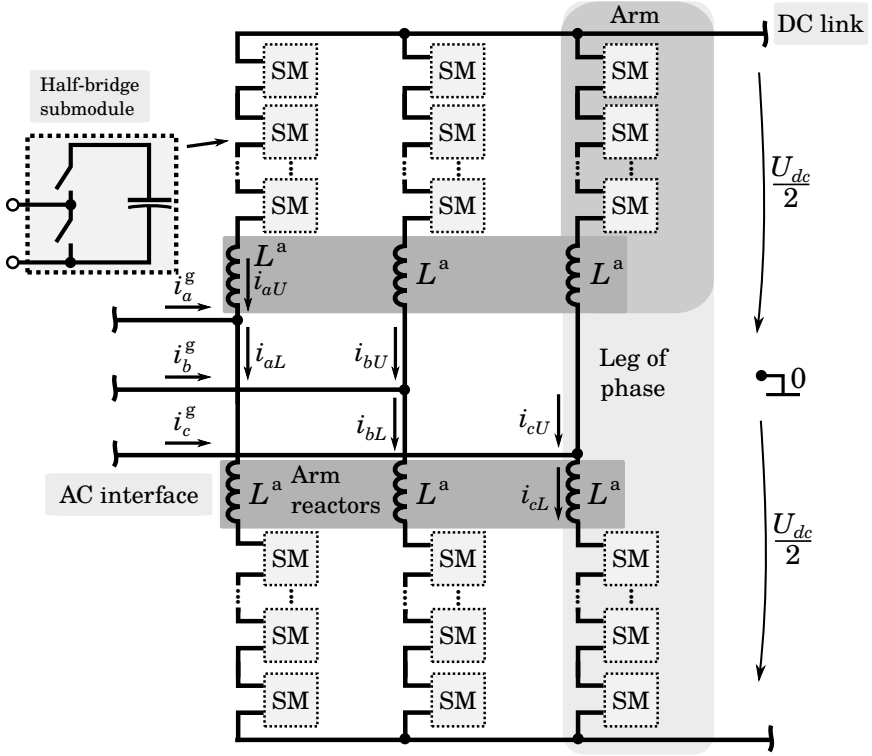


Figure 2.12: Schematic of MMC with half-bridge submodules.

The basic relations used in [143] are redefined to describe the MMC circuit:

$$\left\{ \begin{array}{l} u_k^{\text{diff}} \stackrel{\text{def}}{=} 0.5(u_{kL} - u_{kU}) \\ u_k^{\text{sum}} \stackrel{\text{def}}{=} u_{kU} + u_{kL} \\ i_k^{\text{sum}} \stackrel{\text{def}}{=} 0.5(i_{kU} + i_{kL}) \end{array} \right. \quad \text{and} \quad \left\{ \begin{array}{l} u_{kU} = 0.5u_k^{\text{sum}} - u_k^{\text{diff}} \\ u_{kL} = 0.5u_k^{\text{sum}} + u_k^{\text{diff}} \\ i_{kU} = 0.5i_k^{\text{g}} + i_k^{\text{sum}} \\ i_{kL} = -0.5i_k^{\text{g}} + i_k^{\text{sum}} \end{array} \right. \quad (2.14)$$

where:

- u_k^{diff} = differential voltage (or converter output voltage);
- u_k^{sum} = additive voltage;
- i_k^{sum} = additive current;
- u_{kU}, u_{kL} = upper and lower arm voltage;
- i_{kU}, i_{kL} = upper and lower arm current.

The additive currents (inner or circulating currents) are caused by energy imbalances among the phase legs, upper and lower arms, and the dc side [141]. When uncontrolled, the inner currents might cause higher power losses and a larger arm capacitor voltage ripple. However, the inner current control is addressed thoroughly in literature, e.g. [140], [141], [143]. MMC-HVdc-based projects use a large number of SMs [137], so the selective control of the SMs might be approximated by a voltage source [144]. The arm inductors are modeled by an inductance L^a and its parasitic resistance R^a , whereas the SM stack is represented by a controlled voltage source. Such a model is outlined in detail in [5], [143].

2.3 Reactive power in offshore WPPs

In general, reactive power control in an offshore WPP refers to the exchange of reactive power with the main grid and consequently the internal plant-level reactive power balance [55]. In most GCs, the main requirement on reactive power is demanded at the PCC [95], [97], [102]. By way of example, Fig. 2.13 depicts the reactive power requirements at rated power, Fig. 2.13a, and below rated power, Fig. 2.13b, at the HV network connection point according to the German GC [102]. Active and reactive power are scaled to the rated power P_{rat} . The respective grid operator might choose one of the three options drawn depending on the project characteristics and the respective network requirements. Taking all options combined into account, a reactive power requirement of the equivalent of a power factor of 0.9 for over-excited operation and 0.925 for under-excited operation at full power is demanded. It might be further highlighted that for active power production below 0.1 p.u. no reactive power is needed. The voltage ranges of the diagram on rated power in Fig. 2.13a apply likewise for the requirements below rated power in Fig. 2.13b. A new reactive power set-point must be reached within 4 min [102]. The same standard highlights that the current state-of-the-art MV/HV transformer equipped with an OLTC can change its taps in the complete voltage range within 4 min. The reactive power requirement might be enforced as a power factor (PF) set-point or reactive power set-point. Furthermore, the reactive power set-point might be given as a fixed value or as a voltage- or active-power-dependent characteristic. The set-point might be fixed or transmitted through a communication link [102].

Normally, for ac-connected offshore WPPs the reactive power requirements might be met by appropriate design of the WT converters and MV transformer [145], [146]. For distant ac-connected offshore WPPs the requirements might require additional devices such as static VAR compensators or STATCOMs [147], [148]. Regardless of which transmission technology is used for the offshore WPP, the submarine cable systems and particularly their inherent reactive charging current impact the reactive power balance significantly as already highlighted in Section 2.1.3. Besides the submarine cable systems, other components contribute to the reactive power balance: the power transformers, shunt reactors, capacitor banks, and power-electronics-based

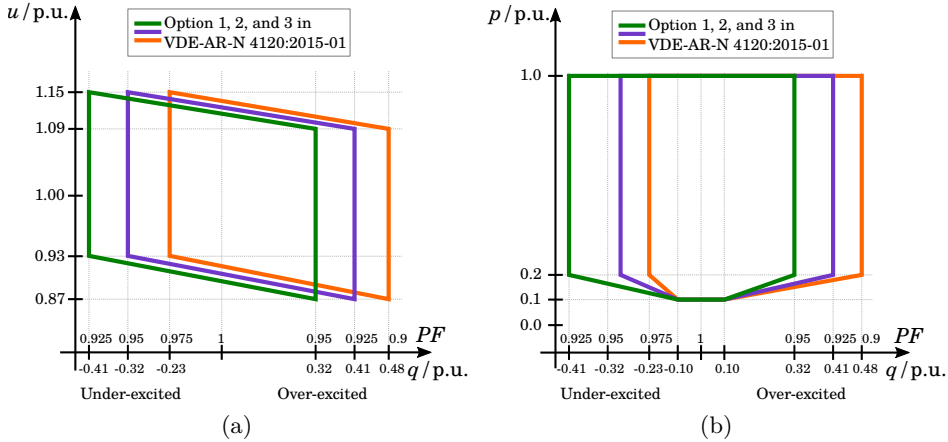


Figure 2.13: Steady-state reactive power requirements at the network connection point (PCC) (a) at rated power and (b) below rated power [102].

devices [i.e. the WT converters and possible flexible ac transmission systems (FACTSs)] among others. For instance, power transformers and shunt reactors absorb reactive power (inductive behavior), whereas capacitor banks and uncompensated submarine cables at no load or low load inject reactive power (capacitive behavior). The power-electronics-based devices might either inject or absorb reactive power within their capability. Moreover, power transformers might adopt their ratio through tap changing with the OLTC and inherently change the amount of reactive power absorbed.

2.3.1 Reactive power dispatch

To fulfill the reactive power requirement at the PCC, a dedicated WPP control system (WPPC) is regulating the measured PF, reactive power, or voltage at the PCC to a given set-point by dispatching set-points to the controlled devices.

2.3.1.1 Conventional dispatch

A standard WPPC approach is depicted in Fig. 2.14. By way of example, the error between the reactive power set-point from the TSO and the measured

value is fed into a PI controller and its output is distributed as individual set-point to the WTs [149]. Also, power factor or voltage set-points might be sent to the WTs. Once the individual set-point is received, the local WT control system (WTC) regulates its output accordingly. Such a control principle foresees at least unidirectional communication and sends a unique reactive power set-point to all WTs. Moreover, the variable used to control reactive power at the WPP-level which is communicated to the WTs might differ from the TSO control variable (power factor, reactive power, and voltage set-points are exchangeable).

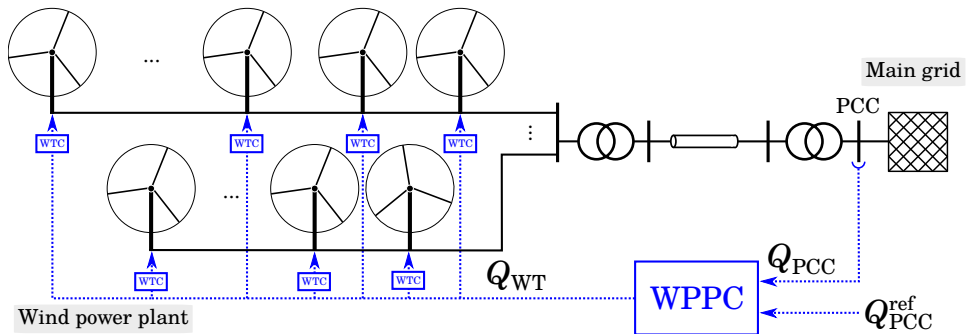


Figure 2.14: Schematic of simplified reactive power dispatch in an ac-connected WPP.

More sophisticated dispatch algorithms are presented in the literature, e.g. [50], [149]–[151]. They might send different set-points to the respective WTs. The decision might be taken upon the actual operating point and available reactive power of the individual WT converters without the use of optimization algorithms [50].

2.3.1.2 Optimization-based dispatch

Optimization-based algorithms are widely used at transmission system level [150], [152]–[155]. TSOs use optimization algorithms to minimize electrical losses in their respective power grids by tuning set-points of the transformer OLTC or other electrical equipment which can control voltage or reactive power (e.g. WPPs, SGs, FACTS, HVdc converters, shunt reactors, and capacitor banks) [149], [150], [153], [154], [156]. The same approach can be applied to an internal WPP grid which has been studied for ac-connected

WPPs in [152], [156]–[166]. Based on the particle swarm optimization (PSO) algorithm of [160], the operation principle was investigated for DFIG–based WPPs in [157]. In [162], a feasible solution search PSO algorithm was applied to the reactive power allocation problem of a DFIG–based WPP. Different control principles are analyzed, concluding that a higher loss reduction is achieved for lower WPP power outputs. In terms of practicability for an online optimal reactive power allocation, the authors of [161], [165] propose OPF controllers based on mean–variance mapping optimization aiming to minimize losses while complying with the GC at the PCC. In [163], the suggested OPF controller additionally considers minimizing the switching actions of the OLTC and uses a neural–network–theory–based wind speed prediction. In [158], the authors discuss a complete loss calculation including generator and converter losses for a DFIG–based WPP to solve the optimal reactive power allocation problem. The analysis made in [164] provides a fruitful insight of the need to include the WT converter losses in the problem formulation of these systems. Ref. [147] proposes an optimization–based Mvar controller for the reactive power management of a distant ac–connected offshore WPP to minimize loss and comply with the onshore GC requirements.

2.3.2 Reactive power in HVdc–connected WPPs

For HVdc–connected WPPs, the reactive power requirements of the TSO are met by the onshore VSC–HVdc [42], [50], [55]. The reactive power balance in the offshore grid is literally independent on this requirement. Nevertheless, regulations might define the sharing, operation and control concept between the offshore VSC–HVdc and the connected WPP(s) [50]. For instance, the grid connection point in Germany is the network connection point to the HV grid and thus the HVdc transmission system and offshore ac grid are operated and owned by the TSO [55], [58]. Contrary, in the UK an independent, so–called offshore transmission owner provides the offshore grid connection and acts as intermediate operator between WPP operator(s) and the TSO [11], [55].

Regardless of the regulatory background, a possible reactive power control scheme for an HVdc–connected WPP cluster is sketched in Fig. 2.15. Each WPP hosts its respective WPPCs and might operate as explained

in Section 2.3.1.1. The offshore VSC–HVdc controls the voltage at the offshore PCC busbar (not shown here). The central dispatcher (CD) sends unique or individual reactive power, PF, or voltage set–points to each WPPs. The onshore GC compliance with respect to reactive power is the entire responsibility of the onshore VSC–HVdc.

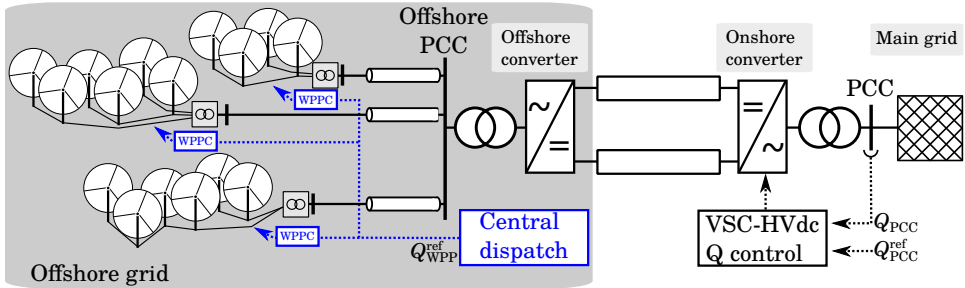


Figure 2.15: Schematic of simplified reactive power dispatch in an HVdc–connected WPP cluster.

Industrial implementation is commented in [42] which discusses the reactive power control concept used in the offshore grid of the *HelWin1*⁴: the offshore VSC–HVdc controls the offshore grid voltage, the WPPs receive PF set–points, and the OLTCs of the WPP transformers maintain the voltage in the adjacent MV collection grid. The same reference sketches different control approaches for those systems:

- voltage control by the VSC–HVdc and voltage control by the WPP with the goal of minimizing the OLTC switching actions;
- voltage control by VSC–HVdc with variable voltage set–points;
- voltage/reactive power droop control by all converters in the system;
- and operation of two parallel VSC–HVdc connected to the offshore grid.

Ref. [168] proposes the use of voltage control with droop compensation at WPP level. The WPPs control the voltage at their respective terminals and

⁴The HelWin alpha HVdc transmission system (576 MW, ± 250 kV, 130 km) connects two offshore WPPs, Nordsee Ost (288 MW) and Meerwind Süd|Ost (288 MW), and is operated by TenneT TSO [167].

dispatch reactive power set-points internally. A coordinated reactive power control scheme for WPP clusters with an optimization-based reactive power set-point at the offshore PCC is used in [169]. Ref. [170] proposes a WPP cluster controller based on voltage control at the respective WPP terminals. Ref. [55] identifies the reactive power/voltage control as an important point for optimization purpose. It is mentioned that the WT converters might be rated to their active power and the reactive power/voltage control responsibility is taken over by the VSC-HVdc. Moreover, it is outlined that the minimum reactive power requirement is the respective balance of the charging current required to energize the submarine cables, both MV collection grid and HV export line. It is further highlighted that an optimized sharing of the reactive power responsibility between the VSC-HVdc and the WT converters might avoid an over-sizing of the respective reactive power capabilities [42], [55].

2.4 Faults in offshore WPPs

Electrical faults might happen in any power system due to natural hazards, equipment failure, human interaction during operation and maintenance, etc. [171]. In the three-phase system faults might be classified into balanced and unbalanced ones, where three-phase (LLL) and three-phase-to-ground (LLLG) faults belong to the symmetrical or balanced faults and SLG, line-to-line-to-ground (LLG), and line-to-line (LL) faults are in the group of asymmetrical or unbalanced faults.

In HV grids, a total share of 67% for SLG, 25% for LL, 5% for LLL and LLLG, and 3% for LLG and a total of 300 measured short-circuits yr^{-1} for the HV grids of England and Wales is mentioned in [171]. Ref.[172] analyzes the Nordic fault statistics for 2000 to 2005 and concludes that most of the faults occur on overhead lines, the SLG fault has the highest share among all faults, and deep voltage sags (down to 0.25 p.u. of the nominal voltage) might last several sec to min, whereas voltage sags up to 0.75 p.u. usually last only some cycles. More recent statistics on overhead lines and cables show a similar number of fault events as depicted in Tab. 2.15 [173]. The data show that SLG have the highest share for overhead lines. Another interesting figure is that 77% of the SLG faults and most balanced and LLG

faults are caused by lightning strikes [171]. Fault statistics of the Nordic and Baltic countries and their respective HV grids disseminate that the main cause leading to faults in overhead lines is lightning, whereas cable failures are rather related to the technical equipment itself [173]. It is obvious that lightning strikes are a minor risk for cables due to their underground or submarine location.

Table 2.15: Fault statistics for the Nordic and Baltic countries¹. Average values for the 2005 to 2014 period [173].

Component	Voltage range $U_{\text{nom}} / \text{kV}$	Line length l / km	Fault events per 100 km $/\text{yr}^{-1}$	SLG faults $/ \%$	Permanent faults $/ \%$
Overhead line	380 to 420	20090	0.44	72.6	7.0
Overhead line	220 to 330	17406	0.64	65.7	8.1
Overhead line	100 to 150	48471	1.52	50.6	6.4
Cable	380 to 420	143	0.55	n/a	n/a
Cable	220 to 330	262	0.80	n/a	n/a
Cable	100 to 150	1882	0.55	n/a	n/a

¹ Comprises the data of the following countries: Denmark, Finland, Iceland, Norway, Sweden, Estonia, Latvia, and Lithuania.

While faults in overhead lines are normally of temporary nature and cleared through re-closing protection algorithms, submarine cable failures are usually permanent and require isolation of the system for the ease of fault localization and reparation [174]. Failure rates of submarine cables are reported to be lower than for underground cables [44].

Three-phase XLPE submarine cables are usually constructed with a metallic water-blocking sheath around each conductor to protect the insulation against water ingress [45]. Therefore, LL faults are not possible in such cable system as all short-circuit between two conductors passes through the metallic sheath which is literally grounded given the water penetration of the outer layers of the cable [175]. However, faults in offshore grids might also occur in the offshore substation, power transformers, auxiliary equipment, compensation devices, etc. and at the electrical infrastructure of the WT.

The fault protection and isolation concept for the offshore grid of an HVdc-connected WPP foresees that a possible fault must be located by

over-current relays and isolated by the adjacent circuit-breakers (CBs) [55], [126]. Internal WT faults might involve the disconnection of the WT from the system. Moreover, the VSC-HVdc and the WT are demanded to provide short-circuit currents to support the detection of the fault by means of FRT schemes [55].

Faults cause balanced or unbalanced voltage sags which propagate depending on the transformer winding setup between different voltage levels [176]. To allow a decoupling of the zero seq. networks, the WT and WPP converters are usually implemented in delta-*wye* configuration [92]. This means, for instance, that a SLG voltage sag in the MV collection grid is seen as a LL voltage sag on the HV-side of the WPP transformers and vice-versa [176, Table 2].

2.4.1 Fault ride through by the WT converters

WT converter control was addressed in Section 2.2.1. The dynamic response during grid faults might be defined as a dynamic voltage support scheme. Pos. seq. voltage support is implemented in most grid codes [92], [102]. The principle demands converter-based generation (e.g. WTs) to support the grid voltage through reactive current injection proportional to the magnitude of the voltage drop. For an improved response, specifically in grids with a high share of converter-based generation [115], also neg. seq. voltage reduction might be requested to allow proper detection of the fault by the adjacent protection system [102]. The voltage drop dependent schemes might be defined by [102]:

$$i_{1q} = k_1(U_{1,\text{pre-fault}} - U_1) \quad (2.15)$$

$$i_{2q} = k_2(U_{2,\text{pre-fault}} - U_2) \quad (2.16)$$

where:

k_1 = pos. seq. gain;

k_2 = neg. seq. gain;

$U_{1,\text{pre-fault}}$ = pos. seq. pre-fault voltage magnitude;

$U_{2,\text{pre-fault}}$ = neg. seq. pre-fault voltage magnitude.

The pre-fault voltage $U_{1,\text{pre-fault}}$ might be an averaged value prior to the fault (e.g. one-minute-mean value). The gain k_1 might take any positive value, but the maximum additional reactive current is limited (to e.g. 1 p.u.). A deadband for continuous operation voltages e.g. 0.95 p.u. to 1.05 p.u. might avoid voltage support during normal steady-state conditions. In normal operation, the grid voltages are balanced, so the magnitude of the pre-fault neg. seq. voltage $U_{2,\text{pre-fault}}$ is zero. During unbalanced voltage conditions, neg. seq. voltage arises and might be attenuated by dynamic voltage reduction by choosing $k_2 \neq 0$.

The FRT requirements from [102] are depicted in Fig. 2.16. The voltage-time profiles for UVRT and over-voltage ride through (OVRT) are displayed Figure 2.16a. The WTs converter must remain connected to the grid for the given ranges. The required reactive current injection during FRT is shown in Fig. 2.16b. A tolerance band according to [102, Annex C] is sketched around the slope. The diagram is valid for both pos. and neg. sequence. A specific response during SLG faults is not demanded as those faults are not considered to be threatening for the voltage stability of the grid. However, the WTs must also stay connected for SLG faults according to Fig. 2.16a.

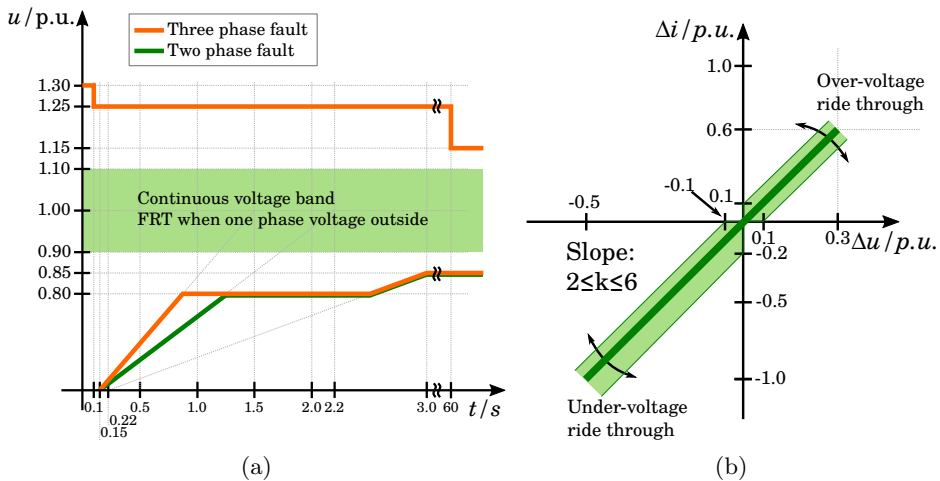


Figure 2.16: FRT (a) voltage-time profile and (b) reactive currents [102].

2.4.2 Fault ride through in HVdc-connected WPPs

As mentioned in Section 2.2, the decoupled operation through the dc link means that the main FRT responsibility is placed on the onshore VSC–HVdc [55], [177]. FRT by the onshore VSC–HVdc for balanced and unbalanced onshore faults is addressed in [112], [123], [178]–[181]. In [179], unbalanced faults in the onshore grid were studied and an injection of neg. seq. currents by the VSC–HVdc was beneficial for the protection system in comparison to suppression thereof. Regardless of whether an onshore grid fault is symmetrical or asymmetrical, it might impede the injection of the actual active power injected by the offshore VSC (and the adjacent WPPs). Therefore, one solution might be the installation of a dynamic braking resistor (dc chopper) to dissipate the surplus energy. The equipment might be placed onshore to make the most of local measurements and lower installation costs than offshore [55], [177].

Moreover, the WPP might also contribute to active power reduction schemes during onshore faults [55]. Possible active power reduction schemes are based on fast communication [60], [182], offshore grid voltage modulation [123], [180], [182]–[185], or frequency modulation [60], [92], [180], [185]. Fast frequency response schemes also cover active power variation although they are not exclusively designed for a FRT response [66]–[69].

In contrast to onshore faults, FRT in the offshore grid is barely covered in literature. One reason might be that faults in the electrical infrastructure based mainly on submarine cable are less likely to be exposed to natural hazard compared to overhead lines and to some extent to land-based cables [60]. However, as in any engineering system, faults might occur and must be handled in a secure manner to protect the system.

The common control concepts of the grid-forming offshore VSC–HVdc, see Section 2.2.2, imply that the converter currents rise and should be limited in the case of an offshore fault. For symmetrical faults in the offshore grid, Ref. [169] proposes a reactive power control for an HVdc-connected WPP cluster and demonstrates how the injection of additional reactive current by the WT converters supports the voltage profile. A coordinated voltage

control is presented in [170] and symmetrical faults at different busbars in the offshore grid are considered. Apart from the local WT FRT scheme, Ref. [170] proposes a WPP-level FRT scheme which uses reactive power margins from the non-faulted WPPs in the cluster to achieve a better voltage profile in the offshore grid.

Asymmetrical/unbalanced faults in the offshore grid were studied in [123], [126], [127], [186], [187]. Ref. [186] focuses on correct protection and isolation without any neg. seq. control by the converters. In [126], [127], different combinations of neg. seq. FRT by the VSC-HVdc, the WTs, or both are analyzed for faults at 33 kV and 150 kV level in the offshore grid. Special focus is paid to double fundamental frequency oscillations during unbalanced voltage conditions rather than on voltage support. Ref. [123] proposes a controlled ac voltage drop imposed by the offshore VSC-HVdc to activate a positive-sequence-voltage-drop-dependent active power reduction from the offshore WPP during onshore faults. Hence, the FRT of unbalanced onshore faults might profit from a larger reactive current margin. The authors further demonstrate that for an offshore LL fault at 33 kV level, reactive currents from the WT converters are not needed. Ref. [187] presents a transient control strategy to provide additional reactive power during asymmetrical faults but lacks a clear explanation of the offshore VSC-HVdc control. Moreover, it uses a PLL system which is not necessary in the real application [42].

2.5 Summary

The literature review sheds light on the state of the art of offshore WPPs and their grid integration by means of HVdc transmission technology. At the beginning, it was highlighted that offshore wind is gaining interest among the renewable energy power generation but still remains more expensive than onshore wind. The offshore WT technology was covered briefly and concluded on the two state-of-the-art power conversion concepts, namely the PSC- and FSC-WT. The latter was identified to be superior at meeting demanding GC requirements. Then, grid connection options by means of ac or dc technology were introduced for offshore WPPs. It was commented that VSC-HVdc transmission technology is the state of the art for the integration of very remote WPPs. It was highlighted that in HVdc-connected WPPs the offshore ac grid is decoupled from the main grid. The decoupled operation was identified to be the key differentiator to conventional ac connected WPPs. Besides that, other academic concepts without current industrial application were summarized.

Furthermore, the control methods for VSCs in grid-connected and grid-forming operation mode were outlined. It was highlighted that the principles for grid-connected converters are well established. In contrast to that, it was identified that for the grid-forming mode the desired response under unbalanced conditions was not fully covered in the literature. Additionally, the prevailing VSC-HVdc topology for offshore wind and other applications, the MMC-HVdc, was explained.

The last part of the literature review concentrated on the two key aspects of HVdc-connected WPPs to be explored in this thesis: i) reactive power control and ii) FRT of faults in the offshore ac grid. Conventional reactive power control and optimization-based proposals for WPPs and for other applications were reviewed. Here it was concluded that reactive power and voltage control inside HVdc-connected WPPs had a potential application for optimization-based approaches. Furthermore, it was highlighted that the FRT of unbalanced faults in a converter-based grid presented a challenge that had been barely covered in the literature to date.

3 Reactive power control in an HVdc-connected WPP

3.1 Introduction

This chapter tackles reactive power control in the offshore grid of a single HVdc-connected WPP. Specifically, the reactive power balance between the VSC-HVdc and WT is investigated. The focus is put on conventional and optimization-based reactive power allocation strategies to obtain the maximum active power output at the HVdc link interface. The literature on optimization-based concepts for ac-connected WPPs was explored in Section 2.3.1.2. Moreover, the sparse studies on reactive power control in the offshore grid of HVdc-connected WPPs were commented in Section 2.3.2.

In this chapter, six different reactive power control strategies are defined and evaluated regarding reactive power sharing, voltage range, and annual energy production (AEP). In addition to that, the impact of wake losses on the reactive power control is explored.

To summarize, this chapter aims to shed light on:

- reactive power allocation strategies in the offshore grid of an HVdc-connected WPP;
- reduction of power losses in the offshore grid regarding reactive power control;
- optimization-based strategies with variable reference voltage;
- impact of wake effects on the reactive power control;
- and sharing of reactive power between the WTs and the offshore VSC-HVdc.

3.1.1 Related publications

The work presented in this chapter was disseminated in:

- K. Schönleber, C. Collados, R.T. Pinto, S. Ratés-Palau, O. Gomis-Bellmunt, Optimization-based reactive power control in HVDC-connected wind power plants, *Renew. Energy*. 109 (2017) 500–509. doi:10.1016/j.renene.2017.02.081.
- K. Schönleber, S. Ratés-Palau, M. De-Prada-Gil, O. Gomis-Bellmunt, Reactive power optimization in HVDC-connected wind power plants considering wake effects, in: U. Betancourt, T. Ackermann (Eds.), 14th Wind Integr. Work., Energynautics GmbH, Brussels, Belgium, 2015.

3.2 Methodology

First, a power loss assessment methodology for the offshore grid of an HVdc-connected WPP system is developed. Then, the reactive power allocation strategies are outlined and the optimization problem is formulated for the system. The strategies are briefly discussed regarding their industrial implementation. Last, the wake modeling used for this work is highlighted.

3.2.1 Calculation of relevant losses

The considered generic HVdc-connected WPP system is shown in Fig. 3.1. In general, there are multiple electrical losses occurring in the operation of generators, converters, filters, transformers, and cables. For the steady-state power flow analysis, lines, filters, and transformers are modeled as lumped circuits (π -models) [188]. In a π -model, the series admittance between two nodes a and b is defined as:

$$y_{ab} = g_{ab} + j \cdot b_{ab} = \frac{r_{ab}}{r_{ab}^2 + x_{ab}^2} - j \frac{x_{ab}}{r_{ab}^2 + x_{ab}^2} \quad (3.1)$$

where:

y_{ab} = admittance between node a and b ;

g_{ab} = series conductance between node a and b ;

b_{ab} = susceptance between the nodes a and b ;

r_{ab} = series resistance;
 x_{ab} = series reactance.

The shunt admittance is calculated as:

$$y_a^{\text{sh}} = y_b^{\text{sh}} = g^{\text{sh}} + j \cdot b^{\text{sh}} \quad (3.2)$$

where:

y_a^{sh} = shunt admittance at node a ;
 g^{sh} = shunt conductance;
 b^{sh} = shunt susceptance.

When considering power cables and lines, the shunt conductance is very small ($g^{\text{sh}} \approx 0$) and can be neglected. The values for the series resistance r_{ab} , series reactance x_{ab} , and shunt susceptance b^{sh} are chosen according to manufacturer data. For transformers, the series resistance r_{ab} models the copper losses (load losses) in the windings having the reactance x_{ab} . The iron/core losses (no-load) due to the magnetizing current can be represented by a shunt element. The active power imbalance or loss Δp can be calculated using Eqn. (3.3) and the reactive power imbalance Δq composed of the reactive power generation by the shunt susceptance and reactive power loss is described in Eqn. (3.4):

$$\Delta p = g_{ab} \cdot [(u_a^2 + u_b^2 - 2u_a u_b \cos(\varphi_a^u - \varphi_b^u))] \quad (3.3)$$

$$\Delta q = -b^{\text{sh}} \cdot [u_a^2 + u_b^2] - b_{ab} \cdot [u_a^2 + u_b^2 - 2u_a u_b \cos(\varphi_a^u - \varphi_b^u)] \quad (3.4)$$

where:

u_a, u_b = voltage of node a and b ;
 φ_a^u, φ_b^u = voltage angle of node a and b .

The compilation of losses is limited to the boundaries of the offshore grid as shown in Fig. 3.1: boundary A is the interface between dc link of the GSCs and boundary B is the dc terminal the offshore VSC–HVdc. These boundaries are set given that the reactive power control at the ac terminal of a VSC is independent from the dc side [61]. Therefore, the control of reactive power at the GSC does not cause additional currents (or losses) in the dc link,

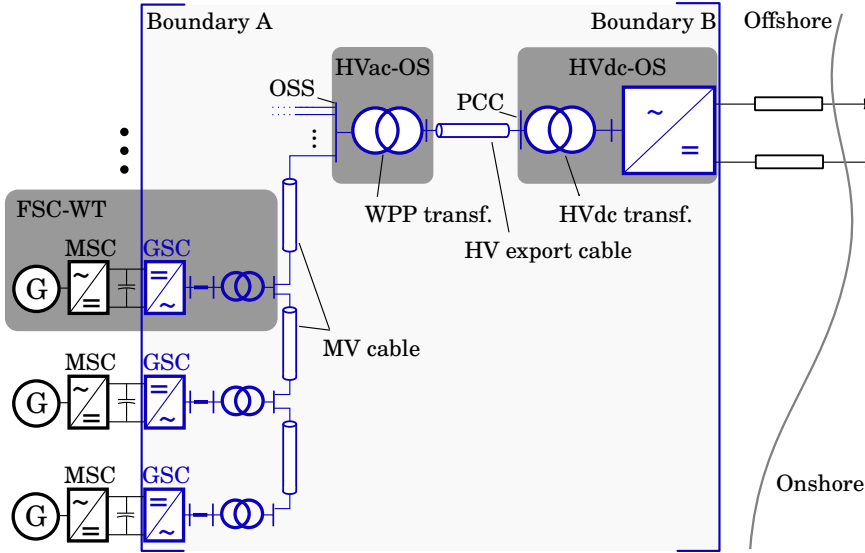


Figure 3.1: Typical arrangement of an HVdc-connected offshore WPP and system boundaries for loss assessment.

the MSC or even the generator. This is also valid for the offshore VSC-HVdc with respect to its HVdc interface. Besides that, the power converter losses might be approximated as described in Appendix A.2. Figure 3.2 shows the relative power losses of the considered power converters deploying Eqn. (A.5) with the parameter values from Tab. A.1. The effect of the absolute loss increase ΔP due to a reactive power exchange in comparison to exclusively active power injection is represented in Fig. 3.3. The additional converter losses in the 555.6 MVA-rated MMC-HVdc are up to 0.9 MW when operated at $p = 0$ p.u. and $q = 1$ p.u.. For $q = 1$ p.u., an equally scaled GSC system causes a value of $\Delta P = 1.0$ MW additional losses at full power and up to $\Delta P = 2.8$ MW additional losses for $p = 0$ p.u.. To sum up, reactive power exchange causes additional power losses in the power converter. This is even more pronounced at low power operation.

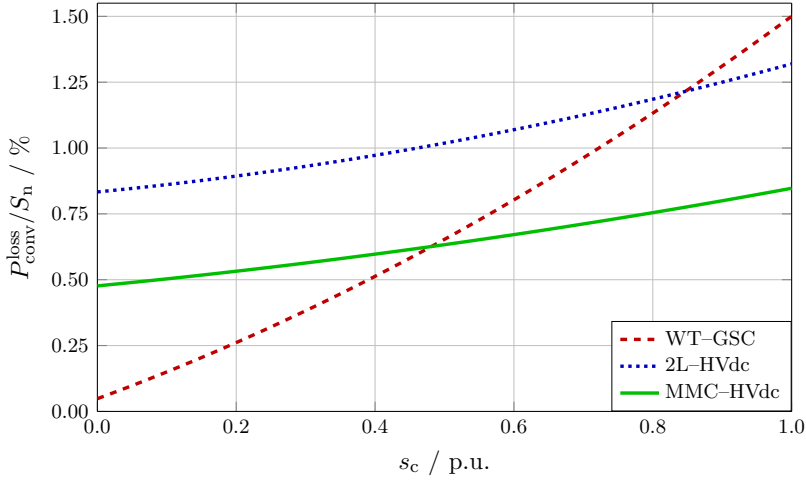


Figure 3.2: Relative losses of VSC systems based on their technology and power output.

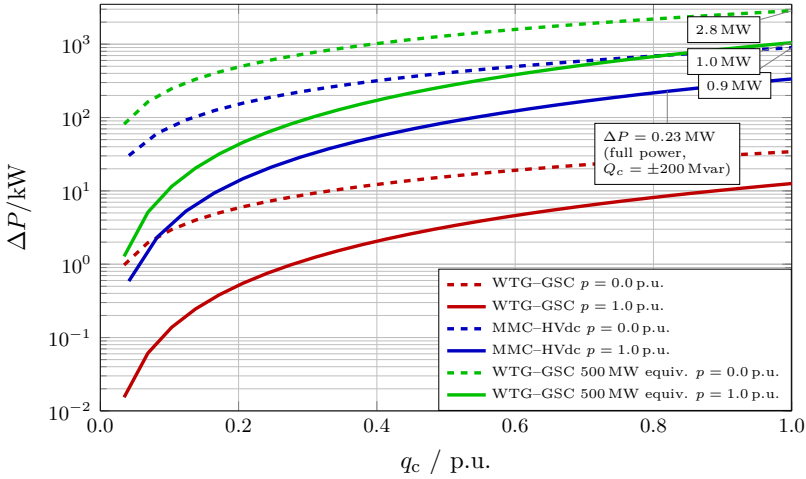


Figure 3.3: Absolute increase of losses caused by the reactive power injection of VSCs. GSC rating: $S_r = 6.67 \text{ MVA}$, $\cos \varphi = 0.9$, $U_{ac} = 0.9 \text{ kV}$; MMC-HVdc $S_r = 555.6 \text{ MVA}$, $\cos \varphi = 0.9$, $U_{ac} = 333 \text{ kV}$ ($U_{dc} = \pm 320 \text{ kV}$, modulation index: $m = 0.85$); GSC 500 MW equivalent to compare with the VSC-HVdc.

3.2.2 Reactive power allocation strategies

The reactive power allocation strategies considered in this chapter focus on the normal operation of the HVdc-connected WPP in steady-state. The WT reactive power limitations due to the availability and PQ capability curve must be respected.

In principle, two conventional strategies might emerge to control reactive power in an HVdc-connected WPP when the control variables are limited to be the reactive power set-points:

- I. Strategy 1 (S1): No reactive power by the WTs. Each GSC operates locally with zero reactive power injection, thus $Q_i = 0$ Mvar. This is equal to a unity PF operation of the GSCs for $P_i \neq 0$ MW.
- II. Strategy 2 (S2): No reactive power by the VSC-HVdc. The VSC-HVdc aims to operate with zero reactive power injection ($Q_{PCC} = 0$ Mvar) by adjusting remotely the reactive power set-points Q_i of the WTs.

Furthermore, an optimization-based strategy is considered:

- III. Strategy 3 (S3): The optimization algorithm aims to maximize the power output of the system and calculates reactive power set-points for the GSCs according to the actual operating point of the complete system.

The strategies S1 to S3 are studied with a fixed PCC voltage reference of $u_{PCC} = 1$ p.u., which is continuously controlled by the VSC-HVdc. Finally, the three initial strategies are extended by the varying voltage reference and introduced as variable strategies:

- IV. Variable strategy 1 (S1var): Optimization-based with the PCC voltage magnitude u_{PCC} as control variable, whereas the WT inject $Q_i = 0$ Mvar ($i \in N_{WT}$).
- V. Variable strategy 2 (S2var): Optimization-based with the PCC voltage magnitude u_{PCC} as control variable and a unique set-point for Q_i of the WTs. No reactive power is provided by the VSC-HVdc.

VI. Variable strategy 3 (S3var): Optimization-based like S3 adjusting the individual reactive power set-points for the GSCs as well as the PCC voltage magnitude u_{PCC} controlled by the offshore VSC-HVdc.

Strategy S1var to S3var allow a variable PCC voltage set-point within continuous voltage operation boundaries. For all strategies, the VSC-HVdc injects or absorbs the active and reactive power to fulfill the power imbalance equations (acting as a reference bus).

Regarding data exchange requirements, the implementation of S1 does not necessarily use the communication system between the local WTC and the central WPPC. In contrast, S2 deploys a closed-loop control to adjust the set-points Q_i controlling the measured Q_{PCC} to the reference of 0 Mvar. The reactive power set-point for S1, S2, S1var, and S2var is the same for all WTs. The strategies S3, S1var, S2var, and S3var necessarily require a communication system as inputs (active power measurements, operation status of WTs) and outputs (reactive power set-points, u_{PCC} set-point in the case of the variable strategies) must be transferred between the WTC and central WPPC. Figure 3.4 sketches the communication and measurement needs for the presented strategies. To sum up, the six strategies and their characteristics are listed in Tab. 3.4.

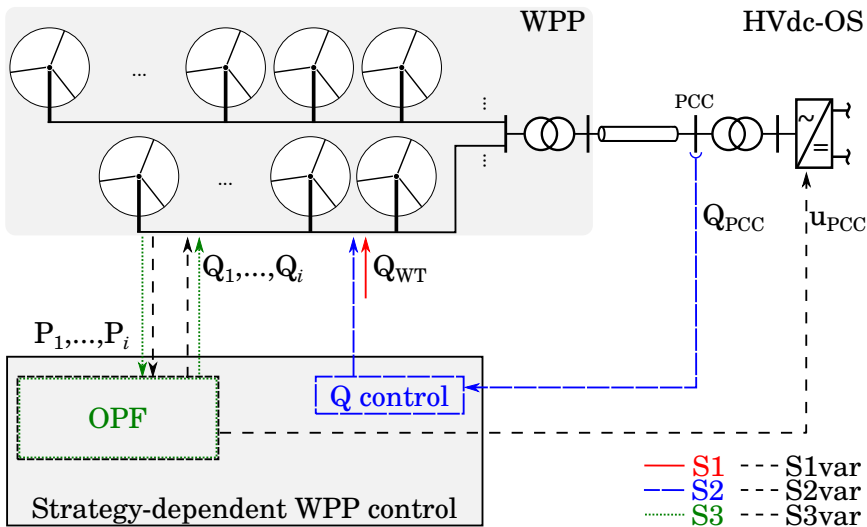


Figure 3.4: Schematic of control concepts and communication paths for all strategies.

Table 3.4: Overview of considered reactive power allocation strategies.

	S1	S2	S3	S1var	S2var	S3var
Objective	No Q by WTs	No Q by VSC-HVdc	min $P_{\text{total}}^{\text{loss}}$			
Communication	Local			Remote		
Q_i set-points	0 Mvar	WPPC	OPF	0 Mvar	OPF	OPF
Q_i distribution	Uniform	Uniform	Variable	Uniform	Uniform	Variable
Q_{PCC} set-point ¹	Power flow	0 Mvar	Power flow			
u_{PCC} set-point		Fixed	Variable			
Average execution time OPF ²	n/a	n/a	188.8 s	1.9 s	9.8 s	243.9 s

¹ The reactive power at the PCC is determined by the power flow in the offshore grid.

² Data is given for the case study.

3.2.3 Formulation of the optimization problem

The total active power losses $P_{\text{total}}^{\text{loss}}$ in the system are calculated as:

$$P_{\text{total}}^{\text{loss}} = \sum_{\forall i} P_{\text{GSC}_i}^{\text{loss}} + P_{\text{grid}}^{\text{loss}} + P_{\text{VSC-HVdc}}^{\text{loss}}. \quad (3.5)$$

where:

$P_{\text{grid}}^{\text{loss}}$ = grid losses including collection grid, export cable(s), and transformer(s);

$P_{\text{GSC}_i}^{\text{loss}}$ = power losses of the GSC;

$P_{\text{VSC-HVdc}}^{\text{loss}}$ = power losses of the VSC-HVdc.

The design vector \mathbf{x} accommodates the voltage set-point u_{PCC} and the reactive power set-points q_i of the GSCs:

$$\mathbf{x} = [u_{\text{PCC}}, q_1, q_2, \dots, q_i]^T \quad i \in \mathbf{N}_{\text{WT}} \quad (3.6)$$

where:

\mathbf{N}_{WT} = vector of all WT elements.

The optimization problem is stated as follows:

$$\text{Minimize } f(\mathbf{x}) = P_{\text{total}}^{\text{loss}}(\mathbf{x}) \quad (3.7)$$

s.t. :

$$0 = -p_r + \sum_{s=1}^N U_r U_s (G_{rs} \cos \theta_{rs} + B_{rs} \sin \theta_{rs}) \quad (3.8)$$

$$0 = -q_r + \sum_{s=1}^N U_r U_s (G_{rs} \sin \theta_{rs} - B_{rs} \cos \theta_{rs}) \quad (3.9)$$

$$\mathbf{u}_{k,\min} \leq \mathbf{u}_k(\mathbf{x}) \leq \mathbf{u}_{k,\max}, \quad k \in \mathbf{N}_{\text{bus}} \quad (3.10)$$

$$|\mathbf{i}_l(\mathbf{x})| \leq \mathbf{i}_{l,\max}, \quad l \in \mathbf{N}_{\text{brs}} \quad (3.11)$$

$$q_{\text{PCC},\min} \leq q_{\text{PCC}}(\mathbf{x}) \leq q_{\text{PCC},\max} \quad (3.12)$$

$$u_{\text{PCC}} \in [u_{\text{PCC},\min}, u_{\text{PCC},\max}] \quad (3.13)$$

$$\mathbf{q}_i \in [q_{i,\min}, q_{i,\max}], \quad i \in \mathbf{N}_{\text{WT}} \quad (3.14)$$

where:

G_{rs}, B_{rs}	= real and imaginary part of the respective element in the admittance bus matrix \mathbf{Y}_{rs} ;
p_r, q_r	= injected active and reactive power at bus r ;
U_r, U_s	= magnitudes of bus voltages at bus r and s ;
θ_{rs}	= phase angle between bus voltages;
\mathbf{N}_{bus}	= vector of all buses (except PCC bus);
N	= total bus number;
\mathbf{N}_{brs}	= vector of all branches;
$\mathbf{u}_k(\mathbf{x})$	= vector of the bus voltages;
$\mathbf{u}_{k,\min}, \mathbf{u}_{k,\max}$	= vector of the minimum and maximum bus voltages;
u_{PCC}	= PCC voltage;
$u_{\text{PCC},\min}, u_{\text{PCC},\max}$	= minimum and maximum PCC voltage;
$\mathbf{i}_l(\mathbf{x})$	= vector of currents in the branches;
$\mathbf{i}_{l,\max}$	= vector of maximum current limits;
$q_{\text{PCC}}(\mathbf{x})$	= reactive power at PCC;
$q_{\text{PCC},\min}, q_{\text{PCC},\max}$	= minimum/maximum reactive power at PCC;
\mathbf{q}_i	= vector of reactive power at each WT;
$q_{i,\min}, q_{i,\max}$	= vector of minimum/maximum reactive power.

Equations (3.8) and (3.9) are the power flow equations for the system. The voltages $\mathbf{u}_k(\mathbf{x})$ in the system are limited to the minimum and maximum voltages $\mathbf{u}_{k,\min}$ and $\mathbf{u}_{k,\max}$ being a deviation of $\pm 10\%$ of the nominal voltage. The current in a branch $\mathbf{i}_l(\mathbf{x})$ represents the highest absolute value of the current at both ends of the branch. It is limited to the corresponding rating $\mathbf{i}_{l,\max}$. The reactive power limitations at the PCC, $q_{\text{PCC},\min}$ and $q_{\text{PCC},\max}$, and for the WTs, $q_{i,\min}$ and $q_{i,\max}$, correspond to a PF of 0.9 at full power. In general, the reactive power converter capability increases beyond this value in the low power range given that the converter current might be calculated by Eqn. (A.4) and is limited by the semiconductor capability. Under consideration that the higher reactive power capability is unlikely to be used due to the additional converter losses and for the sake of simplicity, the limits for full power are selected. The different PCC voltage constraints between the optimization-based strategies (S3, S1var, S2var and S3var) are reflected by $u_{\text{PCC},\min} = u_{\text{PCC},\max} = 1.0$ p.u. for S3 and $u_{\text{PCC},\min} = 0.9$ p.u. and $u_{\text{PCC},\max} = 1.1$ p.u. for S1var to S3var in Eqn. (3.13). Strategy S1var is further restricted by $q_i = q_{i,\min} = q_{i,\max} = 0$ p.u. ($i \in \mathbf{N}_{\text{WT}}$) in Eqn. (3.14). For strategy S2var the reactive power at the PCC is restricted to $q_{\text{PCC}} = q_{\text{PCC},\min} = q_{\text{PCC},\max} = 0$ p.u. Eqn. (3.12) and additionally $q_i = q_j$ ($i, j \in \mathbf{N}_{\text{WT}}$) meaning that all WTs receive an equal reactive power set-point.

3.2.4 Implementation of the optimization-based strategies

The implementation of the optimization-based strategies is done by the combination of the MATLAB-based power flow solver package Matpower [3] and the `fmincon` function of the MATLAB Optimization Toolbox. For this study, lines and transformers are sufficiently modeled as a π -section model [189]. In Matpower, every GSC is defined as static generator G_i connected to a load bus (PQ bus), injecting active power P_i and reactive power Q_i ($i \in \mathbf{N}_{\text{WT}}$). The VSC-HVdc, which sets the PCC voltage reference, is introduced as the reference bus (slack bus). The integration of the converter losses is made sequentially: the GSC losses caused by Q_i are considered as a real power demand at the corresponding WT load bus, whereas the VSC-HVdc losses are calculated after each load flow computation by Eqn. (A.5),

see Appendix A.2. The `fmincon` function uses the interior–point algorithm. The optimization is deterministic as the interior–point algorithm reaches local minimums. Nevertheless, the solver runs from multiple starting points to increase the number of solutions. Furthermore, the total execution time is limited. The best solution is selected and verified through load flow calculation afterwards.

3.2.5 Feasibility for the industrial application

A feasible industrial implementation of the optimization–based strategies might consider a variable refresh rate around 5 min. The optimization algorithm itself might have a maximum execution time (here set to 300 s). The average execution times recorded for the case study in this chapter are listed in the last row of Tab. 3.4. Obviously, the number of the control variables increases the calculation time. For S1var and S2var average calculation times below 10 s are reached (simulations are run on a 3.5 GHz–system with 16 GB RAM). New set–points might be sent as soon as the optimization algorithm ends. Further time requirements are: the communication times for the active power measurements of the WTs and the reference voltage/reactive power set–points, respectively, and the settling time after receiving the new set–points. The communication delays are negligible on the time frame of the proposed controller, as modern communication systems in offshore WPPs consider refresh rates of a few hundreds of ms [190]. The settling times might be established as required for slow reactive power set–point changes in WPPs (e.g. 30 sec [92]). Fast dynamic voltage support to counteract voltage sags acts independently from this and would still supersede the previous reactive power set–points during activation. For the variable strategies, the reference voltage might be changed first and afterwards the reactive power injections by the WTs. Real–time implementation might be improved by either short–term power or wind forecast to offset the time delay [165] or offline calculation of the optimization algorithm.

3.2.6 Wakes effect modeling

The wake effect is one of the most relevant factors when estimating the AEP of a WPP [191]. As is known, there is a wind energy deficit between the

wind arriving in front of the WT (upstream) and the wind leaving the WT (downstream) due to the interaction of the WTs with the wind [192]. This extraction of energy leads to a wind speed reduction for the downwind WTs which causes a decrease of their power outputs. The power losses due to wake effects in offshore WPPs can constitute about 5% to 15% of its total power generation depending on multiple factors such as the incoming wind speed and its direction, the design characteristics of the rotor blades, and the spacing between the WTs [193]. WTs are typically spaced out at least 5 to 9 rotor diameters away from each other in the prevailing wind direction and about 3 to 5 rotor diameters for winds coming perpendicularly [194]. These spacing rules are the result from the trade-off between maximizing the AEP by wake effect reduction and minimizing the costs associated with the collection grid [191].

Wake model development and corresponding studies have been conducted by e.g. [195] (Ainslie's model), [192] (Frandsen's model), [196] (mosaic tile model), [197] (Jensen's model), and [198] (computational fluid dynamics model). In [193], a comparison of different wake models concludes that the sophisticated models have a similar level of accuracy as simpler ones. One of the most widely used wake models, developed by Jensen [197], has been chosen for this chapter, as it provides sufficient accuracy and reduced computational time [199]. It is based on global momentum conservation in the wake downstream of the WT and assumes that the wake downstream of the WT expands linearly. Detailed explanation about this wake model can be found in [191], [194], [197].

The wind speeds of the free-stream WTs have been assumed to be equal, whereas for the downwind turbines the implemented model takes single, partial, and multiple wakes inside the WPP into consideration. Furthermore, when the wind speed of the upstream WTs is above cut-out speed the wake effect within the WPP is not considered since the WTs might be shut down to prevent structural overload. An optimized operation considering wake effects for active power allocation is out of the scope of this study. The reader might be pointed to [36], [191], [199].

3.3 Case study

The analysis made in this chapter aims to draw conclusions based upon realistic data. Therefore, the WPP characteristics were derived from the French Fécamp project [7], [37]. This WPP is planned to output $P_{\text{rat}} = 498$ MW with 83 individual FSC-WTs with a nameplate capacity of $P_{\text{WT}} = 6$ MW each. For the sake of simplicity, it is assumed that each GSC can provide the equivalent reactive power of a PF of $\cos \varphi = 0.9$ (inductive and capacitive) at full power. It must be noted that the intrinsic additional reactive power capability of the power converters at lower powers is not of interest here as they cause even more additional converter losses compared to the unity power factor operation as highlighted in Section 3.2.1.

The graphical data offered in [37] allows us to estimate individual cable lengths and to define the distribution of the turbines as well as how they are interconnected (visualized in Fig. 3.5). Further relevant reference data, including component parameters and voltage levels, are provided in Tab. 3.8. The array cable lengths were calculated according to the distance between the turbines and an additional offset of $l = 100$ m to incorporate the cable routing from the sea bed to the transition piece of the WTs. Table 2.2 gives data for the XLPE submarine cables considered in this study.

Contrary to the reference project which deploys an HVac connection to shore, the transmission grid connection is adapted to an HVdc connection for the study. Loss data for the offshore VSC-HVdc are calculated according to Eqn. (A.5). The loss coefficients for a MMC-HVdc system are used and displayed in Tab. A.1. Strategy S1 is chosen as the base strategy to evaluate the other concepts. The relative loss reduction of one strategy S_n in comparison to the base strategy S1, $P_{\text{rel}}^{\text{loss}}$, is calculated as:

$$P_{\text{rel}}^{\text{loss}} = \frac{P_{S_n}^{\text{loss}}}{P_{S_1}^{\text{loss}}} \cdot 100 \%. \quad (3.15)$$

where:

$P_{S_n}^{\text{loss}}$ = total power losses for strategy S_n ;

$P_{S_1}^{\text{loss}}$ = total power losses for strategy S1.

Table 3.8: Reference data and relevant system parameter of the test system.

WT grid connection	
Nominal voltage (U_{ac}/kV)	0.9
GSC (S_r/MVA , $\cos \varphi$)	6.67, 0.9 (inductive and capacitive)
Coupling impedance ($r/p.u.$, $x/p.u.$)	0.004, 0.13
MV transformer (LV/HV, S_r/MVA , $r/p.u.$, $x/p.u.$, no-load losses/p.u.)	0.9/33, 6.7, 0.009, 0.06, 0.0008
MV collection grid	
Nominal voltage (U_{ac}/kV)	33
Total cable length (l/km)	118
Total number of turbines	83
HV transformer ($\#$, LV/HV, S_r/MVA , $r/p.u.$, $x/p.u.$, no-load losses/p.u.)	2, 33/220, 280, 0.003, 0.15, 0.0004
HV ac export cable	
Nominal voltage (U_{ac}/kV)	220
Export cable(s) ($\#$, A/mm^2 , l/km)	2, 800, 10
HV dc transmission	
Nominal voltages (U_{ac}/kV , U_{dc}/kV)	333, ± 320
Converter (topology, S_r/MVA , $\cos \varphi$)	MMC-HVdc, 555.6, ± 0.9

3.3.1 Wind data

To compute an approximate value of the total energy losses of the WPP, the annual wind speed distribution of the specific site is required. In general, a Weibull probability distribution approximates the annual distribution of the wind speeds for WPP studies. The parameters for the case study are the mean wind speed of 8.8 m s^{-1} [7] and a commonly used shape parameter for offshore locations of 2.2 [200]. For the model considering wake effects, the wind distribution must be given alongside with the wind directions. The annual frequency of wind speed/direction sets was taken from a mesoscale wind model for the project location with a resolution of 16 wind direction bins (22.5° each), and 36 wind speed bins of 0 m s^{-1} to 37 m s^{-1} [7]. The data dependent upon the wind direction are visualized in Fig. 3.6a.

The consideration of outages of WTs or the HVdc system due to maintenance or failure is beyond the scope of the study. To estimate the monetary value of the total energy losses, the French offshore feed-in tariff of

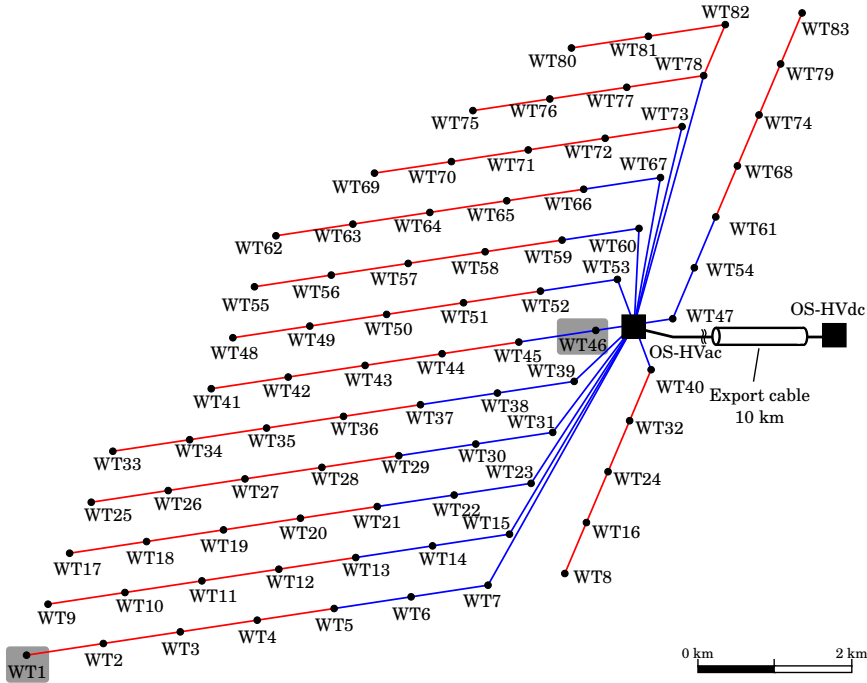


Figure 3.5: Layout of the reference WPP Fécamp (498 MW). WT1 is the most distant and WT46 the closest turbine to the offshore substation.

130 € MWh^{-1} was considered [201].

3.4 Results

The results are presented in two parts. First, the influence of individual active power operating points for the WT is analyzed for the case study and the fixed reference voltage strategies S1, S2, and S3. In the second part, the variable strategies S1var, S2var and S3var are analyzed alongside with the fixed reference voltage strategies for a unique wind speed distribution in the WPP.

3.4.1 Fixed voltage strategy with wake effect

The application of the wake model resulted in an AEP of 1952 GWh excluding the losses in the collection grid and transmission system. This value equals

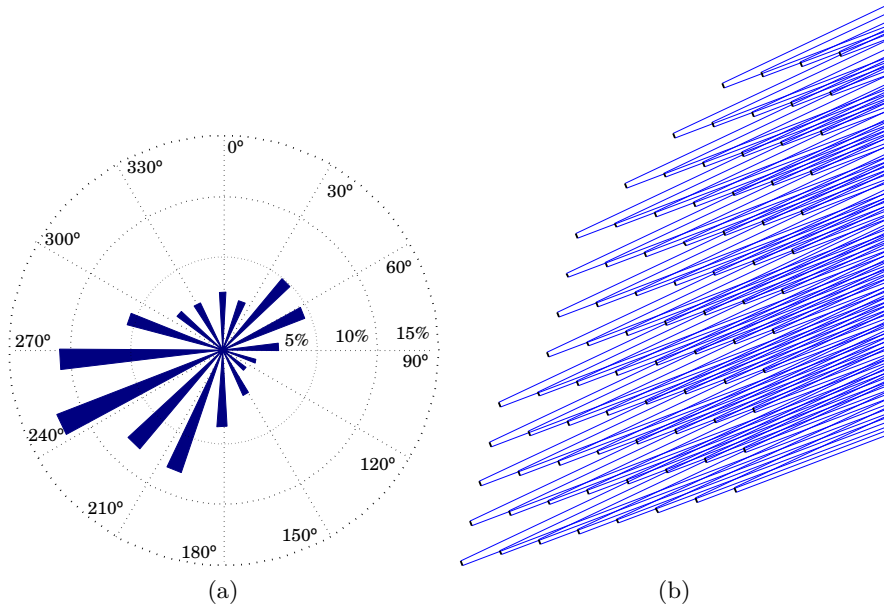


Figure 3.6: Wind direction distribution bins (a) and wake visualization for prevailing wind direction of 112.5° (b).

a wake loss of 7.92 % compared to 2120 GWh for equal wind speeds in the WPP. Within the WPP, individual WTs produced an average of yearly 23.52 GWh (25.54 GWh in the absence of wake losses). Figure 3.7a depicts for each WT position the AEP value in p.u. compared to the base value calculated without wake losses. On an annual basis, the figure demonstrates that free-stream (outer) WTs have rather a higher AEP than WTs inside the WPP. Table 3.10 identifies that WT1 has the maximum yield of 25.04 GWh being advantageously positioned in prevailing wind directions. The minimum yearly AEP of 22.45 GWh was yielded by WT21 which is situated in the center of the WPP and strongly effected by wake losses.

Table 3.11 enumerates the annual reactive power production (ARP) of the WTs and the VSC-HVdc for the different strategies S1, S2, and S3. For strategy S1 and S2, respectively, either the VSC-HVdc or the WT take full responsibility for the reactive power injection into the WPP grid. The set-points are distributed equally leading to the same average, minimum, and maximum ARP. For strategy S3, the WTs and VSC-HVdc share the

Table 3.10: Mean, minimum, and maximum AEP with and without wakes.

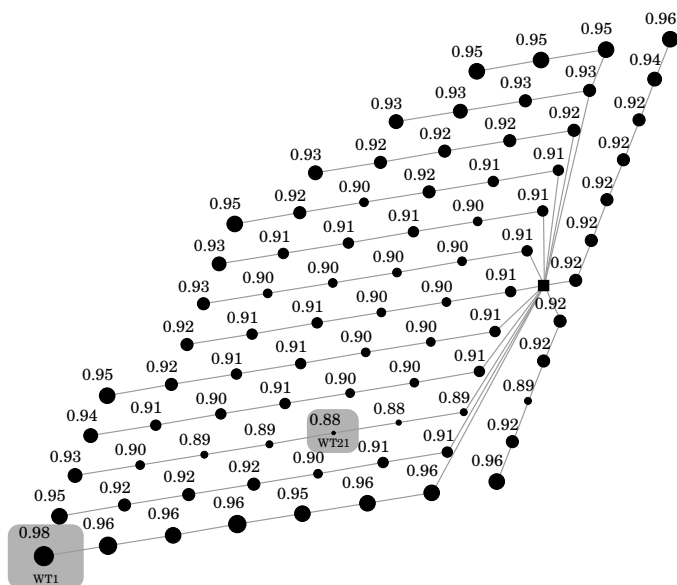
	Wakes	No wakes
Mean / GWh	23.52	25.55
Minimum / GWh (WT#)	22.45 (WT21)	25.55
Maximum / GWh (WT#)	25.04 (WT1)	25.55

responsibility upon the calculations of the optimization algorithm. Here, the results show that the ARP is split in 49.2% for the WTs versus 50.8% for the offshore VSC–HVdc. The ARP by the VSC–HVdc for strategy S3 decreases to 58.6% compared to S1 and the average ARP of the WTs for S3 lowers to 62.4% of the value for S2. The individual ARP deviation of each WT in p.u. based on the average value is visualized for the results of strategy S3 in Fig. 3.7b. The maximum deviation of the ARP among the WTs is less than 6.7%. However, it can be noted that the WTs with the highest ARP values correlate with their electrical vicinity to the PCC and their individual AEP (see Fig. 3.7a).

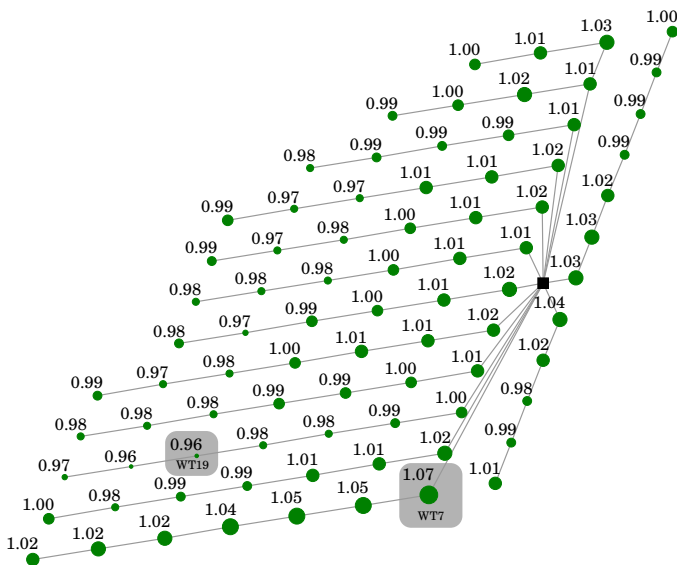
Table 3.11: Mean, minimum and maximum of ARP of individual WTs and VSC–HVdc, respectively.

	S1	S2	S3
Mean / Gvarh	0.00	6.14	3.83
Minimum / Gvarh (WT#)	0.00	6.14 (all WT)	3.70 (WT19)
Maximum / Gvarh (WT#)	0.00	6.14 (all WT)	4.09 (WT7)
VSC–HVdc / Gvarh	560.76	0.00	328.63

The relative loss reduction for S2 and S3 is presented in Fig. 3.8. The simulations are grouped in dependence of the sum of active power production by the WTs $\sum p_{WT}$. The results demonstrate an overall loss reduction of S3 in comparison to S1 and S2. In the lower power range until 0.6 p.u., the concept S2 causes higher losses, whereas up to full power the application of strategy S1 produces the highest losses. The values of loss reduction P_{rel}^{loss} are approximately equal for a specific $\sum p_{WT}$. This observation indicates furthermore the non–correlation between wind direction bin and relative loss reduction.



(a)



(b)

Figure 3.7: AEP of individual WT due to wake losses (a) and absolute annual reactive power production per individual WT under application of strategy S3 (b).

In Figs. 3.9 and 3.10, the reactive power injection by the VSC–HVdc and the WT7 are shown, respectively. As indicated in Tab. 3.11, WT7 has the highest ARP in the WPP. At the PCC, the reactive power production is independent from the wind direction but changes with the $\sum p_{WT}$. In contrast, the individual reactive power injection by WT7 varies for different wind directions. The wind direction inherently influences the active power operating points inside the WPP. It can be deduced that the reactive power production by either the VSC–HVdc and the WT stays within a narrow band between -0.15 p.u. and 0.25 p.u. of the rated power over the whole operation range.

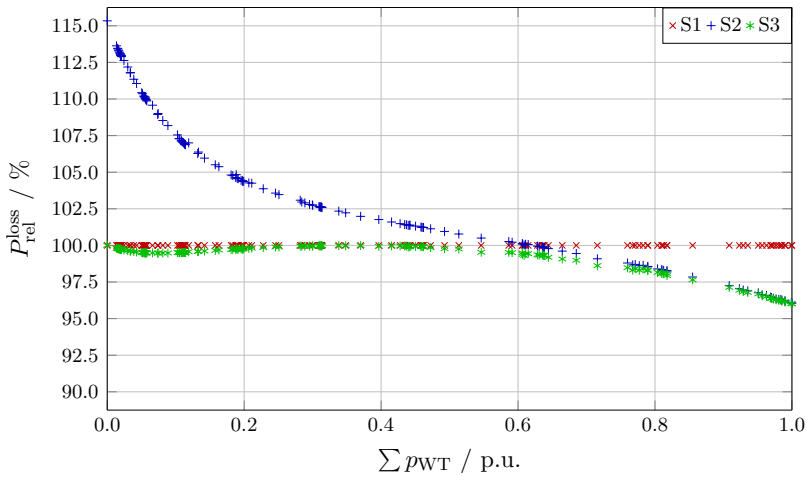


Figure 3.8: Relative losses in comparison to S1 for all simulations as a function of the sum of the produced power.

Table 3.12 gives a breakdown of the AEP of the WPP for different reactive power strategies (obtained at the dc side of the offshore VSC–HVdc). It allows us to evaluate the benefit of annual loss reduction and its monetary equivalent (ME). For the sake of completeness, it is assumed that the VSC–HVdc losses are considered which might not correspond to the legal WPP and HVdc system ownership boundaries in a real application. The application of S3 reduces the loss by 2511 MWh and 1887 MWh in comparison to S1 and S2, which equals to an additional annual benefit of 326 k€ and 245 k€, respectively.

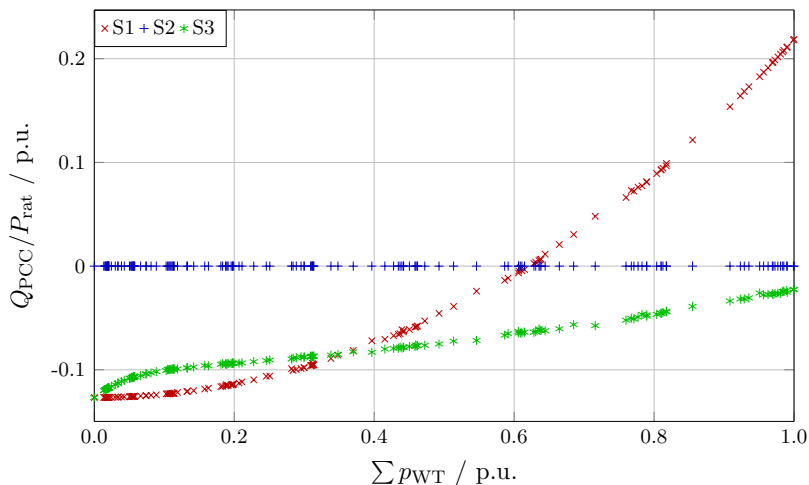


Figure 3.9: Reactive power production by the VSC-HVdc.

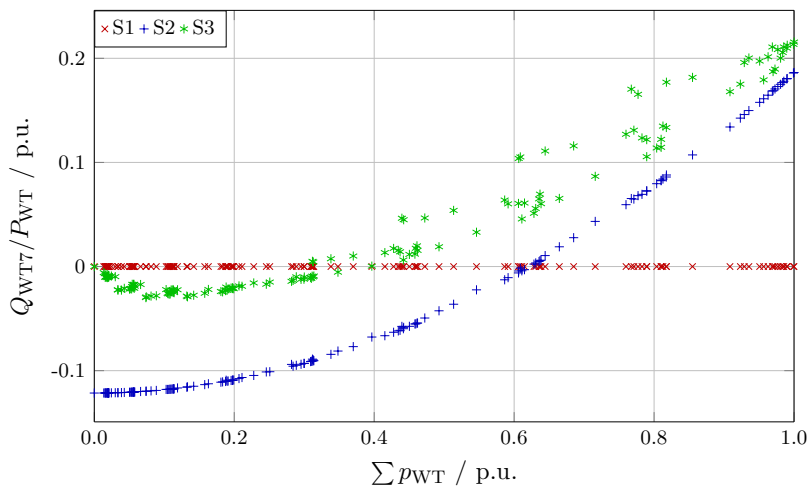


Figure 3.10: Reactive power production by WT7.

Table 3.12: AEP and its ME under consideration of wakes.

	S1	S2	S3
AEP ¹ / GWh	1849.5	1850.2	1852.0
ME of AEP / M€ _{yr} ⁻¹	240.4	240.5	240.7

¹ Refers to the energy injected to the HVdc link on the offshore side.

3.4.2 Variable and fixed voltage strategies

The analysis was performed for the six strategies, S1, S2, S3, S1var, S2var, and S3var, and active power values ranging from zero to full power ($p = 0.0$ p.u. to 1.0 p.u.). Wake effects are not considered anymore and the active power operating point is equal for all WTs. Figure 3.11 depicts the total relative losses for all strategies according to Eqn. (3.15). The results demonstrate that S2 causes higher losses than S1 for $0.0 < p < 0.6$ p.u. and less losses for $p > 0.6$ p.u.. Here, it is worth mentioning that an equal relative loss reduction along the whole power range reflects more valuable absolute loss reductions for higher powers. As expected, the use of the optimization algorithm in S3 has the lowest loss values over the whole power range within the strategies using the fixed PCC voltage reference. Nevertheless, the difference of the total losses between the best conventional strategy (S1 or S2) for individual active power operating points against S3 is of maximal 0.57% (at $p = 0.63$ p.u.). The variable strategies S1var to S3var demonstrate that the PCC voltage as control variable has an important impact on the power losses. Specifically, in the higher power range for $p > 0.4$ p.u. the variable strategy performs better than its fixed voltage reference counterpart (S1var with respect to S1, S2 vs. S2var, and S3 vs. S3var). It is remarkable that S1var causes a similar result as S3var although the latter uses a more complex optimization incorporating the individual reactive power set-points of the WTs.

The total amount of consumption and generation of reactive power by transformers, filters, and submarine cables in the system must be balanced by the GSCs and VSC-HVdc. In the following, the reactive power injections by the VSC-HVdc q_{PCC} and by two GSCs q_{WT} are presented in Figs. 3.12 and 3.13 for the whole power range, respectively. The base power is the rated active power, P_{rat} and P_{WT} , respectively. The most remote WT from the PCC busbar, WT1, and the closest one, WT46, have been selected for visualization.

The results of S1 indicate that the VSC-HVdc absorbs reactive power for lower powers and injects reactive power for higher powers. Similarly, for strategy S2 the reactive powers of the WTs q_{WT} show the same behavior. In both cases, these reactive power sources solely compensate the mentioned amount of reactive power generated in the grid. Thus, the contributions by

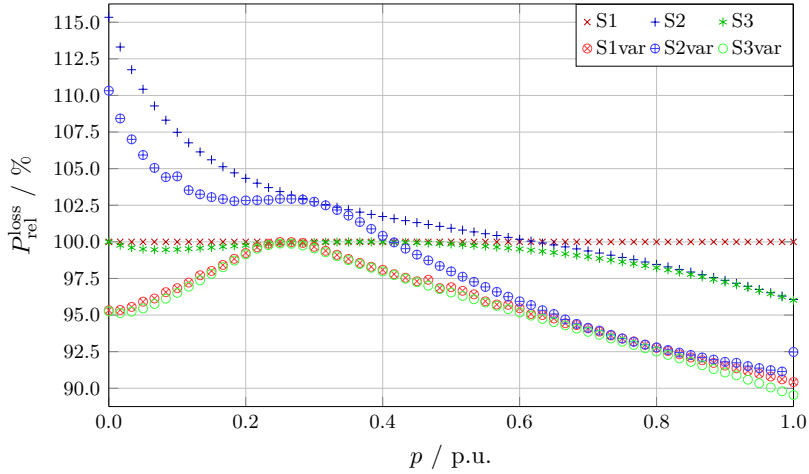


Figure 3.11: Relative total system losses respective to S1 (set equal to 100%).

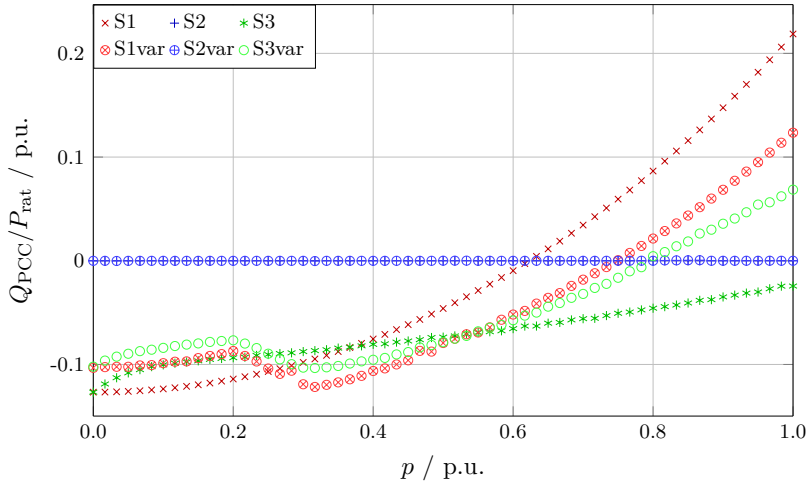
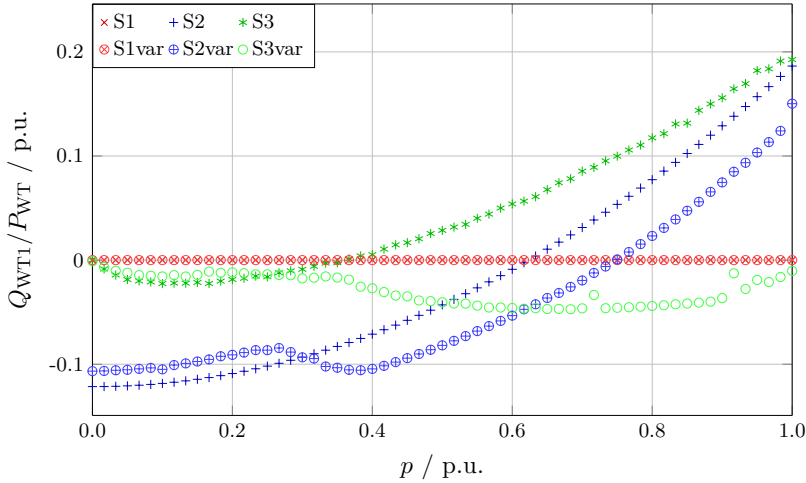
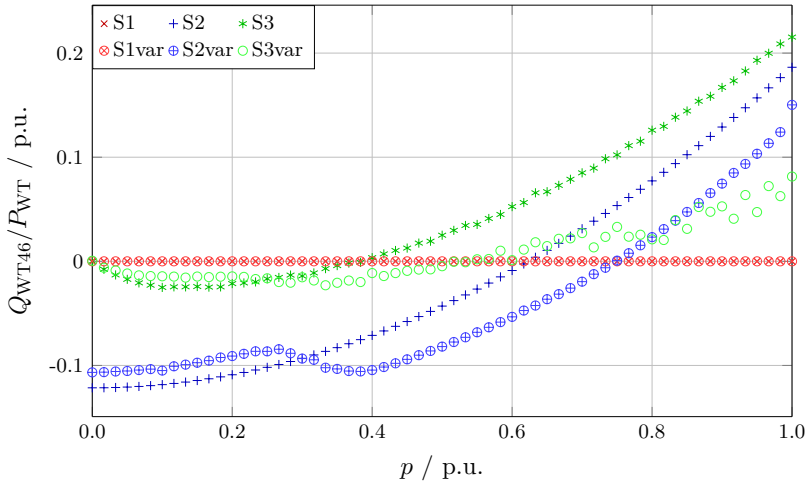


Figure 3.12: Reactive power injection by the VSC-HVdc. Positive values correspond to a reactive power injection (capacitive) by the converter.

the VSC-HVdc for strategy S2 as well as by the WTs for strategy S1 are zero as expected. For strategy S1 and S2, respectively, the q_{WT} of WT1 and WT46 are identical due to the uniform set-point distribution for these strategies. For the strategy S3, the set-points for the closest turbine are only up to 0.02 p.u. higher than for the most remote one specifically for active



(a) WT1



(b) WT46

Figure 3.13: Reactive power injection by (a) the most remote and (b) the closest WT, respectively.

powers higher than $p > 0.8 \text{ p.u.}$. For lower active powers, the difference is marginal. In fact, the optimization does not result in a significant non-uniform distribution of q_{WT} set-points. For the optimization-based strategies cases without uniform q_i set-points (S3 and S3var), the results in Figs. 3.12 and 3.13 depict the contribution to the total amount of necessary reactive

power by the WTs and the VSC-HVdc. Comparing the total reactive power injection Q_{PCC} for S3 and S3var, it can be seen that strategy S3var has a lower value than for S3. This effect is due to the additional variable PCC voltage reference u_{PCC} in strategy S3var which lowers the reactive power generation in the low power range by decreasing the system voltage. Furthermore, regarding the variation of the q_{WT} set-points for strategy S3var it can be seen that the values for WT1 and WT46 differ for active powers $p > 0.6$ p.u., whereas WT1 is absorbing reactive power and WT46 is injecting reactive power. This operation of WT1 avoids a local voltage violation due to the higher PCC voltage for this strategy in this power range. Due to its vicinity to the PCC, WT46 is not facing this constraint and injects reactive power to compensate. The other variable strategies S1var and S2var lower the reactive power requirement with respect to their counterpart S1 and S2, respectively. This holds true expect for an intermediate power range $0.25 \text{ p.u.} < p < 0.68 \text{ p.u.}$ for S1 against S1var, whereas $0.3 \text{ p.u.} < p < 0.7 \text{ p.u.}$ for S2 versus S2var.

Figure 3.14 shows the PCC voltage set-point u_{PCC} . For the strategies S1 to S3 the u_{PCC} is fixed at 1.0 p.u.. The variable strategies S1var and S2var result in similar u_{PCC} profiles as S3var. In the lower power range, the system voltage is decreased to reduce the reactive power requirements (and related power losses) and the associated power losses in the converters, whereas for higher powers the increase in the system voltage leads to lower losses.

The loss distribution in the system appears as component losses of the GSC, the WT transformer and filter, the 33kV collection grid, the WPP transformers, the HVac export cables, and the VSC-HVdc station. The loss distribution results in Fig. 3.15 consider the cases where zero or full power is generated respectively. The power losses differences between the strategies occur mainly in the converters and transformers (no-load losses) for low power (Fig. 3.15a) and in the grid components for the full power case (Fig. 3.15b). The higher voltage in the offshore grid for S1var to S3var reduces the losses of the grid components in general. The converter losses for S2 and S2var in the low power scenario demonstrate that higher losses occur in the GSC and lower losses in the VSC-HVdc compared to the other strategies. Overall, this results in a higher relative loss for strategy S2 compared to S1

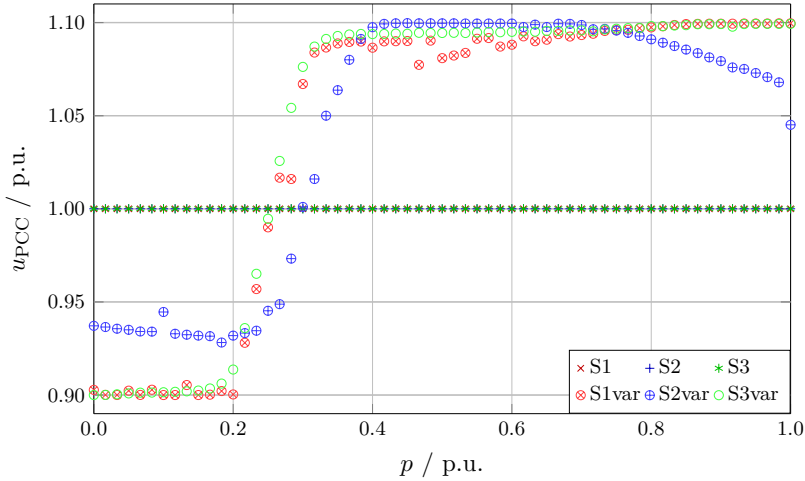
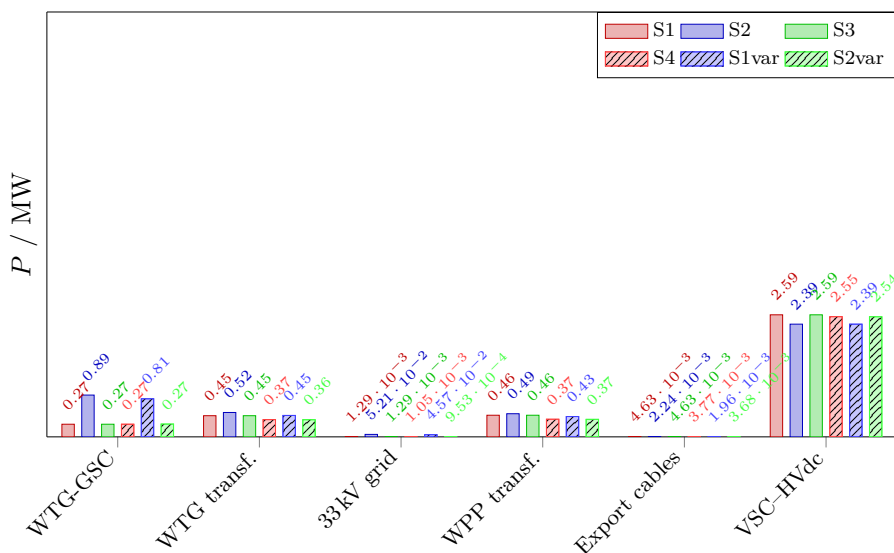


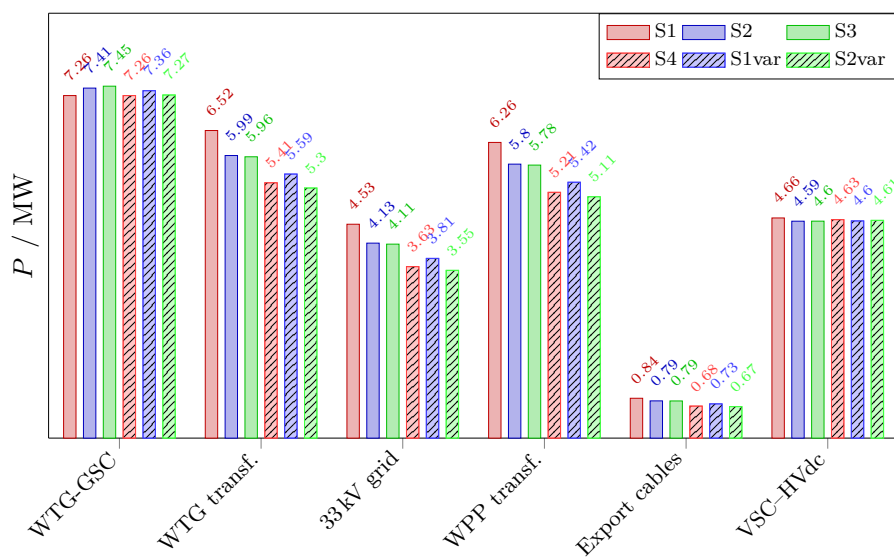
Figure 3.14: Voltage reference at PCC. The value is controlled by the VSC–HVdc. For the fixed strategies, it is continuously set to 1 p.u., whereas for the variable strategies the optimization algorithm determines the respective value.

in the low power range as depicted in Fig. 3.11.

Figure 3.16 provides the information on voltage values for relevant busbars in the system. The plots use boxplots to display mean, 25% and 75% percentiles, as well as minimum and maximum values of the corresponding sets over the whole power range. In Fig. 3.16a, the voltage levels are shown for strategies S1 to S3 specifically for the busbars of the HV–side of the WT transformers, the LV–side of the WPP transformers, denoted as offshore substation (OSS), and the PCC voltage. Figure 3.16b displays the voltage levels for the variable strategies S1var to S3var. Firstly, the voltages are kept within the admissible voltage limitations for all busbars and strategies. Secondly, the mean voltages for the WTs are higher for S3 compared to S1 and S2 due to the optimization procedure. The variable strategies S1var and S2var, explore a wider voltage band compared to their counterparts. For strategy S1var and S3var, the voltages of the WTs are almost exclusively close to the upper limit of 1.1 p.u.. Among the fixed reference voltage strategies, S1 has the most varying voltage profile at the OSS busbar, whereas S2 keeps its values closely below 1 p.u.. The values for S3 demonstrate insignificant variation for this busbar slightly above 1 p.u.. For the variable strategies,



(a) $p = 0.0$ p.u..



(b) $p = 1.0$ p.u..

Figure 3.15: Distribution of losses in the system for (a) no power production $p = 0.0$ p.u. and (b) full power production $p = 1.0$ p.u., respectively.

this busbar voltage correlates with the variable PCC voltage.

Figure 3.17 depicts the boxplots for the reactive power injections by the GSCs and the VSC–HVdc. Again, Fig. 3.17a displays the results for the fixed voltage strategies, whereas Fig. 3.17b contains the results for the variable strategies. Firstly, the plots depict that S1 and S2 both cause a uniform reactive power injection by the WTs. The values for S3 (for S3var, respectively) vary from each other and demonstrate the variable distribution of set–points caused by the optimization routine, respectively. For strategy S3, the reactive power values of the GSC are mainly injections which result in a generally higher voltage in the WPP grid when compared to S1 and S2. In contrast, for strategy S3var the use of a high PCC voltage reference results in a partly inductive operation of the GSCs to keep the voltage below the upper limit. This is specifically the case for those WTs which are very remote to the PCC busbar such as WT1 (see also Fig. 3.13a). Secondly, the variation of the reactive power injection by the VSC–HVdc is the highest for S1, whereas S3 is kept within a moderate range absorbing reactive power. The plot of S2 consequently results to zero reactive power exchange. For strategy S3var, the VSC–HVdc operates mainly absorbing reactive power unless for higher powers where it injects reactive power. Contemplating the combination of both the WT and the VSC–HVdc results, it is obvious that S3 and S3var reach a sharing of reactive power injection within the WPP. The variable strategies result in less reactive power injection variation than their respective fixed strategies. This is caused by the variable PCC voltage which lowers the reactive power requirements of the converters in the system.

The AEP, annual energy loss (AEL), and its ME obtained by applying the different strategies are displayed in Tab. 3.13. For strategy S2, the absolute energy losses are reduced by 696 MWh and for S3 by 2131 MWh compared to strategy S1, respectively. The variable strategies permit a further loss reduction: S1var 6320 MWh, S2var 4224 MWh, and S3var 6819 MWh in comparison to S1, respectively. The monetary saving of these additional active power in–feeds is of 90 k€ for S2, 277 k€ for S3 and oscillates between 549 k€ and 886 k€ for the variable strategies, respectively.

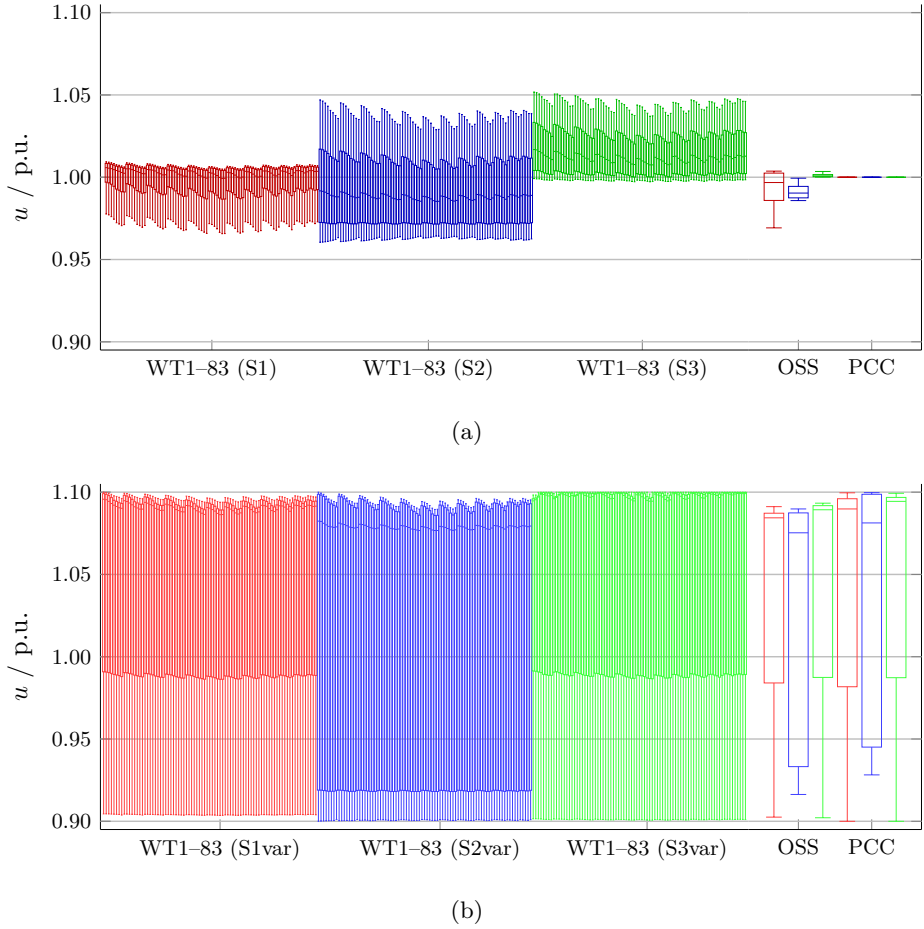


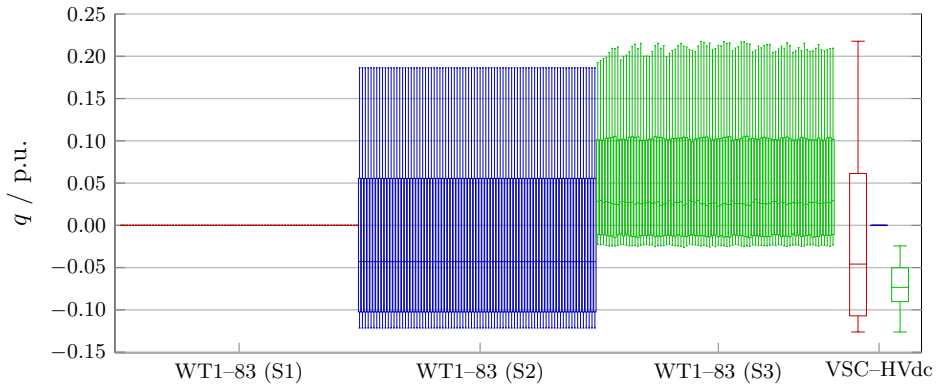
Figure 3.16: Voltage distribution of (a) fixed reference voltage strategies and (b) variable reference voltage strategies. The boxplots show mean, 25 %-, 75 %-percentiles, minimum, and maximum values. The HV-side busbars of the WT transformers, the LV-side of the WPP transformer (OSS) and the PCC busbar are displayed.

Table 3.13: AEL and the ME of the six strategies.

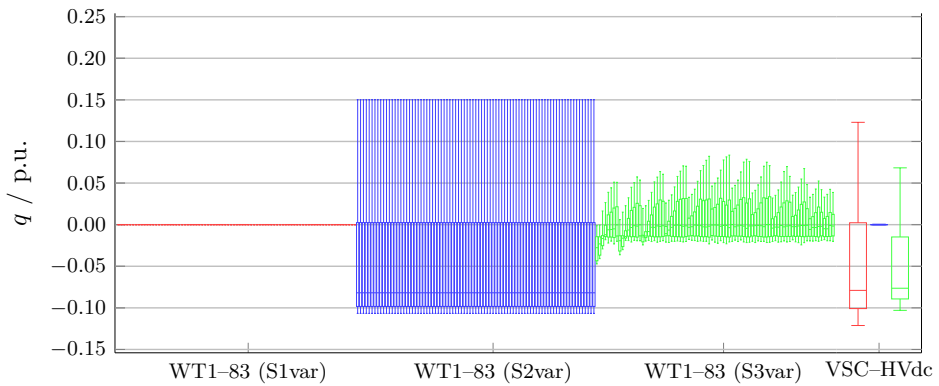
	S1	S2	S3	S1var	S2var	S3var
AEP ¹ / GWh	1811.37	1812.07	1813.50	1817.69	1815.60	1818.19
AEL ² / GWh	94.54	93.84	92.41	88.22	90.30	87.72
ME of AEL / M€yr ⁻¹	12.29	12.20	12.01	11.47	11.74	11.40

¹ Refers to the energy injected to the HVdc link on the offshore side.

² Refers to the energy losses in the offshore grid, including power converter losses.



(a)



(b)

Figure 3.17: Reactive power injections of (a) fixed reference voltage strategies and (b) variable reference voltage strategies. The boxplots show mean, 25%-, 75%-percentiles, minimum, and maximum values. All GSC and VSC-HVdc reactive power injections are plotted. A positive value expresses a reactive power injection (capacitive).

3.5 Summary

This chapter presented reactive power allocation strategies for the operation of an HVdc-connected WPP aiming to minimize overall power losses. Six reactive power allocation strategies were proposed which differ in their nature (conventional or optimization-based), complexity (only reactive power control or additionally regulation of the PCC reference voltage), and implementation (communication needs and sample rate). The most advanced strategy acts on the WT reactive power set-points and the PCC voltage reference imposed by the offshore VSC-HVdc to gain minimal losses in the system.

The power losses in the system were concluded in a common loss model where the collection grid and converter losses of the VSC-HVdc as well as of the WTs are considered. It was highlighted that the converter losses are of utmost importance for a thorough assessment in this application.

A case study for a 498 MW-sized reference WPP was performed for the whole active power range to draw conclusions for three reactive power control concepts, denoted strategy S1, S2, and S3, which all use a fixed PCC voltage reference. Considering the wake effect, it was found that the loss reduction correlates with the sum of active power injections by the WTs and is independent of the wind direction bin. Then, it was demonstrated that the different wind directions influence the individual reactive power injection, whereas the reactive power exchange at the PCC depends again on the total active power production. Furthermore, it was shown that the highest reactive power injections are made by those WTs which are either electrically close to the PCC and/or have a high annual active power production. There is no general benefit from the power converter capability to produce more reactive power at partial load given that it causes additional losses due to the increased converter current.

For the second part of the study, three optimization-based strategies deploying a variable reference voltage, denoted as S1var, S2var, and S3var, were proposed. From the results, it was concluded that the optimization-based reactive power control contributes to a reduction of energy losses by up to 4% for a fixed PCC voltage and up to 10% with the incorporation of a variable PCC voltage set-point in comparison to unity PF operation of the WTs. Moreover, it was found that in the case of the conventional reactive

power allocation strategies, the application of a single reactive power injection responsibility for either WTs or the VSC–HVdc is not optimal considering the whole power range. Consequently, the use of an optimization–based algorithm results in a share of the reactive power injection responsibility between the WTs and the VSC–HVdc. The variable strategies S1var, S2var, and S3var lead to lower losses and principally lower reactive power injections at the expense of a wider usage of the continuous voltage operation band. It was also found that for low powers it is advantageous to lower the system voltage causing a decrease of the total reactive power magnitude, hence lower additional converter losses, whereas for full power scenarios an increased system voltage to lower the electrical losses due to the smaller currents is of interest.

The deployment of the variable strategies might cause the system to operate permanently at its continuous voltage limits. Temporarily, this could lead to a boundary violation if the operating point changes (wind speed variation). An additional security margin on the voltage limits of the optimization algorithm might counteract this drawback. The results of the optimization–based controllers motivate their implementation into the central WPP control. This might be specifically of interest when the generation asset and offshore transmission asset owners/operators agree on a joint optimization. Furthermore, the system could gain an annual cost reduction of calculated 886 k€ for the 498 MW case study performed in this chapter.

4 Reactive power control for HVdc-connected WPP clusters

4.1 Introduction

In Chapter 3, the reactive power control in a single HVdc-connected WPP was investigated. However, actual industrial practice clusters several WPPs and connect them to a common HVdc system. Reactive power management in HVdc-connected WPP clusters increases the complexity compared to a single WPP as multiple system and control layers evolve.

This chapter assesses five reactive power control strategies for HVdc-connected WPP clusters. A benchmark strategy represents the best-case scenario for the system to evaluate the performance of the other strategies. Furthermore, one optimization-based reactive power control strategy is proposed which is especially suitable for the application in HVdc-connected WPP clusters. The active power variation is evaluated for several degrees of wind speed variance inside the WPP cluster. The key performance indicator is the AEP resulting under the operation of the WPP cluster with the respective strategy.

The chapter looks into the following aspects:

- reactive power allocation strategies for WPP cluster connected to HVdc,
- optimization-based strategy with variable reference voltage applied to the WPP cluster application,
- development of WPP power loss function in dependence of their operating point,
- and impact of active power variance between the WPPs of a cluster under use of reactive power control.

4.1.1 Related publication

The work presented in this chapter was published in:

- K. Schönleber, S. Ratés-Palau, O. Gomis-Bellmunt, Analysis of reactive power strategies in HVDC-connected wind power plant clusters, *Wind Energy*, vol. 20, no. 12, pp. 1971–1982, Dec. 2017. doi:10.1002/we.2134

4.2 Methodology

This section is developed in five parts: firstly, a general description of the system and power losses under consideration is given and secondly, the studied reactive power control strategies are presented. The optimization-based concepts are outlined with their respective objective function and constraints. Finally, further considerations about active power variance in WPP clusters are given along with a brief discussion about the feasibility and operational implementation of the reactive power control strategies.

4.2.1 System description and loss assessment

A generic system sketch of an HVdc-connected WPP cluster is shown in Fig. 4.1: The n wind power plants WPP1, WPP2, ..., WPP n with a respective rated power of P_{WPP1} , P_{WPP2} , ..., $P_{\text{WPP}n}$ connect to the offshore VSC-HVdc via HVac submarine cables from their respective high-voltage ac offshore substation (HVac-OS). Each WPP comprises multiple WTs which are linked through radial strings to the HVac-OS. To compensate the charging currents in the HV offshore grid, switchable shunt reactors are deployed at the HV cable ending to the HVac substation [42]. In a simple implementation, they might be equipped with mechanical no-load switches and the on/off status of these shunt reactors does not change during normal operation. The MV collection grids might be compensated with additional, switchable shunt reactors when emergency power supply by diesel generators is required during grid loss periods. Usually, the WPP transformers comprise an OLTC to perform tap changes even under load. OLTCs are not necessary when a single WPP is connected to the offshore VSC-HVdc as the latter might directly

control the grid voltage. In contrast, when several WPPs are connected, each WPP manages its respective MV grid voltage and is therefore expected to be equipped with an OLTC [42], [92].

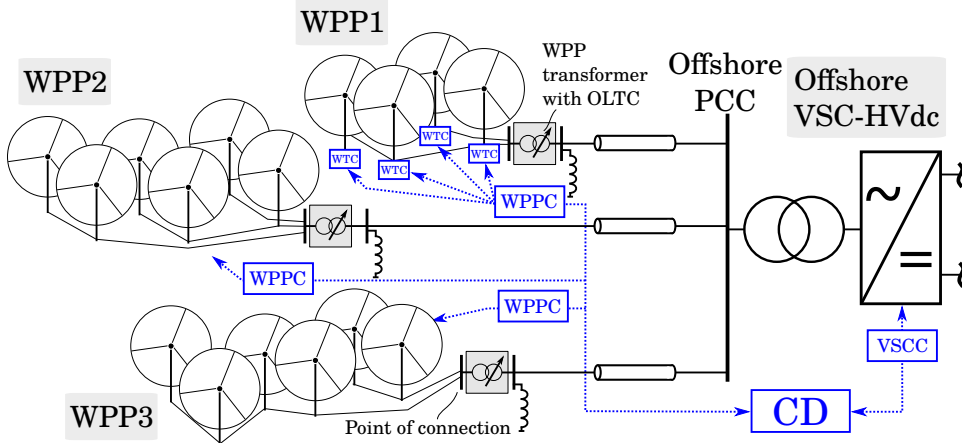


Figure 4.1: Offshore grid of exemplary HVdc-connected WPP cluster. The control system consists of the WTC at each individual WT, the WPPC of each WPP, the VSCC of the offshore VSC-HVdc, and the CD which is e.g. operated by the TSO.

The overall control hierarchy introduced in Section 2.3.2 might be extended according to the schematic shown in Fig. 4.1. First, the WTC regulates active and reactive power exchanged with the offshore grid upon references communicated by the respective WPPC. However, the references might also be set locally. The responsibility of the WPPC encloses the control of active and reactive power at the point of connection which here is defined to be the MV-side of the respective WPP transformers (see also indication for WPP3 in Fig. 4.1). It might incorporate the control of the OLTC and the dispatch of active and reactive power references to the WTs. The VSC-HVdc relies on a proper VSC control system (VSCC) which controls the voltage at the offshore PCC bus (the reference voltage might be communicated by the CD). If required by the control concept, the CD interacts with the WPPC and the VSCC.

The reactive power control strategies are evaluated against the impact on the AEP of the system. The system loss function is defined by:

$$P_{\text{system}}^{\text{loss}} = \sum_{i=1}^n P_{\text{WPP}i,\text{HV}}^{\text{loss}} + P_{\text{off. grid}}^{\text{loss}} + P_{\text{VSC}}^{\text{loss}} \quad (4.1)$$

where:

$$\begin{aligned} P_{\text{WPP}i,\text{HV}}^{\text{loss}} &= \text{power losses inside WPP}i \text{ including the WPP transformer;} \\ P_{\text{off. grid}}^{\text{loss}} &= \text{sum of electrical losses in the HV export cables;} \\ P_{\text{VSC}}^{\text{loss}} &= \text{overall VSC-HVdc station losses.} \end{aligned}$$

The assessment might be done with a complete power flow model covering the whole system (VSC-HVdc, offshore grid, WPP collection grids, and WT converters). However, this approach tends to be very time-consuming for the analysis of a large number of operating points specifically for the optimization-based approaches and is only used for the benchmark strategy elaborated later. Therefore, the WPP power losses are formulated by means of approximated loss functions. The internal WPP losses $P_{\text{WPP}i,\text{HV}}^{\text{loss}}$ are based on the combined converter loss and power load flow model developed in Chapter 3. When the voltage at the MV-side of the WPP transformer (point of connection) is locally controlled, e.g. to $u_i \approx 1$ p.u. by means of the respective OLTC, an approximated WPP loss function $P_{\text{WPP}i,\text{MV}}^{\text{loss}}(p_{\text{WT}}, q_i)$ might be set up in dependence of the active power injection p_{WT} by the WTs and the reactive power injection q_i at the point of connection. Hence, the power losses of a WPP at the HV terminals, $P_{\text{WPP}i,\text{HV}}^{\text{loss}}$, as introduced in (4.1), represent the sum of the power losses inside the WPP until the MV-side terminal of the WPP transformer, $P_{\text{WPP}i,\text{MV}}^{\text{loss}}$, and the WPP transformer losses. For the sake of simplicity, the internal reactive power control strategy inside the WPP uses an equal dispatch of reactive power set-points to the WTs, albeit an optimization-based strategy such as described in Chapter 3 might be used as well.

The approximation function is developed as a m th-grade polynomial function with coefficients c_{jk} and is described in Eqn. (4.2).

$$\begin{aligned}
 P_{\text{WPP}i,\text{MV}}^{\text{loss}}(p_{\text{WT}}, q_i) &= \sum_{\substack{j=0 \\ j+k \leq m}}^m \sum_{k=0}^m c_{jk} \cdot p_{\text{WT}}^j \cdot q_i^k \\
 &= c_{00} + c_{10}p_{\text{WT}} + c_{01}q_i + c_{20}p_{\text{WT}}^2 + c_{11}p_{\text{WT}}q_i \\
 &\quad + c_{02}q_i^2 + c_{30}p_{\text{WT}}^3 + c_{21}p_{\text{WT}}^2q_i + c_{12}p_{\text{WT}}q_i^2 \\
 &\quad + c_{03}q_i^3 + c_{40}p_{\text{WT}}^4 + c_{31}p_{\text{WT}}^3q_i + c_{22}p_{\text{WT}}^2q_i^2 \\
 &\quad + c_{13}p_{\text{WT}}q_i^3 + c_{04}q_i^4 \tag{4.2}
 \end{aligned}$$

The losses in the offshore grid $P_{\text{off. grid}}^{\text{loss}}$ (and in the WPP transformers $P_{\text{WPPtrf}}^{\text{loss}}$ if explicitly specified) are the result of load flow calculations using Matpower [3]. The VSC-HVdc station losses $P_{\text{VSC}}^{\text{loss}}$ might be calculated with the details given in Appendix A.2. The system loss function $P_{\text{system}}^{\text{loss}}$ is integrated in MATLAB using Matpower [3] and fmincon to assess different reactive power control strategies and multiple steady-state operating points.

4.2.2 Reactive power control strategies

A benchmark strategy is formulated as the optimum steady-state operating point of the system. The optimization aims to minimize the system losses under a number of constraints. The control variables are the reference voltage imposed by the offshore VSC-HVdc and the reactive power injections by the WTs. In that case, the OLTC controller is inactive as it would counteract the overall aim. However, the restrictions on real-time data access due to communication constraints and/or operator boundaries might disqualify the benchmark strategy in a real implementation. Thus, the sole purpose of this strategy is the evaluation of the others. It is equal to the strategy S3var introduced in Chapter 3 for a single HVdc-connected WPP.

- I. Benchmark strategy (S0opt): Overall optimization of active power losses by individual reactive power set-points of WTs q_{WT} and reference voltage u_{PCC} to the VSC-HVdc.

Furthermore, five reactive power strategies for the application in an HVdc-

connected WPP cluster are considered:

- II. Strategy 1 (S1): WTs are operating at unity PF ($\cos \varphi = 1$).
- III. Strategy 2 (S2): WPPs are operated at unity PF ($\cos \varphi = 1$).
- IV. Strategy 3a (S3a): VSC-HVdc is operated at $\cos \varphi = 1$ and CD dispatches equal q_i set-points to the WPPs.
- V. Strategy 3b (S3b): VSC-HVdc is operated at $\cos \varphi = 1$. The CD sends equal PF set-points PF_i to the WPPs [42].
- VI. Strategy 4 (S4opt): Optimization-based operation where the system power losses are minimized under use of the WPP reactive power set-points q_i and the reference voltage u_{PCC} .

Another strategy might be the operation of the VSC-HVdc at unity PF and a dispatch of voltage set-points to the WPPs. Nevertheless, this strategy is not further investigated as it is very similar to strategy S3b. The considered reactive power strategies differ in terms of the control concept, for instance, S1 to S3b are conventional control strategies and S4opt is an optimization-based control algorithm. The VSC-HVdc regulates a fixed reference voltage of $u_{PCC} = 1$ p.u. at the PCC bus for the conventional strategies, whereas for strategy S4opt the reference voltage is a control variable of the optimization. The OLTCs of the WPP transformers operate independently in local control mode for all five strategies. Except for the benchmark case S0opt, the internal Q set-points inside the WPP are dispatched equally among the WTs. In case of strategy S4opt, there are additional data exchange requirements between the controllers communicating through the existing channels: each respective WPPC should provide the measured or estimated active power p_i to the CD and receives a reactive power set-point q_i . The strategies S3a and S3b require the communication of a reactive power or PF set-point from the CD to the WPPC, respectively. Table 4.2 gives an overview of the concepts and their respective communication and control principles.

Table 4.2: Summary of the reactive power management strategies. Main differences are highlighted in **bold**. The symbols \rightarrow and \rightleftarrows stand for unidirectional and bidirectional communication, respectively.

Strategy Principle		Control				
		Communication	WTs	WPPs	VSC-HVdc	OLTC of WPP transformer
S0opt	Benchmark (overall optimization)	CD \rightleftarrows WTC, CD \rightleftarrows VSCC	Q set-point from CD	None	Reference voltage set-point by CD	Inactive
S1	No Q by WTs	None	Local ($\cos \varphi = 1$)	None	Local	Local to 1 p.u. at MV-side
S2	No Q by WPPs	WPPC \rightarrow WTC	Q set-point by WPPC	Local ($\cos \varphi = 1$)	Local	Local to 1 p.u. at MV-side
S3a	No Q by VSC, Q dispatch to WPPs	WPPC \rightarrow VSCC, WPPC \rightarrow WTC	Q set-point by WPPC	Q set-point by VSCC	Local ($\cos \varphi = 1$)	Local to 1 p.u. at MV-side
S3b	No Q by VSC, PF dispatch to WPPs	WPPC \rightarrow VSCC, WPPC \rightarrow WTC	Q set-point by WPPC	PF set-point by VSCC	Local ($\cos \varphi = 1$)	Local to 1 p.u. at MV-side
S4opt	Offshore grid optimization	CD \rightleftarrows WPPC, CD \rightleftarrows VSCC, WPPC \rightarrow WTC	Q set-point by WPPC	Q set-point by CD	Reference voltage set-point by CD	Local to 1 p.u. at MV-side

4.2.3 Optimization problem formulation

The benchmark strategy S0opt and strategy S4opt use different optimization approaches to operate the system, respectively.

4.2.3.1 Benchmark strategy S0opt

The optimization problem is defined by Eqns. (4.3) to (4.11), being \mathbf{x} the design vector and $f(\mathbf{x})$ the objective function to minimize.

$$\mathbf{x} = [u_{\text{PCC}}, q_1, q_2, \dots, q_t]^\top \quad (4.3)$$

$$\text{Min. } f(\mathbf{x}) = \sum_{i=1}^n P_{\text{WPP},i,\text{HV}}^{\text{loss}} + P_{\text{off. grid}}^{\text{loss}} + P_{\text{VSC}}^{\text{loss}} \quad (4.4)$$

s.t. :

$$0 = -p_r + \sum_{s=1}^N U_r U_s (G_{rs} \cos \theta_{rs} + B_{rs} \sin \theta_{rs}) \quad (4.5)$$

$$0 = -q_r + \sum_{s=1}^N U_r U_s (G_{rs} \sin \theta_{rs} - B_{rs} \cos \theta_{rs}) \quad (4.6)$$

$$\mathbf{u}_{o,\min} \leq \mathbf{u}_o(\mathbf{x}) \leq \mathbf{u}_{o,\max}, \quad o \in \mathbf{N}_{\text{bus}} \quad (4.7)$$

$$|\mathbf{i}_l(\mathbf{x})| \leq \mathbf{i}_{l,\max}, \quad l \in \mathbf{N}_{\text{brs}} \quad (4.8)$$

$$q_{\text{VSC},\min} \leq q_{\text{VSC}}(\mathbf{x}) \leq q_{\text{VSC},\max} \quad (4.9)$$

$$u_{\text{PCC}} \in [u_{\text{PCC},\min}, u_{\text{PCC},\max}] \quad (4.10)$$

$$\mathbf{q}_t \in [\mathbf{q}_{t,\min}, \mathbf{q}_{t,\max}], \quad t \in \mathbf{N}_{\text{WT}} \quad (4.11)$$

where:

G_{rs}, B_{rs}	= real and imaginary part of the respective element in the admittance bus matrix \mathbf{Y}_{rs} ;
p_r, q_r	= injected active and reactive power at bus r ;
U_r, U_s	= magnitudes of bus voltages at bus r and s ;
θ_{rs}	= phase angle between bus voltages;
N	= total bus number;
\mathbf{N}_{bus}	= vector of all buses (except PCC bus);
\mathbf{N}_{WT}	= vector of all WT elements;
\mathbf{N}_{brs}	= vector of all branches;
$\mathbf{u}_o(\mathbf{x})$	= vector of bus voltages;
$\mathbf{u}_{o,\min}, \mathbf{u}_{o,\max}$	= vector of minimum and maximum bus voltages;

u_{PCC}	= PCC voltage;
$u_{\text{PCC},\min}, u_{\text{PCC},\max}$	= minimum and maximum PCC voltage;
$\mathbf{i}_l(\mathbf{x})$	= vector of currents in the branches;
$\mathbf{i}_{l,\max}$	= vector of maximum current limits;
$q_{\text{VSC}}(\mathbf{x})$	= reactive power of the offshore VSC–HVdc;
$q_{\text{VSC},\min}, q_{\text{VSC},\max}$	= minimum/maximum reactive power of VSC–HVdc;
\mathbf{q}_t	= vector of reactive power at each WT;
$\mathbf{q}_{t,\min}, \mathbf{q}_{t,\max}$	= vector of minimum/maximum reactive power.

Equations (4.5) and (4.6) are the power flow equations for the system. The vectors \mathbf{N}_{WT} , \mathbf{N}_{bus} , and \mathbf{N}_{brs} accommodate all WTs of the n WPPs, buses (except the PCC bus), and branches (lines and transformers), respectively. The bus voltages \mathbf{u}_o are limited to the minimum and maximum admissible voltages considering a security margin of 0.25 p.u.: $\mathbf{u}_{o,\min} = 0.925$ p.u. and $\mathbf{u}_{o,\max} = 1.075$ p.u.. The voltage security margin is applied to counteract temporary violation of the voltage limitations due to extreme wind variations. The highest current of both branch sides \mathbf{i}_l is limited to the branch rating $\mathbf{i}_{l,\max}$. Reactive power limitations for the WTs and the VSC–HVdc are introduced in Eqns. (4.9) and (4.11), respectively. For the benchmark strategy, the local control mode of the OLTCs of the WPP transformers is disabled as it would counteract the overall optimization.

The size of the design vector is proportional to the number of WTs t in the system which results in a calculation time of several tenths of minutes for a WPP cluster comprising 191 WTs.

4.2.3.2 Offshore grid optimization by strategy S4opt

The objective of this strategy is the implementation of a loss optimization by reactive power control and respect the control and ownership boundaries discussed in Section 4.2.1. Thus, it performs an optimization of the offshore grid and leaves the internal reactive power control inside each WPP to the WPPC itself following the same control structure as the conventional strategies. A significantly smaller optimization problem results using the q_i set-points of the WPPs and u_{PCC} as decision variables. Equations (4.12) to (4.20) define the optimization problem (\mathbf{y} contains the decision variables

and $g(\mathbf{y})$ is the objective function).

$$\mathbf{y} = [u_{\text{PCC}}, q_1, q_2, \dots, q_n]^\top \quad (4.12)$$

$$\text{Min. } g(\mathbf{y}) = \sum_{i=1}^n P_{\text{WPP}i,\text{MV}}^{\text{loss}} + P_{\text{WPPtrf}}^{\text{loss}} + P_{\text{off. grid}}^{\text{loss}} + P_{\text{VSC}}^{\text{loss}} \quad (4.13)$$

s.t. :

$$0 = -p_r + \sum_{s=1}^N U_r U_s (G_{rs} \cos \theta_{rs} + B_{rs} \sin \theta_{rs}) \quad (4.14)$$

$$0 = -q_r + \sum_{s=1}^N U_r U_s (G_{rs} \sin \theta_{rs} - B_{rs} \cos \theta_{rs}) \quad (4.15)$$

$$\mathbf{u}_{o,\min} \leq \mathbf{u}_o(\mathbf{y}) \leq \mathbf{u}_{o,\max}, \quad o \in \mathbf{N}_{\text{bus}} \quad (4.16)$$

$$|\mathbf{i}(\mathbf{y})| \leq \mathbf{i}_{,\max}, \quad l \in \mathbf{N}_{\text{brs}} \quad (4.17)$$

$$q_{\text{VSC},\min} \leq q_{\text{VSC}}(\mathbf{y}) \leq q_{\text{VSC},\max} \quad (4.18)$$

$$u_{\text{PCC}} \in [u_{\text{PCC},\min}, u_{\text{PCC},\max}] \quad (4.19)$$

$$\mathbf{q}_s \in [\mathbf{q}_{s,\min}, \mathbf{q}_{s,\max}], \quad s \in \mathbf{N}_{\text{WPP}} \quad (4.20)$$

where:

- \mathbf{N}_{WPP} = vector of all WPP elements;
- \mathbf{q}_s = vector of reactive power at each WPP;
- $\mathbf{q}_{s,\min}, \mathbf{q}_{s,\max}$ = vector of minimum/maximum reactive power WPP.

The objective function $g(\mathbf{y})$ in Eqn. (4.13) uses the developed WPP loss functions $P_{\text{WPP}i,\text{MV}}^{\text{loss}}$ which inherently require the WPP transformer losses to be considered separately. The vector \mathbf{N}_{WPP} contains the corresponding MV-side transformer buses of the n WPPs. The constraints defined by Eqns. (4.14) to (4.20) are set analogue to Eqns. (4.5) to (4.11). The reactive power values at the VSC-HVdc and the respective MV-side of the WPP transformers are considered for q_{VSC} and q_1 to q_n in Eqns. (4.18) to (4.20), respectively. For this strategy, like the conventional strategies, the OLTC of the WPP transformers operates in local control mode. The local control mode foresees controlling the MV-side busbars of the respective WPP transformers to a value of around 1 p.u.. To model this behavior, the voltage constraints for these busbars are set to $u_{o,\min} = 0.99$ p.u. and $u_{o,\max} = 1.01$ p.u..

As this optimization problem makes use of the approximated loss functions of the WPPs, the design vector and the optimization problem itself are

significantly smaller than for the benchmark strategy. The calculation is performed in few seconds for the cluster comprising three WPPs.

4.2.4 Active power variation within the cluster

The performance assessment aims to cover different operating points of the system. The key performance indicator AEP is then calculated with the frequency per year for each operating point and the power flowing into the dc side of the offshore VSC–HVdc for the corresponding operating point. In the following, the decision on the different operating points for the analysis is outlined.

On the one hand, each WT has an individual active power output depending on its operating status (normal operation, de-rated operation or outage) and on the local wind speed. As highlighted in Chapter 3, the local wind speed might be influenced by wake effects inside the WPP. The active power output of a WPP p_i is affected by the combined generation of all WTs and the power losses inside the WPP. According to the analysis performed in Chapter 3, the impact of wake effects inside a single WPP on reactive power control strategies is almost negligible for the power loss variation at WPP level. However, the power loss variation due to reactive power control correlates with the sum of active power generation by all WTs. Therefore, the internal WPP losses functions developed in Section 4.2.1 depend on the equal active power output of all WTs p_{WT} .

On the other hand, the individual WPPs in the cluster might be exposed to different wind conditions due to possible wakes between the WPPs [202], [203]. Such WPP cluster wake effects have been modeled for closely-spaced WPPs in [202], [203]. It was concluded that more operational data is needed for the development of accurate models. Any active power variation between WPPs in a cluster (outages, wakes, de-rated operation) might be expressed by a stochastic variance. Equation (4.21) defines the variance σ^2 of the active power injection in a WPP cluster comprising n WPPs.

$$\sigma^2 = \sum_{i=1}^n (p_i - \mu)^2 \quad (4.21)$$

$$\text{with } \mu = \frac{1}{n} \sum_{i=1}^n p_i$$

where:

p_i = active power injection by WPP i ;

μ = mean value of p_1, p_2, \dots, p_n .

A variance of $\sigma^2 = 0$ means equal p.u. active power injections, whereas a higher σ^2 represents more distinct values by the different WPPs.

As of the writing of this thesis, the annual frequency on active power variations between WPPs in a cluster is not available in the literature. Thus, the AEP calculation in this chapter considers $\sigma^2 = 0$. Additionally, the confidence level of the AEP results is supported with simulations for $\sigma^2 \neq 0$.

4.2.5 Operational feasibility of the proposed strategies

Taking into consideration that this chapter examines exclusively stationary steady-state behavior, a brief description of a possible practical deployment is given. Table 4.6 presents a feasibility summary of the considered reactive power control strategies. The extensive calculation time of the benchmark strategy S0 and the communication requirements between CD, WTC, and VSCC disqualifies it for real implementation in the current setup of HVdc-connected WPP cluster. Strategy S1 uses local control, where the WTs are operated at unity PF. The conventional strategies S2, S3a, and S3b rely on communication although in the case of failure a local control might take over. The needed communication links are common industrial practice. Strategy S4opt represents a cascaded optimization structure which controls reference voltage and reactive power set-points of the WPP. The optimization algorithm is calculated in a few seconds and is fast enough for real implementation in e.g. one-minute-long time steps.

Table 4.6: Feasibility ranking of reactive power control strategies.

Strategy	Principle	Feasibility	OPF execution	Communications
S0opt	Benchmark (overall optimization)	Low	Several minutes	CD to VSCC and WTs; inside WPPs
S1	No Q by WTs	Highest	N/A	Local control
S2	No Q by WPPs	High	N/A	Inside WPPs
S3a	No Q by VSC, Q dispatch to WPPs	Moderate	N/A	CD to WPPs; inside WPPs
S3b	No Q by VSC, PF dispatch to WPPs	Moderate	N/A	CD to WPPs; inside WPPs
S4opt	Offshore grid optimization	Moderate	Few seconds	CD to VSCC and WPPs; inside WPPs

4.3 Case study

The case study defines an HVdc-connected WPP cluster consisting of three WPPs and a total of 191 WTs. A possible geographic distribution of the WPPs is sketched in Fig. 4.2. The system parameters are listed in Tab. 4.7. The WPPs use the same WT model as in Chapter 3. A standard WPP transformer rating of 280 MVA is used, with no-load losses of 0.04 %, load losses of 0.3 %, and a short-circuit voltage of $u_{k0} = 15$ %. The WPP transformers are equipped with OLTCs which can operate in a discrete range of ± 13 % of the turns ratio in ± 6 steps. In local control mode, the OLTCs would be regulated to $u = 1.0$ p.u. at the MV-side busbar. According to the WPP rating up to two transformers are arranged in parallel.

The WPP loss functions according to Eqn. (4.2) are determined for the three WPPs by individual power flow calculation for a fixed voltage of $u_i = 1.0$ p.u.. The polynomial coefficients c_{jk} are calculated on a resolution of 489 samples, by 21 equidistant values for p_{WT} and 23 values for q_i . A polynomial order of $m = 4$ results in high accuracy measured by the coefficient of determination $R^2 = 0.9998$ for the three WPPs. Offshore wind data for the North Sea region can be found in the Forschungsplattformen in Nord- und Ostsee (engl. Research platforms in the North Sea and Baltic Sea) (*FINO*) database [6]. The five-year period wind speed data for 2010 to 2015 of *FINO3* met mast result in a Weibull distribution with a mean wind speed of $\bar{v} = 11.44$ m/s

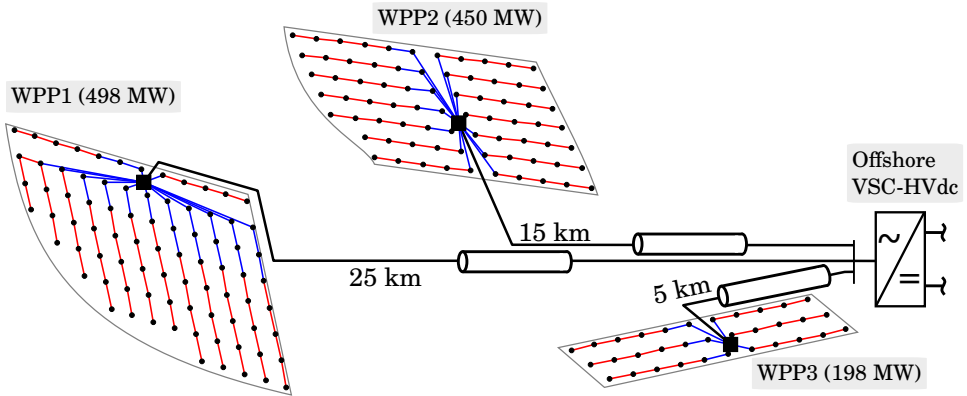


Figure 4.2: Geographical distribution of the WPP cluster under study.

Table 4.7: Relevant parameter of the HVdc-connected WPP cluster.

WPP	WPP1	WPP2	WPP3
Nominal voltage (U_{ac}/kV)		33	
Power rating (P_{WPP_i}/MW)	498	450	198
Collection grid cable length (l/km)	118	93	35
Number of turbines (#)	83	75	33
HVdc export cable system			
Nominal voltage (U_{ac}/kV)		155	
Number of cables (#)	3	3	1
Cross-section (A/mm^2)	630	630	800
Length (l/km)	25	15	5
Shunt compensation ($Q_r/Mvar$)	51.49	30.89	3.79
HVdc transmission			
Nominal voltages ($U_{ac}/kV, U_{dc}/kV$)		333, ± 320	
Converter (topology, $S_r/MVA, \cos \varphi$)		MMC, 1333.33, ± 0.9	
Converter loss coefficients from Tab. A.1 ($a, b, c / p.u.$)		0.0042, 0.0015, 0.0016	

and a shape parameter of $k = 2.27$ used for the AEP calculation.

4.4 Results

This section covers first the determination of the WPP loss functions and second the results of the losses for different operating points when applying

the reactive power strategies. Then, the AEP results are presented with the economic evaluation of the strategies.

4.4.1 Analysis of WPP and VSC loss functions

The WPP loss function is shown for WPP1 in Fig. 4.3. The losses are displayed for different active power injections, namely p_{WT} , and in dependence of the reactive power set-point Q_1 . For a small p_{WT} , there is a large gap of active power losses of approx. $\Delta P = 5.2$ MW between operation at $Q_1 = -200$ Mvar and $Q_1 = 0$ Mvar (unity PF operation). In contrast to that, for full power the difference is only $\Delta P = 3.1$ MW for these operating points. Furthermore, when WPP1 is at full power production, the supply of capacitive reactive power results in higher losses than of inductive reactive power. This is due to the inductive character (consuming reactive power) of the MV collection grid at full load. Therefore, the unity PF operation does not inherently represent the lowest losses in the wind power plant. The polynomial coefficients for the three WPPs are listed in Tab. 4.8.

Table 4.8: Polynomial coefficients of WPP loss functions.

	c_{00}	c_{10}	c_{01}	c_{20}	c_{11}	c_{02}	c_{30}	c_{21}	c_{12}	c_{03}	c_{40}	c_{31}	c_{22}	c_{13}	c_{04}
WPP1	1.28	1.82	-0.36	18.17	0.37	7.79	-6.48	0.90	-3.52	0.55	2.22	-0.30	1.50	-0.37	-0.60
WPP2	1.16	1.65	-0.25	15.24	0.30	6.61	-5.75	0.80	-3.14	0.46	1.99	-0.25	1.35	-0.30	-0.55
WPP3	0.51	0.73	-0.08	6.49	0.11	2.83	-2.51	0.35	-1.38	0.19	0.87	-0.11	0.59	-0.12	-0.24

In contrast to the WPP loss functions, the VSC-HVdc station losses considered in this study result in flatter slopes in dependence on the q_i . As a numerical example from Chapter 3, between unity PF and $Q_{VSC} = -200$ Mvar at full power additional losses of only approx. $\Delta P = 0.23$ MW occur as shown in Fig. 3.3. This is evidently lower than the extra losses caused inside WPP1 for this operating point (3.1 MW). The achievement of a reactive power set-point at the VSC-HVdc terminals causes a lower relative loss increase than at the point of connection of a WPP, mainly due to the reactive power flows provoked in the collection grid and the higher WT converter losses compared to the MMC-HVdc.

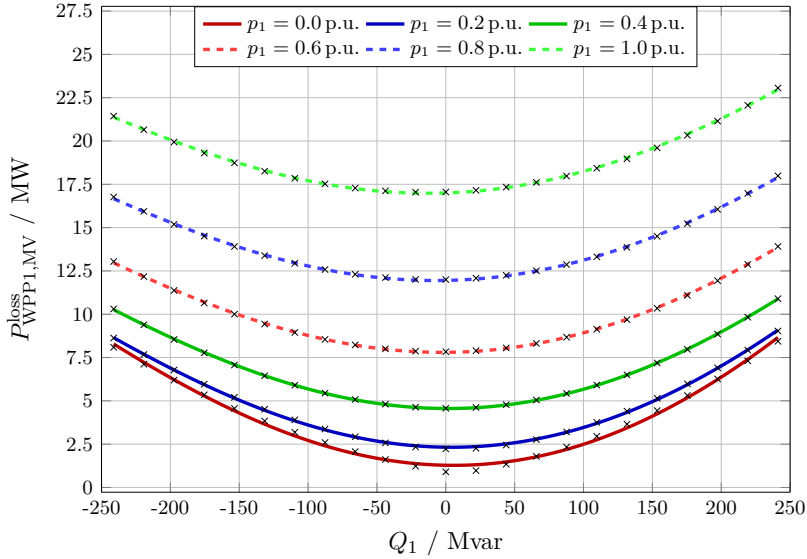
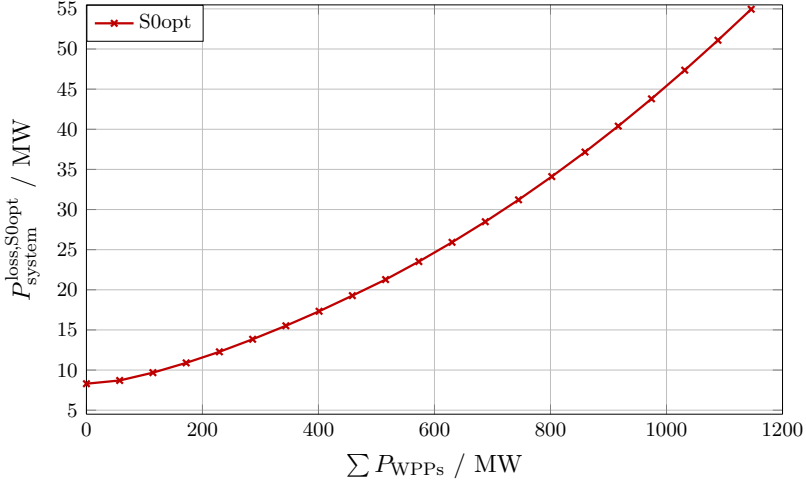


Figure 4.3: Loss functions of WPP1 in dependence of reactive power set-point at the point of connection Q_1 and for different active power injections p_{WT} by the WTs (full power is of 498 MW for WPP1). Losses are measured at the MV-side of the WPP transformer with a fixed voltage of $u = 1.0$ p.u..

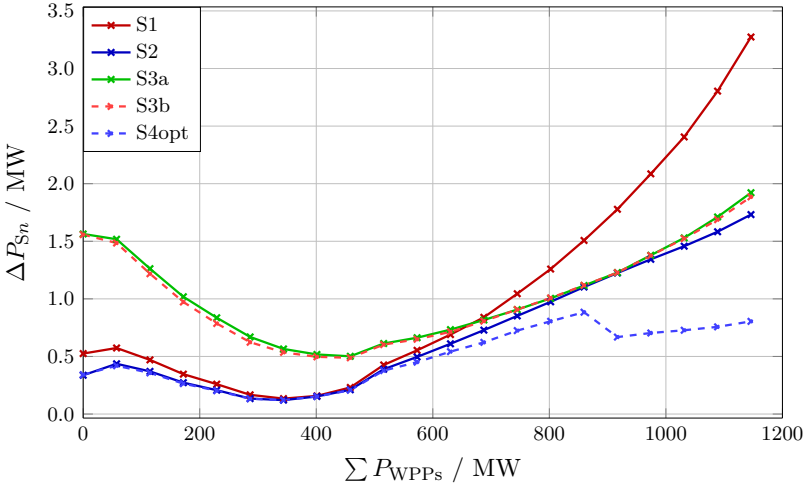
4.4.2 Loss reduction for $\sigma^2 = 0$

The active power losses in the system for the benchmark strategy $S0_{opt}$ are shown in Fig. 4.4a. It is obvious that the absolute losses increase with a higher active power injection by the WPPs. The strategies $S1$ to $S4_{opt}$ are evaluated against $S0_{opt}$ in Fig. 4.4b. The plot shows the difference between the active power losses produced for $S1$ to $S4_{opt}$ and the losses for the benchmark strategy $S0_{opt}$, respectively. The performance of the strategies is dependent on the sum of active power injections. The strategy $S4_{opt}$ has the lowest loss increase varying between 0.1 and 0.8 MW. Strategy $S2$ performs equally to $S4_{opt}$ in the low power range but the loss increase doubles at full power. The strategies $S3a$ and $S3b$ show similar results to each other. In the low power range it is not beneficial to operate the VSC-HVdc at unity PF ($S3a$ and $S3b$), as it causes losses up to three times higher in the whole system compared to the next best strategy ($S2$). Strategy $S1$ has a good performance for the lower power range but losses increase significantly for

high powers and full power.



(a)



(b)

Figure 4.4: Absolute system losses for the benchmark case S0opt in (a) and loss variation with respect to these for strategies S1 to S4opt in (b) ($\Delta P_{S_n} = P_{\text{system}}^{\text{loss}, S_n} - P_{\text{system}}^{\text{loss}, S0\text{opt}}$). Results are shown for simulations performed under $\sigma^2 = 0$.

Table 4.9 lists selected load flow results for the full power case comprising the voltages at the grid connection point of each WPP ($u_{1\text{HV}}$ to $u_{3\text{HV}}$) and

the PCC voltage u_{PCC} as well as reactive power injections by the WPPs at the point of connection and the VSC. It can be seen that the optimization-based strategies (S0opt and S4opt), where u_{PCC} is variable and not constrained to 1 p.u., the deployed overall voltage levels are around 6% to 7% higher than for the conventional strategies. This results clearly in lower overall losses in the grid as observed earlier. Additionally, the optimization proposes reactive power injections by the WPPs which are close to the minimum power losses of the WPPs (e.g. for WPP1 compare to Fig. 4.3 where WPP1 losses for $p_{\text{WT}} = 1$ p.u. are the lowest at around $Q_1 = -12.8$ Mvar). For strategy S1 the high losses result from a high reactive power injection by the VSC to compensate the whole offshore grid. Considering the values of S3a and S3b, there is almost no difference in terms of losses but a variation of the applied reactive power SPs Q_1 to Q_3 .

Table 4.9: Reduced load flow results for a full power scenario
 $p_1 = p_2 = p_3 = 1$ p.u..

	Voltages / p.u.				Reactive power / Mvar			
	u_{PCC}	$u_{1\text{HV}}$	$u_{2\text{HV}}$	$u_{3\text{HV}}$	Q_{VSC}	Q_1	Q_2	Q_3
S0opt	1.072	1.075	1.074	1.073	96.6	-28.0	-26.8	-14.5
S1	1.000	1.000	1.000	1.000	250.3	-80.7	-72.0	-31.9
S2	1.000	1.004	1.002	1.001	54.3	0.0	0.0	0.0
S3a	1.000	1.005	1.003	1.001	0.0	17.6	17.6	17.6
S3b	1.000	1.005	1.003	1.001	0.0	22.9	20.7	9.1
S4opt	1.066	1.069	1.068	1.066	28.7	0.0	0.0	-5.0

4.4.3 Loss reduction for $\sigma^2 \geq 0$

During normal operation, the power output in p.u. will not be continuously equal mainly due to wind speed inequalities, planned, and unplanned WT shut-downs in the different WPPs. Consequently, a total of 1331 operating points are simulated by taking all combinations for p_1 , p_2 , and p_3 in 0.1 p.u. steps into account. The results are grouped by the respective variance value σ^2 , which is calculated according to Eqn. (4.21). The benchmark strategy S0opt is no longer considered because of the expected extensive calculation time and the loss increase is here calculated against strategy S4opt.

Figure 4.5 shows the loss increase for defined variance ranges: a zero-variance case $\sigma^2 = 0$ (11 samples), a low variance group is defined for $0 < \sigma^2 \leq 0.05$ (624 samples), a medium variance group with $0.05 < \sigma^2 \leq 0.15$ (600 samples) and a high variance case for $\sigma^2 > 0.15$ (96 samples). Each data point represents one simulation and the data are overlaid by third grade polynomial approximations for the ease of visualization. As a first general observation, the main tendencies are kept for different values of σ^2 . Especially for low and medium variance, representing situations of slight wind speed differences in the cluster and/or few WT shut-downs, show similar results to $\sigma^2 = 0$. Nevertheless, for a high variance the performance of S1 decreases. The same effect occurs for strategy S3a compared to S3b. The latter is caused by the advantageous power-factor-based control strategy (S3b) which avoids discrimination of unequal active power injections. The similarities observed for all σ^2 values allow the AEP calculation to be made with only equal active power injections ($\sigma^2 = 0$).

4.4.4 Annual energy production and economic value

The AEP of the WPP cluster, the difference in loss production against strategy S0opt, and the economic impact thereof are listed in Tab. 4.10. The calculations are based on the variance case $\sigma^2 = 0$. The economic impact depends entirely on the assumed feed-in tariff which is 100 € MWh^{-1} in this study. The most promising conventional strategy, namely S2, results in a loss increase of 8.77 GWh yr^{-1} equal to 0.88 M€ . The advantage against S1, S3a, and S3b is of 6.30 GWh to 3.18 GWh annually, in the respective order. The optimization-based strategy S4opt results in the lowest loss increase of only 5.00 GWh yr^{-1} compared to S0opt.

Table 4.10: AEP of WPP cluster and its deviation due to the different reactive power strategies with respect to S0opt.

	S0opt	S1	S2	S3a	S3b	S4opt
AEP / GWh yr^{-1}	5833.21	5818.14	5824.44	5821.02	5821.26	5828.22
AEP dev. ¹ / GWh yr^{-1}	0.00	-15.07	-8.77	-12.19	-11.95	-5.00
ME dev. ¹ / M€ yr^{-1}	0.00	-1.51	-0.88	-1.22	-1.20	-0.50

¹ Deviation with respect to the result of the benchmark strategy S0opt.

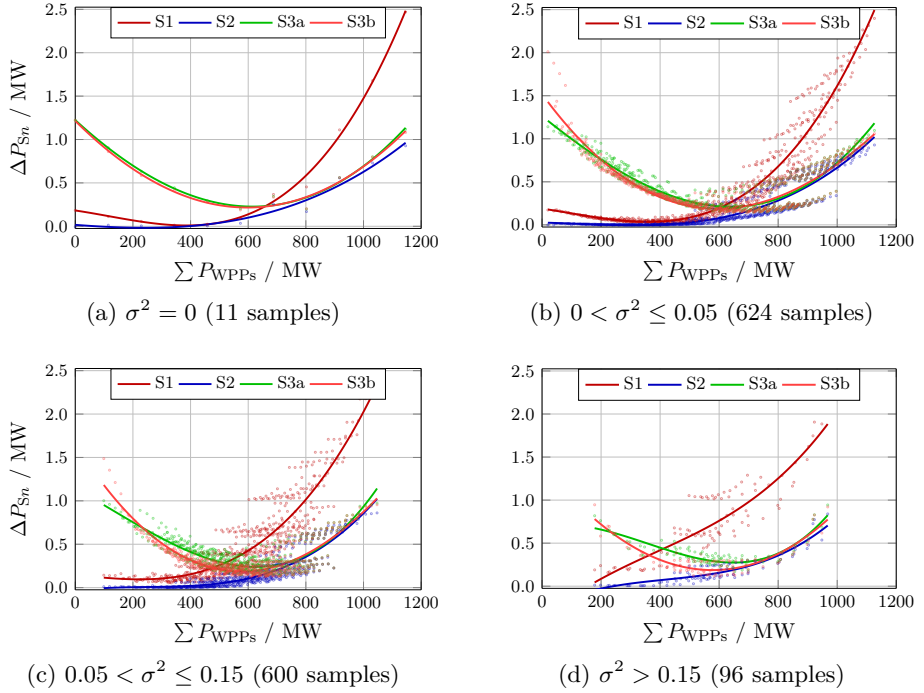


Figure 4.5: Variation of losses with respect to $S4_{opt}$ ($\Delta P_{S_n} = P_{system}^{loss, S_n} - P_{system}^{loss, S4_{opt}}$). Results from different active power injection variance groups are gathered: (a) zero, (b) low, (c) medium and (d) high variance. The solid lines are third grade polynomial approximation of these data.

4.5 Summary

This chapter examined five reactive power control strategies for HVdc-connected WPP clusters. Besides conventional strategies, namely unity PF operation by the WTs, WPPs, or VSC-HVdc, optimization-based strategies are also discovered. The performance of the strategies was quantified by the power losses in the system and evaluated against the benchmark strategy S0opt. Moreover, a case study was defined with three WPPs in the cluster.

First, WPP loss functions in dependence of the operating point (active and reactive power) were developed. The voltage level at the MV-side of the WPP transformer is controlled by the respective OLTC. It was highlighted that reactive power provision at the WPP terminals leads to additional power losses, on the one hand by the WT converters and on the other hand by the power flow through the MV collection grid. Besides that, it was depicted that reactive power provision from a WPP causes higher relative losses than from the VSC-HVdc respectively compared to unity power factor operation.

Secondly, the main dependence for the power losses of the WPP cluster was the sum of the individual WPP active power output. Furthermore, the variance σ^2 of the active power injections by the different WPPs was used to group the results. It was demonstrated that different σ^2 values did not significantly change the power losses associated to the strategies. Thus, the AEP assessment was based on equal wind speeds in the cluster.

Last, the cascaded control based on the optimization algorithm demonstrated the best performance mainly due to a higher reference voltage imposed by the VSC-HVdc. The associated optimization problem deploys only four control variables, i.e. u_{PCC} , q_1 , q_2 , and q_3 , in a cluster with three WPPs, and is therefore fast enough for industrial implementation. Execution times of few seconds were reached on a standard computer. Among the other conventional control strategies, a continuous unity PF operation of each WPP was favorable for the power losses. In such a configuration, the WT converters compensate the reactive power in the MV collection grids and the VSC-HVdc balances the reactive power of the HV export cables and transformers. It results in an effective sharing of reactive power in the offshore grid among all converters.

From an implementation perspective, it was argued that the proposed

optimization-based strategy is feasible due to its low execution time and the moderate communication needs which are already industrial standard in HVdc-connected WPP clusters. However, in the current prevailing market model with split generation and transmission asset ownership in the offshore grid, the optimization-based strategy might be implemented when all owners/operators aim together to increase the AEP of the system. Furthermore, in future market implementations with a single ownership of the generation assets as well as the offshore grid comprising the HVdc link, the proposed strategy might be very attractive for reactive power management.

5 Fault ride through of the offshore MMC–HVdc

5.1 Introduction

Chapters 3 and 4 treat exclusively normal operation of HVdc-connected WPPs in steady-state. Normal operation covers most of the lifetime of the considered systems. However, deviations from the normal operation might occur in the offshore system, e.g. voltage sags caused by electrical faults, and should be handled in an automated and secure manner. Being a power-converter-based grid without any SG connected, the FRT behavior of the WT converters and the offshore VSC–HVdc is of utmost importance. Besides that, conventional short-circuit calculation might not be applicable as the converters might provide a voltage-sag-dependent FRT response. In an HVdc-connected WPP, the converters are the sole sources for fault currents which results in a very low short circuit level (around the nominal current) [42]. The general protection scheme might employ over-current protection relays. For the grid-connected operation mode, FRT strategies might be applied once a fast voltage deviation is measured. For the grid-forming converter, the voltage deviation leads to a current increase and subsequent limitation thereof to protect the converter equipment when the fault occurs in vicinity of the voltage-controlled ac bus. For more remote faults, e.g. at WT level, the offshore VSC–HVdc might not be able to sense the voltage deviation and, thus, not saturate. In general, it is desired to keep the voltage as high as possible. It allows subsequent operation of non-faulted sections of the offshore grid and avoids unnecessary FRT activation and possible active power reduction by the connected WPPs.

Therefore, both grid-forming and grid-connected units are considered for the FRT behavior in this thesis, each in the following and in Chapter 6.

This chapter disseminates:

- control method for the grid-forming VSC–HVdc in symmetrical components;
- impact of balanced and unbalanced voltage conditions on the internal variables of the grid-forming MMC–HVdc;
- and extended saturation method for the VSC–HVdc current references during unbalanced faults in the offshore grid.

5.1.1 Related publication

The work described in this chapter was presented at:

- K. Schönleber, E. Prieto-Araujo, O. Gomis-Bellmunt, Fault ride-through of unbalanced ac grid faults in HVdc-connected offshore wind power plants, in: U. Betancourt, T. Ackermann (Eds.), 16th Wind Integr. Work., Energynautics GmbH, Berlin, Germany, 2017.

Part of the work was submitted to *IEEE Transactions on Power Delivery*.

5.2 Methodology

First, the control method for the offshore VSC–HVdc in symmetrical components is proposed. The operation principle during unbalanced faults is depicted and a suitable current reference limitation presented. Finally, the mathematical expressions for the internal variables of the grid-forming MMC–HVdc are developed.

In this chapter, voltage u_k and current i_k for a phase k are defined by:

$$u_k = U_k \cos(\omega t + \varphi_k^u); \quad i_k = I_k \cos(\omega t + \varphi_k^i) \quad (5.1)$$

$$\varphi_k^{iu} = \varphi_k^i - \varphi_k^u \quad (5.2)$$

where:

- k = phase variable ($k \in \{a, b, c\}$);
 ω = angular grid frequency;
 U_k = voltage magnitude;
 I_k = current magnitude;
 φ_k^u = voltage angle;
 φ_k^i = current angle;
 φ_k^{iu} = angle between u_k and i_k .

5.2.1 Proposed grid-forming VSC–HVdc control

For the offshore VSC–HVdc, two state-of-the-art control options for the grid-forming mode are commented in Section 2.2.2. Option I uses a cascaded VC and CC, and option II applies a direct VC without implicit CC. The lack of inherent CC capability was outlined as the major drawback for option II in earlier research [130].

This thesis proposes a cascaded VC and CC in symmetrical components to regulate the offshore grid voltage by means of the VSC–HVdc. It presents a variation of the control structure introduced as option I. The use of symmetrical components for both VC and CC permits to gain full current controllability even during unbalanced voltage conditions. A detailed overview of the proposed control scheme is given in Fig. 5.1. The cascaded VC and CC are employed in the DSRF, consequently in pos. and in neg. seq., to regulate the offshore grid voltage using the VSC–HVdc.

The measured three-phase grid voltage u^g is transformed into the DSRF through the decoupling network depicted in Fig. 5.2. The decoupling network cancels the double grid frequency oscillations on the signals. No PLL is needed in the grid-forming operation mode. The offshore grid frequency is constantly set to $f = 50$ Hz and the pos. seq. phase angle is obtained as:

$$\theta_1^g = \int 2\pi f dt = 2\pi ft + c_0 \quad (5.3)$$

where:

θ_1^g = pos. seq. phase angle;
 c_0 = integration constant.

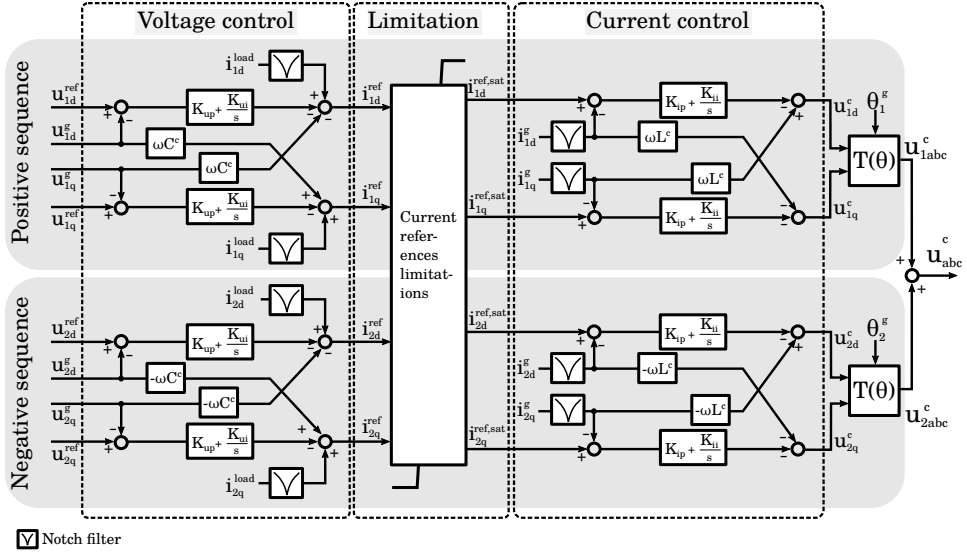


Figure 5.1: Proposed control for the grid-forming VSC–HVdc in symmetrical components.

For the sake of simplicity, the integration constant might be set to zero $c_0 = 0$. Correspondingly, the neg. seq. phase angle, θ_2^g , might be obtained through integration of the negative frequency (rotating clockwise):

$$\theta_2^g = \int -2\pi f dt = -2\pi ft + c_0 \quad (5.4)$$

Again, the integration constant is chosen to be zero. Therefore, the neg. seq. phase angle might be directly obtained from $\theta_2^g = -\theta_1^g$ as depicted on the right-hand side of Fig. 5.2. Hence, the challenge of the neg. seq. phase angle estimation during low neg. seq. voltage magnitudes highlighted for the grid-connected mode in Section 2.2.1, is not present in the grid-forming operation.

Both the measured grid current i^g for the CC as well as the load current i^{load} used for the feed-forward in the VC might contain double fundamental frequency components after transformation into the DSRF. These are intro-

duced by the coupling between the sequences as highlighted in Section 2.2.1. For the ease of a simple implementation, the signals are preprocessed through 100 Hz–tuned notch filters (damping factor $\zeta = 0.5$) to attenuate the oscillations. It must be noted that an alternative implementation might be a similar decoupling network as described for the measured grid voltage or the variations described for the grid–connected application in [17].

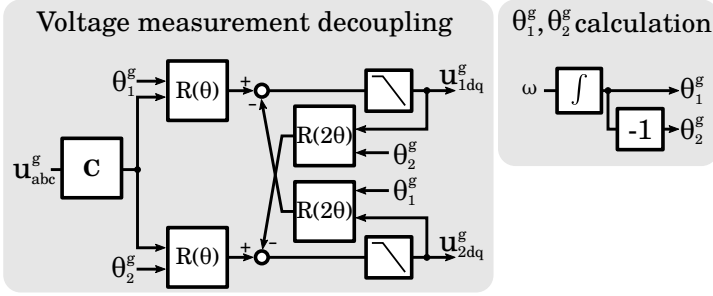


Figure 5.2: Voltage measurement decoupling and phase angle determination for the proposed VSC–HVdc control.

5.2.1.1 Voltage control

The pos. and neg. seq. VC loops are set up with conventional design principles in the SRF with PI controllers and decoupling terms. The VC loops output the current references in pos. seq. $i_1^{\text{ref}} = I_1^{\text{ref}} \exp(j\phi_1^{i,\text{ref}}) = [i_{1d}^{\text{ref}} \ i_{1q}^{\text{ref}}]^T$ and in neg. seq. $i_2^{\text{ref}} = I_2^{\text{ref}} \exp(j\phi_2^{i,\text{ref}}) = [i_{2d}^{\text{ref}} \ i_{2q}^{\text{ref}}]^T$. The ac dynamics regulated by the VC loops are:

$$\begin{bmatrix} i_{1d}^{\text{ref}} \\ i_{1q}^{\text{ref}} \end{bmatrix} = \begin{bmatrix} i_{1d}^{\text{load}} \\ i_{1q}^{\text{load}} \end{bmatrix} - \begin{bmatrix} 0 & -\omega C^c \\ \omega C^c & 0 \end{bmatrix} \begin{bmatrix} u_{1d}^{\text{g}} \\ u_{1q}^{\text{g}} \end{bmatrix} - \frac{1}{C^c} \frac{d}{dt} \begin{bmatrix} u_{1d}^{\text{g}} \\ u_{1q}^{\text{g}} \end{bmatrix} \quad (5.5)$$

$$\begin{bmatrix} i_{2d}^{\text{ref}} \\ i_{2q}^{\text{ref}} \end{bmatrix} = \begin{bmatrix} i_{2d}^{\text{load}} \\ i_{2q}^{\text{load}} \end{bmatrix} - \begin{bmatrix} 0 & \omega C^c \\ -\omega C^c & 0 \end{bmatrix} \begin{bmatrix} u_{2d}^{\text{g}} \\ u_{2q}^{\text{g}} \end{bmatrix} - \frac{1}{C^c} \frac{d}{dt} \begin{bmatrix} u_{2d}^{\text{g}} \\ u_{2q}^{\text{g}} \end{bmatrix} \quad (5.6)$$

The pos. and neg. voltage references are $u_1^{\text{ref}} = U_1^{\text{ref}} \exp(j\phi_1^{u,\text{ref}})$ and $u_2^{\text{ref}} = 0$ p.u., respectively. Basically, any value could be taken for the phase angle reference $\phi_1^{u,\text{ref}}$. The voltage magnitude is the desired nominal voltage $U_1^{\text{ref}} = 1$ p.u.. Here, in dq –components $u_1^{\text{ref}} = [1 \ 0]^T$ and $u_2^{\text{ref}} = [0 \ 0]^T$ are chosen. A dedicated HV capacitor C^c is used to enable feed–forward terms

of the load current i^{load} injected by the connected WPPs. The measured load current i^{load} is fed-forward in symmetrical components.

5.2.1.2 Current control

The current controller is employed in the DSRF with PI controllers and decoupling terms as defined for the pos. seq. in Eqn. (5.7) and for the neg. seq. in Eqn. (5.8). In this work, the current is controlled through the arm inductances of the MMC which lead to an equal inductance of $L^c = 0.5L^a$.

$$\begin{bmatrix} u_{1d}^c \\ u_{1q}^c \end{bmatrix} = \begin{bmatrix} u_{1d}^g \\ u_{1q}^g \end{bmatrix} - \frac{1}{2} \begin{bmatrix} R^a & -\omega L^a \\ \omega L^a & R^a \end{bmatrix} \begin{bmatrix} i_{1d}^g \\ i_{1q}^g \end{bmatrix} - \frac{1}{2} L^a \frac{d}{dt} \begin{bmatrix} i_{1d}^g \\ i_{1q}^g \end{bmatrix} \quad (5.7)$$

$$\begin{bmatrix} u_{2d}^c \\ u_{2q}^c \end{bmatrix} = \begin{bmatrix} u_{2d}^g \\ u_{2q}^g \end{bmatrix} - \frac{1}{2} \begin{bmatrix} R^a & \omega L^a \\ -\omega L^a & R^a \end{bmatrix} \begin{bmatrix} i_{2d}^g \\ i_{2q}^g \end{bmatrix} - \frac{1}{2} L^a \frac{d}{dt} \begin{bmatrix} i_{2d}^g \\ i_{2q}^g \end{bmatrix} \quad (5.8)$$

In that case, the converter reference voltage u^c in that case is applied as u^{diff} in the MMC modulation. The feed-forward concept for the CC was briefly commented in Section 2.2.2. Following the recommendation in [71], no feed-forward is established for the CC. Alternatively, the reference voltage u^{ref} could be fed-forward to improve the response of the current control on reference voltage changes [71], [127].

5.2.2 Current references saturation

The main responsibility of the VSC–HVdc is the provision of the offshore grid voltage and the resulting active power transmission capability. Additionally, during an ac voltage sag caused by a fault in the offshore grid the VSC might be required to inject controlled currents for the ease of fault detection as no SGs are present [55]. In the situation that the VSC feeds a passive offshore grid, e.g. during energization of the network and prior to connection of the WTs, and presents the only power converter in the system, the mentioned fault current provision becomes even mandatory for fault detection [175].

After a voltage sag inception, the VC increases naturally the current reference magnitudes given the difference between u^g and u^{ref} at the VC input. The current references might be limited to the maximum current to

avoid damage of the semiconductors. The maximum current I^{\max} might be defined as the highest operating current for continuous operation. Once the current references are limited, the voltage controllers' integral parts of the PI might be clamped to avoid windup problems.

Two saturation methods are introduced to limit the current references i_1^{ref} , i_2^{ref} in pos. and neg. sequence:

- I. Normal method: Limitation in symmetrical components when one phase current magnitude (in the abc -frame) exceeds the maximum value I^{\max} .
- II. Extended method: Limitation in symmetrical components under determination of the fault conditions and controlled current injection of the maximum value I^{\max} in all faulted phases.

The current references saturation is located between VC and CC as depicted in the control diagram of Fig. 5.5 in the upper part and might switch in either the normal or extended saturation.

5.2.2.1 Normal saturation method

To limit the phase currents to a specified maximum current I^{\max} , the symmetrical components in the DSRF might be modified as depicted in Fig. 5.3. The symmetrical components i_{1d}^{ref} , i_{1q}^{ref} , i_{2d}^{ref} , and i_{2q}^{ref} are scaled by the factor $1/\max_{k=a,b,c} I_k^{\text{ref}}$ when $\max_{k=a,b,c} I_k^{\text{ref}} \geq I^{\max}$. The output variables are $i_{1d}^{\text{ref,sat}}$, $i_{1q}^{\text{ref,sat}}$, $i_{2d}^{\text{ref,sat}}$, and $i_{2q}^{\text{ref,sat}}$, respectively. The phase magnitudes I_k^{ref} might be calculated directly from the seq. component magnitudes (I_1^{ref} , I_2^{ref}) and their respective angles ($\phi_1^{i,\text{ref}}$, $\phi_2^{i,\text{ref}}$) [204], [205]:

$$\begin{cases} I_a^{\text{ref}} = \sqrt{I_1^{\text{ref}2} + I_2^{\text{ref}2} + 2I_1^{\text{ref}}I_2^{\text{ref}}\cos\varepsilon} \\ I_b^{\text{ref}} = \sqrt{I_1^{\text{ref}2} + I_2^{\text{ref}2} + 2I_1^{\text{ref}}I_2^{\text{ref}}\cos(\varepsilon + \frac{4\pi}{3})} \\ I_c^{\text{ref}} = \sqrt{I_1^{\text{ref}2} + I_2^{\text{ref}2} + 2I_1^{\text{ref}}I_2^{\text{ref}}\cos(\varepsilon - \frac{4\pi}{3})} \end{cases} \quad (5.9)$$

where $\varepsilon = \phi_2^{i,\text{ref}} - \phi_1^{i,\text{ref}}$ is the angle between the seq. components of the current references.

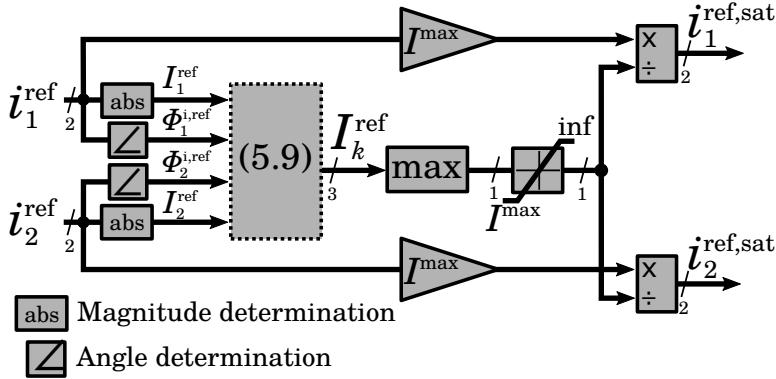


Figure 5.3: Normal saturation method implementation.

As an example, a symmetrical three-phase fault leads to an increase of solely the pos. seq. which is followed by the limitation of all three phases; similarly, in the case of a SLG fault or equivalent at the VSC terminals, the normal saturation method limits the dq -components in both sequences as soon as the faulted phase hits the current limit I^{max} . Here, neg. seq. dq -components appear which must be limited in combination with the pos. sequence.

5.2.2.2 Extended saturation method

In the specific case of one healthy phase (and two faulted phases) at the VSC terminals, the normal saturation method will eventually saturate when the first faulted phase surpasses the maximum current I^{max} . However, the second faulted phase might remain at a lower value than the maximum current I^{max} which could result in an underuse of the converter current capability. Therefore, the extended saturation method is proposed which permits that both faulted phases reach maximum current:

Step 1: Detect the conditions of one healthy phase based on the current disturbance created by the voltage sag. If all or only one phase is faulted, the normal saturation method applies. Being x the healthy phase and y and z the faulted phases, the following phasors are

defined:

$$\begin{cases} i_x^g = I_x^g e^{j\varphi_x^i} \\ i_y^g = I_y^g e^{j\varphi_y^i} \\ i_z^g = I_z^g e^{j\varphi_z^i} \end{cases} \quad (5.10)$$

Step 2: Apply inverse Fortescue in the phasor domain, see Appendix A.1, to obtain magnitudes and angles in abc -frame out of the pos. and neg. seq. current references i_1^{ref} , i_2^{ref} .

Step 3: Select the healthy phase x ; maintain its magnitude and angle.

Step 4: Calculate the angles for the faulted phases (y and z); set I^{max} as magnitude for I_y^g and I_z^g . The angles φ_y^i and φ_z^i can be determined by solving Eqn. (5.11) considering that the vectors i_x^g , i_y^g , and i_z^g form an isosceles triangle (see shaded area in Figure 5.4):

$$\begin{cases} i_x^g + i_y^g + i_z^g = 0 \\ \pi - \frac{1}{2}(\varphi_y^i + \varphi_z^i) + \varphi_x^i = 0 \end{cases} \quad (5.11)$$

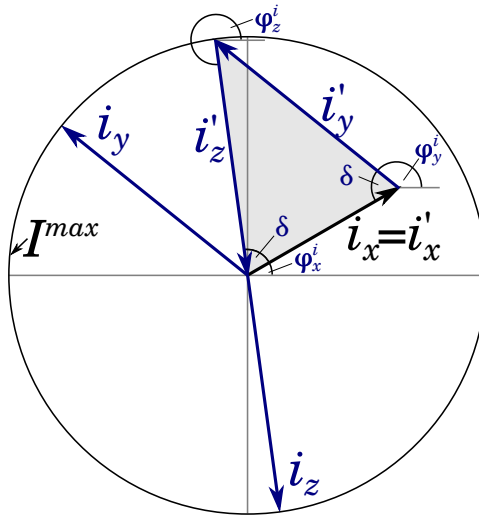


Figure 5.4: Phasor diagram for proposed current vector during the extended saturation method.

Equation (5.12) shows the solutions of Eqn. (5.11):

$$\begin{cases} \varphi_y^i &= \pi + \varphi_x^i \mp \arccos [I_x^g / (2I^{\max})] \\ \varphi_z^i &= \pi + \varphi_x^i \pm \arccos [I_x^g / (2I^{\max})] \end{cases} \quad (5.12)$$

From the two solutions of Eqn. (5.12) the one with least deviation of φ_y and φ_z with respect to the pre-fault conditions is chosen.

Step 5: Apply the Fortescue operator in the phasor domain to obtain pos. and neg. seq. current references and the Park–transformation, see Appendix A.1, to translate them to the DSRF.

Step 6: Set the new current references $i_1^{\text{ref,sat}}$ and $i_2^{\text{ref,sat}}$ at the input of the CC.

After the fault ending, the VC regains control and continuous normal operation.

5.2.3 MMC–HVdc in the grid–forming application

For the proposed control method and current limitation, it is important to take the internal converter characteristics into account. Currently, the three–phase MMC with half–bridge SMs is the state–of–the–art technology used for the offshore VSC–HVdc. The basic equations of the MMC circuit were outlined in Section 2.2.3. To analyze the ac dynamics and the internal energy regulation the use of a type–4–based model provides sufficient accuracy [144], [206]. The individual SM switching, SM voltages, and SM capacitor voltage balancing are not represented by the model. The arm inductors are modeled by an inductance L^a and its parasitic resistance R^a , whereas the SM stack of each arm is represented by a controlled voltage source.

One possible implementation to control the MMC under balanced and unbalanced conditions is a closed–loop energy regulation approach as described in [5]. The control framework is used in this thesis. Six energy PI regulators manage the balancing in vertical direction between upper and lower arm of each branch, denoted ac energy control, and in horizontal direction between the branches, ac, and dc side, denoted dc energy control. The ac power P_{abc}^{FF} is fed forward in the energy controllers determining the dc component

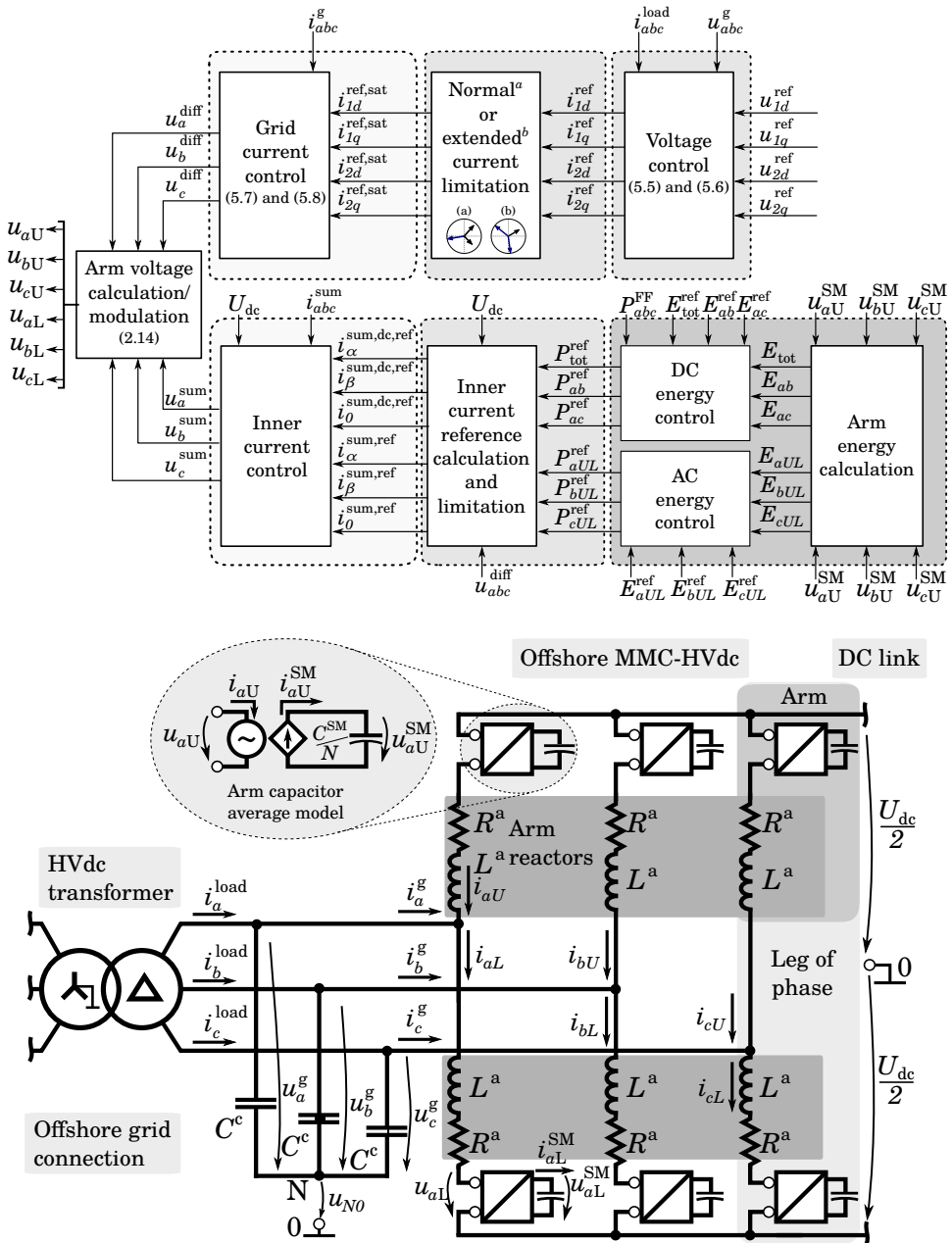


Figure 5.5: MMC model schematic and complete control architecture for the grid-forming application.

of the inner current reference $i^{\text{sum,dc,ref}}$. The dc and ac components of the additive current are limited individually. However, the dc components are prioritized over the ac components which might lead to temporary disabling of the vertical balancing. Furthermore, in [143], different methods (disabling of vertical balancing, kernel-based approach, and pseudo-inverse approach) are pointed out to permit safe converter operation when a singularity in the inner current reference calculation occurs. The singularity happens when the pos. and neg. seq. converter voltage magnitudes are equal or almost equal. In this chapter, the temporary disabling of vertical balancing has been chosen due to its reduced computational burden. Vertical balancing is disabled when the condition $|U_1^c - U_2^c| < 0.1$ p.u. holds. The blocks of the ac and dc energy controls, inner current saturation, and inner current control are depicted on the lower side of the control diagram in Fig. 5.5.

In the following, the analytical expressions for the energy and voltage variation of the SM stacks (arm capacitors) are used to analyze the expected arm currents for the MMC under unbalanced conditions in the grid-forming operation mode. The arm currents represent the actual current stress on the semiconductors in the SM. The capacitor voltage variations are developed as general mathematical expressions in [140]. The impact thereon is studied for three FRT strategies in the grid-connected application in [139]. The power in the k upper SM stack is $p_{kU} = u_{kU}^{\text{SM}} \cdot i_{kU}^{\text{SM}} = u_{kU} \cdot i_{kU}$ (analogous p_{kU} for the lower stack). Ref. [140] develops the analytical expressions of the arm capacitor voltages which are inherently linked with the energy variations. The upper and lower SM stack energies $E_{kU}(t)$ and $E_{kL}(t)$ are, respectively:

$$\begin{aligned} E_{kU}(t) &= \int p_{kU} dt = \int p_{kU}^a - p_{kU}^{Z^a} dt = \\ &= \int \left[\frac{U_{\text{dc}}}{2} - u_k^g - u_{\text{N0}} - \left(R^a i_{kU} + L^a \frac{di_{kU}}{dt} \right) \right] i_{kU} dt \end{aligned} \quad (5.13)$$

$$E_{kL}(t) = \int \left[\frac{U_{\text{dc}}}{2} + u_k^g - u_{\text{N0}} - \left(R^a i_{kL} + L^a \frac{di_{kL}}{dt} \right) \right] i_{kL} dt \quad (5.14)$$

where:

- p_{kU}^a, p_{kL}^a = power of the whole upper/lower arm of phase k ($k \in \{a, b, c\}$);
- $p_{kU}^{Z^a}, p_{kL}^{Z^a}$ = power of the upper/lower arm inductor (inductance plus parasitic resistance) of phase k ;

U_{dc} = dc link voltage;
 u_{N0} = the voltage drop from the neutral N and dc link midpoint 0.

For the ease of simplification, u_{N0} is set to zero in the following. The upper and lower arm capacitor voltages $u_{kU}^a(t)$ and $u_{kL}^a(t)$ result to:

$$u_{kU}^a(t) = \sqrt{(2N/C^{SM})E_{kU}(t)} \quad (5.15)$$

$$u_{kL}^a(t) = \sqrt{(2N/C^{SM})E_{kL}(t)} \quad (5.16)$$

where:

C^{SM} = capacitance of one SM;

N = number of SMs in one arm.

Equations (5.13) to (5.16) contain the respective relation between the arm energies and capacitor voltages with the external ac grid conditions and the dc side. To know the arm currents i_{kU} and i_{kL} , the additive currents i_k^{sum} have to be determined. In steady-state, after balancing of the vertical energy deviation under usage of the described closed-loop energy regulator structure, the additive currents i_k^{sum} result to be purely dc $i_k^{\text{sum}} = I_k^{\text{sum,dc}}$ [143]. Thus, they can be determined by solving the power equation for the upper arm of phase leg k :

$$\underbrace{\frac{U_{dc}I_k^{\text{sum,dc}}}{2}}_{\text{dc output power}} - \underbrace{\frac{U_k^g I_k^g \cos \varphi_k^{iu}}{4}}_{\text{ac input power}} - \underbrace{R^a \left(I_k^{\text{sum,dc}2} + \frac{I_k^g2}{8} \right)}_{\text{arm impedance losses}} = 0 \quad (5.17)$$

Solving the bi-quadratic equation Eqn. (5.17) yields for phase k the following solutions:

$$I_k^{\text{sum,dc}} = \frac{U_{dc}}{4R^a} \pm \sqrt{\left(\frac{U_{dc}}{4R^a} \right)^2 - \frac{I_k^g2}{4} \left(\frac{1}{2} + \frac{U_k^g \cos \varphi_k^{iu}}{R^a I_k^g} \right)} \quad (5.18)$$

Equation (5.18) unveils the additive current $I_k^{\text{sum,dc}}$ dependency on the angle φ_k^{iu} between current and voltage and the grid voltage magnitude U_k^g in steady-state. With the parameter data listed in Tab. 5.5, in Fig. 5.6 the resulting additive current $I_k^{\text{sum,dc}}$ for a controlled ac current $I_k^g = I_k^{\text{max}}$ in dependence

of φ_k^{iu} and U_k^g is depicted. The nominal dc current is $I_{dc}^{nom} = P_{dc}/U_{dc}$. Firstly, for operation with $U_k^g = 1$ p.u. and $\varphi_k^{iu} = 0$ it results in an additive current of 1/3 the nominal current plus the current to compensate the power losses in the arm inductors and their parasitic resistances. For the same apparent power, an angle increase ($\varphi_k^{iu} > 0$) lowers the additive current $I_k^{sum,dc}$ compared to unity power factor operation ($\varphi_k^{iu} = 0$). Furthermore, $I_k^{sum,dc}$ increases with the grid voltage magnitude U_k^g at a given angle φ_k^{iu} . To conclude, the grid-forming MMC–HVdc facing unbalanced voltage/current conditions will solely modify the power exchanged by each branch but not exceed the additive current flowing in normal operation. It must be noted that the additive current might be higher when vertical energy balancing regulation is occurring.

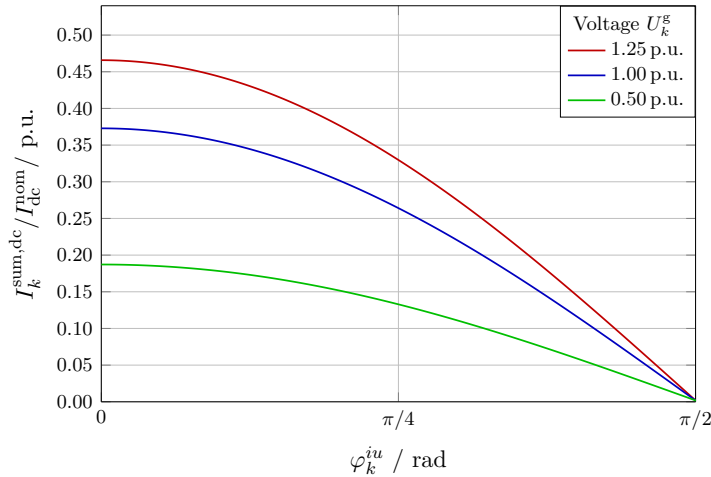


Figure 5.6: Steady-state $I_k^{sum,dc}$ in dependence of angle and for different voltage levels. $\varphi_k^{iu} = 0$ means rectifier mode. For $\varphi_k^{iu} = \pi/2$ current leads voltage; capacitive operation injecting reactive power.

5.3 Case study

A test system is set up to demonstrate the performance of the normal as well as proposed extended saturation during unbalanced faults in the offshore

grid. Network configuration I consists of the VSC–HVdc connected to the passive offshore grid. It represents the operating scenario occurring e.g. after energization of the offshore grid and prior to the power production authorization for the WPPs. The offshore grid hosts three WPPs with different export cable lengths and collection grid aggregations. Besides the offshore VSC–HVdc, the WPP transformers, and the HV and MV cables are connected. The WTs are disconnected. The offshore grid comprises delta–wye transformers to interface the different voltage levels and to decouple the zero seq. networks. The collection grids have also earthing transformers, respectively, to provide adequate grounding in the MV grids. The test system is set up in Matlab/SimPowerSystems as sketched in Fig. 5.7. The used discrete time step in the model is $T_s = 25 \mu\text{s}$. System parameters are further listed in Tab. 5.5.

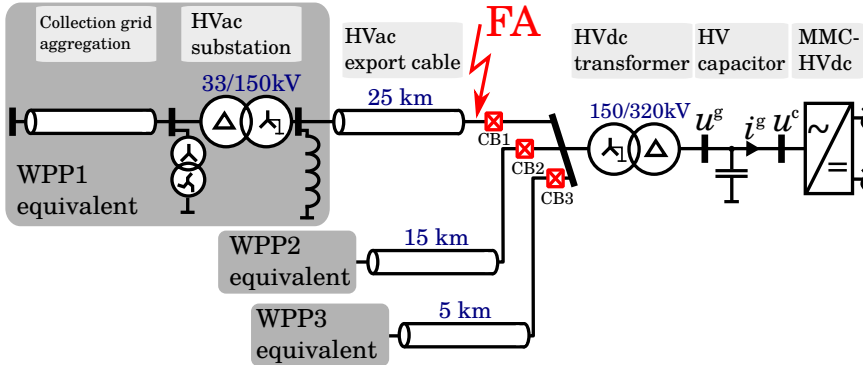


Figure 5.7: Electrical layout of the network configuration I (WT converters and transformers disconnected).

The LLLG, LL, and SLG faults are studied at the HVac export cable connection of the largest WPP at fault location A (FA) in vicinity of the HVdc transformer, respectively. The balanced fault (LLLG fault) is covered for the sake of completeness and to demonstrate the performance of the proposed control method in symmetrical components. Furthermore, only the normal saturation is applied for the simulation of the LLLG and LL fault at the 150 kV busbar. The extended saturation applies only for those cases where the VSC–HVdc aims to inject maximum current in two faulted phases. Therefore, the normal and extended saturation are analyzed for a SLG fault

Table 5.5: Relevant system parameter. Base power is $S_b = 1000$ MVA if referred, otherwise component power rating.

WPP and HV export grid	WPP1	WPP2	WPP3
Rating (P /MW)	498	450	198
Collection grid voltage (U_{ac} /kV)		33	
WPP collection grid impedance (z /p.u.) ¹	0.018 + j0.035	0.014 + j0.023	0.025 + j0.041
WPP grid shunt reactance (x /p.u.) ¹	0.011	0.009	0.003
WPP transformer impedance (z /p.u.)		0.003 + j0.15	
Export grid voltage (U_{ac} /kV)		150	
Export cable compensation (Q_r /Mvar)	50.5	30.9	4.0
Export cable impedance (z /p.u.) ¹	0.13 + j0.40	0.08 + j0.24	0.01 + j0.03
Export shunt reactance (x /p.u.) ¹	0.025	0.041	0.597
VSC–HVdc			
Rating (S /MVA, U_{ac} /kV, P_{dc} /MW, U_{dc} /kV)		1333.3, 320, 1200, \pm 320	
Transformer impedance (z /p.u.)		0.003 + j0.150	
Filter capacitance (C^c / μ F)		4.14	
MMC number of SMs (N /per arm)		400	
MMC arm impedance (Z^a / Ω)		0.77 + j15.36	
MMC arm impedance (Z^a /p.u.)		0.01 + j0.2	
MMC SM capacitance (C^{SM} /mF)		13.7	
MMC equivalent stored energy (E_{tot} /kJ/MVA)		35	
Time constants VC, CC, MMC inner CC (τ /ms)		1.5, 0.5, 0.2	

¹ Base power S_b applies.

at the 150 kV busbar which results in the described situation at the VSC terminals.

In submarine cables, it is unlikely to have temporary faults like in overhead lines as highlighted in Section 2.4. Therefore, a permanent fault is applied which might be detected through over-current relays and isolated by means of CBs. The post-fault operation is consequently considering only the remaining healthy system in operation. The MMC model used is adopted from the described model in [143].

5.4 Results

The results are shown over the time from some cycles before the fault inception at $t = 0.0$ s to the fault clearance (includes disconnection of faulted system) at $t = 0.5$ s and an additional post-fault period from $t = 0.5$ s to 1.0 s. The usual ac fault breaking time of around 150 ms is extended with the sole purpose of better visualization to 500 ms. The Figs. 5.8 and 5.11 list grid-related results, whereas Figs. 5.9 and 5.12 combine diagrams from the electrical variables of the MMC–HVdc, respectively. Results with higher time resolution for specific three-phase variables are displayed in Figs. 5.10 and 5.13. For fair comparison, all currents ($i_k^g, i_k^{\text{sum}}, i_{kU}$) are scaled to the ac base current of the converter.

5.4.1 LLLG fault at 150 kV

The left column of the Figs. 5.8 to 5.10 presents the results for a LLLG fault at the 150 kV busbar. It should further depict how the proposed control method for the grid-forming VSC–HVdc performs during normal operation without any WT converter connected. Row 1 and 2 of Fig. 5.8 show the three-phase currents by the offshore VSC–HVdc and the grid voltage obtained at the offshore grid connection. The results are depicted with a detailed time resolution after the fault inception in row 1 and 2 of Fig. 5.10. Prior to the fault inception, the grid voltage u_k^g is regulated to 1 p.u. and the grid current i_k^g of around 0.12 p.u. corresponds to the sum of the charging current for the MV and HV export cables and the HV capacitor as well as the current to compensate the power losses (mainly of the transformers). However, it should be mentioned that it is mainly reactive current as the dc current flowing from onshore at the same time is only 0.01 p.u. (refer to row 4). The balanced fault occurring at the 150 kV busbar causes the voltage in the offshore grid to drop and the converter current i_k^g to raise. After the fault, the VC successfully readopts the voltage to 1 p.u.. In row 3, the grid voltage magnitude is depicted in symmetrical components U_{12}^g . As expected, the balanced grid conditions mainly affect the positive sequence. During a very short transient after the fault inception and after the fault ending, the neg. seq. voltage raises due to the imbalance during this transient. The control

system in symmetrical components regulates the voltage satisfactorily and limits the current during the fault. However, it must be stated that a control method developed only in pos. seq. might act similarly in such conditions. In row 5 the dc voltage is shown and reveals that the fault does not impact the dc voltage control performed by the onshore converter.

The MMC–related results for the LLLG fault are displayed in Fig. 5.8 (left column). In that case, during the fault the vertical balancing is deactivated given the proximity between the symmetrical component magnitudes of the converter voltage $|U_1^c - U_2^c| < 0.1$ p.u.. Zoomed results of the three–phase signals i_k^{sum} , i_{kU} , and u_{kU}^a are also displayed in row 3 to 5 of Fig. 5.10. Row 1 of Fig. 5.9 presents the additive current i_k^{sum} which is used to balance the converter energy vertically and horizontally. Given the deactivation of the vertical balancing, the balanced conditions between the phase branches, and little power exchange between ac and dc side, the additive current i_k^{sum} is almost zero prior and during the fault. After the fault ending, the 50 Hz component of i_k^{sum} regulates the energies in vertical direction. It can be seen in rows 3 and 4 that the fault inception causes a vertical energy deviation E_{UL} within each phase branch and thus a deviation of the arm capacitor voltages u_{kU}^a . The nature of the deviation depends on the voltage and current snapshot at fault inception. Because of the deactivation of the vertical energy control during the fault period, the offset is sustained during the fault period and regulated once the fault ends and the vertical energy balancing reactivated. Row 2 depicts the upper arm current i_{kU} . During the fault, it increases to around 0.5 p.u. due to the injection of maximum grid current by the MMC–HVdc. Lastly, row 5 presents the horizontal energy deviation between the phase branches (E_{ab} and E_{ac}) which is constantly zero except during the transient period after the fault ending. It is caused by the transient conditions occurring when the MMC–HVdc regains its grid–forming operation and controls the voltage with the introduced cascaded control framework in symmetrical components.

5.4.2 LL fault at 150 kV

The right column of the Figs. 5.8 to 5.10 display the results for a LL fault applied between phase a and b at the 150 kV busbar. The first two rows of

Fig. 5.8 show the three-phase currents i_k^g and voltages u_k^g at the offshore grid connection. The results are again shown with a detailed time resolution in row 1 and 2 of Fig. 5.10. It demonstrates that u_k^g is regulated to the reference of 1 p.u. prior and after the fault. The pos. seq. voltage drop and neg. seq. voltage raise measured after fault inception cause the respective current references to increase. The LL fault at 150 kV is seen as two healthy (b and c) and one faulted phase (a) at the VSC terminals. In that case, the normal saturation method applies and the current references are limited as soon as the faulted phase hits the maximum current (here phase a). From the results shown in row 1 it can be concluded that the VSC-HVdc injects unbalanced currents to ride through the unbalanced conditions. In row 3, the seq. components magnitudes U_{12}^g of the grid voltage are depicted. The neg. seq. voltage U_2^g is controlled to zero prior and after to the fault. In row 4 and 5, the dc current and voltage are displayed. It can be deduced that the double grid frequency oscillations are kept away from the dc side and the dc current drawn from dc side increases slightly to compensate the additional losses due to the fault current provision.

In row 1 of Fig. 5.9, the additive currents i_k^{sum} are depicted (right column). An initial transient with 50 Hz components demonstrate the activity of the vertical energy regulators. Once the arm energies are vertically balanced, the circulating currents remain constant until the fault ending. The dc offset is caused by the unbalanced conditions which leads to a sustained horizontal energy deviation between the phase branches (refer to row 5). In row 2, the upper arm currents i_{kU} are shown. It is remarkable that phase a has the highest current magnitude during the fault. This is due to the maximum current injection in this phase. With exception of the initial transient, where the vertical balancing is active, the arm currents i_{kU} remain in the same range as for the LLLG fault in the left column. Row 3 displays the upper arm capacitor voltages of the MMC-HVdc. It is remarkable that there is an initial dc offset due to the almost instantaneous energy change at the fault inception. As highlighted earlier for the LLLG fault, the deviation depends on the exact fault inception. Additionally, the asymmetrical energy exchange between grid and the three converter phase legs results in unequal arm capacitor voltages. Zoomed results of the three-phase signals i_k^{sum} , i_{kU} ,

and u_{kU}^a are also displayed in row 3 to 5 of Fig. 5.10. The rows 4 and 5 of Fig. 5.9 depict the vertical energy difference per phase leg (E_{UL}) and the horizontal energy difference between phase leg a and b as well as a and c (E_{ab} and E_{ac}), respectively. The plots demonstrate that the regulators manage the energies successfully during the transients after fault inception and after fault ending.

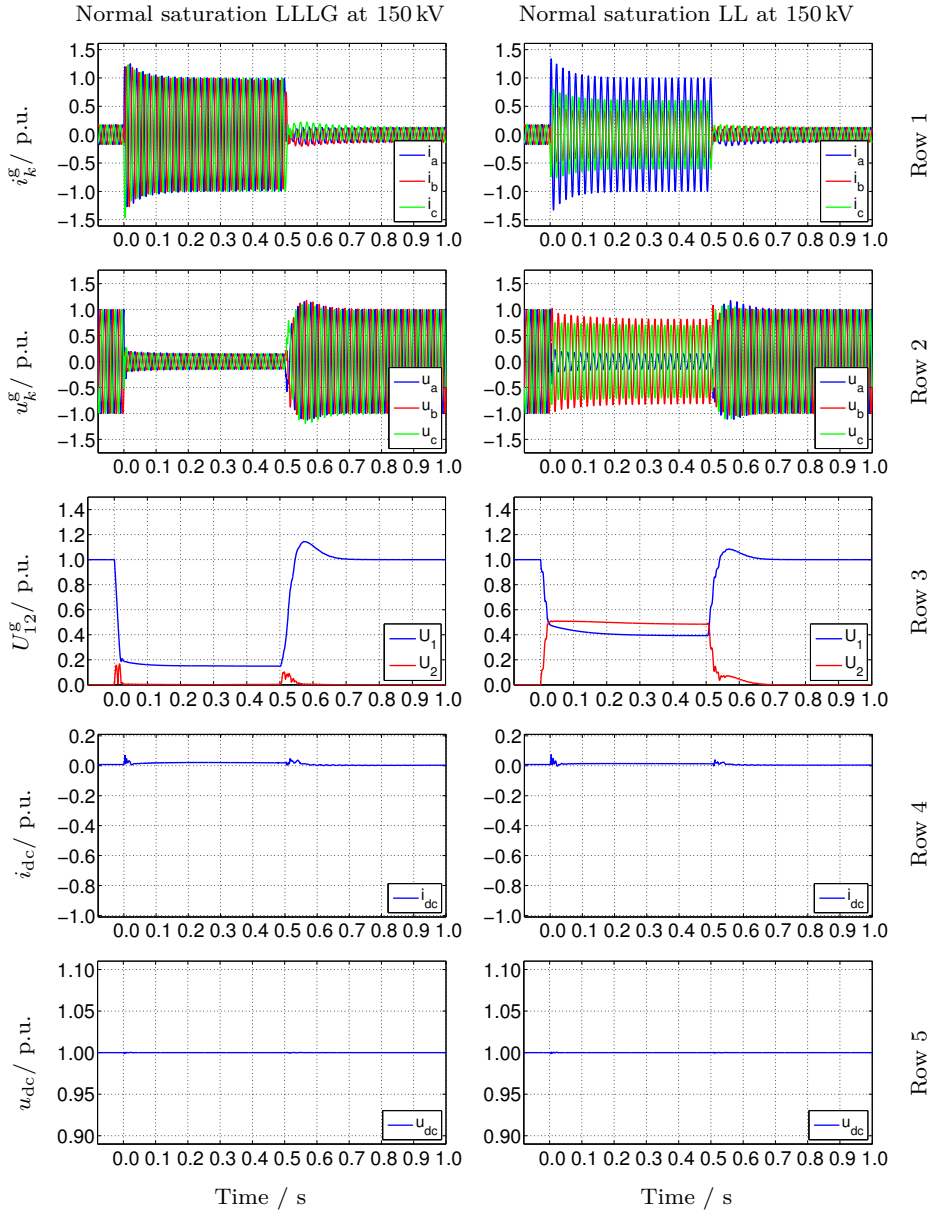


Figure 5.8: Grid-related results for the LLLG and LL fault in network configuration I. Plots are ordered row-wise by grid current, grid voltage, voltage magnitudes of symmetrical components at VSC-HVdc, dc current and voltage, in respective order.

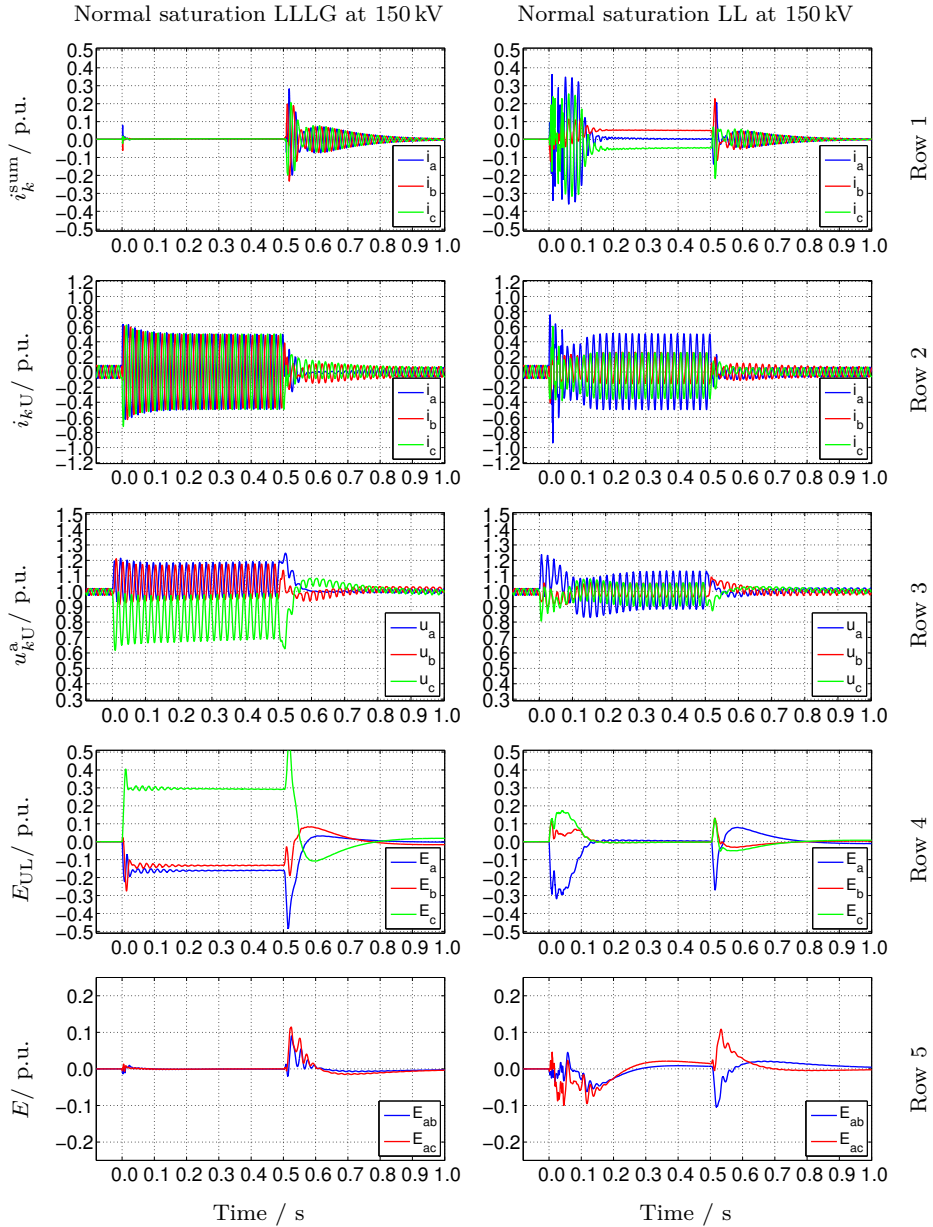


Figure 5.9: MMC-related results for the LLLG and LL fault in network configuration I. Plots are ordered row-wise by inner currents, upper arm currents, upper arm capacitor voltages, and internal energy variations of the MMC–HVdc in vertical and horizontal direction, in respective order.

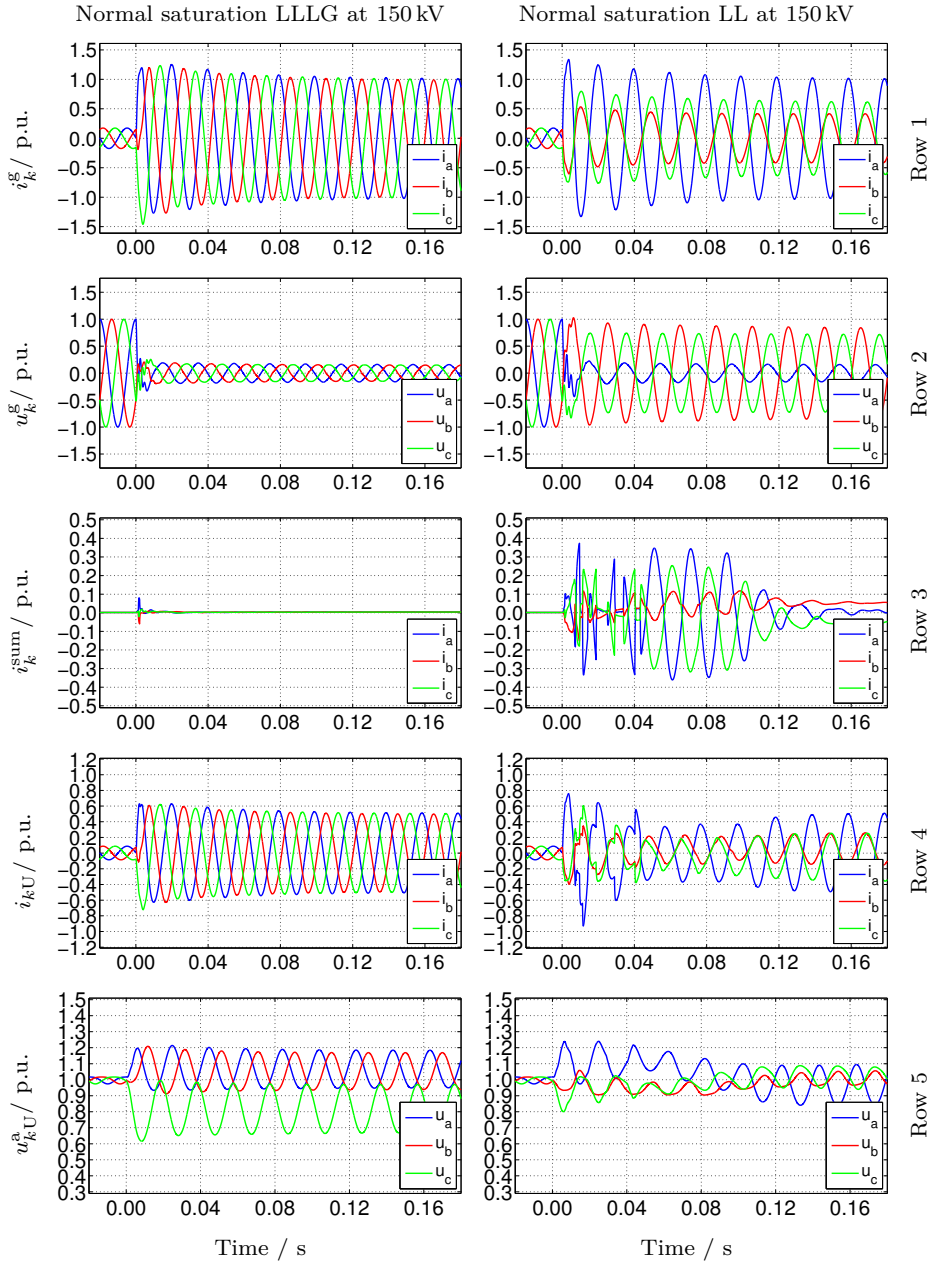


Figure 5.10: Zoomed results for Figs. 5.8 and 5.9. Plots are ordered row-wise by grid current, grid voltage, inner currents, upper arm currents, and upper arm capacitor voltages, in respective order.

5.4.3 SLG fault at 150 kV

Figures 5.11 to 5.13 show the results for a SLG fault of phase a at FA. The left column displays the results for the normal saturation, whereas the right column considers the proposed extended saturation. The three-phase currents i_k^g and voltages u_k^g are depicted in row 1 and 2 of Fig. 5.11. The currents raise after the fault inception and are limited by the converter. It can be seen that the normal method saturates when the first phase hits the maximum (here phase c). Phase a peaks at a value of only 0.88 p.u. of the maximum current. Contrary to that, the extended saturation provides an improved current response where phase a and c are controlled to the maximum current. Row 2 demonstrates that for both saturation methods u_k^g is controlled to 1 p.u. prior to the fault inception and smoothly controlled back to this value after the fault. During the fault, the voltages are impacted by the current injection of the VSC. The response of the extended saturation improves the voltage balance which is also demonstrated in row 3 having a higher pos. seq. and a lower neg. seq. voltage magnitude U_{12}^g than the normal saturation. The offset between the two saturation methods for the pos. seq. is of 0.22 p.u. and for the neg. seq. 0.13 p.u.. In row 4 and 5, the dc current and voltage are shown. As earlier observed for the LL fault, double grid frequency power oscillations are kept away from the dc link. The dc current drawn from dc side increases marginally to compensate the losses during the fault (increased arm currents through the arm impedances).

Figure 5.12 depicts the MMC-related results. Zoomed plots of the three-phase signals i_k^{sum} , i_{kU} , and u_{kU}^a are also depicted in row 3 to 5 of Fig. 5.13. In row 1, the additive or inner currents are depicted. As a reminder, no limitation has been applied to the inner current references to allow full visibility of the system behavior. The fault causes a significant change in the power exchange between the ac grid and the MMC. Furthermore, the unbalanced conditions cause a continuous energy deviation between the phase legs which is handled by the horizontal energy controllers. The initial transient after the fault inception of i_k^{sum} is caused by the activity of the MMC energy controllers between upper and lower arms (vertical) and between the phase legs (horizontal). Once the vertical energy deviations (50 Hz component) cease, the horizontal energy control between the phase

legs causes a maintained dc component of i_k^{sum} . For the normal saturation, the initial transient is larger in magnitude and duration, whereas for the extended saturation it settles faster. The higher dc component of i_k^{sum} results from the higher energy imbalance between the phase legs inside the MMC to provide the maximum grid currents in both faulted phases. In row 2, the upper arm current i_{kU} is displayed. It can be seen that the vertical balancing activity and resulting inner currents cause a higher upper phase leg current after fault inception for the normal saturation. Row 3 depicts the upper arm capacitor voltages. Despite the unbalanced conditions on ac side for both voltages and currents, the capacitor voltages remain controlled.

The rows 4 and 5 show the vertical energy deviation between upper and lower arms (E_{UL}) and the horizontal energy difference between the phase legs (E_{ab} and E_{ac}), respectively. The plots show that the regulators manage the energies successfully after fault inception and after fault ending, respectively. Moreover, the vertical energy deviation stays within a tolerance band of ± 0.3 p.u. of the stored phase leg energy. The vertical imbalance lasts slightly longer for the normal saturation than for the extended saturation. The results from row 8 exhibit that the impact of the converter response on the horizontal energy deviation and regulation is slightly increased for the normal saturation.

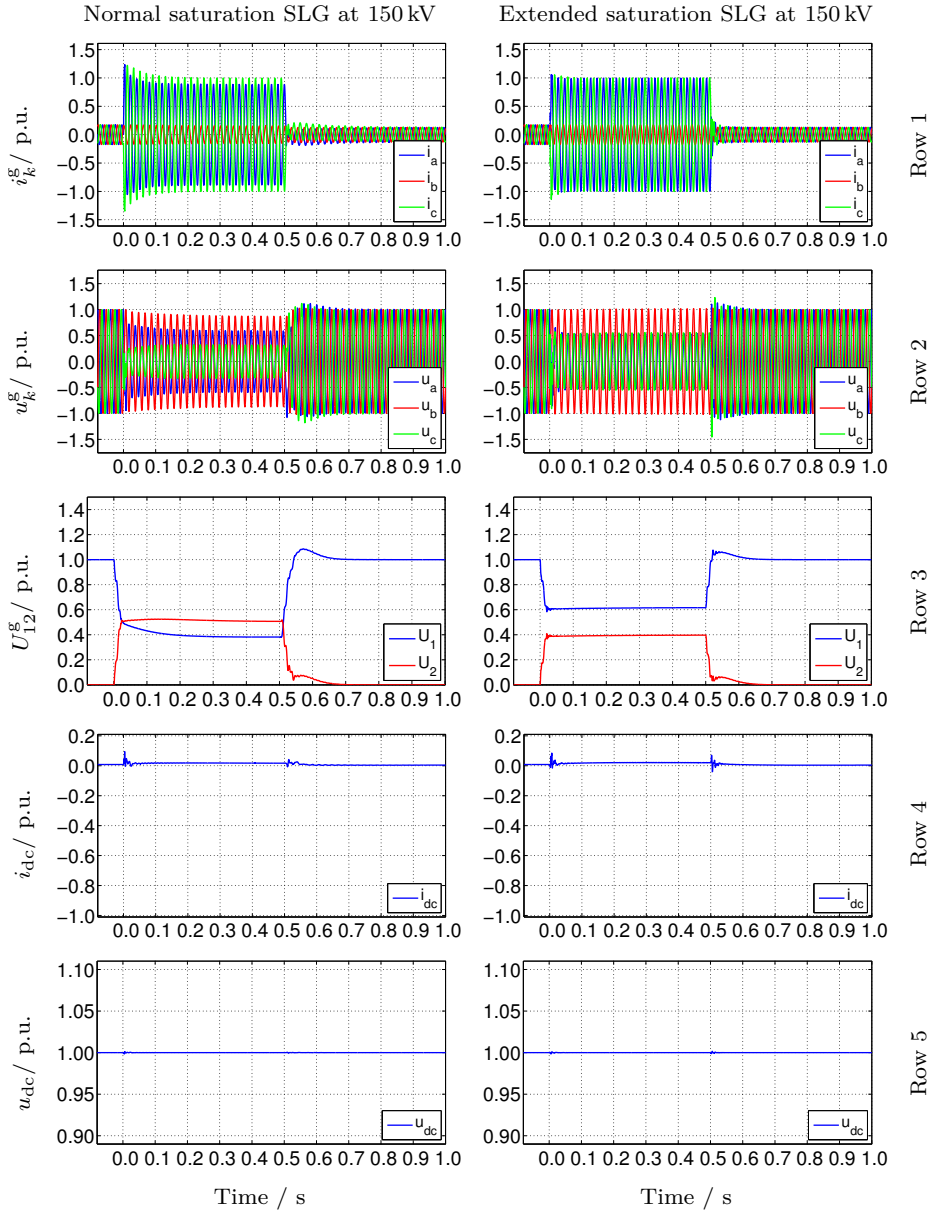


Figure 5.11: Grid-related results for the SLG fault at the 150kV busbar in network configuration I. Plots are ordered row-wise by grid current, grid voltage, voltage magnitudes of symmetrical components at VSC–HVdc, dc current and voltage, in respective order.

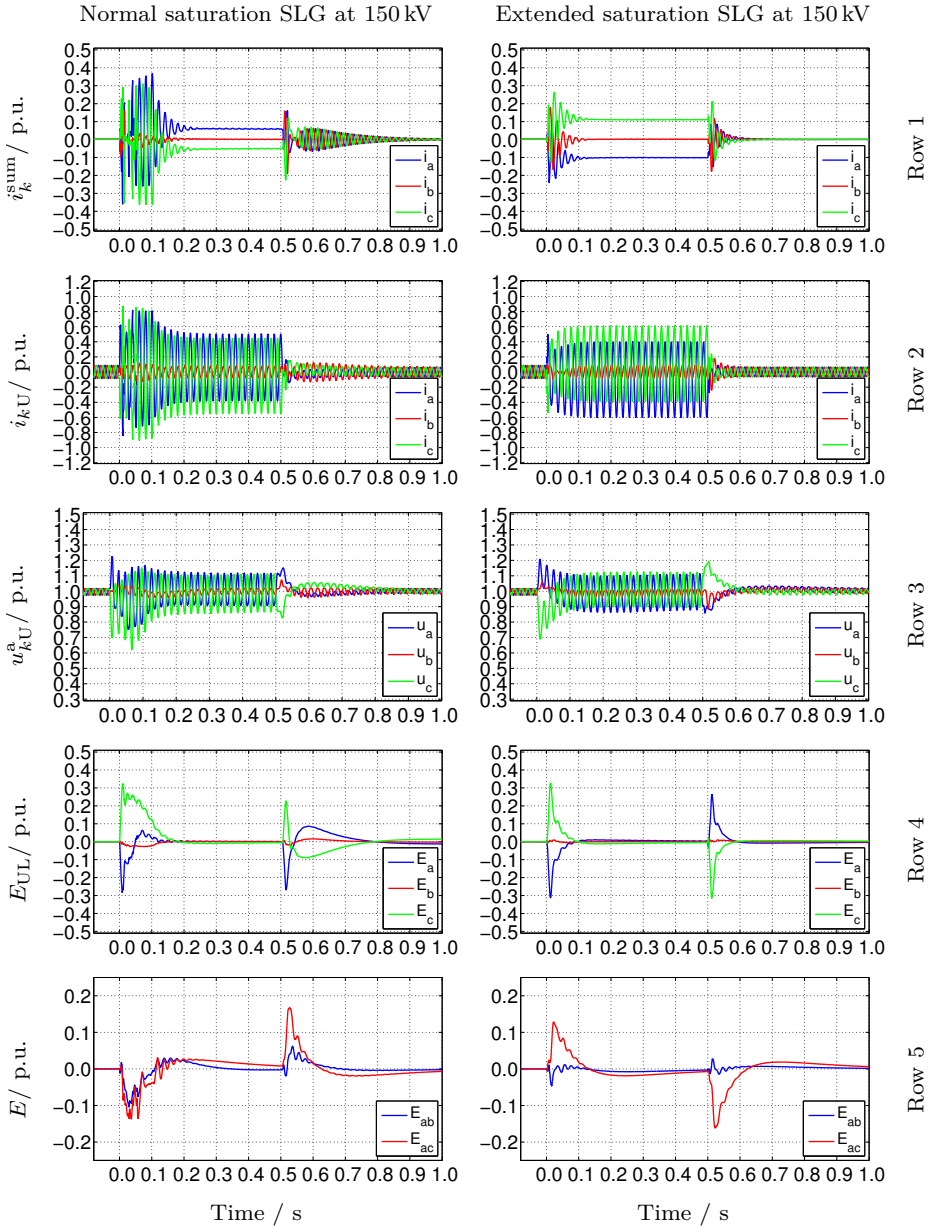


Figure 5.12: MMC-related results for the SLG fault at the 150 kV busbar in network configuration I. Plots are ordered row-wise by inner currents, upper arm currents and capacitor voltages, and internal energy variations of the MMC-HVdc in vertical and horizontal direction, in respective order.

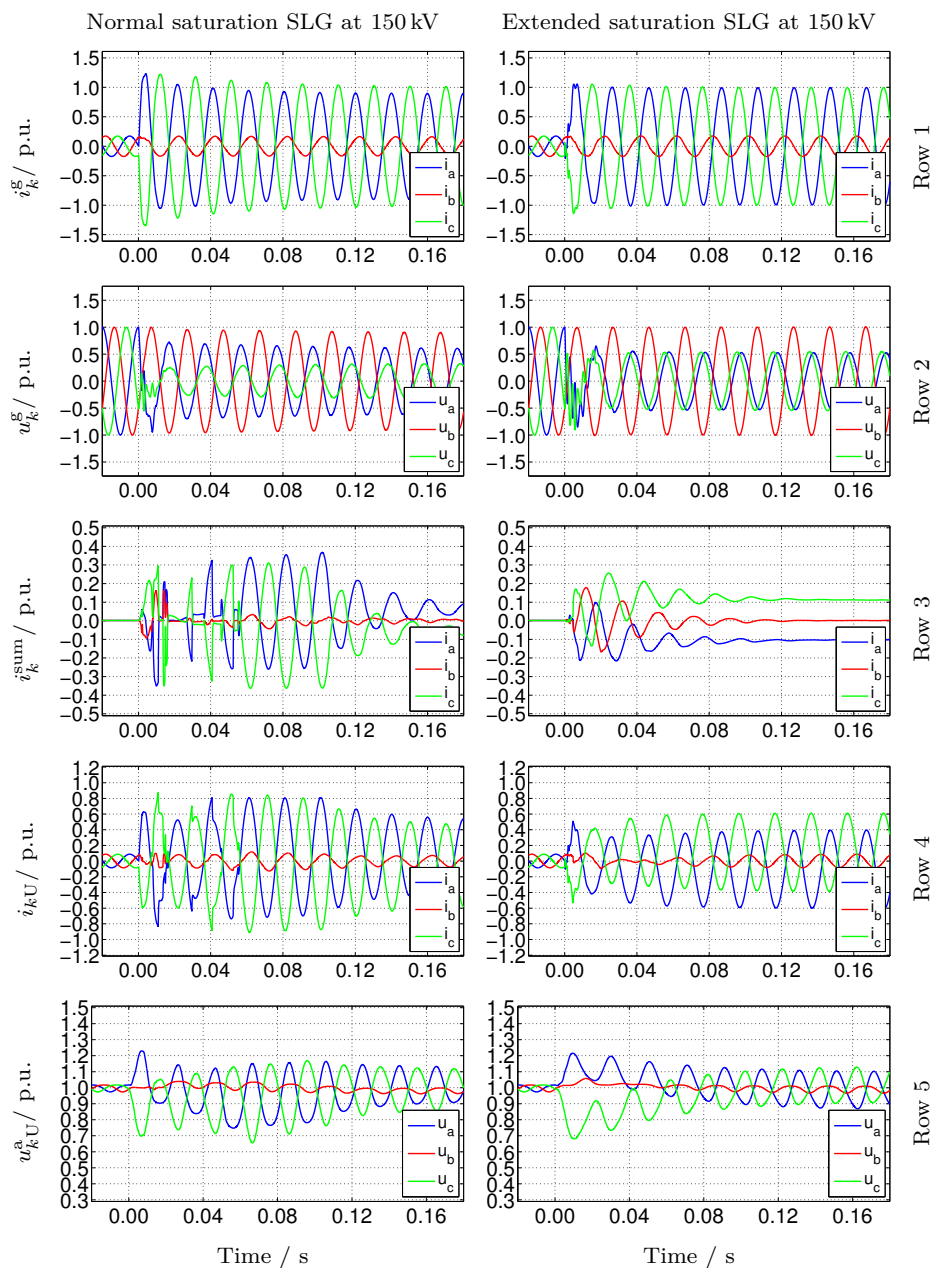


Figure 5.13: Zoomed results for Figs. 5.11 and 5.12. Plots are ordered row-wise by grid current, grid voltage, inner currents, upper arm currents, and upper arm capacitor voltages, in respective order.

5.5 Summary

This chapter proposed a control method for the grid-forming offshore VSC-HVdc. To enhance the current provision under specific unbalanced conditions an extended saturation method was presented. Furthermore, the impact of the grid-forming operation mode on the MMC-HVdc and its internal control was investigated. The concepts were simulated in the time domain for various fault scenarios, namely LLLG, LL, and SLG faults in the passive offshore grid, i.e. without connected WT converters.

The control scheme was defined as an evolution of a state-of-the-art option and formulated as a cascaded VC and CC system in symmetrical components. It aims to have a controlled converter response during imposed unbalanced voltage conditions in the operated grid. The advantage of the control scheme is the potential of rigorous limitation of the current references prior to feeding them into the CC. It was presented that the neg. seq. loops have no influence in normal operation as the reference and measured voltage in neg. seq. are generally zero. Thus, in normal operation, there is no unbalanced current injection by the grid-forming VSC-HVdc. During balanced faults, the VSC-HVdc injects balanced currents and the neg. seq. control acts only during the fault inception and ending transient to balance the voltages. It was stated that a similar response might be achieved with the original control implementation in pos. sequence. Contrary, during unbalanced faults, neg. seq. voltage arises and therefore the converter injects neg. seq. current with the proposed control scheme. In that case, the current references limitation in each phase is of utmost importance to avoid over-currents. The desired fault behavior foresees maximum current injection in the faulted phases for the ease of detection.

A normal saturation was used to limit the currents as soon as one phase hits the maximum current limitation. This solution is satisfactory for most faults, e.g. one or three faulted phases at the VSC-HVdc terminals. However, when two faulted phases must be fed at the VSC terminals, the dynamics of the VC output in combination with the normal saturation might not result in the desired current response. Therefore, an extended saturation method for the current references was suggested. The extended saturation method uses an online calculation of the grid currents and readjusts the respective magnitudes

and angles. It was shown that for unbalanced conditions with two faulted phases at the VSC–HVdc terminals, the proposed extended saturation leads to a better utilization of the converter capability. Furthermore, it improves the grid voltage and current profile. It was demonstrated that the neg. seq. voltage is reduced, whereas the pos. seq. counterpart is augmented.

Finally, the MMC–HVdc internal variables were drawn for the grid–forming mode under consideration of balanced and unbalanced grid conditions. It was demonstrated that the MMC–HVdc responds satisfactorily to both balanced and unbalanced conditions with the proposed control scheme. It was highlighted that, in the grid–forming application under unbalanced faults, the arm capacitor voltages do not face higher variations than during normal operation. Even the provision of rated current in the faulted phases keeps the arm capacitor voltages inside the expected limits.

This chapter presented the simulation results on the operation of a passive offshore grid. When the WTs are connected and in operation, they draw their own FRT response. Therefore, Chapter 6 covers the FRT response of the WTs in combination with the control methods proposed in this chapter.

6 Fault ride through of the WTs during unbalanced faults

6.1 Introduction

In Chapter 5, a control method in symmetrical components for the grid-forming MMC–HVdc was proposed which is suitable for unbalanced faults in the offshore grid. The current contribution by the offshore VSC is augmented during unbalanced faults to utilize the full converter capability and facilitate the fault detection. The analysis was focused solely on the operation of a passive offshore grid without any contribution from the WT converters. When the WTs are in operation, their FRT strategy inherently influences the system behavior during unbalanced fault conditions.

In this chapter, four FRT strategies for the WTs in the offshore grid are compared and evaluated in terms of fault and post-fault performance. The strategies differ in their implementation regarding the voltage support in symmetrical components and/or OM limitation.

This chapter aims to provide:

- synthesis and proposition of FRT strategies for the WT converters regarding unbalanced faults in the offshore grid;
- analysis and comparison of the fault and post-fault performance of the FRT strategies;
- and investigation on the overall system performance with the grid-forming MMC–HVdc.

6.1.1 Related publications

The main work described in this chapter was published in:

- K. Schönleber, E. Prieto-Araujo, S. Ratés-Palau, O. Gomis-Bellmunt, Handling of unbalanced faults in HVDC-connected wind power plants, *Electr. Power Syst. Res.* 152 (2017) 148–159.
doi:10.1016/j.epsr.2017.06.026.

A part of the work was submitted to *IEEE Transactions on Power Delivery*.

6.2 Methodology

The system behavior is analyzed by means of transient simulations in the time domain. The models are developed in MATLAB Simulink/SimPowerSystems. The used discrete sample time for the simulation is $T_s = 25 \mu\text{s}$.

Converter control in symmetrical components for the grid-connected application was reviewed in Section 2.2.1. The described controllers in symmetrical components and specifically the CC with a decoupling network based on the reference and error signals as depicted in Fig. 2.8 are used for the WT converters. The grid-forming offshore VSC-HVdc is set up with the proposed control method from Chapter 5.

In the following, three main challenges are commented: implementation of the pos. and neg. seq. phase angle detection by means of a DDSRF-PLL, voltage sag sensing during unbalanced faults and the appearance/reduction of OM in such conditions. Then, four FRT concepts or so-called reference calculation (RC) strategies are introduced to cope and ride through unbalanced faults in the offshore grid with the WT converters.

6.2.1 DDSRF implementation

The phase angles in the pos. and neg. seq. are obtained through a decoupled double synchronous reference frame (DDSRF) system. The diagram of the DDSRF-PLL is sketched in Fig. 6.1. As highlighted in Section 2.2.1, the neg. seq. phase angle is aligned to the respective voltage vector which is challenging for very low magnitudes [119]. In this thesis, the solution

for this is proposed as follows: for a magnitude smaller than 0.05 p.u., the neg. seq. phase angle is set to $\theta_2^g = -\theta_1^g$; otherwise the neg. seq. phase angle is locked by the mentioned PLL. A hysteresis characteristic on the neg. seq. voltage magnitude avoids toggling for the neg. seq. phase angle. The hysteresis is applied on U_2^g and switches between the two states with a lower boundary of 0.05 p.u. and an upper boundary of 0.2 p.u.. The nominal frequency $f_{\text{nom}} = 50 \text{ Hz}$ is fed-forward through the angular frequency of $\omega_{\text{nom}} = 2\pi f_{\text{nom}}$ in the DDSRF-PLL.

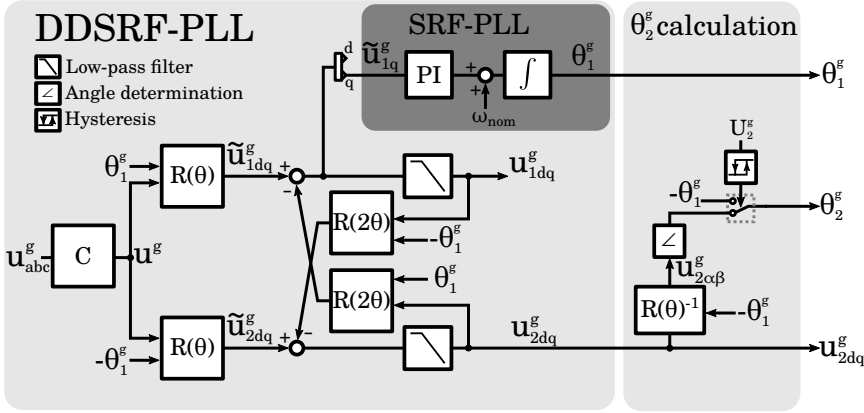


Figure 6.1: DDSRF-PLL implementation and neg. seq. phase angle determination. \mathbf{C} is the Clarke-transformation, whereas $\mathbf{R}(\theta)$ rotates the input vector by θ (refer to Appendix A.1).

6.2.2 Voltage sag detection

The voltage sag detection signal might activate the respective FRT behavior of the WT converter. To track the magnitudes of the three phase voltages and possible deviation of one phase voltage from the predefined continuous voltage band, independent single-phase PLLs might be used. Nevertheless, the DDSRF-PLL is already implemented for the phase angle tracking. Therefore, the magnitudes of the seq. components are obtained as $U_1^g = \sqrt{u_{1d}^{g2} + u_{1q}^{g2}}$ and $U_2^g = \sqrt{u_{2d}^{g2} + u_{2q}^{g2}}$. The phase magnitudes U_a^g , U_b^g , and U_c^g might be calculated from the seq. components U_1^g , U_2^g and the respective angles ϕ_1^g , ϕ_2^g through Eqn. (6.1) like the calculation of the current magnitudes in

Eqn. (5.9).

$$\begin{cases} U_a^g = \sqrt{U_1^{g2} + U_2^{g2} + 2U_1^g U_2^g \cos(\phi_2^g - \phi_1^g)} \\ U_b^g = \sqrt{U_1^{g2} + U_2^{g2} + 2U_1^g U_2^g \cos(\phi_2^g - \phi_1^g + \frac{4\pi}{3})} \\ U_c^g = \sqrt{U_1^{g2} + U_2^{g2} + 2U_1^g U_2^g \cos(\phi_2^g - \phi_1^g - \frac{4\pi}{3})} \end{cases} \quad (6.1)$$

The full information of a sine wave is available within one quarter of the fundamental cycle. The waveforms change significantly at the respective start and end of a voltage event (transient after fault inception and ending). The described time range of one quarter of a grid cycle is valid for the sensing of the fault start, whereas the end of the fault after isolation of the faulted system might be more challenging as the system is affected by the dynamics during the fault. The power converter controls might introduce a post-fault transient although the fault is physically already cleared from the system. The use of the three to five grid cycles-long mean average filtered value of the measurement during the post-fault situation revealed a good performance to avoid toggling of the sag detection signal.

6.2.3 Active current limitation and reduction

Reactive currents might be prioritized during dynamic voltage support and therefore demand for an active current limitation [102]. Without immediate active power in-feed reduction by the WT, e.g. by torque or pitch control, an active current limitation of the GSC ultimately leads to an increase of the dc voltage. The dynamic braking resistor (dc chopper) in the dc link is a usual solution to dump the surplus energy. Contrary to active current limitation, active power reduction is referred to the desired operation of reducing active current fed to the grid, e.g. for active power scheduling, wake management, or de-rated operation due to environmental conditions.

6.2.4 Current and voltage limitations

The controller design and reference calculation should prevent current and voltage references exceeding the converter capability and might unnecessarily trigger the internal converter/semiconductor protection.

For the current limitation in the DSRF in symmetrical components, there are four components which constitute the three phase currents: i_{1d} , i_{1q} , i_{2d} , and i_{2q} . If the neg. seq. magnitude I_2 is zero, the pos. seq. magnitude I_1 can be limited straightforward to the maximum current I^{\max} :

$$I_1 = \sqrt{i_{1d}^2 + i_{1q}^2} \leq I^{\max} \quad (6.2)$$

In case of unbalanced conditions, the simplest limitation is made for the pos. and neg. seq. components by:

$$I_1 + I_2 \leq I^{\max} \quad (6.3)$$

Equation (6.3) might be too strict in dependence of the seq. angle difference and the full capability of the WT converter can be reached by calculating the phase currents expressed by Eqn. (5.9). Thus, the current limitation for the grid-connected converter using symmetrical components foresees the same saturation concept as the normal saturation method described for the grid-forming converter in Chapter 5.

In terms of voltage, the maximum applied voltage at the ac terminals of a VSC is limited by the available dc link voltage [121]:

$$U_k^{c,\text{ref}} \leq m_k \frac{u_{\text{dc}}}{2} \quad (6.4)$$

where:

- $U_k^{c,\text{ref}}$ = applied ac voltage magnitude of the converter for phase k ;
- k = phase variable ($k \in \{a, b, c\}$);
- m_k = modulation index for phase k .

The linear region is defined for $m_k \leq 1$, whereas for $m_k > 1$ the fundamental voltage does not increase linearly and OM occurs. Third harmonic injection allows an increase of the modulation index barrier m_{bar} to $\frac{2}{\sqrt{3}} \approx 1.154$. An over-modulated applied voltage waveform contains harmonics of even order [121]. OM might also occur in a MMC as the dc voltage is defined by the voltage sum of the inserted SMs [refer to Eqn. (2.14)]. Thus, the ac voltage limitation as described in Eqn. (6.4) might occur in a MMC like a conventional VSC.

The total harmonic distortion (THD) in % is defined by:

$$\text{THD} = \sqrt{\frac{1}{U_{1h}^2} \sum_{n=2}^N U_{nh}^2} \cdot 100 \quad (6.5)$$

where:

U_{1h} = magnitude of fundamental voltage;

U_{nh} = magnitude of n -th harmonic voltage;

N = the highest harmonic order under consideration.

Figure 6.2a shows the applied VSC phase voltage $U_k^{c,\text{ref}}$ for $m_k = 1.0$, $m_k = 1.3$, and $m_k = 2.0$. Figure 6.2b plots the evolution of the THD of over-modulated signals up to $m_k = 2$ for two different modulation index barriers. For $U_k^{c,\text{ref}} \leq m_{\text{bar}}$ the THD is zero, whereas larger values cause an over-modulated signal with non-zero THD values. The highest output voltage of the fundamental can be reached with a square-wave waveform leading to a magnitude of $4/\pi \approx 1.273$ [121]. Nevertheless, the converter currents are then distorted as they result from the voltage drop between the distorted converter voltage and the grid voltage.

OM is undesired due to loss of controllability and waveform distortion. The avoidance of OM might be achieved through an appropriate converter design which allows an extensive continuous voltage range operation in the linear region. However, an over-specification of the converter voltage might increase the converter costs. To the author's knowledge, the active limitation of OM is not specified by actual GCs. Limited current references, regardless of whether according to Eqn. (5.9) or Eqn. (6.3), do not ensure that the applied voltages at the output of the current controllers are not affected by OM. Nevertheless, two possibilities arise to reduce OM:

- limitation of the applied converter voltage seq. components u_1^c and u_2^c (after the current controller),
- or current reference reduction of i_1^{ref} and i_2^{ref} (before the current controller).

It is obvious that the first option does not allow tracking of the original current references and leads to uncontrollability [according to Eqns. (2.8)

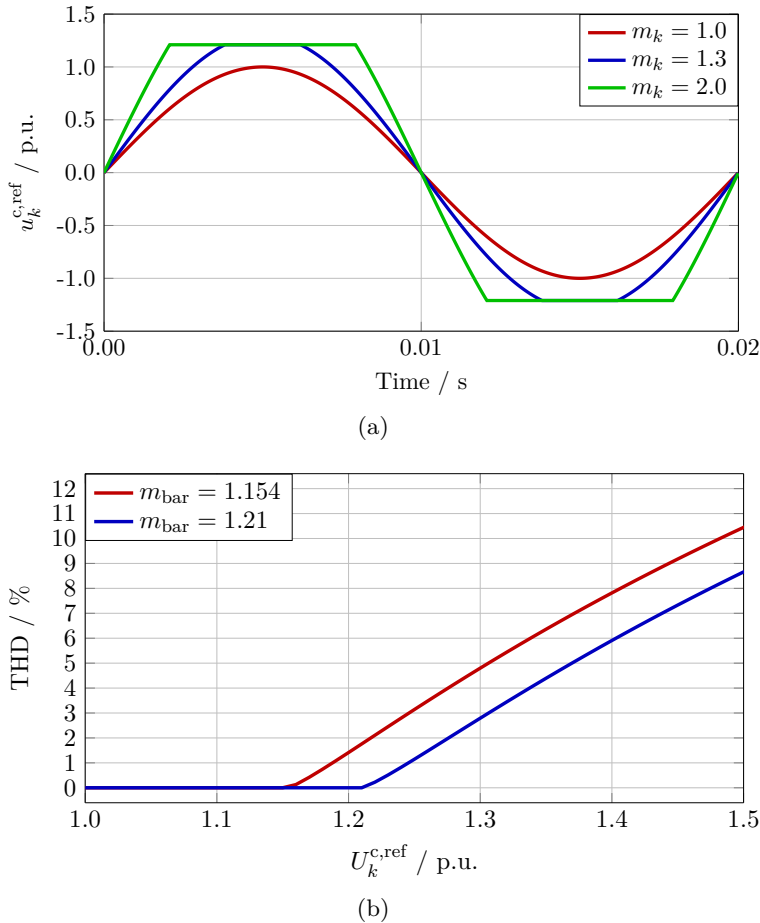


Figure 6.2: Impact of voltage limitation by converter OM on (a) applied voltage reference signal $u_k^{c,\text{ref}}$ and (b) THD.

and (2.9)]. The second option reduces either the reactive or active pos. seq. current reference to limit OM similar to [119]. Either the q -component (reactive current) or d -component (active current) references is reduced to zero, respectively, through a closed-loop controller detecting OM in the converter reference voltage $u^{c,\text{ref}}$.

6.2.5 Considered FRT strategies

Four WT converter current RCs are discussed in the following. These strategies have been selected based on their pre-qualification for the application in the offshore grid. It is known from onshore systems that the choice on active or reactive current prioritization for power converters during FRT depends on the nature of the connected grid and is generally defined in the respective GC. Active current generally sustains grid frequency, whereas reactive current supports grid voltage. For instance, islanded synchronous power systems, e.g. Ireland or UK, require active current prioritization because a possible frequency deviation due to a large active power generation drop might be more critical to the system stability than the eventual gain from voltage support [55]. On the other hand, strong synchronous power systems, e.g. Continental Europe, favorize reactive power prioritization because frequency deviations are not expected due to the strong interconnection and meshing. Reactive current is then utilized to support the voltage magnitude. For the isolated offshore grids without any SG connected, frequency deviations are obviously not linked to the rotating mass acceleration or braking of the SGs. Frequency is rather a control variable imposed by the offshore VSC-HVdc which might be changed through control action by the grid-forming converter. The conventional relation that a power generation/consumption imbalance causes a frequency deviation does not hold true. Frequency might be used as communication mechanism, for instance, for frequency-dependent active power reduction as commented in Section 2.4.2. Hence, FRT strategies for offshore grid faults might focus mainly on voltage support. Therefore, reactive currents are permanently prioritized over active current during the FRT for all strategies presented in the following. Other strategies were disqualified prior to the study due to their poor performance, e.g. no voltage support without OM limitation. To sum up, Tab. 6.3 concludes the characteristics of the considered strategies.

- I. RC strategy 1 (RC1): No dynamic voltage support and OM limitation on the active current.

The converter avoids any additional reactive currents and OM limitation is active through reduction of pos. seq. d -axis component (active

current). The short-term active power reduction might be buffered by the dc chopper. The neg. seq. current is controlled to zero.

- II. RC strategy 2 (RC2): Pos. seq. dynamic voltage support and control of neg. seq. current to zero.

Additional pos. seq. reactive current is applied according to Eqn. (2.15). The neg. seq. current is controlled to zero. The OM limitation control is not applied.

- III. RC strategy 3 (RC3): Pos. seq. dynamic voltage support and OM limitation on the reactive current.

The converter controls pos. and neg. seq., the latter to zero. Dynamic voltage support is applied according to Eqn. (2.15). OM limitation control is active and reduces the reactive current to lower the magnitude of the applied voltage. It counteracts the dynamic voltage support when OM appears.

- IV. RC strategy 4 (RC4): Pos. and neg. seq. dynamic voltage support.

The respective pos. and neg. seq. reactive current references, i_{1q} and i_{2q} , are altered by the additional references in Eqns. (2.15) and (2.16), respectively. The OM limitation control is inactive for this strategy.

Table 6.3: Characteristics of current reference calculations.

RC	Pos. seq. ctrl	Neg. seq. ctrl	OM limitation
RC1	No voltage support	Zero	Yes (active current)
RC2	Voltage support	Zero	No
RC3	Voltage support	Zero	Yes (reactive current)
RC4	Voltage support	Voltage support	No

In the case of dynamic voltage support, the scheme defined by Eqns. (2.15) to (2.16) is set with the default gains of [102]: RC1 $k_1 = k_2 = 0$; RC2 $k_1 = 2$, $k_2 = 0$; RC3 $k_1 = 2$, $k_2 = 0$; and RC4 $k_1 = k_2 = 2$. Furthermore, a voltage deadband of 0.1 p.u. in the neg. seq. controller is implemented to avoid neg.

seq. current injection outside fault transients and/or under an erroneous phase angle as emphasized in [119] (see also Section 2.2.1). The tolerance band in [102, Annex C] might allow the implementation of such a deadband.

6.3 Case study

A case study is set up to evaluate the performance of the four considered FRT strategies for unbalanced faults in the offshore grid. The WPPs are connected and in operation, denoted as network configuration II. The simulation model is built in Matlab/Simscape Power Systems for the HVdc-connected offshore grid system of 1.2 GW as shown in Fig. 6.3. Three WPPs link under different distances to the VSC-HVdc station. WPP1 is rated to 498 MW in 25 km distance, WPP2 represents 450 MW in 15 km and WPP3 injects 198 MW in 5 km. The WPPs are modeled with a respective aggregated WT converter average model (grid-side converter and wind-dependent power injection in the dc link), a lumped π -model of the collection grid cabling, the transformers, and the export cable system (distributed elements line model). The reactive power in the system is provided solely by the VSC during normal operation (prior and posterior to the fault).

For the first assessment, the offshore VSC-HVdc station is modeled as a controlled three-phase voltage source. The upper level control is implemented as indicated in Chapter 5 in symmetrical components with a separate VC and CC loop. For the second part of the study, the MMC-HVdc model according to Chapter 5 is used to verify its applicability. Relevant system parameters are listed in Tab. 6.4.

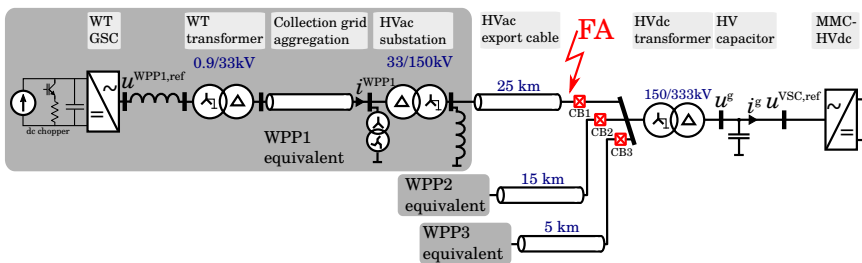


Figure 6.3: Electrical layout of the network configuration II (WPPs connected).

Table 6.4: Relevant parameter of the test system. Base power is $S_b = 1000$ MVA if referred, otherwise component power rating.

WPP and HV export grid	WPP1	WPP2	WPP3
Number of turbines	83	75	33
WT conv. rating (S/MVA , U_{ac}/kV)		6.7, 0.9	
OM limitation of $u^{\text{WPP,ref}}$ ($m_{\text{bar}}/\text{p.u.}$)		1.21	
WT conv. coupling impedance ($z/\text{p.u.}$)		$0.01 + j0.05$	
WT transformer impedance ($z/\text{p.u.}$)		$0.01 + j0.06$	
Collection grid voltage (U_{ac}/kV)		33	
WPP grid impedance ($z/\text{p.u.}$) ¹	$0.018 + j0.035$	$0.014 + j0.023$	$0.025 + j0.041$
WPP grid shunt reactance ($x/\text{p.u.}$) ¹	0.011	0.009	0.003
WPP transformer impedance ($z/\text{p.u.}$)		$0.003 + j0.15$	
Export grid voltage (U_{ac}/kV)		150	
Export cable compensation (Q_r/Mvar)	50.5	30.9	4.0
Export cables impedance ($z/\text{p.u.}$) ¹	$0.13 + j0.40$	$0.08 + j0.24$	$0.01 + j0.03$
Export shunt reactance ($x/\text{p.u.}$) ¹	0.025	0.041	0.597
VSC–HVdc			
Rating (S/MVA , U_{ac}/kV , U_{dc}/kV)	1333.3, 333, ± 320		
Transformer impedance ($z/\text{p.u.}$)	$0.003 + j0.150$		
Coupling impedance ($z/\text{p.u.}$)	$0.010 + j0.120$		
Filter capacitance ($C^c/\mu\text{F}$)	4.14		
OM limitation of $u^{\text{VSC,ref}}$ ($m_{\text{bar}}/\text{p.u.}$)	1.3		
PI controllers			
Time constants WT conv. dc VC, CC (τ/ms)	3.2, 0.4		
WT OM limitation (K_{OMP} , K_{OMi})	2, 200		
WT CC feed–forward LPF bandwidth (rad s^{-1})	40		
Time constants VSC–HVdc VC, CC (τ/ms)	1.2, 0.4		

¹ Base power S_b applies.

6.4 Results

First, the four FRT strategies are compared for the faults at the 150 kV busbar for network configuration II. For the sake of simplicity, two temporary faults are considered for a duration of $t_f = 250$ ms each at FA. Circuit breaker triggering and protection algorithms are out of scope. A LL fault with a fault resistance of $R_{LL} = 2$ m Ω between phase a and b as well as a SLG fault with a total fault resistance of $R_{SLG} = 2$ Ω between phase a and ground are applied. Prior to the faults, the system is operating at full power. In the second part of the results, the best RC strategy from the first assessment is evaluated for different faults and saturation methods using the MMC–HVdc model of Chapter 5 instead of the three–phase voltage source.

6.4.1 Comparison of the FRT strategies

Figures 6.4 to 6.6 plot voltages and currents for the considered strategies in the time window of interest for the LL fault. Figures 6.6 to 6.8 display the results for the SLG fault. The FRT strategies are arranged column–wise, whereas each row exhibits a different variable.

6.4.1.1 LL fault at 150 kV

Row 1 of Fig. 6.4 shows the three–phase voltage u^g at the PCC busbar (according to Fig. 6.3). The values are 1.0 p.u. during pre–fault conditions and return to this value after the fault. Due to the delta–star configuration of the converter transformer, the PCC voltages have the shape of a SLG fault. The voltage magnitude differs: two phase voltages increase transiently up to 1.45 p.u. for RC2 and RC3, whereas it stays below 1.3 p.u. for RC1. The plot of strategy RC4 peaks below 1.3 p.u.. The post–fault recovery (starting from $t = 0.25$ s) indicates the fastest return to balanced voltages by RC1 and RC4 and slightly slower responses for RC2 and RC3. The applied voltages at the converter of WPP1 and the VSC–HVdc are illustrated in row 2 and 3, respectively. These voltages are subject to their inherent converter limitations (e.g. designed voltage limitation whose exceedance causes OM). Row 4 of Fig. 6.4 depicts the seq. magnitudes of the voltages at the LV terminals of WPP1 converter. The voltage magnitudes for RC1 are lower

during the fault than for the other strategies. For RC2 and RC3, harmonic oscillation can be observed during the fault which are inherently caused by the OM. The OM limitation in RC3 results in an improvement. For RC4, the neg. seq. voltage magnitude at the WPP1 terminals is lowered through neg. seq. voltage support.

The qualitative effect of OM might be analyzed by the zoomed plots in Fig. 6.5 (row 1 and 2) detailing the shape of the applied voltage around $t = 0.22$ s. For the WPP1 converter, OM occurs for RC2, RC3, and RC4. However, the largest OM happens for RC2 and RC3 where phase b and c are almost square waveforms. The VSC–HVdc is also subject to OM, in particular for RC2, RC3, and RC4. No OM appears for RC1 (both converters). In Fig. 6.5, rows 3 and 4, the three–phase modulation indexes of the WPP1 converter $m_k^{\text{WPP1,ref}}$ and the VSC–HVdc $m_k^{\text{VSC,ref}}$ are depicted. Moreover, the modulation index barrier m_{bar} is sketched as a horizontal line at 1.21 for the WPP1 and 1.3 for the VSC–HVdc, respectively. It can be observed that the RCs relying on pos. seq. voltage support (RC2 and RC3) face higher modulation indexes and thus OM which is in line with the observed over–voltages in the respective phases.

Figure 6.6 displays converter–related results for the LL fault. Row 1 and 2 plot the dq –components of pos. and neg. seq. current measurements i_{1d} , i_{1q} , i_{2d} , and i_{2q} for WPP1 and VSC–HVdc, respectively. For RC1 and RC4, the active current injection i_{1d} demonstrates a significant reduction during the fault to around 0.0 p.u. and 0.5 p.u., respectively. For RC1, this is due to the OM limitation control on active current. For RC4, the q –components in both sequences have priority during the fault and force the limitation of active power. Row 3 depicts the three–phase currents from the WPP1 converter. It underlines that the current injection differs significantly: for RC1 the current injection is reduced during the fault, whereas for RC2 and RC3 balanced currents are injected. For RC4, the neg. seq. voltage support leads to the injection of unbalanced currents. Row 4 displays the WPP1 converter dc voltage. It is obvious that for all strategies the increase in dc voltage leads to a subsequent triggering of the dc chopper. The waveforms of RC2 and RC3 show the typical double fundamental frequency affected dc voltage ripple during the unbalanced faults. For RC1 and RC4, the active

current limitation and subsequent permanent dc chopper activation revokes this oscillation.

Table 6.5 summarizes the mean THDs of applied converter voltages and currents at fault location. The THD values are calculated as the average of the three phases over two grid cycles and 200 ms after the respective fault inception. The values are rather indicative as the concept of THD is usually applied to steady-state values and not evaluated during faults. Nevertheless, the results related to the LL fault demonstrate low values for RC1 and RC4, as expected, higher values for RC3, and the highest for RC2. It should be mentioned that a distortion in the applied converter voltage obviously causes a distortion in the injected current.

Table 6.5: Indicative mean THDs of three-phase values: Applied voltages at the VSCs ($u_{abc}^{\text{WPP1,ref}}$, $u_{abc}^{\text{VSC,ref}}$) and fault currents ($i_{\text{FA}}^{\text{WPP1}}$, $i_{\text{FA}}^{\text{VSC}}$) for LL and SLG fault in %.

Variable		LL				SLG			
		RC1	RC2	RC3	RC4	RC1	RC2	RC3	RC4
$u^{\text{c,ref}}$	WPP1	1.2	22.7	17.5	1.2	1.2	8.4	9.1	4.5
	VSC	1.2	11.3	11.6	1.2	2.8	6.7	7.8	3.8
i_{FA}^1	WPP1	8.5	21.2	12.1	2.6	3.8	5.0	8.3	6.0
	VSC	2.8	6.7	7.8	3.8	1.8	3.5	8.5	5.8

¹ Fault current coming from WPP1 and VSC at location FA, respectively.

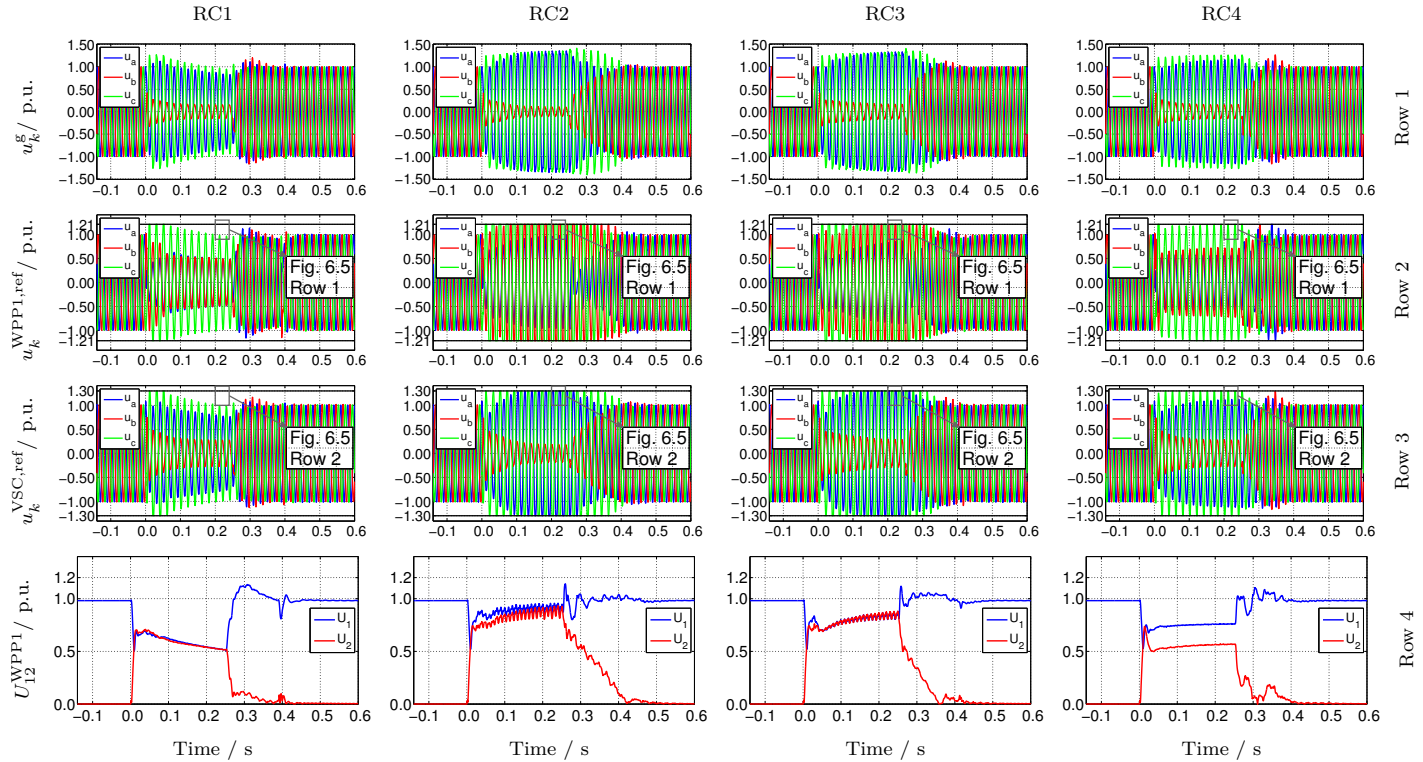


Figure 6.4: Grid-related results for the LL fault. Plots are ordered column-wise by strategy RC1 to RC4, and row-wise by grid voltage, applied voltage at WPP1, applied voltage at VSC-HVdc, and voltage magnitudes in symmetrical components at WPP1, in respective order.

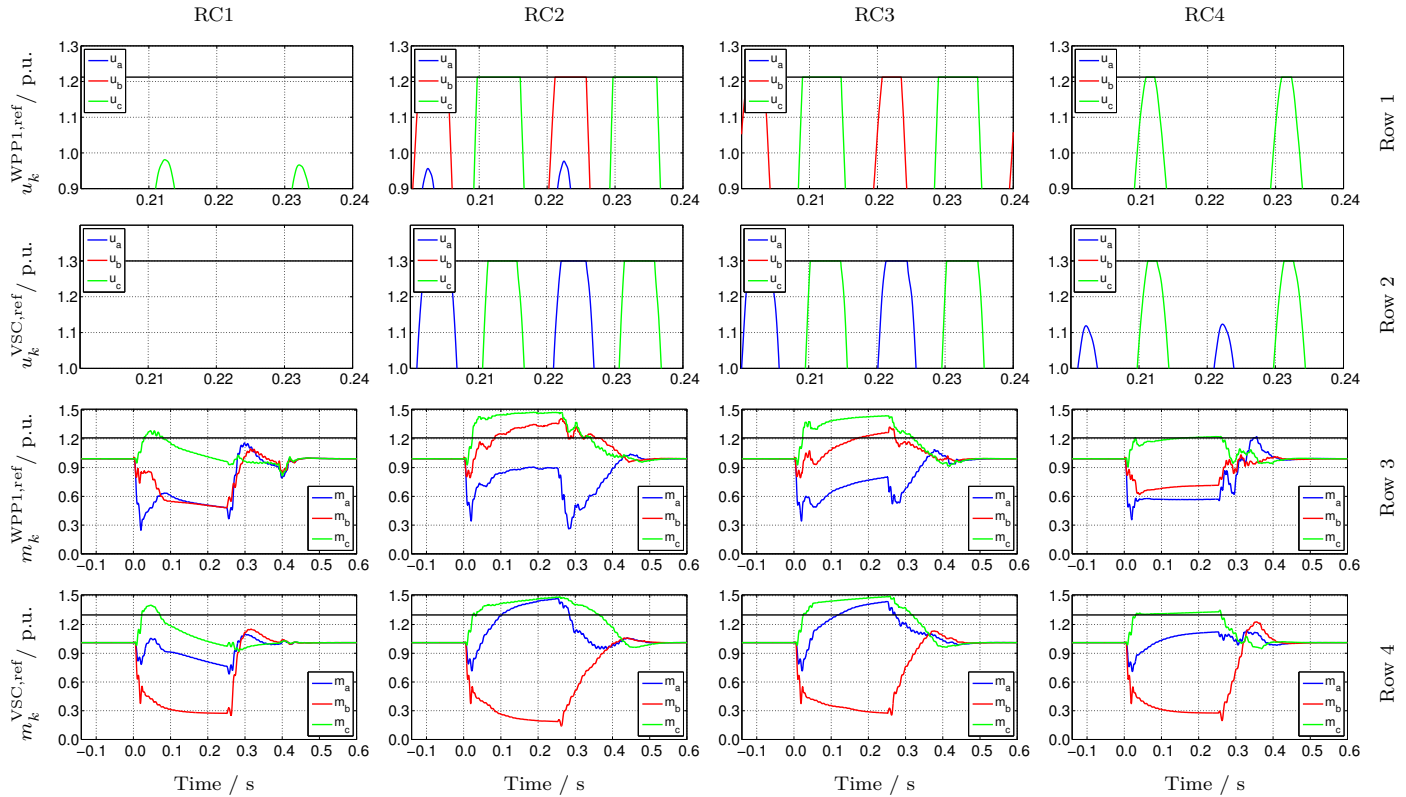


Figure 6.5: Detailed results for the LL fault. Plots are ordered column-wise by strategy RC1 to RC4, and row-wise by zoomed time ranges of applied voltage at WPP1 and at VSC-HVdc, and three-phase modulation indexes of WPP1 converter and VSC-HVdc, in respective order.

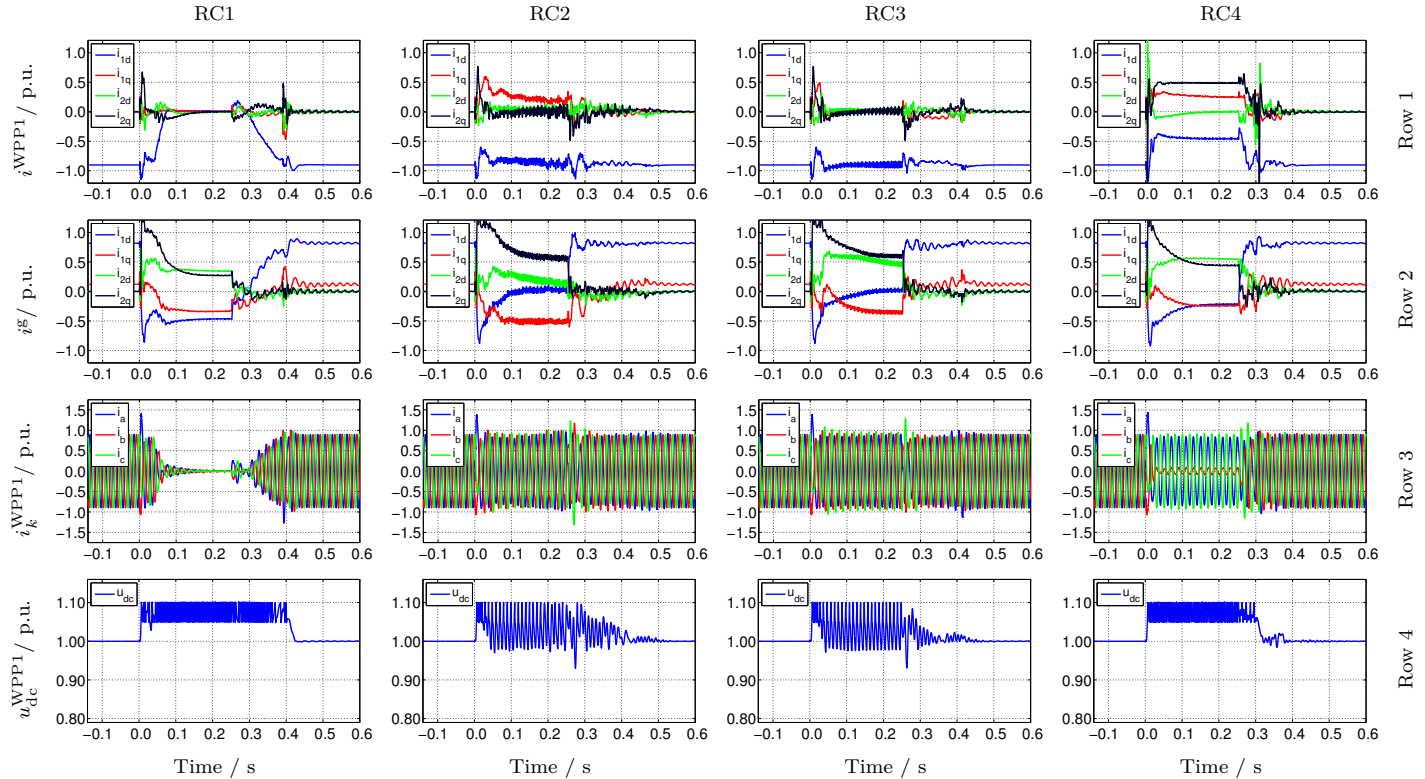


Figure 6.6: Converter-related for the LL fault. Plots are ordered column-wise by strategy RC1 to RC4, and row-wise by dq -components of seq. currents injected by WPP1 and VSC-HVdc, the three-phase current by WPP1, and the WPP1 converter dc voltage, in respective order.

6.4.1.2 SLG fault at 150 kV

The SLG fault results are presented in Figs. 6.7 to 6.9 following the similar scheme as the LL fault. In row 1 of Fig. 6.7, the voltage waveforms at the PCC busbar u^g demonstrate comparable results for all RC strategies. However, the values of RC1 show the fastest post-fault recovery. The applied voltages (of the WPP1 converter and the VSC–HVdc), in row 2 and 3 of Fig. 6.7 and row 1 and 2 of Fig. 6.8, are not affected by OM for RC1. For RC2 and RC3, OM occurs in at least one phase voltage for both WPP1 converter and VSC–HVdc due to over-voltage. The VSC–HVdc voltage corresponding to RC4 represents slight OM. The qualitative assessment can be complemented by the indicative THD values outlined in Tab. 6.5. For instance, during the faults for the WPP1 converter, the value is the highest for RC2 and RC3, whereas RC4 and RC1 follow in respective order. In row 4 of Fig. 6.7, the seq. voltage magnitudes at the LV terminals of WPP1 are visualized. It can be highlighted that both pos. and neg. seq. magnitudes are lowered for RC1. For RC2 and RC3, the magnitudes measured face oscillations due to the converters operating in OM. The neg. seq. magnitude reduction can be observed for RC4, whereas the pos. seq. magnitude is kept at a higher level than RC1.

To reiterate how the applied voltages are affected by OM, the modulation indexes of the WPP1 converter and VSC–HVdc are outlined in row 3 and 4 of Fig. 6.8. It can be concluded that significant OM occurs only for RC2 and RC3, whereas the results for RC4 demonstrate slight OM for the VSC–HVdc. For RC1, the OM limitation control on active current successfully omits the WPP converter to operate in the OM area. For strategy RC4, the FRT scheme with pos. seq. voltage support and neg. seq. voltage reduction allows the modulation indexes to be kept below the defined barrier m_{bar} .

Row 1 and 2 of Fig. 6.9 illustrate the pos. and neg. seq. current measurements in the SRF for WPP1 i^{WPP1} and VSC–HVdc i^g , respectively. For RC2 and RC3, the i_{1q} is 0.1 p.u. and zero, respectively. For the strategies RC1, RC2, and RC3, the WPP1 converter achieves the injection of almost balanced currents due to control of i_2 -components to zero. The reason is that the applied voltage is successfully adjusted without causing a (significant) OM. It can be noticed that the WPP1 converter absorbs neg. seq. current

of 0.5 p.u. for RC4 during the fault leading also to a reduction of the pos. seq. headroom. The VSC–HVdc injects i_{1q} during the fault for RC1 and RC2 (that means it absorbs reactive power generated by the WPPs and the collection grid). In contrast, the active current reduces below zero. The neg. seq. support is clearly visible by the non-zero components i_{2d} and i_{2q} . This indicates that the converter is injecting actively i_2 components to balance the PCC voltage. Row 3 of Fig. 6.9 depicts the three-phase current injection by the WPP1 converter which underlines the balanced currents for RC1, RC2, and RC3 and the grid support with unbalanced currents when applying RC4. Row 4 of Fig. 6.9 displays the dc voltage of the WPP1 converter and draws similar results as during the LL fault. The dc chopper operates continuously during the fault when active current is limited (RC1 and RC4), whereas the dc voltage unveils the known double fundamental frequency oscillations during the unbalanced faults. This is visible for the strategies RC2 and RC3, where active current is barely limited.

6.4.1.3 Discussion

To conclude briefly on the presented analysis of the four FRT strategies, an advantage was demonstrated from combined pos. and neg. seq. voltage control (RC4) as well as simply no voltage support with OM limitation on active current (RC1). The use of only pos. seq. support leads to more significant OM and consequently harmonics (RC2) or higher phase voltages even in healthy phases (RC3). The results for RC1 and RC4 exhibit that both strategies provide a good fault response. However, when strategy RC1 is chosen there is a low or even no short-circuit current flowing from the WPP-side which might lead to problems for protection measures. From an overall perspective, under consideration of the fault currents, over-voltages, and OM, RC4 provides the best results. Likewise, the active current reduction by RC1 leads to lower over-voltages than RC4. Therefore, for the detailed analysis of FRT with connected WPPs and the MMC–HVdc, it is proposed to deploy strategy RC4 with higher gains $k_1 = k_2 = 6$. The increased gains in combination with reactive current priority lead to a stricter limitation of active current during the fault. Compared to RC1, the injected fault currents from the WPPs might enhance fault detection.

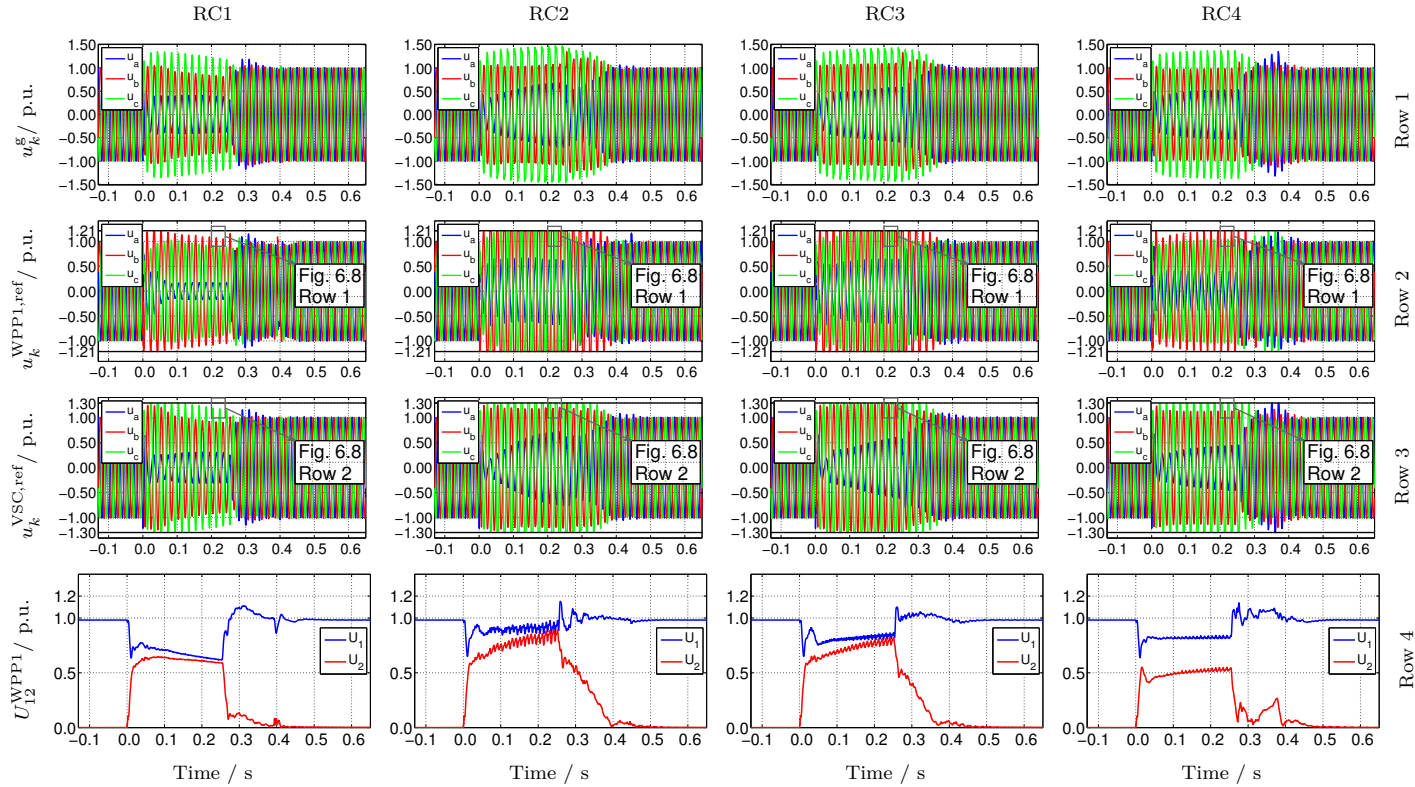


Figure 6.7: Grid-related results for the SLG fault. Plots are ordered column-wise by strategy RC1 to RC4, and row-wise by grid voltage, applied voltage at WPP1, applied voltage at VSC-HVdc, and voltage magnitudes in symmetrical components at WPP1, in respective order.

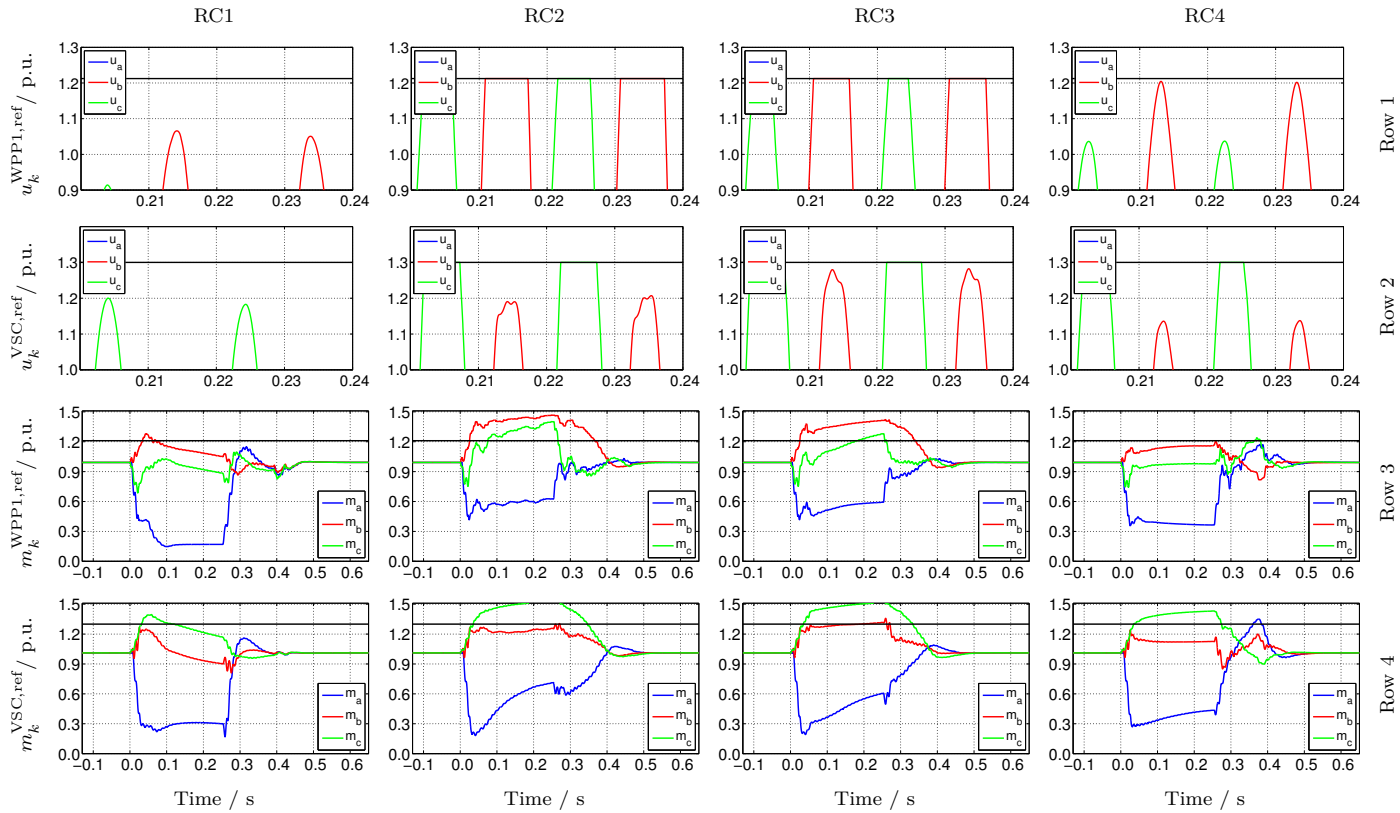


Figure 6.8: Detailed results for the SLG fault. Plots are ordered column-wise by strategy RC1 to RC4, and row-wise by zoomed time ranges of applied voltage at WPP1 and at VSC-HVdc, and three-phase modulation indexes of WPP1 converter and VSC-HVdc, in respective order.

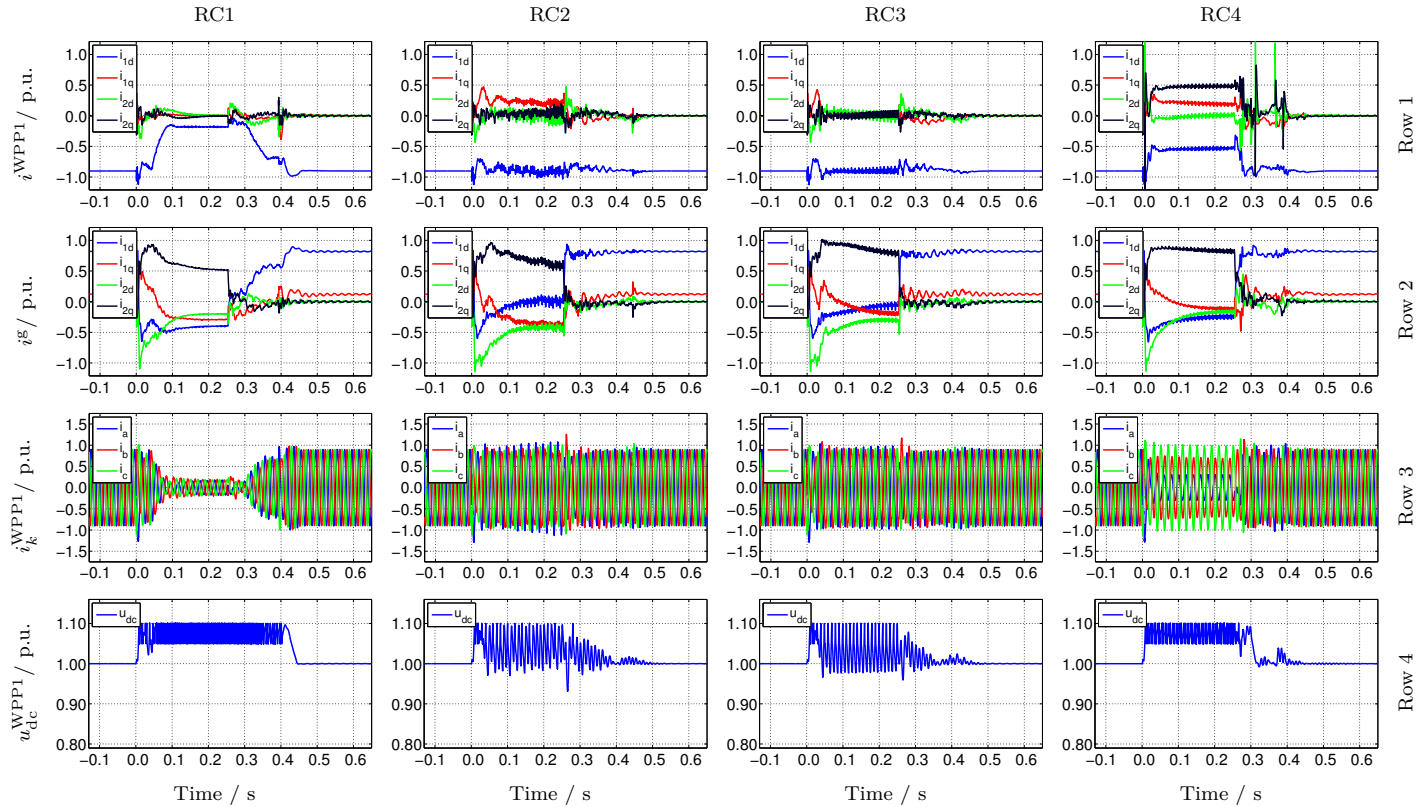


Figure 6.9: Converter-related for the SLG fault. Plots are ordered column-wise by strategy RC1 to RC4, and row-wise by dq -components of seq. currents injected by WPP1 and VSC-HVdc, the three-phase current by WPP1, and the WPP1 converter dc voltage, in respective order.

6.4.2 FRT and impact on the offshore MMC–HVdc

The results for the FRT behavior of the LLLG, LL, and SLG fault under prior nominal power operation with the MMC–HVdc (network configuration II) are outlined in the Figs. 6.10 to 6.12. As mentioned in the previous discussion, strategy RC4 is now deployed with gains of $k_1 = k_2 = 6$. Instead of controlled three-phase voltage sources, the MMC–HVdc model from Chapter 5 is used. In principle, it is expected that the ac side of the MMC behaves equal to the controlled three-phase voltage sources but in addition the internal variations of energy, current, and voltage of the MMC–HVdc might be explored. For the SLG fault, the normal and extended saturation method introduced in Chapter 5 are analyzed. The limitations on OM are relaxed in comparison to the previous analysis to avoid the harmonic oscillations during over-voltages ($m_{\text{bar}}^{\text{WPP}} = m_{\text{bar}}^{\text{VSC}} = 1.5$). It must be noticed that the parameters of the MMC–HVdc are set to the ones listed in Tab. 5.5. This implies slightly larger time constants for the VC and CC compared to the previous analysis. Regarding the faults themselves, the duration is changed to $t_f = 0.5$ s for ease of a better visualization. Likewise, permanent faults are simulated which lead to a disconnection of the faulted WPP, in that case WPP1. Note that zoomed plots with a higher time resolution of specific three-phase signals (grid currents, grid voltages, inner currents, arm currents, and arm voltages) are displayed in Fig. 6.12.

6.4.2.1 Normal saturation method for LLLG and LL faults

First, column 1 to 2 of Figs. 6.10 to 6.12 are contemplated. These columns present the results of the LLLG and LL fault under usage of the normal saturation method by the MMC–HVdc. As a reminder, the extended saturation is not applicable for the voltage conditions caused by the LLLG and LL fault. For the SLG fault, the results for the normal and extended saturation are displayed in column 3 and 4, respectively.

Row 1 to 5 of Fig. 6.10 present grid currents i^g , grid voltages u^g , and voltage magnitudes of symmetrical components at VSC–HVdc U_{12}^g , and WPP2 converter currents i^{WPP2} and voltages U_{12}^{WPP2} . WPP2 has been chosen for visualization because WPP1 disconnects after the fault and therefore neglects the post-fault behavior. For the LLLG fault, it can be deduced that

the grid voltage drops, whereas the converters supply maximum balanced currents according to their FRT behavior. Here, the WPPs inject reactive currents according to RC4 with a gain of $k_1 = 6$ and the VSC–HVdc reaches its maximum current injection with the normal saturation method. Neg. seq. voltage components occur only during short transient periods at fault inception and ending. After the fault ending, the limited active current is quickly ramped up to the pre–fault value. For the LL fault, the converter currents reach their maximum value after the fault inception and both WPPs and offshore VSC inject unbalanced currents into the offshore grid. Over–voltages in the offshore grid voltage are avoided due to the grid support by the WPPs on the one side and to the reduction of active current on the other side. This might be directly observed when comparing the grid voltage profile of the LL fault with the results in row 1 of Fig. 6.4. Furthermore, the magnitudes for the seq. components at WPP1 are equal for the pos. seq. and halved for the neg. seq. compared to RC1 of the previous analysis.

Figure 6.11 presents the internal results of the MMC–HVdc. Row 1 and 2 display the inner currents i^{sum} and the upper arm currents i_{kU} . Their respective values are kept within reasonable range during the fault duration compared to the normal full load operation prior to the fault. From the LLLG results, it can be deduced that the inner currents are reduced to almost zero during the fault. That behavior is expected because the converter does not experience a horizontal energy deviation (balanced conditions), row 5, and the injected current is almost purely reactive. The vertical energy deviation (row 4, E_{UL}) is caused by the individual phase voltage and current magnitudes at fault inception. The offset is sustained during the fault as the vertical energy balancing is switched off. In row 3, it can be seen that consequently the upper arm capacitor voltages u_{kU}^a remain with a dc offset during the fault and are rebalanced afterwards.

For the LL fault, the results of the MMC–HVdc internal variables reveal that the vertical balancing regulates the energies instantaneous after fault inception. This can be deduced from the short transient with 50 Hz component of i^{sum} in row 1 and the vertical energy deviation E_{UL} in row 4. Besides that, the sustained horizontal energy unbalance can be concluded from the unequal dc offset of the three phases for the inner current and the

unbalanced arm currents i_{kU} and arm capacitor voltages u_{kU}^a (only the upper arm is displayed). To sum up, the MMC–HVdc can successfully handle both faults described and the strategy RC4 with higher gains avoids consequently over–voltages in the offshore grid.

6.4.2.2 Extended and normal saturation method for SLG fault

In column 3 and 4 of Figs. 6.10 and 6.11, the results for the SLG fault under usage of the normal or extended saturation method are depicted. Row 1 and 2 of Fig. 6.10 display the grid currents and voltages, respectively. During the fault, the grid voltage profile depends on the current injection of the VSC–HVdc (depicted in row 1) and the WPP converters (WPP2 current injection is drawn in row 4). Regardless of the saturation method, over–voltages are avoided using the strategy RC4 with higher gains than in the previous analysis (refer to Fig. 6.7, column RC4, row 1). As can be seen from the three–phase voltage results, the extended saturation method leads to an increased balance of the voltages. This observation might be supported by the grid voltage magnitude results shown for pos. and neg. seq. in row 3. The increase of the pos. seq. of 0.23 p.u. and the reduction by 0.11 p.u. of the neg. seq. voltage magnitude is achieved through the application of the extended saturation compared to the results of the normal saturation.

Rows 4 and 5 reveal the pos. and neg. seq. voltages at the WPP2 converter terminals u^{WPP2} as well as the converter currents of WPP2 i^{WPP2} , respectively. As a difference between the saturation methods, it might be highlighted that the extended method causes an increase of 0.11 p.u. for the pos. seq. voltage magnitude u^{WPP2} . The neg. seq. component is slightly augmented by 0.04 p.u.. The WPP2 converter current i^{WPP2} contains neg. seq. for both saturation methods and is limited phase–wise to the maximum current of 1 p.u.. During the fault, the reactive currents in pos. and neg. seq. required by the FRT strategy lead to a reduction of the active current. After the fault, balanced currents are injected as the WPPs terminate the voltage support and recover their active current provision. At WPP level, the effect is less pronounced which is displayed in row 5. Besides that, it must be noted that the extended saturation method leads to a more determined response with a shorter transient period to reach steady–state values during the fault.

The rows 1 to 5 of Fig. 6.11 display the inner currents i_k^{sum} , upper arm currents i_{kU} , upper arm capacitor voltages u_{kU}^a , and internal energy variations of the MMC–HVdc in vertical and horizontal direction, E_{UL} , E_{ab} , and E_{ac} , respectively. From row 1, it might be observed that for both saturation principles the inner currents i_k^{sum} are similarly affected by the vertical balancing activity instantaneously after the fault inception (refer also to row 3 of Fig. 6.12). The initial oscillations are caused by periodic enabling and disabling of the vertical balancing components of the inner current due to the condition on the difference of the pos. and neg. seq. converter voltage magnitudes. However, for the extended saturation the vertical energy is balanced faster (50 Hz oscillation ceases). During the continuation of the fault, the dc component of i_k^{sum} of phase a and c is higher for the extended saturation due to the increased converter capability utilization. For the upper arm currents i_{kU} (row 2), it can be seen that the initial transient is considerably shorter for the extended saturation. The commented increase of the dc component of i_k^{sum} for the extended saturation method results in sustained higher peak values of the arm currents. It should be mentioned that the arm currents stay within 0.61 p.u. of the ac base current which is comparable to the nominal conditions prior to the fault. Row 3 reveals the upper arm capacitor voltage u_{kU}^a which exhibit the unbalanced conditions of the asymmetrical power exchange during the fault. The rows 4 and 5 depict the energy regulation in vertical and horizontal direction which performs adequately. The vertical energy is regulated around 0.1 s faster for the extended saturation than for the normal saturation.

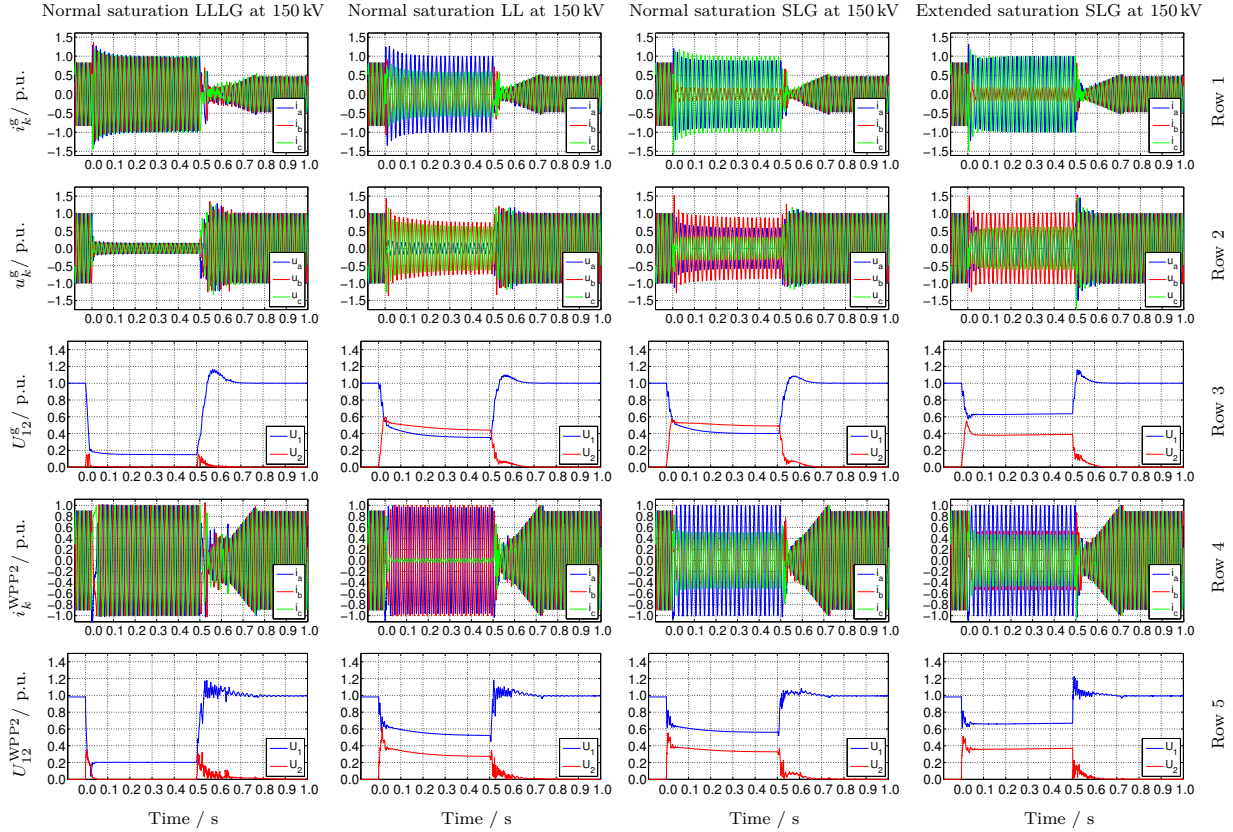


Figure 6.10: Grid-related results for network configuration II. Plots are ordered column-wise by different faults, and row-wise by grid current, grid voltage, and voltage magnitudes of symmetrical components at VSC-HVdc, converter current and WPP2 voltage magnitudes of symmetrical components, respectively.

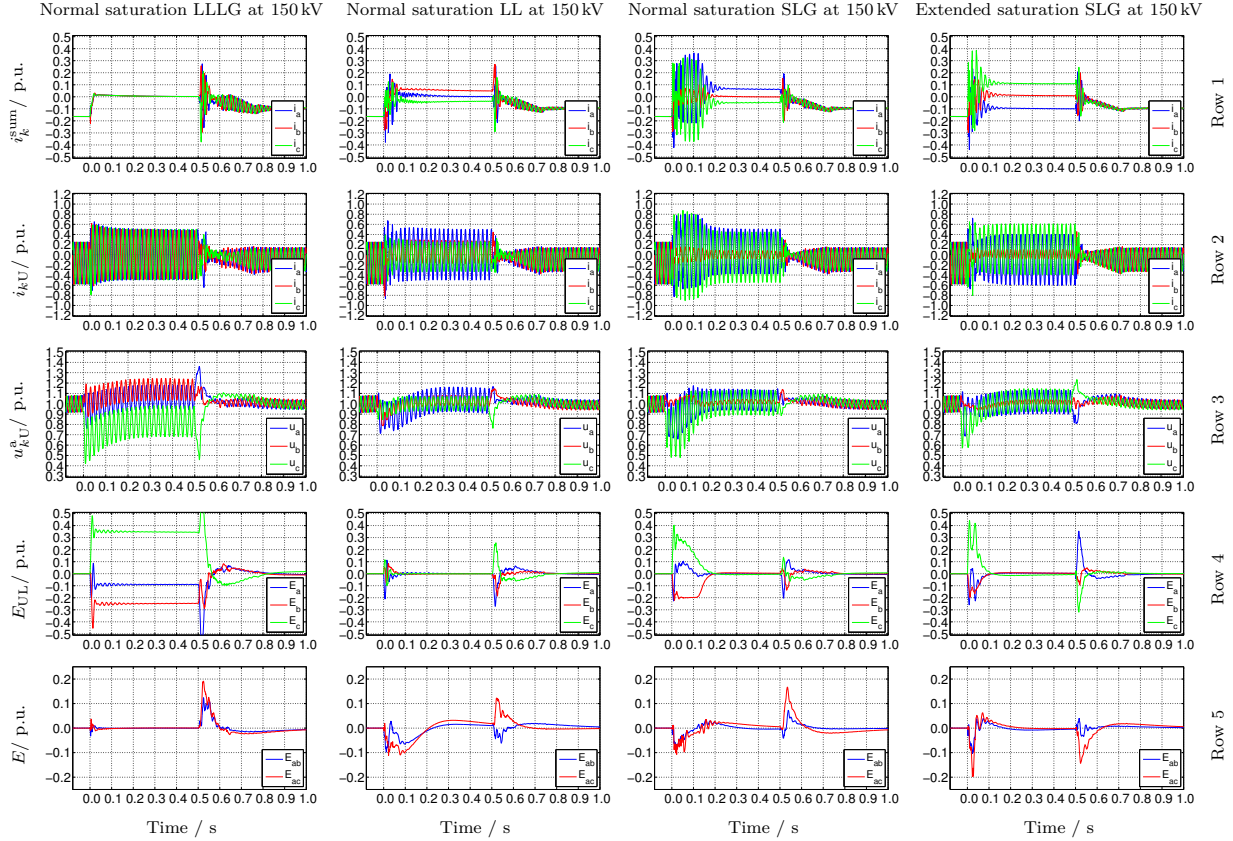


Figure 6.11: MMC-related results for network configuration II. Plots are ordered column-wise by different faults, and row-wise by inner currents, upper arm currents, upper arm capacitor voltages, and internal energy variations of the MMC-HVdc in vertical and horizontal direction, in respective order.

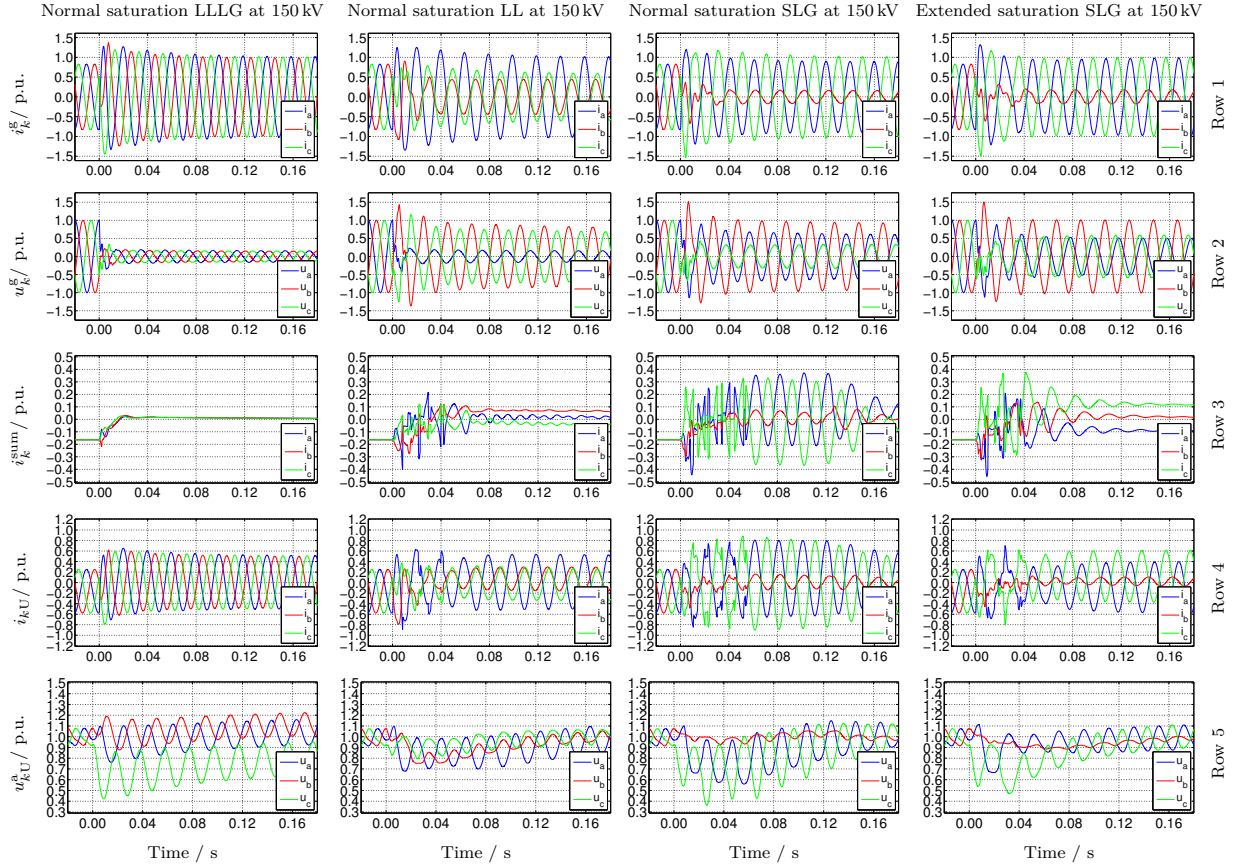


Figure 6.12: Zoomed results for Figs. 6.10 and 6.11. Plots are ordered column-wise by different faults, and row-wise by grid currents, grid voltages, inner currents, upper arm currents, and upper arm capacitor voltages, in respective order.

6.5 Summary

This chapter addressed the FRT behavior of the WT converters during unbalanced voltage conditions in the offshore ac grid. For HVdc-connected WPPs, the offshore grid presents a network configuration with the WT converters operating in grid-connected mode and the offshore VSC-HVdc in grid-forming mode. Unbalanced faults present severe interruptions of the normal operation. Each converter in the system might be designed to react upon the implemented FRT strategy. Four FRT strategies for the WT converters were outlined. With specific focus on unbalanced faults, the FRT strategies ranged from no grid support, solely pos. seq. support, or joint pos. and neg. seq. dynamic voltage support. It was elaborated that OM occurs when the applied converter modulation index exceeds a predefined modulation index barrier. Therefore, two of the strategies are using OM limitation control on the active or reactive converter current. Transient simulations were performed for LLLG, LL, and SLG faults at the 150 kV busbar in vicinity of the offshore VSC-HVdc. Dynamic voltage support in both pos. and neg. seq. represented the most appropriate solution to support both the offshore grid and the VSC-HVdc to ride through the fault and continue to normal operation in a smooth manner.

The first part of the analysis was performed with a simplified offshore VSC-HVdc model using a regulated three-phase voltage source. The upper level controllers for the grid-forming operation mode were implemented according to Chapter 5. Contrary to the operation without any WT converters connected, over-voltages and OM represented a serious threat during unbalanced faults in the offshore grid. On the one hand, an OM-dependant limitation of active current by the WTs (strategy RC1) was seen beneficial for the magnitude of the offshore grid voltage. Moreover, OM was avoided by any converter in the system. However, in that case, there is no fault current contribution from the WPPs. On the other hand, pos. and neg. seq. voltage support by the WTs (strategy RC4) provided fault currents and limited active current only if necessary. Consequently, the OM in one or more phase(s) appeared due to the over-voltages in the system.

In the second part, the MMC-HVdc model introduced in Chapter 5 was included to discuss the impact on the internal variables of the MMC-HVdc

when the WT converters were in operation. Additionally, it was proposed to deploy dynamic voltage support in symmetrical components with higher gains to limit the active current injection during the fault. It was demonstrated that the FRT of the WT converters with higher gains diminished the earlier experienced over-voltages. It was further presented that the extended saturation method introduced in Chapter 5 causes similar improvements regarding the offshore grid voltage and the MMC-HVdc response as already highlighted for the passive offshore grid. The MMC internal variables coped with different FRT strategies applied by the WT converters. To sum up, the control method in symmetrical components introduced in Chapter 5 was successfully demonstrated for the WPPs in operation and the FRT in pos. and neg. seq. with high gains was found to be the best fit for the application.

7 Conclusions

This chapter wraps up the conclusions of thesis and future work regarding the control and operation of HVdc-connected WPPs.

7.1 Main conclusions

The main conclusions are summarized per each chapter:

- Chapter 2 provided a summary of the state of the art within the scope of the thesis. Operation and control of HVdc-connected WPPs and the well-known control methods for grid-connected and grid-forming power converters were highlighted. The chapter shed light on conventional reactive power control in WPPs and aspects regarding the FRT of power system faults. For HVdc-connected WPPs, two main gaps were identified in the literature: i) application of optimization-based reactive power control and ii) FRT of unbalanced faults in the offshore;
- Chapter 3 covered optimization-based reactive power control of a single HVdc-connected WPP in steady-state. It was demonstrated that, to reduce power losses, reactive power was advantageously shared among the different converters in the system (WT converters and offshore VSC-HVdc). From the optimization-based reactive power dispatch, it was demonstrated that those WTs which were close to the PCC and/or had a high individual active power production were contained to produce more reactive power than others. A wake model was used to cover a large set of realistic operating points. Optimization-based reactive power dispatch using a variable reference voltage for the offshore VSC-HVdc demonstrated an increased potential for power loss reduction. It was shown that the appropriate voltage reference depends primarily on the active power output of the whole WPP;

- consequently, Chapter 4 extended the work to HVdc-connected WPP clusters. The expected operator framework defined a multi-layered approach for the reactive power/voltage control methods. It was presented that reactive power provision from a WPP generally caused higher power loss than from an offshore VSC-HVdc. Furthermore, it was demonstrated that the division in different grid layers (HV export grid, MV collection grid) presents a good trade-off for the success of the reactive power/voltage control. It was then concluded that optimization strategies with variable voltage reference gain an even higher loss reduction. Besides that, it was highlighted that incorporation of power converter losses in the optimization-based reactive power control application is of utmost importance for increased accuracy;
- Chapter 5 proposed a control method using symmetrical components for the grid-forming offshore MMC-HVdc. It was shown that the suggested control method with VC and CC loops in pos. and neg. seq. allows us to gain full converter current controllability during unbalanced conditions. Additionally, it was outlined that the internal variables of the MMC, e.g. inner currents, arm currents, and arm capacitor voltages, in principle do not exceed their design values when the grid-forming converter injects maximum current during faults. An extended saturation method was presented which aims to inject maximum currents during unbalanced faults with two faulted phases at the VSC-HVdc terminals. Simulations were performed and discussed for the operation of a passive offshore grid where the offshore VSC-HVdc represented the only active converter;
- and finally, Chapter 6 evaluated four FRT strategies for the WPPs during unbalanced faults in the offshore grid. The FRT strategies differed in terms of pos. and/or neg. seq. dynamic voltage support and specifically OM limitation on active or reactive current. It was explained that over-voltages might occur in the offshore ac grid during unbalanced faults when the active current injection by the WPPs was not limited. Furthermore, the control method and proposed saturation principles of Chapter 5 were applied to the network configuration with the WT converters in operation. It was highlighted that the combination of dynamic voltage support in symmetrical components and active power

limitation delivers good results for the system behavior during FRT. Hence, the best implementation to ride through unbalanced faults demonstrated the dynamic voltage control with high gains.

7.2 Future work

In the field of connection of remote offshore wind resources, there are a series of topics which might be further investigated. On the reactive power and voltage control methods presented in Chapters 3 and 4, it might be beneficial to define in more detail the implementation in a real setup. This might be first supported by dynamic simulations using real WPP (cluster) data, i.e. wind speed or active power generation time series. The strategy on how to adopt to a new set of reactive power and voltage reference set–point might be explored. Furthermore, it might be of interest to develop a joint optimization algorithm which targets wake reduction, reactive power and voltage control.

One emerging topic is also the use of HV collection grids, namely 66 kV, which is the logical consequence when larger turbines are deployed. The higher nominal voltage lowers the currents and, consequently, the power losses. Simultaneously, it increases the reactive power requirements in the offshore grid. The reactive power dispatch concepts presented in this thesis might gain importance as two factors become unfavorable for the conventional dispatch: i) higher reactive power requirement by the HV collection grid itself and ii) larger distances between the turbines due to the increased rotor diameter. Furthermore, the accuracy of the used data might be increased, specifically using better power converter loss models in dependence of active and reactive power and grid voltage, and/or validated field data. To follow up the analysis performed on reactive power control in HVdc–connected WPP clusters, it might be of interest to have real data on wind speeds among the cluster and especially on cluster wake effects. Besides that, the implementation in a dynamic simulation environment might be of interest.

For the EMT simulations in Chapters 5 and 6, it might be of interest to build up an experimental setup and validate the presented techniques. Furthermore, as recent and future GC might incorporate neg. seq. current provision and control during FRT in their requirements, generic and

manufacturer-specific models might be used in the future to perform detailed studies and adopt their functionalities. Besides that, it would be of interest to test the current limitation methods presented for the grid-forming converter in a hardware setup, particularly with a MMC.

In this thesis, FRT by the offshore MMC-HVdc in the offshore grid was analyzed with one possible grid-forming control concept (option I). The control framework was further proposed without decoupling networks in the CC or on the fed-forward load current to avoid double fundamental frequency oscillations. Although they have been attenuated by notch filters, superior performance might be gained by the consequent use of such decoupling networks (well known for the grid-connected application, refer to [17], and performed in Chapter 5 for the voltage measurements). The general control concept, either with or without symmetrical components, has the advantage of a dedicated current controller but might employ a physical HV capacitor not needed for the proper MMC-HVdc topology but the offshore grid control. More research efforts might be needed on how exactly the physical HV capacitor might be replaced by advanced control methods (e.g. real-time estimation of the offshore grid impedance). Another option might be the enhancement of alternative control methods, both derivations of option II or new proposals, to allow their use during faults. From the industrial perspective, recently, an important topic is the reported experience on over-voltages in the offshore grid after unplanned trips of the offshore VSC-HVdc. In that case, it might be useful to explore control methods which blend the boundaries between the grid-connected and the grid-forming operation of power converters. Data on unplanned offshore system trips, e.g. reported on the transparency portal of ENTSO-E¹, are also a clear indicator that reliability of the systems deployed offshore is very important and a bold item for the future competitiveness of the offshore wind industry.

¹ENTSO-E Transparency Platform: <https://transparency.entsoe.eu/>.

Bibliography

- [1] C. Buchhagen, C. Rauscher, A. Menze, and J. Jung, „BorWin1 - First Experiences with harmonic interactions in converter dominated grids“, in *Int. ETG Congr. 2015; Die Energiewende - Blueprints new energy age*, 2015, pp. 1–7 (see p. 2).
- [2] R. Teixeira Pinto, „Multi-terminal DC networks: system integration, dynamics and control“, Ph.D. dissertation, TU Delft, 2014. DOI: 10.4233/uuid:9b0a88cf-c2c6-43d3-810d-b64a211ab419 (see pp. 2, 21, 23, 25).
- [3] R. D. Zimmerman, C. E. Murillo-Sanchez, and R. J. Thomas, „MAT-POWER: steady-state operations, planning, and analysis tools for power systems research and education“, *IEEE Trans. Power Syst.*, vol. 26, no. 1, pp. 12–19, 2011. DOI: 10.1109/TPWRS.2010.2051168 (see pp. 8, 70, 97).
- [4] A. Egea-Àlvarez, „Multiterminal HVDC transmission systems for offshore wind“, Ph.D. dissertation, Universitat Politècnica de Catalunya, 2014 (see pp. 9, 25, 37).
- [5] E. Prieto-Araujo, „Power converter control for offshore wind energy generation and transmission“, Ph.D. dissertation, Universitat Politècnica de Catalunya, 2016 (see pp. 9, 47, 124).
- [6] Bundesministerium für Wirtschaft und Energie (BMWi) and Projektträger Jülich (PTJ), *Data of Forschungsplattform in Nord- und Ostsee (FINO)*, 2013. [Online]. Available: <http://www.fino-offshore.de> (visited on 08/01/2016) (see pp. 11, 105).
- [7] Parc éolien en mer de Fécamp, „Étude de la ressource en vent“, Parc éolien en mer de Fécamp, Tech. Rep., 2011. [Online]. Available:

- <http://www.parc-eolien-en-mer-de-fecamp.fr> (see pp. 11, 73 sq.).
- [8] P. Kiss, „Analysis of the European wind power climatology and the possible cosmic radiation forcing on global lightning activity“, Ph.D. dissertation, Eötvös Loránd University, 2009, p. 143 (see p. 11).
- [9] I. Troen and E. Lundtang Petersen, „European wind atlas“, Risø National Laboratory, Roskilde, Tech. Rep., 1989, 656 pp (see p. 11).
- [10] A. R. Henderson, C. Morgan, B. Smith, *et al.*, „Offshore wind energy in Europe- a review of the state-of-the-art“, *Wind Energy*, vol. 6, no. 1, pp. 35–52, Jan. 2003. DOI: 10.1002/we.82 (see pp. 11 sq.).
- [11] The Crown Estate, „Offshore wind cost reduction-Pathways study“, The Crown Estate, Tech. Rep., 2015, 88 pp. [Online]. Available: <http://www.thecrownestate.co.uk/media/5462/ei-offshore-wind-operational-report-2015.pdf> (visited on 12/13/2015) (see pp. 11 sq., 51).
- [12] Ernst & Young et Associés, „Offshore wind in Europe. Walking the tightrope to success.“, Ernst & Young et Associés, Tech. Rep., 2015. [Online]. Available: <https://www.ewea.org/fileadmin/files/library/publications/reports/EY-Offshore-Wind-in-Europe.pdf> (visited on) (see pp. 11 sq.).
- [13] X. Sun, D. Huang, and G. Wu, „The current state of offshore wind energy technology development“, *Energy*, vol. 41, no. 1, pp. 298–312, 2012. DOI: 10.1016/j.energy.2012.02.054 (see p. 12).
- [14] LM Wind Power, *World’s longest wind turbine blade successfully completes its first journey*, 2016. [Online]. Available: <http://www.lmwindpower.com/en/stories-and-press/stories/news-from-lm-places/transport-of-longest-blade-in-the-world> (visited on 12/05/2016) (see p. 12).
- [15] European Wind Energy Association (EWEA), „The European offshore wind industry - key trends and statistics 2015“, Tech. Rep. February, 2016 (see p. 12).

- [16] Siemens AG, *Wind turbine SWT-7.0-154 technical specification*, 2016. [Online]. Available: <http://www.siemens.com/> (visited on 12/13/2016) (see pp. 13, 15).
- [17] R. Teodorescu, M. Liserre, and P. Rodriguez, *Grid converters for photovoltaic and wind power systems*. Chichester, UK: John Wiley and Sons, Ltd, Jan. 2011, p. 416, ISBN: 9780470667057. DOI: 10.1002/9780470667057 (see pp. 13–15, 31–37, 42, 119, 180).
- [18] M. Liserre, R. Cárdenas, M. Molinas, and J. Rodríguez, „Overview of multi-MW wind turbines and wind parks“, *IEEE Trans. Ind. Electron.*, vol. 58, no. 4, pp. 1081–1095, 2011. DOI: 10.1109/TIE.2010.2103910 (see p. 13).
- [19] H. Polinder, J. A. Ferreira, B. B. Jensen, *et al.*, „Trends in wind turbine generator systems“, *IEEE J. Emerg. Sel. Top. Power Electron.*, vol. 1, no. 3, pp. 174–185, Sep. 2013. DOI: 10.1109/JESTPE.2013.2280428 (see pp. 13 sq.).
- [20] H. Polinder, F. Van Der Pijl, G.-J. De Vilder, and P. Tavner, „Comparison of direct-drive and geared generator concepts for wind turbines“, *IEEE Trans. Energy Convers.*, vol. 21, no. 3, pp. 725–733, Sep. 2006. DOI: 10.1109/TEC.2006.875476 (see pp. 13 sq., 210 sq.).
- [21] Adwen, *Adwen AD 5-135 and Adwen AD 5-132*, 2016. [Online]. Available: <http://www.adwenoffshore.com/> (visited on 12/04/2016) (see p. 13).
- [22] General Electric, *Haliade 150-6MW specifications*, 2015. [Online]. Available: <https://www.gerenewableenergy.com/> (visited on 01/13/2015) (see pp. 13, 15).
- [23] MHI Vestas Offshore, *V164-8.0 MW: technical data*, 2015. [Online]. Available: <http://www.mhivestasoffshore.com/> (visited on 01/13/2015) (see p. 13).
- [24] Senvion SE, *Senvion 6.XM series technical data*, 2015. [Online]. Available: <http://www.senvion.com/> (visited on 01/13/2015) (see p. 13).
- [25] The Switch, „PMG vs. DFIG – the big generator technology debate“, The Switch, Tech. Rep., 2014, 6 pp (see pp. 14 sq.).

- [26] G. Lalor, A. Mullane, and M. O'Malley, „Frequency control and wind turbine technologies“, *IEEE Trans. Power Syst.*, vol. 20, no. 4, pp. 1905–1913, 2005. DOI: 10.1109/TPWRS.2005.857393 (see p. 14).
- [27] D. Zhou, F. Blaabjerg, T. Franke, M. Tonnes, and M. Lau, „Comparison of wind power converter reliability with low-speed and medium-speed permanent-magnet synchronous generators“, *IEEE Trans. Ind. Electron.*, vol. 62, no. 10, pp. 6575–6584, Oct. 2015. DOI: 10.1109/TIE.2015.2447502 (see p. 14).
- [28] F. Blaabjerg and K. Ma, „Future on power electronics for wind turbine systems“, *IEEE J. Emerg. Sel. Top. Power Electron.*, vol. 1, no. 3, pp. 139–152, 2013. DOI: 10.1109/JESTPE.2013.2275978 (see pp. 14 sq.).
- [29] G. Gohil, L. Bede, R. Teodorescu, T. Kerekes, and F. Blaabjerg, „Line filter design of parallel interleaved VSCs for high power wind energy conversion system“, *IEEE Trans. Power Electron.*, vol. 30, no. 12, pp. 6775–6790, Dec. 2015. DOI: 10.1109/TPEL.2015.2394460 (see p. 15).
- [30] U. Shipurkar, H. Polinder, and J. A. Ferreira, „Modularity in wind turbine generator systems — opportunities and challenges“, in *2016 18th Eur. Conf. Power Electron. Appl.*, IEEE, Sep. 2016, pp. 1–10. DOI: 10.1109/EPE.2016.7695592 (see p. 15).
- [31] J. Birk and B. Andresen, „Parallel-connected converters for optimizing efficiency, reliability and grid harmonics in a wind turbine“, in *2007 Eur. Conf. Power Electron. Appl. EPE*, 2007, pp. 4–10. DOI: 10.1109/EPE.2007.4417318 (see p. 15).
- [32] E. Prieto-Araujo, A. Junyent-Ferre, D. Lavernia-Ferrer, and O. Gomis-Bellmunt, „Decentralized control of a nine-phase permanent magnet generator for offshore wind turbines“, *IEEE Trans. Energy Convers.*, vol. 30, no. 3, pp. 1103–1112, Sep. 2015. DOI: 10.1109/TEC.2015.2412550 (see p. 15).
- [33] L. Trilla, J. Pegueroles, J. Urresty, C. Muniz, and O. Gomis-Bellmunt, „Generator short-circuit torque compensation in multi-channel wind

- turbines“, *IEEE Trans. Ind. Electron.*, vol. 46, no. c, pp. 1–1, 2017. DOI: 10.1109/TIE.2017.2650870 (see p. 15).
- [34] A. D. Hansen, N. A. Cutululis, H. Markou, P. Sørensen, and F. Iov, „Grid fault and design-basis for wind turbines“, Risø National Laboratory for Sustainable Energy, Tech. Rep. Risø-R-171, 2010 (see p. 15).
- [35] International Electrotechnical Commission (IEC), *IEC 61400-1 wind turbines - part 1: design requirements*, Geneva, Switzerland, 2005 (see p. 15).
- [36] M. de Prada Gil, „Design, operation and control of novel electrical concepts for offshore wind power plants“, Ph.D. dissertation, Universitat Politècnica de Catalunya, 2014 (see pp. 15, 17, 26 sq., 72).
- [37] Éoliennes Offshore des Hautes Falaises, „Projet de parc éolien au large de Fécamp“, Dossier du Maître d’Ouvrage (Project Management Report), Tech. Rep., 2013. [Online]. Available: <http://www.parc-eolien-en-mer-de-fecamp.fr> (see pp. 16 sq., 73).
- [38] A. Ferguson, P. D. Villiers, B. Fitzgerald, and J. Matthiesen, „Benefits in moving the inter-array voltage from 33 kV to 66 kV AC for large offshore wind farms“, in *EWEA 2012 Proc.*, 2012, p. 8 (see p. 16).
- [39] R. Mc Dermott, „Investigation of use of higher AC voltages on offshore wind farms“, in *EWEA 2009 Proc.*, 2009, p. 6 (see p. 16).
- [40] P. K. Steimer and O. Apeldoorn, „Medium voltage power conversion technology for efficient windpark power collection grids“, in *2nd Int. Symp. Power Electron. Distrib. Gener. Syst.*, IEEE, Jun. 2010, pp. 12–18. DOI: 10.1109/PEDG.2010.5545750 (see p. 16).
- [41] T. Gjengedal, „Large-scale wind power farms as power plants“, *Wind Energy*, vol. 8, no. 3, pp. 361–373, 2005. DOI: 10.1002/we.165 (see p. 17).
- [42] CIGRE Working Group B3.36, „Special considerations for AC collector systems and substations associated with HVDC-connected wind power plants“, CIGRE, Tech. Rep., Mar. 2015, 100 pp (see pp. 17, 23, 30, 39, 42 sq., 51–53, 58, 94 sq., 98, 115).

- [43] S. Lumbreras and A. Ramos, „Offshore wind farm electrical design: a review“, *Wind Energy*, vol. 16, no. 3, pp. 459–473, Apr. 2013. DOI: 10.1002/we.1498 (see p. 17).
- [44] A. MacPhail, C. J. Convenor, B. Mampaey, *et al.*, „Third-party damage to underground and submarine cables“, CIGRE WG B1.21, Tech. Rep., 2009, 117 pp (see pp. 17 sq., 54).
- [45] T. Worzyk, *Submarine Power Cables*, ser. Power Systems. Berlin, Heidelberg: Springer Berlin Heidelberg, 2009, ISBN: 978-3-642-01269-3. DOI: 10.1007/978-3-642-01270-9 (see pp. 18, 54).
- [46] Nexans, *2XS(FL)2YRAA RM 19/33 (36)kV cable datasheets for different cross-sections*, 2014. [Online]. Available: <http://www.nexans.de> (visited on 11/05/2014) (see p. 19).
- [47] ABB, *XLPE submarine cable systems rev. 5*, 2010. [Online]. Available: <http://www.abb.com/cables> (visited on 05/01/2014) (see p. 19).
- [48] B. Franken, H. Breder, M. Dahlgren, and E. Nielsen, „Collection grid topologies for off-shore wind parks“, in *18th Int. Conf. Exhib. Electr. Distrib. (CIRED 2005)*, IET, 2005. DOI: 10.1049/cp:20051326 (see p. 18).
- [49] International Electrotechnical Commission (IEC), „IEC 60038-2002-07 Edition 6.2 IEC standard voltages“, International Electrotechnical Commission (IEC), Tech. Rep., 2002, p. 18 (see p. 20).
- [50] D. Van Hertem, O. Gomis-Bellmunt, and J. Liang, Eds., *HVDC grids*. Hoboken, NJ, USA: John Wiley and Sons, Inc., Feb. 2016, ISBN: 9781119115243. DOI: 10.1002/9781119115243 (see pp. 21–26, 50 sq.).
- [51] Prysmian Cables and Systems B.V., „Wire and cable engineering guide“, Prysmian Cables and Systems B.V., Tech. Rep., 2006, pp. 1–20 (see p. 21).
- [52] T. Leibfried, *Lecture notes Elektroenergiesysteme*. Institute of Electrical Energy Systems and High-Voltage Engineering (IEH), Karlsruhe Institute of Technology (KIT), 2012 (see p. 21).

- [53] W. Wiechowski and P. B. Eriksen, „Selected studies on offshore wind farm cable connections - challenges and experience of the Danish TSO“, in *Power Energy Soc. Gen. Meet. - Convers. Deliv. Electr. Energy 21st Century, 2008 IEEE*, IEEE, 2008, pp. 1–8. DOI: 10.1109/PES.2008.4596124 (see p. 22).
- [54] S. Lauria, M. Schembari, and F. Palone, „EHV AC interconnection for a GW-size offshore wind-farm cluster: Preliminary sizing“, in *ENERGYCON 2014 - IEEE Int. Energy Conf.*, 2014, pp. 366–373. DOI: 10.1109/ENERGYCON.2014.6850453 (see p. 22).
- [55] CIGRE Working Group B4.55, „HVDC connection of offshore wind power plants“, CIGRE, Tech. Rep., May 2015, 92 pp (see pp. 23 sq., 26, 30, 48, 51, 53, 55, 57, 120, 152).
- [56] L. Xu and B. R. Andersen, „Grid connection of large offshore wind farms using HVDC“, *Wind Energy*, vol. 9, no. 4, pp. 371–382, 2006. DOI: 10.1002/we.185 (see p. 23).
- [57] Alstom Grid, *HVDC: connecting to the future*. Levallois-Perret: Alstom, 2010 (see p. 23).
- [58] 50Hertz Transmission GmbH, Amprion GmbH, TenneT TSO GmbH, and TransnetBW GmbH, „Offshore- Netzentwicklungsplan 2030, Version 2017, 1. Entwurf“, 50Hertz Transmission GmbH Amprion GmbH TenneT TSO GmbH TransnetBW GmbH, Tech. Rep., 2017. [Online]. Available: <https://www.netzentwicklungsplan.de/> (see pp. 23, 51).
- [59] J. Glasdam, J. Hjerrild, L. H. Kocewiak, and C. L. Bak, „Review on multi-level voltage source converter based HVDC technologies for grid connection of large offshore wind farms“, in *2012 IEEE Int. Conf. Power Syst. Technol. POWERCON*, 2012, pp. 1–6. DOI: 10.1109/PowerCon.2012.6401377 (see p. 23).
- [60] L. Xu, L. Yao, and C. Sasse, „Grid integration of large DFIG-based wind farms using VSC transmission“, *IEEE Trans. Power Syst.*, vol. 22, no. 3, pp. 976–984, Aug. 2007. DOI: 10.1109/TPWRS.2007.901306 (see pp. 23, 39, 57).

- [61] A. Yazdani and R. Iravani, *Voltage-sourced converters in power systems*. Hoboken, NJ, USA: John Wiley and Sons, Inc., Jan. 2010, 451 pp, ISBN: 9780470551578. DOI: 10.1002/9780470551578 (see pp. 24 sq., 31 sq., 37–40, 42, 45, 63).
- [62] N. Flourentzou, V. Agelidis, and G. Demetriades, „VSC-based HVDC power transmission systems: an overview“, *IEEE Trans. Power Electron.*, vol. 24, no. 3, pp. 592–602, 2009. DOI: 10.1109/TPEL.2008.2008441 (see pp. 25 sq.).
- [63] R. Sellick and M. Åkerberg, „Comparison of HVDC Light (VSC) and HVDC Classic (LCC) site aspects, for a 500MW 400kV HVDC transmission scheme“, in *10th IET Int. Conf. AC DC Power Transm. (ACDC 2012)*, IET, 2012, pp. 23–23. DOI: 10.1049/cp.2012.1945 (see p. 25).
- [64] J. Liang, T. Jing, O. Gomis-Bellmunt, J. Ekanayake, and N. Jenkins, „Operation and control of multiterminal HVDC transmission for offshore wind farms“, *IEEE Trans. Power Deliv.*, vol. 26, no. 4, pp. 2596–2604, Oct. 2011. DOI: 10.1109/TPWRD.2011.2152864 (see p. 25).
- [65] M. Aragüés Peñalba, „Operation and control of transmission systems for offshore wind power plants“, Ph.D. dissertation, Universitat Politècnica de Catalunya, 2016 (see p. 26).
- [66] O. D. Adeuyi, M. Cheah-Mane, J. Liang, and N. Jenkins, „Fast frequency response from offshore multi-terminal VSC-HVDC schemes“, *IEEE Trans. Power Deliv.*, vol. 8977, no. c, pp. 1–1, 2016. DOI: 10.1109/TPWRD.2016.2632860 (see pp. 26, 57).
- [67] I. Martinez Sanz, B. Chaudhuri, and G. Strbac, „Inertial response from offshore wind farms connected through DC grids“, *IEEE Trans. Power Syst.*, vol. 30, no. 3, pp. 1518–1527, May 2015. DOI: 10.1109/TPWRS.2014.2349739 (see pp. 26, 57).
- [68] A. Junyent-Ferre, Y. Pipelzadeh, and T. C. Green, „Blending HVDC-link energy storage and offshore wind turbine inertia for fast frequency response“, *IEEE Trans. Sustain. Energy*, vol. 6, no. 3, pp. 1059–1066, Jul. 2015. DOI: 10.1109/TSTE.2014.2360147 (see pp. 26, 57).

- [69] A. Egea-Alvarez, F. Bianchi, A. Junyent-Ferre, G. Gross, and O. Gomis-Bellmunt, „Voltage control of multiterminal VSC-HVDC transmission systems for offshore wind power plants: design and implementation in a scaled platform“, *IEEE Trans. Ind. Electron.*, vol. 60, no. 6, pp. 2381–2391, Jun. 2013. DOI: 10.1109/TIE.2012.2230597 (see pp. 26, 57).
- [70] M. Raza and O. Gomis-Bellmunt, „Multi infeed control of VSC HVDC transmission system for offshore wind power plant integration“, in *13th Wind Integr. Work.*, T. Ackermann and U. Betancourt, Eds., Berlin, 2014, pp. 376–381 (see pp. 26, 41).
- [71] L. Zeni, „Power system integration of VSC-HVDC connected offshore wind power plants“, Ph.D. dissertation, Danmarks Tekniske Universitet, 2015, ISBN: 9788793278455 (see pp. 26, 39, 41, 43, 120).
- [72] T. Ackermann, *Wind Power in Power Systems*, T. Ackermann, Ed. Chichester, UK: John Wiley & Sons, Ltd, Jan. 2005, ISBN: 9780470012680. DOI: 10.1002/0470012684 (see p. 26).
- [73] N. Qin, S. You, Z. Xu, and V. Akhmatov, „Offshore wind farm connection with low frequency AC transmission technology“, in *2009 IEEE Power Energy Soc. Gen. Meet.*, vol. 3, IEEE, Jul. 2009, pp. 1–8. DOI: 10.1109/PES.2009.5275262 (see pp. 26 sq.).
- [74] I. Erlich, F. Shewarega, H. Wrede, and W. Fischer, „Low frequency AC for offshore wind power transmission – prospects and challenges“, in *AC DC Power Transm. 11th IET Int. Conf.*, 2015, pp. 1–7. DOI: 10.1049/cp.2015.0017 (see pp. 26 sq.).
- [75] J. L. Domínguez-García, D. J. Rogers, C. E. Ugalde-Loo, J. Liang, and O. Gomis-Bellmunt, „Effect of non-standard operating frequencies on the economic cost of offshore AC networks“, *Renew. Energy*, vol. 44, pp. 267–280, Aug. 2012. DOI: 10.1016/j.renene.2012.01.093 (see pp. 26 sq.).
- [76] L. Trilla, O. Gomis-Bellmunt, A. Junyent-Ferre, and A. Sudrià-Andreu, „Analysis of total power extracted with common converter wind farm topology“, in *XIX Int. Conf. Electr. Mach. - ICEM 2010*, Rome:

- IEEE, Sep. 2010, pp. 1–6. DOI: 10.1109/ICELMACH.2010.5608072 (see pp. 26 sq.).
- [77] O. Gomis-Bellmunt, A. Junyent-Ferre, A. Sumper, and J. Bergas-Jane, „Control of a wind farm based on synchronous generators with a central HVDC-VSC converter“, *IEEE Trans. Power Syst.*, vol. 26, no. 3, pp. 1632–1640, Aug. 2011. DOI: 10.1109/TPWRS.2010.2091654 (see pp. 26 sq.).
- [78] P. Menke, R. Zurowski, T. Christ, *et al.*, „Breakthrough in DC grid access technology for large scale offshore wind farms“, *EWEA Offshore*, pp. 1–5, 2015 (see pp. 26 sq.).
- [79] P. Menke, R. Zurowski, T. Christ, *et al.*, „2nd Generation DC grid access for large scale offshore wind farms“, in *14th Wind Integr. Work.*, U. Betancourt and T. Ackermann, Eds., Brussels: Energynautics GmbH, 2015, pp. 1–5 (see pp. 26–28).
- [80] S. Bernal-Perez, S. Añó-Villalba, R. Blasco-Gimenez, and J. Rodríguez-D’Derlée, „Efficiency and fault ride-through performance of a diode-rectifier-and VSC-inverter-based HVDC link for offshore wind farms“, *IEEE Trans. Ind. Electron.*, vol. 60, no. 6, pp. 2401–2409, 2013. DOI: 10.1109/TIE.2012.2222855 (see pp. 26 sq.).
- [81] R. Blasco-Gimenez, S. Añó-Villalba, J. Rodríguez-D’Derlée, F. Morant, and S. Bernal-Perez, „Distributed voltage and frequency control of offshore wind farms connected with a diode-based HVdc link“, *IEEE Trans. Power Electron.*, vol. 25, no. 12, pp. 3095–3105, 2010. DOI: 10.1109/TPEL.2010.2086491 (see pp. 26 sq.).
- [82] R. Blasco-Gimenez, S. Añó-Villalba, J. Rodríguez-D’Derlée, S. Bernal-Perez, and F. Morant, „Diode-based HVdc link for the connection of large offshore wind farms“, *IEEE Trans. Energy Convers.*, vol. 26, no. 2, pp. 615–626, 2011. DOI: 10.1109/TEC.2011.2114886 (see pp. 26–28).
- [83] C. Prignitz, H.-G. Eckel, and H.-J. Knaak, „DFIG wind turbines operating in a fixed reference frame“, in *2015 17th Eur. Conf. Power Electron. Appl. (EPE’15 ECCE-Europe)*, IEEE, Sep. 2015, pp. 1–8. DOI: 10.1109/EPE.2015.7309114 (see pp. 26 sq.).

- [84] O. Martander, „DC grids for wind farms“, Ph.D. dissertation, Chalmers University of Technology, 2002 (see pp. 26, 28).
- [85] S. Lundberg, „Wind farm configuration and energy efficiency studies - series DC versus AC layouts“, Ph.D. dissertation, Chalmers University of Technology, 2006 (see pp. 26, 28).
- [86] L. Max, „Design and control of a DC collection grid for a wind farm“, Ph.D. dissertation, Chalmers University of Technology, 2009 (see pp. 26, 28).
- [87] F. Deng, „Design and control of a DC grid for offshore wind farms“, Ph.D. dissertation, Aalborg University, 2012 (see pp. 26, 28).
- [88] P. Lakshmanan, J. Liang, and N. Jenkins, „Assessment of collection systems for HVDC connected offshore wind farms“, *Electr. Power Syst. Res.*, vol. 129, pp. 75–82, Dec. 2015. DOI: 10.1016/j.epsr.2015.07.015 (see pp. 26, 28).
- [89] N. Strachan and D. Jovicic, „Offshore wind farm with centralised power conversion and DC interconnection“, *IET Gener. Transm. & Distrib.*, vol. 3, no. 6, pp. 586–595, Jun. 2009. DOI: 10.1049/iet-gtd.2008.0372 (see pp. 26, 28).
- [90] A. Garcés Ruiz, „Design, operation and control of series-connected power converters for offshore wind parks“, PhD thesis, Norwegian University of Science and Technology, 2012, ISBN: 9788247137123 (see pp. 26, 28).
- [91] S. Kenzelmann, „Modular DC/DC converter for DC distribution and collection networks“, Ph.D. dissertation, EPF Lausanne, 2012 (see p. 28).
- [92] TenneT TSO GmbH, „Requirements for offshore grid connections in the grid of TenneT TSO GmbH“, TenneT TSO GmbH, Tech. Rep. December, 2012. [Online]. Available: <http://www.tennet.eu> (see pp. 29 sq., 38, 55, 57, 71, 95).
- [93] —, „Grid code for high and extra high voltage“, TenneT TSO GmbH, Tech. Rep. December, 2012, pp. 1–45 (see pp. 29 sq.).

- [94] Energinet.dk, „Technical regulation 3.2.5 for wind power plants above 11 kW“, Energinet.dk, Tech. Rep., 2016 (see p. 30).
- [95] Réseau de transport d'électricité (Rte), „Documentation technique de référence“, Réseau de transport d'électricité (Rte), Tech. Rep., 2014, pp. 1–17 (see pp. 30, 48).
- [96] 50Hertz Transmission GmbH, „Netzanschluss- und Netzzugangsregeln der 50Hertz Transmission GmbH“, 50Hertz Transmission GmbH, Tech. Rep., 2008 (see p. 30).
- [97] National Grid, „The grid code“, National Grid, Tech. Rep. 5, 2016, p. 656 (see pp. 30, 48).
- [98] European Commission, „COMMISSION REGULATION (EU) 2016/631 of 14 April 2016 establishing a network code on requirements for grid connection of generators“, *Off. J. Eur. Union*, pp. 10–54, 2016 (see p. 30).
- [99] —, „COMMISSION REGULATION (EU) 2016/1447 of 26 August 2016 establishing a network code on requirements for grid connection of high voltage direct current systems and direct current-connected power park modules“, *Off. J. Eur. Union*, no. L 241, pp. 1–65, 2016 (see p. 30).
- [100] E. Belenguer, R. Vidal, H. Beltran, and R. Blasco-Gimenez, „Control strategy for islanded operation of offshore wind power plants connected through a VSC-HVDC link“, in *IECON 2013 - 39th Annu. Conf. IEEE Ind. Electron. Soc.*, IEEE, Nov. 2013, pp. 5254–5259. DOI: 10.1109/IECON.2013.6699989 (see p. 30).
- [101] J. Conroy and R. Watson, „Low-voltage ride-through of a full converter wind turbine with permanent magnet generator“, *IET Renew. Power Gener.*, vol. 1, no. 3, pp. 182–189, 2007. DOI: 10.1049/iet-rpg:20070033 (see p. 32).
- [102] Forum Netztechnik/Netzbetrieb im VDE (FNN), „VDE-AR-N 4120:2015-01 technical requirements for the connection and operation of customer installations to the high-voltage network“, VDE (FNN), Tech. Rep., Jan. 2015 (see pp. 32, 37, 48 sq., 55 sq., 148, 153 sq.).

- [103] H. Akagi, Y. Kanazawa, and A. Nabae, „Instantaneous reactive power compensators comprising switching devices without energy storage components“, *IEEE Trans. Ind. Appl.*, vol. IA-20, no. 3, pp. 625–630, May 1984. DOI: 10.1109/TIA.1984.4504460 (see p. 33).
- [104] H. Akagi, E. H. Watanabe, and M. Aredes, *Instantaneous power theory and applications to power conditioning*. Hoboken, NJ, USA: John Wiley and Sons, Inc., Feb. 2007, 379 pp, ISBN: 9780470118931. DOI: 10.1002/0470118938 (see pp. 33, 35).
- [105] S. Golestan, J. M. Guerrero, and J. C. Vasquez, „Three-phase PLLs: a review of recent advances“, *IEEE Trans. Power Electron.*, vol. 32, no. 3, pp. 1894–1907, Mar. 2017. DOI: 10.1109/TPEL.2016.2565642 (see p. 33).
- [106] P. Rodriguez, J. Pou, J. Bergas, *et al.*, „Decoupled double synchronous reference frame PLL for power converters control“, *IEEE Trans. Power Electron.*, vol. 22, no. 2, pp. 584–592, Mar. 2007. DOI: 10.1109/TPEL.2006.890000 (see pp. 33 sq.).
- [107] M. Reyes, P. Rodriguez, S. Vazquez, *et al.*, „Decoupled double synchronous reference frame current controller for unbalanced grid voltage conditions“, *2012 IEEE Energy Convers. Congr. Expo. (ECCE 2012)*, vol. 27, no. 9, pp. 4676–4682, 2012. DOI: 10.1109/ECCE.2012.6342184 (see pp. 33 sq.).
- [108] M. Ciobotaru, R. Teodorescu, and F. Blaabjerg, „A new single-phase PLL structure based on second order generalized integrator“, in *37th IEEE Power Electron. Spec. Conf.*, IEEE, 2006, pp. 1–6. DOI: 10.1109/PESC.2006.1711988 (see pp. 33 sq.).
- [109] P. Rodriguez, A. Luna, M. Ciobotaru, R. Teodorescu, and F. Blaabjerg, „Advanced grid synchronization system for power converters under unbalanced and distorted operating conditions“, in *IECON 2006 - 32nd Annu. Conf. IEEE Ind. Electron.*, IEEE, Nov. 2006, pp. 5173–5178. DOI: 10.1109/IECON.2006.347807 (see p. 34).
- [110] P. Rodriguez, A. Luna, I. Candela, *et al.*, „Multiresonant frequency locked loop for grid synchronization of power converters under dis-

- torted grid conditions“, *IEEE Trans. Ind. Electron.*, vol. 58, no. 1, pp. 127–138, Jan. 2011. DOI: 10.1109/TIE.2010.2042420 (see p. 34).
- [111] T. Neumann and I. Erlich, „Comparison between separated and not separated positive and negative sequence control in a high voltage direct current transmission system during unbalanced grid faults“, *IFAC-PapersOnLine*, vol. 48, no. 30, pp. 102–107, 2015. DOI: 10.1016/j.ifacol.2015.12.361 (see p. 35).
- [112] L. Xu, B. R. Andersen, and P. Cartwright, „VSC transmission operating under unbalanced AC conditions - analysis and control design“, *IEEE Trans. Power Deliv.*, vol. 20, no. 1, pp. 427–434, 2005. DOI: 10.1109/TPWRD.2004.835032 (see pp. 37, 57).
- [113] S. Alepuz, S. Busquets-Monge, J. Bordonau, *et al.*, „Control strategies based on symmetrical components for grid-connected converters under voltage dips“, *IEEE Trans. Ind. Electron.*, vol. 56, no. 6, pp. 2162–2173, 2009. DOI: 10.1109/TIE.2009.2017102 (see p. 37).
- [114] I. Erlich, T. Neumann, F. Shewarega, P. Schegner, and J. Meyer, „Wind turbine negative sequence current control and its effect on power system protection“, in *2013 IEEE Power Energy Soc. Gen. Meet.*, IEEE, 2013, pp. 1–5. DOI: 10.1109/PESMG.2013.6672880 (see p. 37).
- [115] T. Wijnhoven, „Evaluation of fault current contribution strategies by converter based distributed generation“, Ph.D. dissertation, KU Leuven, 2015 (see pp. 37, 55).
- [116] Ö. Göksu, „Control of wind turbines during symmetrical and asymmetrical grid faults“, Ph.D. dissertation, Aalborg Universitet, 2012 (see p. 37).
- [117] M. Curzi, R. Sharma, and F. Martin, „In fault ride through reactive current rise time requirements of various European grid codes-analysis based on a full-converter wind turbine“, *Wind Energy*, vol. 19, no. 6, pp. 1121–1133, Jun. 2016. DOI: 10.1002/we.1889 (see p. 37).

- [118] T. Wijnhoven, G. Deconinck, T. Neumann, and I. Erlich, „Control aspects of the dynamic negative sequence current injection of type 4 wind turbines“, in *2014 IEEE PES Gen. Meet. / Conf. Expo.*, IEEE, Jul. 2014, pp. 1–5. DOI: 10.1109/PESGM.2014.6938931 (see p. 37).
- [119] T. Neumann, T. Wijnhoven, G. Deconinck, and I. Erlich, „Enhanced dynamic voltage control of type 4 wind turbines during unbalanced grid faults“, *IEEE Trans. Energy Convers.*, vol. 30, no. 4, pp. 1650–1659, 2015. DOI: 10.1109/TEC.2015.2470126 (see pp. 37, 146, 151, 154).
- [120] Infineon, „FZ1200R45HL3 technical information“, Infineon, Tech. Rep., 2014. [Online]. Available: <http://www.infineon.com> (see p. 37).
- [121] N. Mohan, T. M. Undeland, and W. P. Robbins, *Power electronics: converters, applications, and design*. Wiley, 2003, p. 824, ISBN: 978-0-471-22693-2 (see pp. 38, 149 sq.).
- [122] V. Andreas and M. Hornkamp, *IGBT modules: technologies, driver and application*. Munich: Infineon Technologies AG, 2012, 534 pp, ISBN: 978-3-00-040134-3. [Online]. Available: <https://www.igbtmodulesbook.com/> (see pp. 38, 210).
- [123] M. Ndreko, M. Popov, and M. A. Van Der Meijden, „Study on FRT compliance of VSC-HVDC connected offshore wind plants during AC faults including requirements for the negative sequence current control“, *Int. J. Electr. Power Energy Syst.*, vol. 85, pp. 97–116, 2017. DOI: 10.1016/j.ijepes.2016.08.009 (see pp. 38, 57 sq.).
- [124] X. Hu, J. Liang, D. J. Rogers, and Y. Li, „Power flow and power reduction control using variable frequency of offshore AC grids“, *IEEE Trans. Power Syst.*, vol. 28, no. 4, pp. 3897–3905, 2013. DOI: 10.1109/TPWRS.2013.2257884 (see p. 38).
- [125] L. Zeni, B. Hesselbaek, P. E. Sorensen, A. D. Hansen, and P. C. Kjaer, „Control of VSC-HVDC in offshore AC islands with wind power plants: comparison of two alternatives“, in *2015 IEEE Eindhoven PowerTech*, IEEE, Jun. 2015, pp. 1–6. DOI: 10.1109/PTC.2015.7232291 (see pp. 39, 41).

- [126] S. Chaudhary, „Control and protection of wind power plants with VSC-HVDC connection“, Ph.D. dissertation, Aalborg Universitet, 2011, p. 168 (see pp. 39, 42 sq., 55, 58).
- [127] S. K. Chaudhary, R. Teodorescu, P. Rodriguez, P. C. Kjaer, and A. M. Gole, „Negative sequence current control in wind power plants with VSC-HVDC connection“, *IEEE Trans. Sustain. Energy*, vol. 3, no. 3, pp. 535–544, 2012. DOI: 10.1109/TSTE.2012.2191581 (see pp. 39, 41 sq., 58, 120).
- [128] L. Zhang, „Modeling and control of VSC-HVDC links connected to weak AC systems“, Ph.D. dissertation, KTH, 2010 (see p. 39).
- [129] M. B. Delghavi and A. Yazdani, „A control strategy for islanded operation of a distributed resource (DR) unit“, in *2009 IEEE Power Energy Soc. Gen. Meet. (PES '09)*, 2009, pp. 1–8. DOI: 10.1109/PES.2009.5275592 (see p. 42).
- [130] N. A. Cutululis, L. Zeni, A. G. Endegnanew, *et al.*, „OffshoreDC DC grids for integration of large scale wind power“, DTU Wind Energy E; No. 0124, Tech. Rep., 2016, p. 98 (see pp. 44, 117).
- [131] R. Marquardt, „Stromrichterschaltungen mit verteilten Energiespeichern“, DE Patent App. DE2,001,103,031, Jan. 2001 (see p. 45).
- [132] R. Marquardt, J. Hildinger, and A. Lesnicar, „Modulares Stromrichterkonzept für Netzkupplungsanwendung bei hohen Spannungen“, in *Tagungsband der ETG Fachtagung 2002, Bad Nauheim, Ger.*, 2002 (see p. 45).
- [133] M. Saeedifard and R. Iravani, „Dynamic performance of a modular multilevel back-to-back HVDC system“, *IEEE Trans. Power Deliv.*, vol. 25, no. 4, pp. 2903–2912, 2010. DOI: 10.1109/TPWRD.2010.2050787 (see p. 45).
- [134] U. N. Gnanarathna, S. K. Chaudhary, A. M. Gole, and R. Teodorescu, „Modular multi-level converter based HVDC system for grid connection of offshore wind power plant“, in *AC DC Power Transm. 2010. ACDC. 9th IET Int. Conf.*, 2010, pp. 1–5. DOI: 10.1049/cp.2010.0984 (see p. 45).

- [135] U. N. Gnanarathna, A. M. Gole, A. D. Rajapakse, and S. K. Chaudhary, „Loss estimation of modular multi-level converters using electromagnetic transients simulation“, in *Int. Conf. Power Syst. Transients*, Delft, 2011, pp. 2–7 (see pp. 45, 211).
- [136] U. N. Gnanarathna, A. M. Gole, and R. P. Jayasinghe, „Efficient modeling of modular multilevel HVDC converters (MMC) on electromagnetic transient simulation programs“, *IEEE Trans. Power Deliv.*, vol. 26, no. 1, pp. 316–324, 2011. DOI: 10.1109/TPWRD.2010.2060737 (see p. 45).
- [137] J. Peralta, H. Saad, S. Denetière, J. Mahseredjian, and S. Nguéfeu, „Detailed and averaged models for a 401-level MMC-HVDC system“, *IEEE Trans. Power Deliv.*, vol. 27, no. 3, pp. 1501–1508, 2012. DOI: 10.1109/TPWRD.2012.2188911 (see pp. 45, 47).
- [138] H. Liu, K. Ma, Z. Qin, P. C. Loh, and F. Blaabjerg, „Lifetime estimation of MMC for offshore wind power HVDC application“, *IEEE J. Emerg. Sel. Top. Power Electron.*, vol. 4, no. 2, pp. 504–511, Jun. 2016. DOI: 10.1109/JESTPE.2015.2477109 (see p. 45).
- [139] M. Vasiladiotis, N. Cherix, and A. Rufer, „Impact of grid asymmetries on the operation and capacitive energy storage design of modular multilevel converters“, *IEEE Trans. Ind. Electron.*, vol. 62, no. 11, pp. 6697–6707, 2015. DOI: 10.1109/TIE.2015.2437329 (see pp. 45, 126).
- [140] —, „Accurate capacitor voltage ripple estimation and current control considerations for grid-connected modular multilevel converters“, *IEEE Trans. Power Electron.*, vol. 29, no. 9, pp. 4568–4579, 2014. DOI: 10.1109/TPEL.2013.2286293 (see pp. 45, 47, 126).
- [141] S. Debnath, J. Qin, B. Bahrani, M. Saeedifard, and P. Barbosa, „Operation, control, and applications of the modular multilevel converter: a review“, *IEEE Trans. Power Electron.*, vol. 30, no. 1, pp. 37–53, Jan. 2015. DOI: 10.1109/TPEL.2014.2309937 (see pp. 45, 47).
- [142] B. Jacobson, P. Karlsson, G. Asplund, L. Harnefors, and T. Jonsen, „VSC-HVDC transmission with cascaded two-level converters“, *CIGRE Sess.*, B4–B110, 2010 (see p. 45).

- [143] E. Prieto-Araujo, A. Junyent-Ferre, G. Clariana-Colet, and O. Gomis-Bellmunt, „Control of Modular Multilevel Converters Under Singular Unbalanced Voltage Conditions With Equal Positive and Negative Sequence Components“, *IEEE Trans. Power Syst.*, vol. 32, no. 3, pp. 2131–2141, May 2017. DOI: 10.1109/TPWRS.2016.2598617 (see pp. 46 sq., 126 sq., 130).
- [144] CIGRE Working Group B4.57, „Guide for the development of models for HVDC converters in a HVDC grid“, CIGRE, Tech. Rep. December, 2014 (see pp. 47, 124).
- [145] J. Saenz, A. Tapia, G. Tapia, *et al.*, „Reactive power control of a wind farm through different control algorithms“, in *4th IEEE Int. Conf. Power Electron. Drive Syst. (IEEE PEDS 2001)*, vol. 1, 2001, pp. 203–207. DOI: 10.1109/PEDS.2001.975311 (see p. 48).
- [146] S. Engelhardt, I. Erlich, C. Feltes, J. Kretschmann, and F. Shewarega, „Reactive power capability of wind turbines based on doubly fed induction generators“, *IEEE Trans. Energy Convers.*, vol. 26, no. 1, pp. 364–372, 2011. DOI: 10.1109/TEC.2010.2081365 (see p. 48).
- [147] T. Van Acker, B. Rawn, D. Van Hertem, S. Hendrix, and E. Lemaire, „Optimal design of the Mvar controller of far shore HVAC grid connections“, in *14th Wind Integr. Work.*, U. Betancourt and T. Ackermann, Eds., Brussels: Energynautics GmbH, 2015, pp. 1–5 (see pp. 48, 51).
- [148] B. Ronner, P. Maibach, and T. Thurnherr, „Operational experiences of STATCOMs for wind parks“, *IET Renew. Power Gener.*, vol. 3, no. August 2008, p. 349, 2009. DOI: 10.1049/iet-rpg.2008.0075 (see p. 48).
- [149] G. Tapia, A. Tapia, and J. X. Ostolaza, „Proportional-integral regulator-based approach to wind farm reactive power management for secondary voltage control“, *IEEE Trans. Energy Convers.*, vol. 22, no. 2, pp. 488–498, 2007. DOI: 10.1109/TEC.2005.858058 (see p. 50).
- [150] A. Tapia, G. Tapia, and J. X. Ostolaza, „Reactive power control of wind farms for voltage control applications“, *Renew. Energy*, vol. 29, no. 3, pp. 377–392, 2004. DOI: 10.1016/S0960-1481(03)00224-6 (see p. 50).

- [151] A. D. Hansen, P. Sørensen, F. Iov, and F. Blaabjerg, „Centralised power control of wind farm with doubly fed induction generators“, *Renew. Energy*, vol. 31, no. 7, pp. 935–951, 2006. DOI: 10.1016/j.renene.2005.05.011 (see p. 50).
- [152] R. G. de Almeida, E. D. Castronuovo, and J. A. Peças Lopes, „Optimum generation control in wind parks when carrying out system operator requests“, *IEEE Trans. Power Syst.*, vol. 21, no. 2, pp. 718–725, 2006. DOI: 10.1109/TPWRS.2005.861996 (see pp. 50 sq.).
- [153] L. Meegahapola, S. Durairaj, D. Flynn, and B. Fox, „Coordinated utilisation of wind farm reactive power capability for system loss optimisation“, *Eur. Trans. Electr. Power*, vol. 21, no. 1, pp. 40–51, 2011. DOI: 10.1002/etep.410 (see p. 50).
- [154] L. G. Meegahapola, E. Vittal, A. Keane, and D. Flynn, „Voltage security constrained reactive power optimization incorporating wind generation“, in *2012 IEEE Int. Conf. Power Syst. Technol. (POWERCON 2012)*, 2012, pp. 1–6. DOI: 10.1109/PowerCon.2012.6401436 (see p. 50).
- [155] S. Lauria, M. Maccioni, M. Schembari, A. Codino, and A. Faza, „Optimal power flow application to EHVAC interconnections for GW-sized Offshore Wind Farms“, in *2016 IEEE 16th Int. Conf. Environ. Electr. Eng.*, IEEE, Jun. 2016, pp. 1–6. DOI: 10.1109/EEEIC.2016.7555650 (see p. 50).
- [156] H. Van Pham, I. Erlich, and J. L. Rueda, „Probabilistic evaluation of voltage and reactive power control methods of wind generators in distribution networks“, *IET Renew. Power Gener.*, vol. 9, no. 3, pp. 195–206, 2015. DOI: 10.1049/iet-rpg.2014.0028 (see pp. 50 sq.).
- [157] M. Wilch, V. S. Pappala, S. N. Singh, and I. Erlich, „Reactive power generation by DFIG based wind farms with AC grid connection“, in *Power Tech, 2007 IEEE Lausanne*, 2007, pp. 626–632. DOI: 10.1109/PCT.2007.4538389 (see p. 51).
- [158] B. Zhang, W. Hu, P. Hou, and Z. Chen, „Reactive power dispatch for loss minimization of a doubly fed induction generator based wind

- farm“, in *2014 17th Int. Conf. Electr. Mach. Syst.*, 2014, pp. 1373–1378. DOI: 10.1109/ICEMS.2014.7013688 (see p. 51).
- [159] W. Nakawiro, I. Erlich, and J. L. Rueda, „A novel optimization algorithm for optimal reactive power dispatch: a comparative study“, *2011 4th Int. Conf. Electr. Util. Deregul. Restruct. Power Technol.*, no. 1, pp. 1555–1561, 2011. DOI: 10.1109/DRPT.2011.5994144 (see p. 51).
- [160] V. S. Pappala, M. Wilch, S. N. Singh, and I. Erlich, „Reactive power management in offshore wind farms by adaptive PSO“, in *2007 Int. Conf. Intell. Syst. Appl. to Power Syst.*, IEEE, Nov. 2007, pp. 1–8. DOI: 10.1109/ISAP.2007.4441595 (see p. 51).
- [161] H. Van Pham, J. L. Rueda, and I. Erlich, „Online optimal control of reactive sources in wind power plants“, *IEEE Trans. Sustain. Energy*, vol. 5, no. 2, pp. 608–616, 2014. DOI: 10.1109/TSTE.2013.2272586 (see p. 51).
- [162] M. Martinez-Rojas, A. Sumper, O. Gomis-Bellmunt, and A. Sudrià-Andreu, „Reactive power dispatch in wind farms using particle swarm optimization technique and feasible solutions search“, *Appl. Energy*, vol. 88, no. 12, pp. 4678–4686, 2011. DOI: 10.1016/j.apenergy.2011.06.010 (see p. 51).
- [163] V. S. Pappala, W. Nakawiro, and I. Erlich, „Predictive optimal control of wind farm reactive sources“, in *2010 IEEE PES Transm. Distrib. Conf. Expo. Smart Solut. a Chang. World*, 2010, pp. 1–7. DOI: 10.1109/TDC.2010.5484587 (see p. 51).
- [164] B. Zhang, P. Hou, W. Hu, *et al.*, „A reactive power dispatch strategy with loss minimization for a DFIG-based wind farm“, *IEEE Trans. Sustain. Energy*, vol. 7, no. 3, pp. 914–923, Jul. 2016. DOI: 10.1109/TSTE.2015.2509647 (see p. 51).
- [165] I. Erlich, W. Nakawiro, and M. Martinez, „Optimal dispatch of reactive sources in wind farms“, in *2011 IEEE Power Energy Soc. Gen. Meet.*, Jul. 2011, pp. 1–7. DOI: 10.1109/PES.2011.6039534 (see pp. 51, 71).

- [166] L. Willnauer and A. Marchand, „Offshore wind farm cluster design: the ClusterController“, in *EWEA Offshore 2013*, Frankfurt, 2013, p. 5 (see p. 51).
- [167] TenneT TSO GmbH, *Factsheet HelWin1*, 2016. [Online]. Available: http://www.tennet.eu/fileadmin/user_upload/Our_Grid/Offshore_Germany/HelWin1/2015_Factsheet-HelWin1_DE.pdf (visited on 02/03/2017) (see p. 52).
- [168] Ö. Göksu, J. N. Sakamuri, C. A. Rapp, P. Sørensen, and K. Sharifabadi, „Cluster control of offshore wind power plants connected to a common HVDC station“, *Energy Procedia*, vol. 94, pp. 232–240, Sep. 2016. DOI: 10.1016/j.egypro.2016.09.230 (see p. 52).
- [169] J. N. Sakamuri, N. A. Cutululis, Z. H. Rather, and J. Rimez, „Dynamic reactive power control in offshore HVDC connected wind power plants“, in *14th Wind Integr. Work.*, U. Betancourt and T. Ackermann, Eds., Brussels: Energynautics GmbH, 2015, p. 6 (see pp. 53, 57).
- [170] J. N. Sakamuri, Z. H. Rather, J. Rimez, *et al.*, „Coordinated voltage control in offshore HVDC connected cluster of wind power plants“, *IEEE Trans. Sustain. Energy*, vol. 7, no. 4, pp. 1592–1601, 2016. DOI: 10.1109/TSTE.2016.2569430 (see pp. 53, 58).
- [171] N. D. Tleis, *Power systems modelling and fault analysis : theory and practice*. Elsevier/Newnes, 2008, ISBN: 9780750680745 (see pp. 53 sq.).
- [172] F. Iov, A. D. Hansen, P. Sørensen, and N. A. Cutululis, „Mapping of grid faults and grid codes“, Risø National Laboratory, Risø, Tech. Rep. July, 2007, pp. 1–41 (see p. 53).
- [173] ENTSO-E, „Nordic and Baltic Grid Disturbance Statistics 2014“, ENTSO-E, Tech. Rep., 2015, pp. 1–79 (see pp. 53 sq.).
- [174] M. Bawart, M. Marzinotto, and G. Mazzanti, „Diagnosis and location of faults in submarine power cables“, *IEEE Electr. Insul. Mag.*, vol. 32, no. 4, pp. 24–37, Jul. 2016. DOI: 10.1109/MEI.2016.7528987 (see p. 54).

- [175] A. Abdalrahman and E. Isabegovic, „DolWin1 - challenges of connecting offshore wind farms“, in *2016 IEEE Int. Energy Conf.*, IEEE, Apr. 2016, pp. 1–10. DOI: 10.1109/ENERGYCON.2016.7513981 (see pp. 54, 120).
- [176] M. Bollen and L. D. Zhang, „Different methods for classification of three-phase unbalanced voltage dips due to faults“, *Electr. Power Syst. Res.*, vol. 66, no. 1, pp. 59–69, 2003. DOI: 10.1016/S0378-7796(03)00072-5 (see p. 55).
- [177] B. Silva, C. L. Moreira, H. Leite, and J. A. Pecas Lopes, „Control strategies for AC fault ride through in multiterminal HVDC grids“, *IEEE Trans. Power Deliv.*, vol. 29, no. 1, pp. 395–405, 2014. DOI: 10.1109/TPWRD.2013.2281331 (see p. 57).
- [178] M. Ndreko, M. Popov, J. C. Boemer, and M. A. M. M. Van Der Meijden, „Sensitivity analysis on short-circuit current contribution from VSC-HVDC systems connecting far and large offshore wind power plants“, in *IEEE PES Innov. Smart Grid Technol. Eur.*, 2014, p. 6. DOI: 10.1109/ISGTEurope.2014.7028961 (see p. 57).
- [179] M. Ndreko, M. Popov, A. A. van der Meer, and M. A. M. M. Van Der Meijden, „The effect of the offshore VSC-HVDC connected wind power plants on the unbalanced faulted behavior of ac transmission systems“, in *2016 IEEE Int. Energy Conf.*, Leuven, Belgium: IEEE, 2016, pp. 1–6. DOI: 10.1109/ENERGYCON.2016.7513950 (see p. 57).
- [180] M. Ndreko, J. L. Rueda, M. Popov, and M. A. M. M. Van Der Meijden, „Optimal fault ride through compliance of offshore wind power plants with VSC-HVDC connection by meta-heuristic based tuning“, *Electr. Power Syst. Res.*, vol. 145, pp. 99–111, 2017. DOI: 10.1016/j.epsr.2016.12.024 (see p. 57).
- [181] M. Ndreko, J. L. Rueda, M. Popov, and M. A. M. M. Van Der Meijden, „Optimal FRT compliance of offshore wind power plants in VSC-HVDC connection based on genetic algorithms“, in *19th Power Syst. Comput. Conf. PSCC 2016*, 2016, pp. 1–7. DOI: 10.1109/PSCC.2016.7540960 (see p. 57).

- [182] M. Mohammadi, M. Avendano-Mora, M. Barnes, and J. Y. Chan, „A study on fault ride-through of VSC-connected offshore wind farms“, in *2013 IEEE Power Energy Soc. Gen. Meet.*, IEEE, 2013, pp. 1–5. DOI: 10.1109/PESMG.2013.6672514 (see p. 57).
- [183] A. A. Van Der Meer, R. L. Hendriks, and W. L. Kling, „A survey of fast power reduction methods for VSC connected wind power plants consisting of different turbine types“, in *EPE Wind energy chapter 2nd Semin.*, Stockholm, 2009, p. 11 (see p. 57).
- [184] C. Feltes, H. Wrede, F. W. Koch, and I. Erlich, „Enhanced fault ride-through method for wind farms connected to the grid through VSC-based HVDC transmission“, *IEEE Trans. Power Syst.*, vol. 24, no. 3, pp. 1537–1546, Aug. 2009. DOI: 10.1109/TPWRS.2009.2023264 (see p. 57).
- [185] S. I. Nanou, G. N. Patsakis, and S. A. Papathanassiou, „Assessment of communication-independent grid code compatibility solutions for VSC–HVDC connected offshore wind farms“, *Electr. Power Syst. Res.*, vol. 121, pp. 38–51, Apr. 2015. DOI: 10.1016/j.epsr.2014.12.002 (see p. 57).
- [186] S. K. Chaudhary, R. Teodorescu, P. Rodriguez, and P. C. Kjaer, „Control and operation of wind turbine converters during faults in an offshore wind power plant grid with VSC-HVDC connection“, in *IEEE Power Energy Soc. Gen. Meet.*, 2011, pp. 1–8. DOI: 10.1109/PES.2011.6039804 (see p. 58).
- [187] A. Moawwad, M. S. El Moursi, and W. Xiao, „A novel transient control strategy for VSC-HVDC connecting offshore wind power plant“, *IEEE Trans. Sustain. Energy*, vol. 5, no. 4, pp. 1056–1069, Oct. 2014. DOI: 10.1109/TSTE.2014.2325951 (see p. 58).
- [188] G. Andersson, *Power system analysis*. Lecture 227-0526-00, ITET ETH Zürich, 2012 (see p. 62).
- [189] R. D. Zimmerman and C. E. Murillo-Sanchez, *Matpower 5.1 user’s manual*, 2015 (see p. 70).

- [190] A. Pettener, „SCADA and communication networks for large scale offshore wind power systems“, in *IET Conf. Renew. Power Gener. (RPG 2011)*, IET, 2011, pp. 11–11. DOI: 10.1049/cp.2011.0101 (see p. 71).
- [191] M. De-Prada-Gil, C. G. Alías, O. Gomis-Bellmunt, and A. Sumper, „Maximum wind power plant generation by reducing the wake effect“, *Energy Convers. Manag.*, vol. 101, pp. 73–84, Sep. 2015. DOI: 10.1016/j.enconman.2015.05.035 (see pp. 71 sq.).
- [192] S. Frandsen, R. Barthelmie, S. Pryor, *et al.*, „Analytical modelling of wind speed deficit in large offshore wind farms“, *Wind Energy*, vol. 9, no. 1-2, pp. 39–53, Jan. 2006. DOI: 10.1002/we.189 (see p. 72).
- [193] R. J. Barthelmie, G. C. Larsen, S. T. Frandsen, *et al.*, „Comparison of wake model simulations with offshore wind turbine wake profiles measured by sodar“, *J. Atmos. Ocean. Technol.*, vol. 23, no. 7, pp. 888–901, Jul. 2006. DOI: 10.1175/JTECH1886.1 (see p. 72).
- [194] M. Ali, J. Matevosyan, J. V. Milanović, and L. Söder, „Effect of wake consideration on estimated cost of wind energy curtailments“, in *8th Int. Work. Large Scale Integr. Wind Power into Power Syst. as well as Transm. Networks Offshore Wind Farms*, T. Ackermann and U. Betancourt, Eds., Bremen, Germany, 2009, pp. 1–9 (see p. 72).
- [195] J. Ainslie, „Calculating the flowfield in the wake of wind turbines“, *J. Wind Eng. Ind. Aerodyn.*, vol. 27, no. 1-3, pp. 213–224, Jan. 1988. DOI: 10.1016/0167-6105(88)90037-2 (see p. 72).
- [196] O. Rathmann, S. Frandsen, and R. J. Barthelmie, „Wake modelling for intermediate and large wind farms“, in *Wind Energy Conf. Exhib.*, Milan, Italy, May 2007 (see p. 72).
- [197] N. Jensen, „A note on wind generator interaction“, Risø National Laboratory, Roskilde, Tech. Rep., 1983 (see p. 72).
- [198] P.-E. Réthoré, A. Bechmann, N. N. Sørensen, *et al.*, „A CFD model of the wake of an offshore wind farm: using a prescribed wake inflow“, *J. Phys. Conf. Ser.*, vol. 75, no. 1, p. 012047, Jul. 2007. DOI: 10.1088/1742-6596/75/1/012047 (see p. 72).

- [199] M. de Prada Gil, O. Gomis-Bellmunt, A. Sumper, and J. Bergas-Jané, „Power generation efficiency analysis of offshore wind farms connected to a SLPC (single large power converter) operated with variable frequencies considering wake effects“, *Energy*, vol. 37, no. 1, pp. 455–468, Jan. 2012. DOI: 10.1016/j.energy.2011.11.010 (see p. 72).
- [200] Carbon Trust, „Offshore wind power: big challenge, big opportunity“, Carbon Trust, Tech. Rep., 2008, p. 112. [Online]. Available: <http://www.carbontrust.com/media/42162/ctc743-offshore-wind-power.pdf> (visited on 01/13/2015) (see p. 74).
- [201] French Government, „Arrêté du 17 novembre 2008 fixant les conditions d’achat de l’électricité produite par les installations utilisant l’énergie mécanique du vent“, French Government, Tech. Rep., 2008, pp. 1–7 (see p. 75).
- [202] K. S. Hansen, R. J. Barthelmie, S. C. Pryor, *et al.*, „Benchmark report on wake models at the wind farm scale“, The European Energy Research Alliance Design Tools for Offshore Wind Farm Cluster, Tech. Rep. June 2013, 2013, pp. 1–38 (see p. 103).
- [203] K. S. Hansen, P.-E. Réthoré, J. Palma, *et al.*, „Simulation of wake effects between two wind farms“, *J. Phys. Conf. Ser.*, vol. 625, Jun. 2015. DOI: 10.1088/1742-6596/625/1/012008 (see p. 103).
- [204] C.-T. Lee, C.-W. Hsu, and P.-T. Cheng, „A low-voltage ride-through technique for grid-connected converters of distributed energy resources“, *IEEE Trans. Ind. Appl.*, vol. 47, no. 4, pp. 1821–1832, Jul. 2011. DOI: 10.1109/TIA.2011.2155016 (see p. 121).
- [205] A. Camacho, M. Castilla, J. Miret, R. Guzman, and A. Borrell, „Reactive power control for distributed generation power plants to comply with voltage limits during grid faults“, *IEEE Trans. Power Electron.*, vol. 29, no. 11, pp. 6224–6234, Nov. 2014. DOI: 10.1109/TPEL.2014.2301463 (see p. 121).
- [206] L. Harnefors, A. Antonopoulos, S. Norrga, L. Angquist, and H.-P. Nee, „Dynamic analysis of modular multilevel converters“, *IEEE*

- Trans. Ind. Electron.*, vol. 60, no. 7, pp. 2526–2537, Jul. 2013. DOI: 10.1109/TIE.2012.2194974 (see p. 124).
- [207] R. H. Park, „Two-reaction theory of synchronous machines-I“, *Trans. Am. Inst. Electr. Eng.*, vol. 52, no. 2, pp. 352–354, Jun. 1933. DOI: 10.1109/T-AIEE.1933.5056309 (see p. 209).
- [208] C. L. Fortescue, „Method of symmetrical co-ordinates applied to the solution of polyphase networks“, *Trans. Am. Inst. Electr. Eng.*, vol. XXXVII, no. 2, pp. 1027–1140, 1918. DOI: 10.1109/T-AIEE.1918.4765570 (see p. 210).
- [209] A. Wintrich, U. Nicolai, W. Tursky, and T. Reimann, *Applikationshandbuch Leistungshalbleiter*. SEMIKRON International GmbH, 2010, ISBN: 978-3-938843-56-7 (see p. 210).
- [210] J. Beerten, S. Cole, and R. Belmans, „A sequential AC/DC power flow algorithm for networks containing multi-terminal VSC HVDC systems“, in *IEEE PES Gen. Meet. PES 2010*, IEEE, 2010, pp. 1–7. DOI: 10.1109/PES.2010.5589968 (see p. 210).
- [211] G. Daelemans, K. Srivastava, M. Reza, S. Cole, and R. Belmans, „Minimization of steady-state losses in meshed networks using VSC HVDC“, in *2009 IEEE Power Energy Soc. Gen. Meet.*, IEEE, 2009, pp. 1–5. DOI: 10.1109/PES.2009.5275450 (see p. 211).
- [212] A. António-Ferreira and O. Gomis-Bellmunt, „Modular multilevel converter losses model for HVdc applications“, *Electr. Power Syst. Res.*, vol. 146, pp. 80–94, May 2017. DOI: 10.1016/j.epsr.2017.01.010 (see p. 211).
- [213] P. S. Jones and C. C. Davidson, „Calculation of power losses for MMC-based VSC HVDC stations“, in *2013 15th Eur. Conf. Power Electron. Appl. EPE 2013*, 2013. DOI: 10.1109/EPE.2013.6631955 (see p. 211).
- [214] J. Freytes, F. Gruson, P. Delarue, F. Colas, and X. Guillaud, „Losses estimation method by simulation for the modular multilevel converter“, in *2015 IEEE Electr. Power Energy Conf.*, IEEE, Oct. 2015, pp. 332–338. DOI: 10.1109/EPEC.2015.7379972 (see p. 211).

- [215] T. Modeer, H.-P. Nee, and S. Norrga, „Loss comparison of different sub-module implementations for modular multilevel converters in HVDC applications“, *EPE J.*, vol. 22, no. 3, pp. 32–38, Sep. 2012. DOI: 10.1080/09398368.2012.11463829 (see p. 211).

Appendix A

Mathematical transformations and converter losses

A.1 Reference frame and sequence transformations

In the time domain, the Clarke- and Park-transformations relate the stationary abc -reference frame with the stationary $\alpha\beta 0$ - and synchronous $dq 0$ -reference frames, respectively. The Clarke-transformation \mathbf{C} transforms the abc -reference frame vector x_{abc} into the $\alpha\beta 0$ -reference frame vector $x_{\alpha\beta 0}$:

$$x_{\alpha\beta 0} = \mathbf{C} x_{abc}; \quad \mathbf{C} = \frac{1}{3} \begin{bmatrix} 2 & -1 & -1 \\ 0 & \sqrt{3} & -\sqrt{3} \\ 1 & 1 & 1 \end{bmatrix} \quad (\text{A.1})$$

The transformation of the vector x_{abc} in the stationary abc -reference frame into the synchronous $dq 0$ -reference frame vector $x_{dq 0}$ is made by the so-called Park-transformation $\mathbf{T}(\theta)$ which results from the Clarke-transformation under rotation of angle θ [207]:

$$x_{dq 0} = \underbrace{\mathbf{C}\mathbf{R}(\theta)}_{\mathbf{T}(\theta)} x_{abc}; \quad \mathbf{R}(\theta) = \begin{bmatrix} \cos \theta & \sin \theta & 0 \\ -\sin \theta & \cos \theta & 0 \\ 0 & 0 & 1 \end{bmatrix} \quad (\text{A.2})$$

In the phasor domain, the stationary abc -reference frame vector x_{abc} might be transformed by the Fortescue-transformation \mathbf{F} into symmetrical

components x_{120} [208]:

$$x_{120} = \mathbf{F} x_{abc}; \quad \mathbf{F} = \frac{1}{3} \begin{bmatrix} 1 & \alpha & \alpha^2 \\ 1 & \alpha^2 & \alpha \\ 1 & 1 & 1 \end{bmatrix} \quad (\text{A.3})$$

$$\alpha = \exp(j2\pi/3)$$

where:

α = Fortescue-operator (rotates a phase vector by 120° counter-clockwise).

The inverse Clarke-, Park-, and Fortescue-transformations are consequently denoted \mathbf{C}^{-1} , $\mathbf{T}(\theta)^{-1}$, and \mathbf{F}^{-1} , respectively.

A.2 Converter loss model for power system studies

Power losses in a power converter appear mainly in the semiconductor switches during the switching and conducting process [122], [209]. Detailed loss models depend, apart from the converter current, from the used modulation strategy, switching frequency, and semiconductor switch characteristics [122], [209]. However, approximated models are sufficient for power system studies [210].

The converter current magnitude I_c the most significant factor for the loss calculations. The injection of active and reactive power, P_c and Q_c , define the ac converter current I_c according to Eqn. (A.4):

$$I_c = \frac{\sqrt{P_c^2 + Q_c^2}}{\sqrt{3} \cdot U_{LL,rms}} \quad (\text{A.4})$$

The switching and conduction losses P_{conv}^{loss} of a VSC might be approximated by a quadratic polynomial function in dependence of the converter current I_c , considering three parts: constant, linear, and quadratic losses [20].

$$P_{conv}^{loss} = \left[a + b \cdot \frac{I_c}{I_r} + c \cdot \left(\frac{I_c}{I_r} \right)^2 \right] \cdot S_r \quad (\text{A.5})$$

where:

I_r = rated converter current;

S_r = rated apparent power.

Typical loss data for a system rated to $U_{dc} = \pm 300$ kV, $S_n = 600$ MVA based on a 2L–HVdc can be found in [211]. For a MMC–HVdc the current–dependent losses in the converter valves are approximately halved compared to a 2L–HVdc mainly because of the reduced switching frequency [135]. More detailed loss models for power system studies with the MMC–HVdc might be found in [212]–[215].

Table A.1: Typical converter loss parameter values used in [20], [135], [211].

System	a	b	c
Wind turbine GSC	0.0005	0.0097	0.0048
2L–HVdc rectifier ¹	0.0083	0.0030	0.0032
MMC–HVdc rectifier ¹	0.0042	0.0015	0.0016

¹ All studies in the thesis consider solely the offshore converter which acts primarily as rectifier.

Appendix B

List of publications

The thesis-related publications as well as co-authored publications are listed.

B.1 Journal publications

- [J1] K. Schönleber, C. Collados, R.T. Pinto, S. Ratés-Palau, O. Gomis-Bellmunt, Optimization-based reactive power control in HVDC-connected wind power plants, *Renew. Energy*. 109 (2017) 500–509.
doi:10.1016/j.renene.2017.02.081.
- [J2] K. Schönleber, E. Prieto-Araujo, S. Ratés-Palau, O. Gomis-Bellmunt, Handling of unbalanced faults in HVDC-connected wind power plants, *Electr. Power Syst. Res.* 152 (2017) 148–159.
doi:10.1016/j.epsr.2017.06.026.
- [J3] K. Schönleber, S. Ratés-Palau, O. Gomis-Bellmunt, Analysis of reactive power strategies in HVDC-connected wind power plant clusters, *Wind Energy*, vol. 20, no. 12, pp. 1971–1982, Dec. 2017.
doi:10.1002/we.2134.

B.2 Journal publications submitted/under revision

- [S–J4] K. Schönleber, E. Prieto-Araujo, S. Ratés-Palau, O. Gomis-Bellmunt, Extended Current Limitation for Unbalanced Faults in MMC–HVDC-connected Wind Power Plants, *submitted to IEEE Trans. on Power Delivery in July 2017*.

B.3 Conference publications/presentations

- [C1] K. Schönleber, S. Ratés-Palau, M. De-Prada-Gil, O. Gomis-Bellmunt, Reactive power optimization in HVDC-connected wind power plants considering wake effects, in: U. Betancourt, T. Ackermann (Eds.), 14th Wind Integr. Work., Energynautics GmbH, Brussels, Belgium, 2015.
- [C2] K. Schönleber, S. Ratés-Palau, O. Gomis-Bellmunt, Optimization-based reactive power control in HVDC-connected wind power plants, Poster Session in Special Session on Offshore and HVDC grids in: Energy Conference (ENERGYCON) 2016 IEEE International, Leuven, Belgium, 2016.
- [C3] K. Schönleber, E. Prieto-Araujo, O. Gomis-Bellmunt, Fault ride-through of unbalanced ac grid faults in HVdc-connected offshore wind power plants, in: U. Betancourt, T. Ackermann (Eds.), 16th Wind Integr. Work., Energynautics GmbH, Berlin, Germany, 2017.

B.4 Co-authored publications (not included in thesis)

- [J5] M. Raza, K. Schönleber, O. Gomis-Bellmunt, Droop Control Design of Multi-VSC Systems for Offshore Networks to Integrate Wind Energy, *Energies*. 9 (2016) 826. doi:10.3390/en9100826.
- [J6] S. Wenig, F. Rojas, K. Schönleber, M. Suriyah, T. Leibfried, Simulation framework for DC grid control and ACDC interaction studies based on modular multilevel converters, *IEEE Trans. Power Deliv.* 31 (2016) 780–788. doi:10.1109/TPWRD.2015.2417681.
- [C4] D. Ricchiuto, K. Schönleber, S. Ratés-Palau, L. Trilla, J.L. Dominguez-Garcia, O. Gomis-Bellmunt, Overview of high-power medium-frequency DC/DC converter topologies for wind turbines interfaced to a MVDC collection grid, in: EWEA 2015 Proc., EWEA, Paris, 2015.

B.5 Patent applications (not included in thesis)

- [P1] K. Schönleber, S. Ratés-Palau, and A. Langel, SYSTEMS AND METHODS FOR PROVIDING ELECTRICAL POWER TO WIND TURBINE COMPONENTS, EP17382357, 09-Jun-2017.

Curriculum vitae



Kevin Schönleber was born in Mannheim, Germany, on September 27, 1986. In October 2006 he started studying Electrical Engineering at Karlsruhe Institute of Technology (KIT) in Karlsruhe, Germany. From December 2011 to October 2012 he was with ABB in Turgi, Switzerland, as an intern and student employee in the medium-voltage power converter for wind department. He carried out his diploma thesis on MMC-HVdc modeling at the Institute of Electrical Energy Systems and High-Voltage Engineering (IEH) at KIT. In January 2013, he received the Diplom-Ingenieur degree in Electrical Engineering from KIT. In January 2014, he joined wind turbine manufacturer Alstom Renovables España (now General Electric Renewable Energy) in Barcelona, Spain, as an early-stage-researcher in the *MEDOW* project in the Energy Conversion department. Consequently, he enrolled his Doctoral studies in Electric Engineering at Universitat Polytecnic de Catalunya (UPC) in Barcelona, Spain. During 2015 and 2016, he conducted two research stays of three months at Cardiff University in Cardiff, Wales, and at Danmarks Tekniske Universitet (DTU) in Risø, Denmark, respectively.